Modal Filtering for Active Control of Floor Vibration under Impact Loading

Kai Xue

2018

Modal Filtering for Active Control of Floor Vibration under Impact Loading

A Dissertation

Submitted to

the Department of Urban Management Graduate School of Engineering of Kyoto University

In Partial Fulfillment

of the Requirements for the Degree of

Doctor of Engineering

By

Kai Xue

2018

For my family...

Declaration

I hereby declare that except where specific reference is made to the work of others, the contents of this dissertation are original and have not been submitted in whole or in part for consideration for any other degree or qualification in this, or any other University. This dissertation is the result of my own work and includes nothing which is the outcome of work done in collaboration, except where specifically indicated in the text. This dissertation contains less than 60,000 words including appendices, bibliography, footnotes, tables and equations and has less than 300 figures.

Kai Xue

2018

Acknowledgements

Time passes quickly, I have spent more than three years at Kyoto University without noticing it and I have acquired so much new knowledge and skills during my Ph.D. period. I would like to take this opportunity to thank those special individuals who gave me invaluable advice and contributed to my work and life.

I would like to firstly express my gratitude to the Ministry of Education, Culture, Sports, Science and Technology, Japan (MEXT) for granting me the financial support "Monbugakakusho Scholoship" during my stay in Japan.

My foremost and sincere appreciation goes to Prof. Akira Igarashi, my supervisor for his course corrections and thoughtful input which shaped my dissertation. I have never experienced such a nice professor from whom I learned a lot about how to conduct research and treat it with heart. He inspired me with kind smile and positive attitude when I felt disappointed and confused. He also provided me many opportunities to attend kinds of summer school activities and international conferences, by which my abilities of conveying my ideas to others were well improved. I was deeply impressed on his serious attitude on research, as well as the amiable feeling he gave me during the daily communication. I am eternally grateful for everything that he has done for me.

I would also like to acknowledge Prof. Yagi Tomomi and Prof. Aiko Furukawa for their generous and invaluable guidance in reviewing my dissertation. I wish to express my gratitude to Prof. Nozomu Yoneyama for his generous and continuous support. I deeply thank Dr. Dang Ji of Saitama University for his continuous encouragement, support, and giving me the opportunity to study at Kyoto University. He provided me a lot of advices on doing research, oral presentation and writing paper.

I acknowledge Mr. Takahiro Kachi, Mr. Naoto Ohazama and Mr. Ido of the Sumitomo Riko Co. Ltd. With the help of them, I was able to do the experiments at the company. The work I did and the people I met there improved my career development path a lot.

I appreciate it very much that I had excellent colleagues in my lab. Prof. Su yi, William J. Pringle, Nagashima hiroshi, Liu yanyan, He xinhao, Wei wei, Hiroto Nishiike, Yutaka Tanaka, Jun Kitagawa, Masahiro Kita, Yusuke Sugano, Subaru Gigyo, Toru Kuriyama, Taichi Krao, Shota Kurino, Hiroshi Takii and Shintaro Hata. I enjoyed every moment with them.

I would also like to thank my friends in Uji campus. Wan li, Song Shaotang, Chen chen, Lu xiangxun and Wang tiehua. I appreciated everyone and I was so happy that they kept me company during these oversea years.

Meanwhile, I would like to thank my friends in China. They helped me with spirits on my way of pursuing my Ph.D. degree.

Finally, I am grateful to my family and girlfriend, the most important people for me in this world. They always support me silently. Without their support and care, I would not be able to achieve my goals and pursue my dream.

Abstract

Excessive floor vibration that annoys occupants is an important and growing problem in residential buildings. Active control of these vibrations using sensors, actuators and controllers is a promising way because of its simplicity and its high effectiveness in vibration cancellation and the ability to deal with multiple modal responses compared to the passive and semi-active control. Methods currently used to suppress the floor vibrations are direct-output feedback control and model-based control. In the model-based control, a state estimator is used to approximate the controlled mode states, upon which a gain matrix is applied to generate the actuator commands. This enables controlling the floor modes of interest and meticulous control manipulation for each mode to make the system more amenable to the introduction of significant damping and stability margins.

Modal filtering is one type of the state estimators. The modal filtering method applies sets of spatial weighting coefficients to the responses measured by sensors to extract individual modal responses from the global responses of the structure. The actuator commands are then obtained as the summation of control signals for individual modes. The focus of this research is to develop approaches for active control of floor vibrations based on the modal filtering technique and the efforts are mainly toward algorithm development and experimental verification.

The optimal sensor and actuator placement is first studied. Because only a few number of lower modes or modes in the bandwidth of interest are considered to be controlled in general, the truncated modes may cause spillover effects when the system is subjected to disturbance excitations or control forces. Sensor and actuator placement determination procedures are developed so that enhancement of the separation performance of the modelled modes and reduction of the spillover effects of the truncated modes are achieved at the same time. It is realized by combining the minimum spillover method, effective independence method (EFI) and modal assurance criterion (MAC).

After determination of the sensor and actuator placement, modal filtering can then be used to extract the desired modes. Since the actuator and digital signal processor (DSP) dynamics involving large phase delays of the actuator forces from the input signals can strongly influence the dynamics of the controlled floor system, the phase-lead velocity feedback controller is developed for each control mode using the root locus method. Through this controller, high damping ratios and high stability margins for the control modes are achieved.

In most cases, the actuator is not the only dynamic component that affects the system dynamics. Avoiding the tedious procedure of the root locus method when multiple dynamic components are involved, a simple and cost-effective framework, taking advantage of the

mode-by-mode control approach is preferable. For this purpose, automatic phase compensation techniques are proposed. Phase compensation can be implemented by a simple weighted linear combination of integration with the target modal control signal itself, which is similar to the proportional-integral (PI) technique. The PI parameters can be obtained automatically through a series of real-time experiments and the only information needed for the phase compensation is the modal frequencies of the controlled modes.

Finally, as the generalization of modal filtering, the spatio-temporal filter is utilized to filter the global responses. The spatio-temporal filtering extends the capabilities of the conventional modal filtering by applying temporal (time) information. For the conventional modal filtering, the floor structure must be accurately modelled to ensure control stability and performance. However, in many real world applications, this modelling effort can take the majority work required to develop an active control strategy. In addition, the conventional modal filtering technique combined with low pass filter cannot totally eliminate the spillover effects of the residual modes. Therefore, the spatio-temporal filtering combined with the phase compensated velocity feedback controller is developed to achieve a simple and robust active control strategy with less model information of both the actuator and floor system. Time delays and spillover effects are considered inherently in this control strategy.

Contents

List of Figures

List of Tables

Abbreviations

ADC (A/D)	Analog-to-Digital Conversion
AVC	Active Vibration Control
BNC	Bayonet Neil-Concelman
CAF	Compensated Acceleration Feedback
CCS	Code Composer Studio
DAC (D/A)	Digital-to-Analog Conversion
DAF	Direct Acceleration Feedback
DOFB	Direct Output Feedback
DOF	Degree of Freedom
DSK	DSP Starter Kit
DSP	Digital Signal Processor
DVF	Direct Velocity Feedback
DVF with FTT	Direct Velocity Feedback with Feed-through Term
EFP	Effective Points
EFI	Effective Independence Method
ELP	Elite Point
ERA	Eigensystem Realization Algorithm
EV	Elite Value
FEM	Finite Element Method

FFT	Fast Fourier Transform
FIR	Finite Impulse Response
FRF	Frequency Response Function
GA	Genetic Algorithm
ICP	Integrated Circuit Piezoelectric
IIR	Infinite Impulse Response
IMSC	Independent Modal Space Control
IV	Instrument Variable
LMA	Lebenberg-Marquardt Algorithm
LMS	Least Mean Square
LQG	Linear Quadratic Gaussian
LSS	Large Space Structure
LTI	Linear Time Invariant
MAC	Modal Assurance Criterion
MB	Model Based
MDOF	Multi-Degree-of Freedom
MDVF	Modal Direct Velocity Feedback
MF	Modal Filtering
MIMO	Multi-input Multi-output
MSISO	Multiple Single-input Single-output
MTMD	Multiple Tuned Mass Damper
NS	Number of Sensors
OAP	Optimal Actuator Placement
OSP	Optimal Sensor Placement
PCVFB	Phase Compensated Velocity Feedback

PLVFB	Phase-lead Velocity Feedback
PI	Proportional Integral
PI	Performance Index
RDVF	Response-dependent Velocity Feedback
RLS	Recursive Least Squares
RMS	Root Mean Square
RMV	Reciprocal Modal Vector
SDOF	Single Degree of Freedom
SISO	Single-input Single-output
STF	Spatio-Temporal Filter
TF	Transfer Function
TMD	Tuned Mass Damper

Chapter 1 Introduction

1.1 Floor vibration problem

In recent years, with the advancements in structural technology and modern trends in building layouts, unwanted vibrations of structures are sometimes experienced due to less inherent damping under human induced excitation [1]. For the case of residential houses and buildings, the vibration problems caused by human-induced excitation spoil the environmental quality and the acoustical comfort for the occupants. In general, the human live loads can be classified into two broad categories: in situ and moving [2]. Periodic jumping, sudden object dropping and random in-place movements are examples of in situ activities. Walking and running are examples of moving activities. It should be noted that these kinds of human-induced vibrations are in fact a serviceability problem and rarely do they affect the fatigue behavior or safety of floor structures [3]. Design codes and standards are primarily concerned with avoiding structural failure and deal with excessive vibrations only to a limited degree [4]. However, the structure should not only be sufficiently strong but also comply with comfort and serviceability criteria.

The human perception of vibrations is, at one level, very sensitive, the acceptance criterion is possible to be set at a low level. At another level, it is very insensitive, a small quantitative change in the amplitude of vibration corresponds to a relatively small change in perception [2]. Human reaction at these levels depends on a number of factors such as the task or activity of the perceiver, the remoteness of the source, other objects movement in the surroundings and the orientation of body (standing or sitting). Perception is also affected by the characteristics of vibration response including frequency, amplitude and duration [5]. It must be point out that although floor vibration may cause a sense of insecurity in some people, it does not necessarily imply any lack of structural safety.

One important parameter that determines the responses of floor structures is natural frequency. The floors can be divided into ‘low frequency floor’ and ‘high frequency floor’ depending on the natural frequency of the first mode [2], [6], [7]. If the fundamental mode is below 10Hz, the floor is called low frequency floor. Large space and long span offices and sports stadiums are examples of ‘low frequency floor’. On the other hand, if the fundamental mode is beyond 10Hz. The floor is considered as ‘high frequency floor’. Small space collective housing is one example of the ‘high frequency floor’. For ‘low frequency floor’, the floor is considered to be prone to resonant vibration under excitations like walking-induced force, which means that the harmonics of force frequency can excite structural modes. For example, walking pacing rates have been measured to have frequency vary between 1.4Hz and 2.5Hz. Some of the harmonics have a frequency that potentially can excite structural modes greater than 4Hz [1]. On the other hand, for ‘high frequency floors’, it has been found that the response from each excitation dissipates before the next occurs, so the floor behaves impulsively to each excitation [8].

Another key parameter that affects the floor responses is the level of damping present in the floor system [1]. As damping increases, the steady-state responses due to walking become a series of transient responses, resulting in a less significant responses for ‘low frequency floor’. On the other hand, the impulsive responses attenuate quickly for the ‘high frequency floor’ if a large damping ratio exists. Increasing the level of damping in the floor structure is one of the general strategies for suppression of the human-induced vibrations.

1.2 Vibration control for floors

In most cases, the floors found to vibrate at levels annoying to building occupants after the completion of their construction. Several vibration mitigation techniques are currently used for controlling the vibration of floor structures. These are structural modification, passive control, active control and semi-active control.

1.2.1 Structural modification

The traditional methods for improving the vibration performance of floors involve major additions to the original structures. The addition of non-structural full-height partitions is one of the solutions [9]. This can add support and increase the damping of a floor, however, research has been shown that there is the possibility that annoying vibrations can be transfer to another location. This might extend the excessive vibration problem to other locations within the building.

An alternative method is to stiffen the floor by installing extra columns to the most flexible members [2]. The extra stiffness can reduce the amplitude of vibration and increase the frequencies of vibration of the floor at the same time. It is possible to shift the floor frequencies so that resonance with the excitation is avoid or reduced if the excitation frequency is known [10]. The addition of columns or increasing beam or girder sections by cover plating are also implemented when the excessive floor vibrations exist.

It should be noted that correcting these floors using structural modification is extremely difficult and can be expensive. Usually, these retrofits must be done in the occupied building which adds significantly to the cost [11]. The modification is extremely disruptive if the building is occupied.

1.2.2 Passive control

In general, there is no fixed frame of reference against which a passive device can react, therefore, Tuned Mass Damper (TMD) consisting of a mass, a spring and a damper has been proposed to reduce the responses of floor structures to human-induced vibrations [10], [11]. The mechanism of suppressing floor vibrations by attaching a TMD is to transfer the vibration energy of the floor to the TMD and to dissipate the energy at the damper of the TMD. In order to increase the ability of energy dissipation in a TMD, it is essential to tune the natural frequency to that of the floor motion and to select the appropriate capacity of the damper, which means there exist optimum parameters of a TMD [12]–[14].

There are some disadvantages using a TMD to reduce the vibrations. First, a TMD's effectiveness is sensitive to a fluctuation in the natural frequency or that in the damping ratio of the TMD. Also, the performance of a TMD is decreased by the mistuning or the off-optimum damping of the TMD [15].

Multiple Tuned Mass Dampers (MTMD) with distributed natural frequencies has been proposed to improve the robustness of TMD [16]. It is found that for the given total number of TMD's, there exists an optimum MTMD with the optimum frequency range and the optimum damping ratio. For convenience of manufacture, the mass and damping of each TMD are usually the same. The effectiveness and robustness of MTMD is significantly improved from a TMD for the same amount of mass ratio.

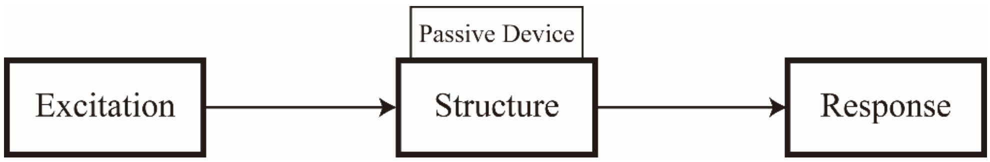

Figure 1.1 Passive control

The advantages of passive devices are that no external power source is used and that their unconditional stability as the whole system is guaranteed since no phase delay issue accompanied with feedback mechanism is utilized for vibration suppression, as shown in Figure 1.1 [17]. However, due to their passive characteristics, the vibration reduction is often of limited effectiveness. The required level of reduction of sound-source vibration would be in the order of 10dB or more so that the cancellation be perceivable with significance, but application of existing passive devices to floor vibration problem has not been successful in achieving this level of reduction. Also, for each passive device, such as TMD, it often has to be tuned to damp a single frequency-band vibration related to the specified natural mode of the structural system. Furthermore, since the reduction of response at one frequency may cause a large response at other frequencies, care must be taken in the case of human-induced vibrations possibly involving occur over a range of excitation frequencies [1].

1.2.3 Active control

Recent advances in digital signal processing, sensor and actuator technology have prompted interest in active vibration control (AVC) [18]. Active control makes use of small units than some of their passive counterparts, and it can be a promising way to suppress the vibration of floor structures because of its high effectiveness of vibration cancellation and the ability to damp multiple modes easily. The concept of active control of structures is often viewed as an attempt to make them behave like machines or human-beings in the sense that they can be make adaptive or responsive to outside excitations [1]. It is based on monitoring of structural responses by sensors at pre-selected locations to disturbing forces and application of control forces calculated by the controller through an external energy source like actuator to improve the dynamic behavior of the floor structure, as shown in Figure 1.2 [17], [19]. Even though the concept is very simple, it is only with the development of low-cost fast digital processing systems during the last decades that the implementation of practical active control systems has become feasible [20]. The most challenging aspect of active control in civil engineering is the fact that it is an integration of a number diverse disciplines which are in general not within the domain of traditional civil engineering [21], [22]. These include control theory, signal processing, computer science, sensing dynamics as well as stochastic processing and structural dynamics. This facilitates collaborative research efforts among researchers from different background and accelerates the research-to-implementation process as one sees today.

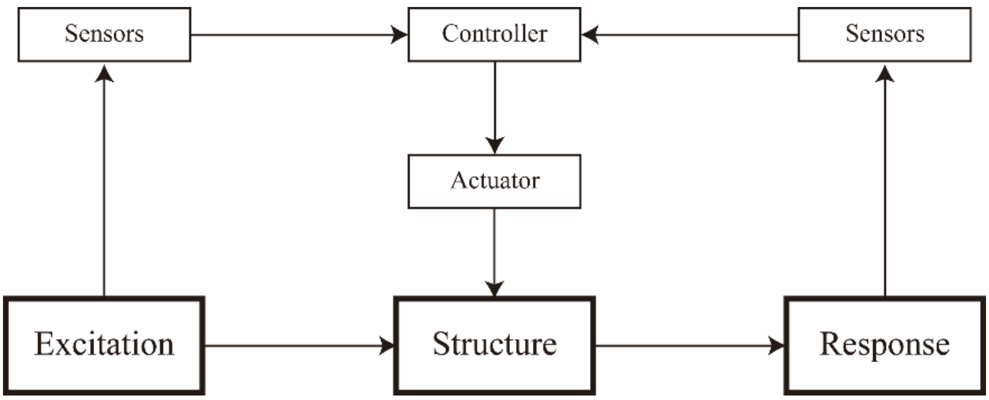

Figure 1.2 Active control

In terms of the information that is processed by the controller, control laws can be divided into the following three categories [1]:

1. Feedforward control (open loop), where the excitation force is measured and used to calculate the control force in a pre-defined manner without responding to how the load reacts.
2. Feedback control (closed loop), where the structural response is measured and used to calculate the control force.
3. Feedforward-feedback control, where both of the excitation force and response force are measured and used to calculate the control force.

In the case of human-induced vibrations, since it is very difficult to detect the excitation force, feedback control laws are in general used for the vibration control [11]. Direct-Output feedback (DOFB) controllers and Model Based (MB) controllers are served as two different categories for the feedback control. In DOFB controllers, the sensor outputs are multiplied by a gain matrix to produce the actuator commands and most previous research in the floor vibration suppression field has focus on these controllers. The advantage of these controllers are their robustness to spillover effects due to un-modelled modes and it is unconditionally stable in the absence of actuator and sensor dynamics [23]. However, when the sensors and actuators are not collocated and their dynamics are considered, unconditional stability is no longer accomplished [24], [25]. Model-based controllers, on the other hand, use a state estimator to approximate the controlled mode states, upon which a gain matrix is applied to generate the actuator commands and these controllers are widely used in civil engineering for wind and seismic response cancellation [26], [27]. An accurate structural model is usually needed for model-based controllers. For the floor vibration control, these methods are not widely used mainly due to the requirement of the higher processing power and difficulty in the implementation compared with DOFB methods [1].

1.2.4 Semi-active control

A compromise between active and passive control systems has been developed in the form of the semi-active control system, see Figure 1.3 [17]. The semi-active control system maintains the reliability of the passive control system while has the feature of adjusting parameter characteristics of an active control system [28]. Semi-active control typically requires a small external power source for operation and uses the motion of the structure to generate the control forces for vibration suppression. The magnitude of control forces can be adjusted by the external power source. Same as the active control, the control forces are generated based on feedback signals from sensors that measure the structural responses. Note that the semi-active control devices cannot inject the mechanical energy into the controlled floor system implying that the semi-active control devices do not have the potential to destabilize the floor system [29].

The advantages of semi-active control enhance the vibration control performance of these devices over their passive counterparts during proper functioning, while still have some functionality in case of power failure. Electrorheological and magnetorheological dampers, semi-active TMD's [30] and semi-active constrained layer damping are currently investigated for the implementation of structural vibration control. Although semi-active control has great potential for control of vibration in floors, it requires more research before this technology is applied at a stage for implementation in floor structures [1].

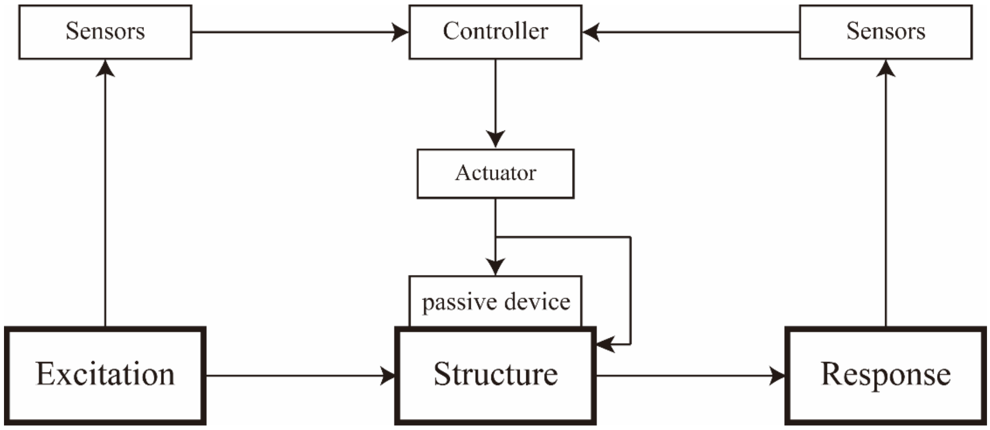

Figure 1.3 Semi-active control

1.3 Modal model

The number of degrees of freedom (DOF) of a floor structure is theoretically infinite. The finite element method (FEM) is typically employed to approximate the continuous structure. This is done by discretizing the structure into elemental simple shapes of known mass and stiffness matrices. The global mass and stiffness matrices synthesised from local mass and stiffness matrices can be used to analyse the original complex structural model with good accuracy.

It is effectively a mathematical approximation of the continuous structure as a lumped system. The continuous system are lumped at discrete locations resulting in n multi-degree-of freedom (MDOF) system. The size of n is on the order of millions for large complex structures [31]. A reduced set of coordinates known as modal coordinates are typically used for analysis.

The modal model of the system assumes that the deflections at all points of a structure are equal to a linear combination of an infinite number of mode shapes. Since the responses of high modes are negligible, the deformation can be approximated by a reduced set of modal coordinates and mode shapes which dominate the responses as:

$$x(t) \approx q_1(t)\phi_1 + q_2(t)\phi_2 + \cdots + q_m(t)\phi_m \tag{1-1}$$

where $x(t)$ is the point responses with dimensions $n \times 1$. $q_1(t), q_2(t), \ldots, q_m(t)$ are modal coordinate scalars varying with time t and $\phi_1, \phi_2, \ldots, \phi_m$ are mode shape functions with dimensions $n \times 1$ which satisfy the boundary conditions. A mode is the manifestation of energy that is trapped within the boundaries of the structure and cannot readily escape. Generally $m \ll n$ after modal truncation. Each mode shape corresponds to a particular modal natural frequency. Since the level of excitation of each mode will depend on the frequency and action location of external forces, certain mode shapes can be included in the modal model and certain can be ignored. The lower frequency mode shapes tend to be excited and to dominate the responses in most environments.

The modal coordinates also characterize the dynamics of a structure. They can be used to represent modal velocities and accelerations of a system. Thus they have a dynamic nature, which can be very useful in moving the response of the structure if controlled. It has been shown above that the linear response is a function of the combined motions of its modes of vibration when a structure is excited. Likewise, when the excitation source is removed, the trapped energy within the structure will slowly decay out until it no longer vibrates. The rate at which energy decays out of the structure is determined by the amount of damping involved. Damping is also a modal property, each mode having a certain value of damping associated with it and the motion of heavily damped modes will decay out more quickly than that part of the motion comprised of more lightly damped modes. However, it should be noted that superposition of mode shapes to represent general deformation is only true for small deformations. For the human-induced floor vibrations, small deformations are usually the case. Therefore, it is of significant interest and applicability to use modal coordinates in human-induced floor control system as the basis of control system development.

Literatures have shown that the modal coordinates can be estimated from measured responses and used for purposes of control, identification and structural monitoring. Modal filtering techniques, e.g. modal filtering (MF) and spatio-temporal filtering (STF), are typically used to abstract modal responses. The development of modal filtering techniques will be reviewed in the next chapter.

1.4 Objective of the study

The objective of this study is to develop simple model-based feedback active control algorithms and implementations for the vibration control of floor structures. As has been introduced in Sec. 1.2, the active control technique has the greatest potential to suppress the floor vibrations compared to its passive or semi-active counterparts. Loss of effectiveness of active control in case of power failure would not be a critical problem for floor vibration suppression, since it is essentially a comfort improvement application during a regular service, as opposed to the case of safety problems in which interruption of the system’s functioning becomes a critical factor.

As described in Sec. 1.3, in practice, the continuous system is often treated as a lumped n multi-degree-of-freedom (n-MDOF) system established by using the responses at discrete locations on the system as the degrees of freedom. The dynamic responses of a floor can be expressed as the combination of its natural vibration modes, which are determined by the dimensions of the floor, material properties and boundary conditions. Using the modal filtering techniques, the measured responses can be decomposed into dynamic behavior of the natural modes, and the control of the responses can be considered for the individual modes based on the filtered modal responses.

The advantages of this independent modal space control technology can be explained by several reasons. Firstly, in general, the 'modal contents' in the floor impact sound that cause the practical problem are within a specific frequency range, therefore, concentrating the control energy to the reduction of the responses of the natural modes in that problematic frequency range while neglecting the other natural modes can greatly contribute to minimize the required capacity of the control system in achieving the objective of the active control application. Secondly, the independent modal space control can simplify the frequency response compensation of the dynamic components such as the actuator with respect to amplitude and phase. It is known that the actuators and sometimes other dynamic components are involved in the control system, and their dynamics may introduce large time delays to the command control signals as shown in Figure 1.4, where the blue line represents the control force command signal and the red line represents the actual control forces. Since each natural mode components in the control signal is expected to be a single narrow frequency band, time delays (phase lags) can be easily compensated around the natural frequency of the control mode. If this idea is used, complicated compensation schemes or high-order controllers for phase compensation, which are effective in a wide frequency range, are not necessary. Furthermore, the independent modal space active control makes it possible to use different controllers and choose different control gains for different control modes, which contributes the control systems more flexible to deal with practical problems. Therefore, a simple and effective framework is expected to be achieved to the control system implementation by taking advantage of the mode-by-mode control approach.

In this study, the modal filtering techniques (MF and STF) combined with modal direct velocity feedback controller are utilized as the basis of the active control testing that incorporate modal phase compensation techniques for time delays of dynamic components. The modal direct velocity feedback controller has the advantage of simple implementation and is used mainly to increasing the modal damping of the modes of interest. Efforts are mainly toward algorithm development and experimental verification. There are four major components in this study: (a) optimal sensor and actuator placement, (b) phase lead velocity feedback controller design, (c) automatic phase compensation design, and (d) spatial temporal filter controller design.

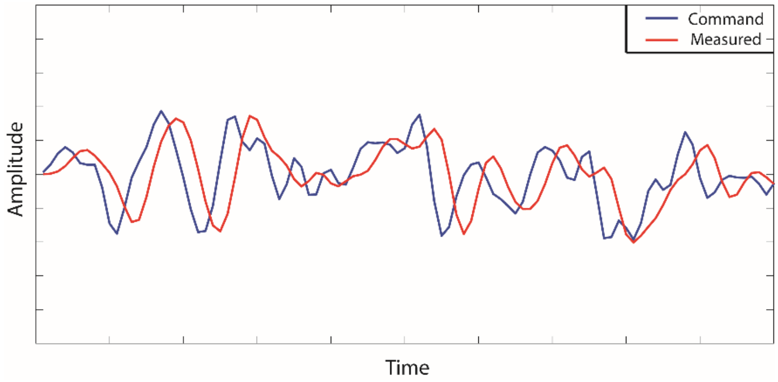

Figure 1.4 Time delay caused by dynamic components

The floor structures considered in this study are floors with high frequency modes which is different from the traditional low frequency floors. The excitations to these structures can then be considered as impulsive excitations. A hammer is used to generate the impact loadings in this study. However, the methods developed in this study are readily applicable to low frequency floors.

Because the focus of this study is to develop algorithms for active control of floor vibrations, the floor structure used in this study is of small scale, which is a rectangular steel plate with all four edges clamped. The techniques developed herein should also be suitable to larger test structures.

The aim of the study presented in this dissertation is to develop a control algorithm that uses as little information (floor, actuator and other dynamic components) of the whole system as possible, in view of the fact that the floor structures are different from each other and quite complicated for modelling. Use of the spatio-temporal filter makes a great step to achieve this goal. The study demonstrates that model-based feedback control can be used as an effective technique to reduce the human induced floor vibrations. Furthermore, the methods and techniques presented in this dissertation also contribute to the development of model-based phase compensation that can be adopted in other control algorithms.

1.5 Organization of the report

Chapter 2 presents a detailed review of previous studies on active control of human-induced floor vibrations, which contains Direct Output Feedback control and Model-Based control. The development of modal filtering techniques for active control is also reviewed.

Chapter 3 provides the technical background for this study. The algorithms of MF, modal direct velocity feedback controller, the control and observation spillover effects, the actuator-floor interaction, low pass and high pass filters, and finally the types of delays are described. All of these will be used in the subsequent chapters.

In Chapter 4, the experimental setup for the active control testing is presented. It first introduces the steel plate test bed, hardware and software that are used in this study. And then the dynamic identification of the steel plate and actuator are conducted. Finally, time delays associated with the experimental setup are studied. The testing system is extensively used in subsequent chapters to conduct real-time active control experiments and evaluate proposed methods and algorithms.

Optimal sensor and actuator placement considering spillover effects is presented in Chapter 5. Enhancement of the separation performance of the modelled modes and reduction of the spillover effects of the truncated modes in modal filtering are achieved by combining the minimum spillover method, effective independence method (EFI) and modal assurance criterion (MAC). Performance of the proposed procedure is investigated by conducting verification tests to control vibrations of the steel plate, and the sensor and actuator placement determined by the proposed approach achieves preferable results.

In Chapter 6, phase lead compensator combined with the modal direct velocity feedback controller is developed to enhance the stability margins and increase the damping of each filtered mode. The generalized actuator system G_A, which can accurately express the time lags caused by the actuator and DSP, is identified and the root-locus method is used for the compensator design based on this model. Verification experiments show that effective reduction of the vibration level is successfully achieved on the control modes.

Chapter 7, an automatic phase compensation technique without the dynamic information of the actuator and other dynamic components (such as bandpass filter) is developed. Phase compensation can be implemented by a simple weighted linear combination of integration with the target modal control signal itself, which is similar to the proportional-integral (PI) technique. Verification experiments using the steel plate are conducted and the control performance achieved shows the validity of this approach.

The generalization of modal filtering, spatio-temporal filter, is studied in Chapter 8. For modal filtering, the floor structure must be accurately modelled to ensure control stability and performance, while in many real world applications, this modelling effort can take the majority work required to develop an active control strategy. On the other hand, it has been shown that the spillover effects of higher modes cannot be totally eliminated using the MF if a small number of sensors are used, even when the low pass filter is involved. The spatio-temporal filter combined with less model information of both the actuator and floor system is developed. The validity of this technique is verified by the control experiments that are conducted on the same steel plate.

Chapter 9 summarizes the studies presented in this dissertation and provides recommendations and possible future research directions on model-based feedback control under impact loading.

A flowchart representing the detailed organization is shown in Figure 1.5.

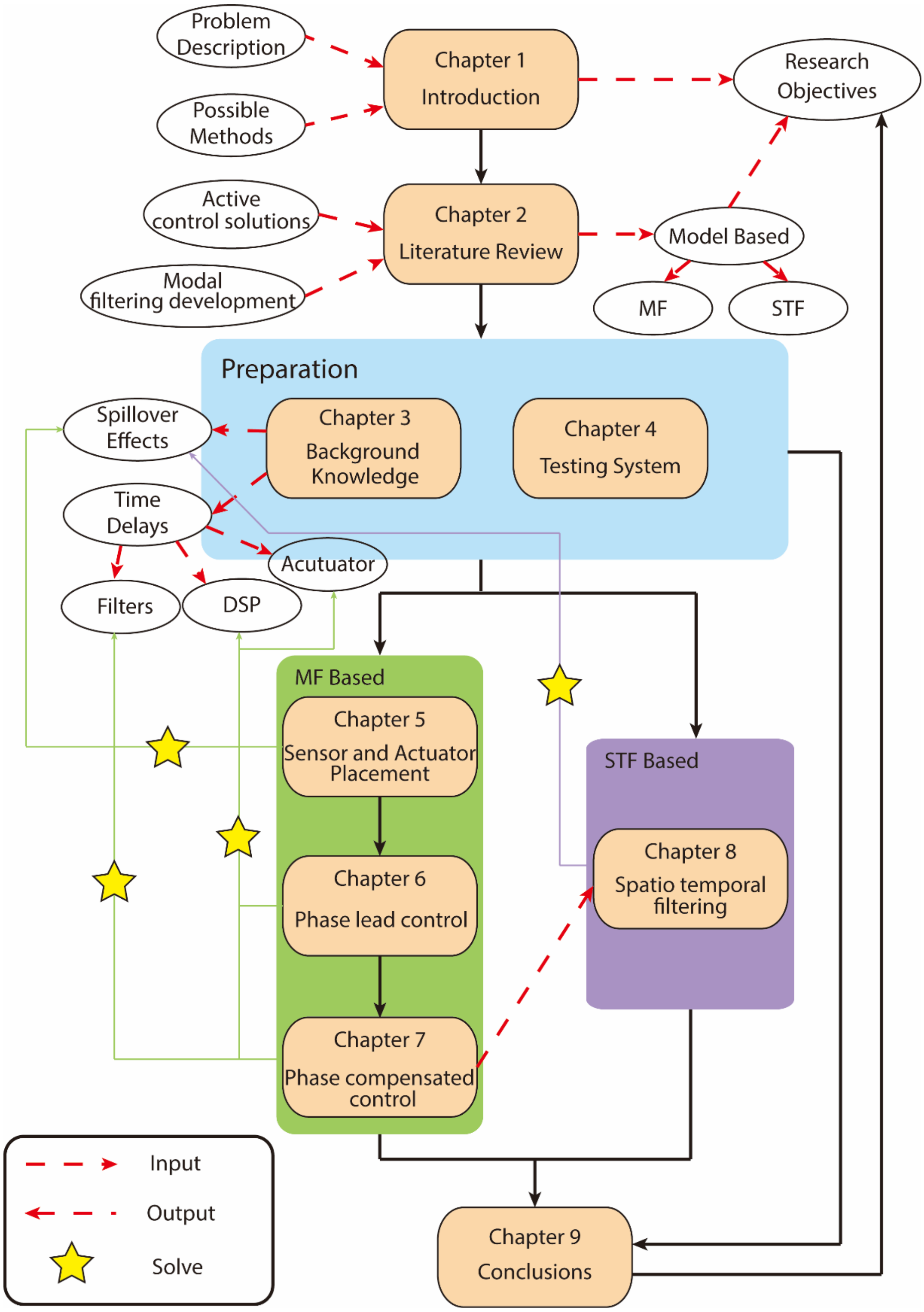

Figure 1.5 Dissertation Overview

Chapter 2 Literature Review

This chapter presents a review of the active control of human-reduced vibrations on floor structures, focusing on the extensions of methods for Direct Output Feedback control and Model-Based Feedback control. The development of the modal filtering techniques is also reviewed.

2.1 Direct output feedback control

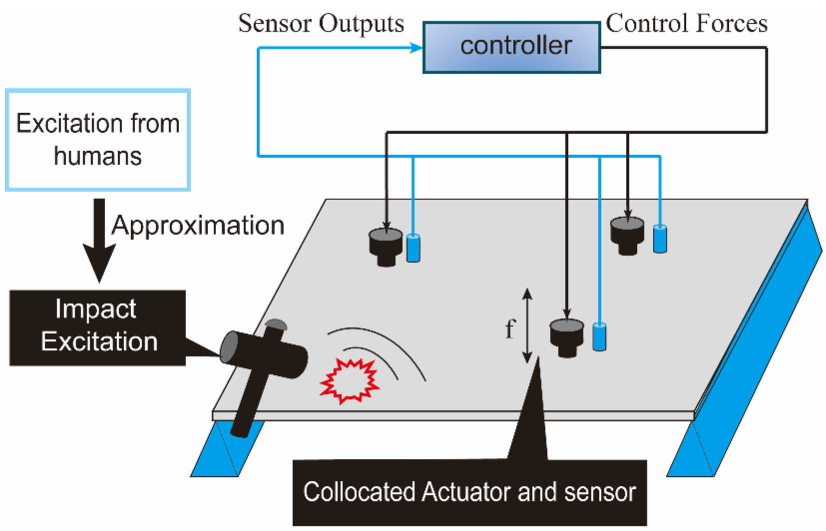

Figure 2.1 Concept of the Direct Output Feedback control

The schematics of the concept of the Direct Output Feedback control is shown in Figure 2.1. In this control strategy, collocated actuators and sensors are used. The previous research includes direct velocity feedback, direct velocity feedback with feed-through term, compensated acceleration feedback, response-dependent velocity feedback and multi-input multi-output direct output feedback and so forth. It should be noted that the Direct Output

Feedback control does not require a highly accurate model of the floor structure. More details about these controllers are provided below.

The idea of direct velocity feedback (DVF) control of large space structures was initially proposed by Balas for the purpose of creating a simple-implement control strategy [23]. Direct velocity means that the output velocity signal is multiplied by a control gain and the resulting signal is then directly fed back to the collocated actuator, as shown in Figure 2.2. Accelerometers are often used to measure the responses of floors. The control gain should be non-negative in this method. The author concluded that the direct velocity feedback controller cannot destabilize any part of the system no matter what the choice of feedback gain and the stability margins of the whole closed-loop system will never fall below the open-loop system because of the well-known interlacing property of poles and zeros of collocated systems. As the feedback control gain is increased, the damping ratio of each mode is also increased because the poles of each mode have moved away from the imaginary axis.

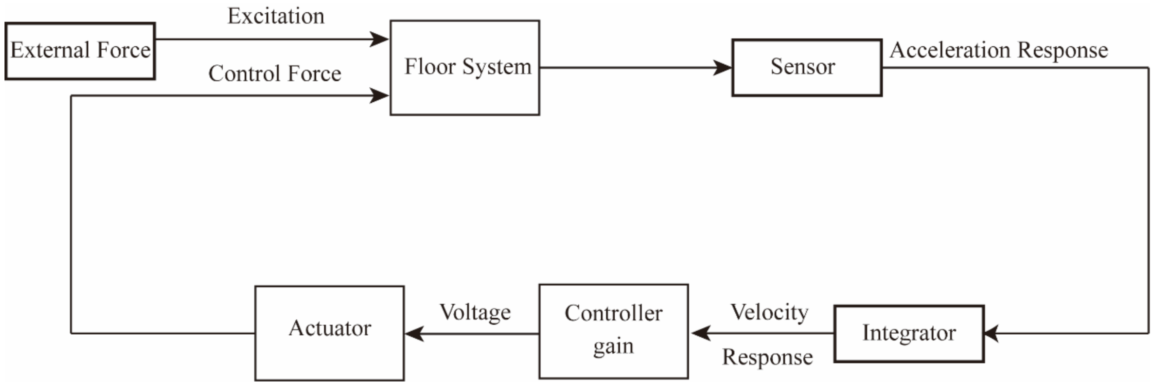

Figure 2.2 Direct velocity feedback

This idea was successfully implemented by Hanagan to the human-induced floor vibrations [5], [11], [32]. The direct velocity feedback control algorithm was first implemented and studied analytically and experimentally on a lightweight steel floor system [5]. An electromagnetic proof-mass actuator was used to apply the control forces. Only the modes of the structure under 30Hz were included in the analytical model since the lower-frequency modes of vibrations dominated the dynamic responses to heel drop excitation or walking. Analysis of the control system using the root locus method showed that the control system and the structure did not behave as independent dynamic systems, rather an interaction between them was observed. When the dynamics of the actuator and the sensor are considered, the interlacing property for the collocated case no longer holds since additional poles and zeros are introduced. Therefore, the control gain is limited by control system stability condition. The root locus of the control system also showed that as the control gain increases, the damping ratio of the actuator decreases, implying that the force output at this frequency will be increased - potentially inducing stroke saturation [1], and the feedback gain has to be decreased even further to avoid this situation. In order to avoid the actuator force saturation and stroke saturation, a saturation nonlinearity was introduced to avoid unstable behavior that may be caused by both saturations, while the actuator was possibly involved in a stable limit cycle [33]. Despite this limitation, the direct velocity feedback controller has reduced the vibration of human-reduced vibrations to a large degree on a problematic office floor and a chemistry laboratory. Performance was evaluated using the peak values of running root mean square accelerations using 8s integration time. Over 70% vibration reduction was achieved for the office floor and the results for the chemistry laboratory showed over 75% reduction in vibration level.

An improvement in the stability of the DVF controlled system was proposed by Díaz and Reynolds through introducing of a feed-through term (DVF with FTT) [34]. The feed-through term here contains a small portion of the actuator signals to the sensor signals as shown in Figure 2.3. Typically, the natural frequency of the control actuators used for floor vibration control is chosen to be significantly lower than the lowest modal frequency of the floors [33]. In this situation, a conveniently designed feed-through term would allow the two zeros located at the origin to be displaced to a position between the actuator poles and the floor poles corresponding to its lowest natural frequency. The controlled system can exhibit an alternating pole-zero pattern even though the dynamics of the proof-mass actuator is involved. A high control gain without exhibiting a limit cycle behavior can be achieved. Control results showed that this method is robust with respect to stability and achieved excellent reductions in human-induced vibrations.

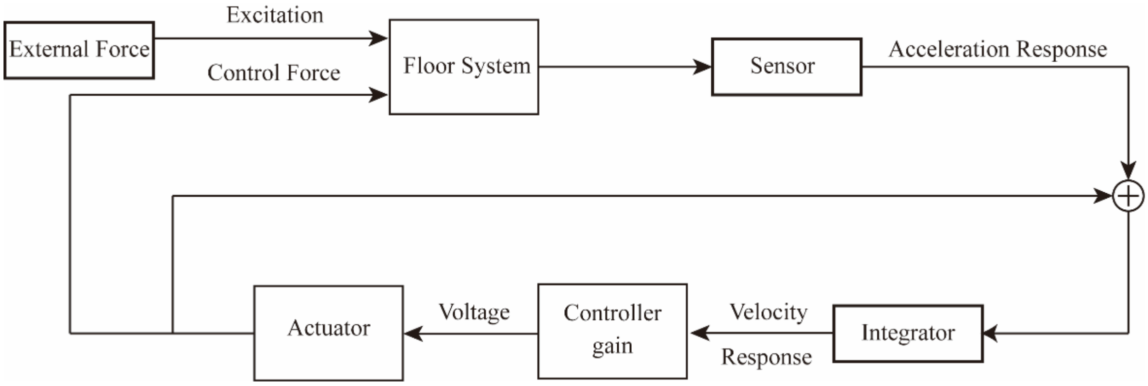

Figure 2.3 DVF with feed-through term

Direct acceleration feedback (DAF) control is another choice for vibration suppression using the acceleration outputs from the sensors as the inputs to the control gain matrix. The research done by Shahabpoor [35] found that the effectiveness of DAF significantly depends on the frequency of the mode to be controlled, and it was discovered that instability occurs for the lower frequencies easily while large increases in damping can be achieved for higher frequencies. Compensated acceleration feedback (CAF) control is much more reliable than DAF that was proposed by Díaz and Reynolds [24], with the schematic shown in Figure 2.4. Compensators are designed to obtain high stability margins and to introduce possible significant damping. First, a phase-lag compensator was introduced to account for the interaction between the structure and the actuator dynamics using the root locus method so that high damping in the fundamental vibration mode and high stability margins can be achieved. Then a phase-lead compensator, which functions as a high pass filter, was developed to prevent stroke saturation at low frequencies through a frequency domain analysis and optimization study. The control test results using an office floor showed that the duration of the time exceeding a response factor (a common vibration limit for high quality office environments) was reduced by 97% for the in-service condition.

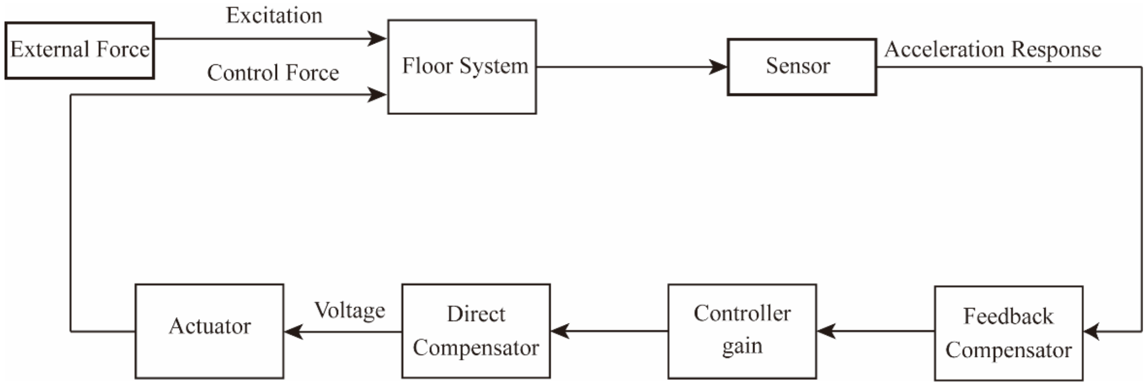

Figure 2.4 Compensated acceleration feedback

On-off nonlinear active control and response-dependent velocity feedback (RDVF) control are introduced for the purpose of preventing the onset of limit cycles [33], [36] by changing the gain matrix that is applied to the velocity measurements, as shown in Figure 2.5. In the RDVF control law, a maximum voltage to the amplifier was pre-set and a variable gain proportional to the reciprocal of the maximum of the absolute value of a sampled signal in a fixed block of response data was derived. The use of a high gain matrix for low velocities while the use of a low gain matrix for high velocities can be achieved, which implies that the gain can be automatically selected through this method. Also, a non-linear element was used so that once a minimum level of vibrations is detected, the actuator signals is set zero, thus preventing the onset of limit cycles due to high gain [36]. On-off nonlinear active control, on the other hand, varies the gain matrix so that the command voltage signal is always in one of three states – maximum positive voltage, zero voltage or maximum negative voltage. A non-linear velocity feedback with a switching-off level controller and a non-linear velocity feedback with dead-zone controller were investigated for this purpose[33].

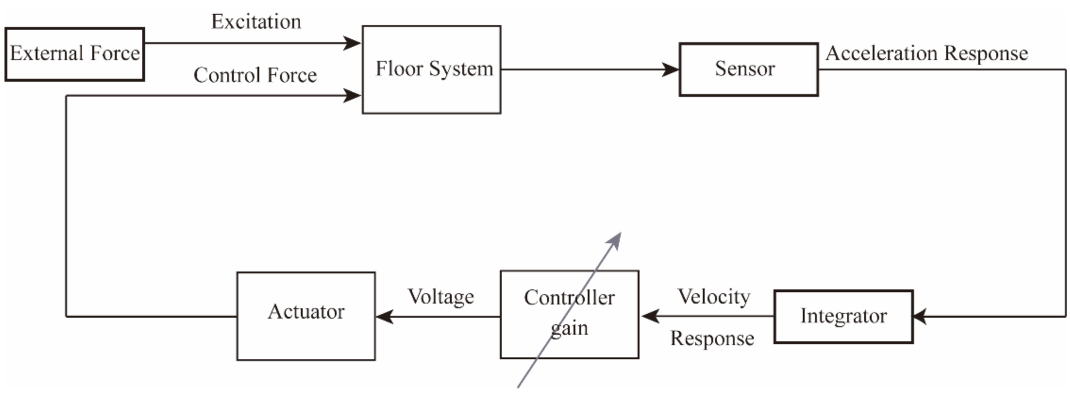

Figure 2.5 On-off and response-dependent velocity feedback

Nyawako and Reynolds incorporated a disturbance observer with direct velocity feedback to deal with both on-resonance and off-resonance excitations of floor structures from human activities [37], as shown in Figure 2.6. Since human activities contain energy not only at the activity frequency but also at harmonics of this frequency, if the harmonics coincide with resonant frequencies, the vibrations may excite the resonance of the structure, while if it does not coincide with the resonant frequencies, the energy from activities may still be significant to cause annoyance or disturbance. Analytical studies indicated that there is a great potential to deal with off-resonance excitation forces within a certain frequency bandwidth by adding a disturbance observer to an outer loop DVF controller.

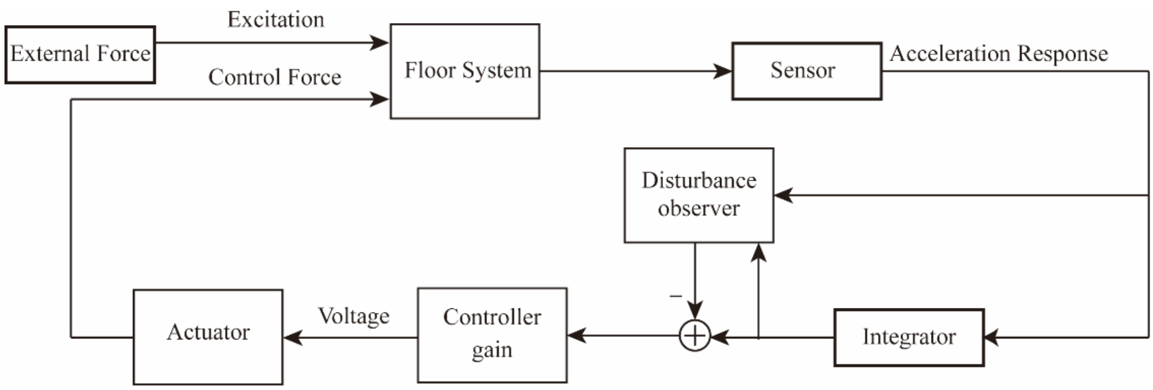

Figure 2.6 Incorporating a disturbance observer with DVF feedback

Although most of the research discussed above made use of a single-input single-output (SISO) collocated control structure, the excessive level of vibrations is usually a problem of a wide area and not of just a single location. In order to achieve the vibration reduction requirement in an area, several collocated actuators and sensors would be required. Use of multiple single-input and single-output (MSISO) control schemes, in which each SISO controller is independently designed for each location was investigated first. It was shown that the MSISO control system has limited efficiency in which a reduction of the control gain of each SISO is needed to guarantee stability, since the structural system does not act independently at each control location [38]. Multi-input and multi-output (MIMO) was then used for the global vibration control of floor structures [39], [40]. The DVF MIMO control strategy found the optimal gain matrix and the optimal location for a predefined number of actuators and sensors obtained by minimizing a performance index PI. It was observed that MIMO control improved the results compared with the SISO control strategy [40].

While the DOFB controllers are very simple, because they are based on the direct output feedback, their control is effective to a limited subset of the active modes in the system, the higher modes largely remain unaffected. Another disadvantage of this approach is that the choice of the modes to be controlled is affected by the sensor and actuator locations [41].

2.2 Model-based feedback control

Model-based feedback control, on the other hand, do not need to be collocated and a different number of sensors and actuators can be used to selectively control any of the active modes in the system, as shown in Figure 2.7. Pole-placement method, the Linear Quadratic Gaussian (LQG) control, Independent Modal Space Control (IMSC) are the common approaches among model-based controllers.

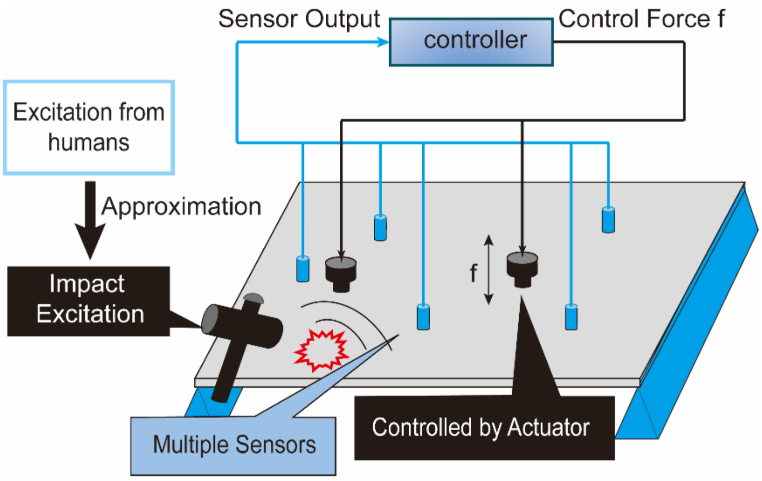

Figure 2.7 Concept of model-based feedback control

Model-based controllers have been extensively investigated and implemented on other sectors such as the mechanical engineering and aerospace industries and structure control for the reduction of effects of seismic and wind loading [42]–[45]. However, applications for the control of human-induced floor vibrations remain very limited since usually an accurate structure model is necessary, some of which are reviewed as follows.

An approximate pole-placement controller was designed by Nyawako via the inversion of the floor model dynamics [46], which was based on the previous research for remotely located vibration control [47]. This method has been found to avoid the numerical difficulties associated with the algebraic pole-placement approach. Both analytical and experimental studies were done on a laboratory floor using the derived approximate pole placement control and the control performance was compared to that of the DVF scheme. It was found that vibration mitigation performance between both methods are comparable and the analytical predictions correlate well with the experimental results. It was pointed out that a potential advantage of the approximate pole-placement controller is that it can be designed to isolate and control target modes of vibration [46].

Nyawoka and Reynolds investigated three controllers, two of which are model-based controllers, on a pedestrian walkway structure for active control of human-induced vibrations [48]. They comprised DVF, observed-based and independent modal space controllers that were implemented in SISO, MSISO and MIMO configurations. For SISO schemes, the objective was to compare vibration mitigation performances from global control versus selective control. For MSISO and MIMO control, the aims were to investigate the impact of isolation and control of specific structural resonant frequencies simultaneously at different locations on the structure with the objective of imposing global control. The observer based controllers were designed as shown in Figure 2.8. The symbols $(\mathrm{A}_p, \mathrm{B}_p, \mathrm{C}_p)$ and $(\mathrm{A}_{po}, \mathrm{B}_{po}, \mathrm{C}_{po})$ denote state-space parameters representing the existing structural dynamics and a reduced order model of the structure used in the controller design. The symbol K_p denotes the feedback gain to achieve desired closed-loop eigenvalues and K_e is the observer feedback gain. Also, $\mathrm{v}_o(t), \mathrm{x}_o(t), u(t)$ and $y(t)$ are the estimated modal velocity, modal displacement, control input and the structural response, respectively. The independent modal space control was realized via spatial filtering which will be reviewed later. The results showed that the model-based controller can isolate and control specific vibration modes at different locations, being a more beneficial procedure for dealing with modally dense structures, in which particular resonant frequencies are found to be problematic [48].

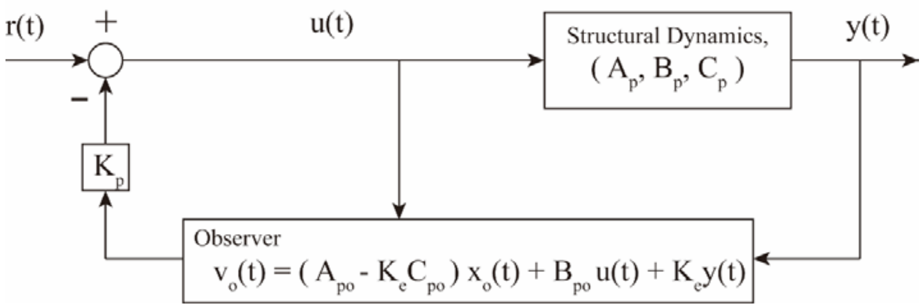

Figure 2.8 Observer-based compensator

2.3 Modal filtering techniques

Spatial modal filters were first proposed by Meirovitch and Baruh as alternatives to observer techniques such as Luenberger observer to estimate the modal states from distributed measurements of the system [49]. The concept of modal filter is that the modal coordinates at any instant of time can be determined from motion variable information measured at the same instant of time. For an *n*-DOF structural system, the modal filter was derived from the modal expansion theorem as:

$$\bar{x}(P,t) = \sum_{r=1}^{n} q_r\,(t)\bar{\phi}_r(P) \tag{2-1}$$

where $\bar{x}(P,t) \in R^{n\times 1}$ and $\bar{\phi}_r(P) \in R^{n\times 1}$ are the displacements at instant time *t* and the mass normalized eigenvectors of point *P* on the structure, respectively. The modal states $q_r(t)$ can be determined by Eq. (2-2):

$$q_r(t) = \bar{\phi}_r(P)^T M\bar{x}(P,t) \tag{2-2}$$

where *M* is the mass matrix, $M \in R^{n\times n}$. The method is exact if all of the *n* displacements of the structure are known in real-time. If the distributed measurements are not available, they can be reconstructed via interpolation from measurements at discrete points. Then the modal states were obtained by Meirovich and Baruh as:

$$q_r(t) = \int_D \; M(P)\phi_r(P)\sum_{j=1}^{K}\sum_{s=1}^{K}\psi_s(P)U^{-1}[x(P_j) + v(P_j)]dD \tag{2-3}$$

where $M(P)$ is the mass distributed at point *P*, $\psi_s(P)$ is a global admissible interpolation function estimated at *P*. The matrix $U \in R^{k\times k} = [\psi_1, \psi_2, \dots \psi_s]$ consists of interpolation functions evaluated at sensor locations P_j, *K* is the total number of sensors, $v(P_j)$ is the zero-mean Gaussian stochastic noise, and *D* is the domain of the physical system. Since structural properties is needed in Eq. (2-3), which are available from simple structures, Meirovich and Baruh suggested using FEM to apply this method to more complex cases by breaking the domain *D* into smaller sub-domains $D_t, t = 1..T$. Eq. (2-3) changes to:

$$q_r(t) = \sum_{t=1}^{T}\int_{D_t} M(P)\phi_r(P){L_t}^T\,[x^t(P_j) + v^t(P_j)]dD_t \tag{2-4}$$

where L_t is a vector of interpolation functions for element D_t, $x^t(P_j)$ and $v^t(P_j)$ are the measured deformations and zero-mean Gaussian stochastic noise on the *t*th element at sensor location P_j. This equation can then be used to filter the modal coordinates of complex structures. However, the equation in this form is still hard in its implementation since it generally requires a considerable number of degrees of freedom in order to accurately generate the dynamics of the structure over the frequency range of interest. It would not be possible in many cases to measure all these degrees of freedom to implement the modal filter.

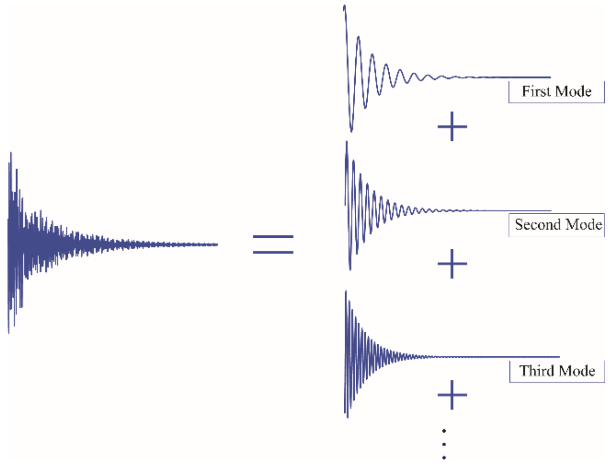

Figure 2.9 The concept of modal filtering

Two improvements of this method were proposed by Zhang and Shelley et al. in a more practical manner [50], [51]. These are the frequency response function (FRF) method and the pseudo-inverse method, which use only experimental data to derive the modal filter parameters. They pointed out that modal filtering techniques utilize the characteristic that the dynamic response of any real structure is composed of the sum of individual modal responses, as shown in Figure 2.9, each behaving as a single degree of freedom system and each having a particular response shape or eigenvector. The basis for modal filtering is the standard modal coordinate transformation to simplify the solution of the systems of linear differential equations.

FRF method calculates a weighting vector, which is named reciprocal modal vector (RMV) or modal filter vector, such that the weighted sum of a number of FRFs approaches the FRF of a single-degree-of-freedom system as close as possible. As the first step, assuming N_o and N_i are the number of displacement measurements and the number of inputs, then the $N_o \times N_i$ FRF matrix is defined as:

$$H(\omega) = \sum_{r=1}^{N} [\frac{\phi_r Q_r \hat{\phi}_r^T}{j\omega - \lambda_r} + \frac{{\phi_r}^* {Q_r}^* \hat{\phi}_r^H}{j\omega - \lambda_r^*}] \tag{2-5}$$

where N is the number of modes, λ_r and Q_r are the pole value and modal scale factor corresponding to mode r, respectively. The modal vector $\hat{\phi}_r$ contains N_i components corresponding to the input locations for modes r. The modal vectors, ϕ_r, may be scaled such that they are real-valued for a real normal mode system, which means $\phi_r = {\phi_r}^*$, and Q_r is a negative imaginary number for displacement response data, such that $Q_r = -{Q_r}^*$.

RMV is assumed to be a vector which is orthogonal to the remainder of the response subspace for the choice of sensor locations, which means that it should satisfy the following orthogonality relationship:

$$\psi_i^T \phi_k = 0, \qquad i \neq k \tag{2-6}$$

The RMV ψ_i can then be scaled by Q_i such that:

$$\psi_i^T \phi_i Q_i \hat{\phi}_{1i} = -j \tag{2-7}$$

where $\hat{\phi}_{1i}$ is the element of the modal vector corresponding to the first input location and j is the imaginary unit. Then, for the remaining input locations, the following relationship holds:

$$\psi_i^T \phi_i Q_i \hat{\phi}_{qi} = \frac{\hat{\phi}_{qi}}{\hat{\phi}_{1i}}(-j) \tag{2-8}$$

From Eq. (2-5) to (2-8), the following relationship can be obtained:

$$\psi_i^T H(\omega) = [1, \frac{\hat{\phi}_{2i}}{\hat{\phi}_{1i}}, \frac{\hat{\phi}_{3i}}{\hat{\phi}_{1i}}, \ldots, \frac{\hat{\phi}_{N_i i}}{\hat{\phi}_{1i}}] \, [\frac{-j}{j\omega - \lambda_i} + \frac{j}{j\omega - \lambda_i}] \tag{2-9}$$

Eq. (2-9) can be evaluated at a sufficient number of discrete frequencies to form an overdetermined problem which may be solved for RMV ψ_i in a least squares manner if the information of the FRF matrix and the pole value of the mode to be extracted is known. The total number of unknowns is $(N_o + N_i + 1)$ in Eq. (2-9). The poles of the system can be derived from the experimental FRF matrix using parameter estimation technique.

The pseudo-inverse method, on the other hand, extracts the modal coordinates in a real-time and frequency independent manner. Shelley et al. proposed the pseudo-inverse approach given as [51]:

$$\psi^T = (\Phi^T \Phi)^{-1} \Phi^T \tag{2-10}$$

such that:

$$q(t) = \psi^T x(P, t) \tag{2-11}$$

where $q(t) \in R^{N \times 1}$ is the modal coordinates at instant of time *t*, *N* is the number of modes to be considered. $\Phi \in R^{N_o \times N}$ is the modal vector with N_o as the total number of sensors.

These two methods was tested on a 5 meter truss structure to extract modal coordinates. The calculations of modal filter matrix from the on-line implementation are discussed and compared with the off-line implementation. They chose to record 24 modes, and varied the number of sensors for this task. The results showed that both methods can extract low frequency modal coordinates with satisfactory accuracy, and higher frequency mode coordinates with less success because of the spatial aliasing. Indeed, the higher modes are not spatially independent and are more coupled than lower order modes. However, this is not an obstruction for implementation of these methods in civil engineering structures because the natural frequencies of civil engineering structures are far below the frequencies where spatial aliasing could be a concern.

Shelley et al. noted that these two methods have disadvantages, and the most significant of these disadvantages is the need for a complete and accurate model of the plant dynamics. However, the real-world structural systems are typically very complex. Therefore Shelley et al. extended modal filtering into adaptive works [52] that need only the information of measured force and pole values of modes of interest. An error is introduced which is the difference between the true modal coordinate, $\eta(k)$, and the modal coordinate estimated by the modal filter, $\hat{\eta}(k)$, at time *k*:

$$\begin{aligned} e(k) &= \eta(k) - \hat{\eta}(k) \\ &= \eta(k) - \psi(k)^T \mathrm{x(k)} \end{aligned} \tag{2-12}$$

However, the true modal coordinate is not known. In fact, estimating $\eta(k)$ is the purpose of the modal filter vector. Shelley et al. introduced a reference modal coordinate $\eta^r(k)$, which is highly correlated with the true coordinate. $\eta^r(k)$ can be generated by driving a SDOF system utilizing the pole of the mode of interest. For the *i*th mode:

$$\begin{Bmatrix} \dot{\eta}^r(k+1) \\ \ddot{\eta}^r(k+1) \end{Bmatrix} = \begin{bmatrix} 0 & 1 \\ -\omega_{n_i}{}^2 & 2\omega_{n_i}\sigma_i \end{bmatrix} \begin{Bmatrix} \dot{\eta}^r(k) \\ \ddot{\eta}^r(k) \end{Bmatrix} + \begin{bmatrix} 0 \\ 2\omega_{d_i} \end{bmatrix} f_k \tag{2-13}$$

where f_k is the measured driving force and σ_i is the modal damping. After solving Eq. (2-13), the reference modal coordinate can then be used in Eq. (2-12) in place of the true modal coordinate to calculate the error. The solution problem of Eq. (2-12) is to adaptively find ψ to minimize this error over a number of time steps. The structure of this estimation problem is illustrated in Figure 2.10.

Then each of the SDOF system can be described as a first order state space model:

$$\begin{Bmatrix} \dot{\eta}_i(t) \\ \ddot{\eta}_i(t) \end{Bmatrix} = \begin{bmatrix} 0 & 1 \\ -\omega_{n_i}{}^2 & 2\omega_{n_i}\sigma_i \end{bmatrix} \begin{Bmatrix} \dot{\eta}_i(t) \\ \ddot{\eta}_i(t) \end{Bmatrix} + \begin{bmatrix} 0 \\ 2\omega_{d_i} \end{bmatrix} l_i^T f(t) \tag{2-14}$$

where l_i is an vector of complex force appropriation coefficients (also called modal participation vector). Shelley et al. used the simple “collocated in modal space” rate feedback controller as the control method by choosing a control force as:

$$f_i(t) = -G_i \dot{\eta}_i(t) \tag{2-15}$$

where G_i is the scalar feedback gain. Substituting Eq. (2-15) into Eq. (2-14) yields the resulting closed loop system matrix:

$$\begin{Bmatrix} \dot{\eta}_i(t) \\ \ddot{\eta}_i(t) \end{Bmatrix} = \begin{bmatrix} 0 & 1 \\ -\omega_{n_i}{}^2 & 2\omega_{n_i}\sigma_i \end{bmatrix} \begin{Bmatrix} \dot{\eta}_i(t) \\ \ddot{\eta}_i(t) \end{Bmatrix} + \begin{bmatrix} 0 \\ 2\omega_{d_i} \end{bmatrix} l_i^T \big(f(t) - G_i \dot{\eta}_i(t)\big) \tag{2-16}$$

$$= \begin{bmatrix} 0 & 1 \\ -{\omega_{n_i}}^2 & 2(\omega_{n_i}\sigma_i - \omega_{d_i} l_i^T G_i) \end{bmatrix} \begin{Bmatrix} \dot{\eta}_i(t) \\ \ddot{\eta}_i(t) \end{Bmatrix} + \begin{bmatrix} 0 \\ 2\omega_{d_i} \end{bmatrix} l_i^T f(t)$$

Eq. (2-16) shows that the modal damping has been increased from $2\sigma_i$ to $2(\sigma_i - \omega_{d_i}/\omega_{n_i} l_i^T G_i)$ for mode i.

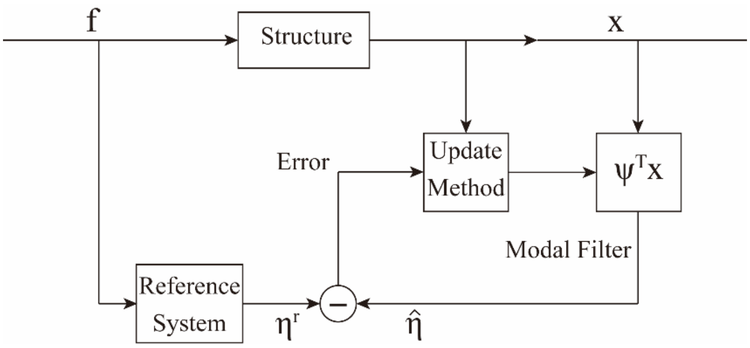

Figure 2.10 Structure of modal filter estimation problem

Adaptive modal filtering was successfully implemented for controlling the Big Creek bridge in Ohio [53] and a 4.5 meter vertically hung truss[54]. A Luenberger observer for estimation of the true modal coordinate was used, and the Least Mean Square (LMS) algorithm was used to find the modal filter vector adaptively.

It has been shown that a large number of point sensors are required for all the modal filter methods mentioned above. Typically more than two times the number of modes are required to analyze the structures. Since use of a large number of sensors is not recommended for the economic and aesthetic considerations, more efforts are needed for modal filtering techniques. Although the distributed modal sensors/actuators have been implemented to overcome the spillover phenomena [55], it seems extremely difficult to put the distributed materials on the floor if the building is occupied.

To improve the traditional modal filtering, Shelley et al. proposed the Spatio-Temporal filter (STF) by extending the traditional modal filter from space domain into space and time domain to achieve higher accuracy with fewer sensors [56]–[58]. An *Nth* order spatio-temporal filter utilizes N past response samples at time k is defined as:

$$\hat{q}_k = \boldsymbol{\psi}^T \begin{pmatrix} \mathbf{x}_k \\ \mathbf{x}_{k-1} \\ \vdots \\ \mathbf{x}_{k-N} \end{pmatrix} = \boldsymbol{\psi}^T X_{k,N} \qquad (2\text{-}17)$$

which in fact introduces a different *Nth* order finite impulse response (FIR) on each sensor channel. The FIR filters perform different functions depending on the specific implementation: pole-zero cancellation if spatial resolution alone is insufficient to separate modes;

accommodating the relative phase shift between sensors caused by non-proportional damping modes and correction for some sensor dynamics. In the same manner as the adaptive modal filter, an error is introduced as:

$$e_k = q_k - \hat{q}_k = q_k - \Psi^T X_{k,N} \tag{2-18}$$

Eq. (2-13) can then be used as the reference modal coordinate which is highly correlated with the true modal coordinate. Shelly et al. suggested using adaptive, on-line methods for STF parameter estimation since they recover from sensor and actuator failure and Recursive Least Squares (RLS) was chosen as the real-time adaptive STF update method. A STF based, multiple-input multiple-output active controller is designed by selecting only a single scalar control gain for each mode to be controlled [58].

The modal filters reviewed above may all be implemented with discrete sensor arrays, such as accelerometers, strain gauges, or piezoelectric patches[59], etc. However, the discrete nature of the array can result in spatial aliasing[60]. Spatial aliasing is defined as when the wave number *k* of one mode exceeds the number of sensors *n* regularly spaced in that direction, the sensor output appears as generated by a mode with a lower wave number (2*n*-*k*) [61]. Continuous modal filtering methods are developed to solve this problem using continuous distributed sensors such as piezoelectric films and optical fibers [62]–[65]. These methods are not reviewed here, but it seems that these continuous type distributed sensing techniques are promising ways for high frequency mode applications.

2.4 Summary

This section reviews some of the studies about the direct output feedback control, model-based feedback control as well as modal filtering techniques. Although active control of floor structure vibration using DOFB is becoming a mature and reliable technique, further development is required, and MB active control is an attractive approach. Several modal filtering methods have been reviewed in this chapter and some of them will be used later on.

Chapter 3 Background on Model-Based Active Control

In this chapter, research background regarding the modal filtering method, the modal direct velocity feedback control technique and the spillover effects are reviewed. Then the interaction between structure and actuator dynamics and the effects of actuator dynamics on active vibration control (AVC) are described. The effects of low pass and high pass filters on AVC are also presented. Finally, the types of delays are explained.

3.1 Principle of modal filtering

The equations of motion for free vibration of an N-DOF system is written as:

$$\boldsymbol{M}\ddot{\boldsymbol{u}} + \boldsymbol{C}\dot{\boldsymbol{u}} + \boldsymbol{K}\boldsymbol{u} = 0 \tag{3-1}$$

where $\boldsymbol{M}$, $\boldsymbol{C}$, $\boldsymbol{K}$ are the mass matrix, stiffness matrix and damping matrix, respectively, of size N, and $\boldsymbol{u}$ is the displacement vector with the same order. Neglecting the damping, the equations of motion become:

$$\boldsymbol{M}\ddot{\boldsymbol{u}} + \boldsymbol{K}\boldsymbol{u} = 0 \tag{3-2}$$

The free vibration of an undamped structure in one of its natural modes can be expressed by:

$$\boldsymbol{u} = \boldsymbol{\varphi}\exp(j\omega t) \tag{3-3}$$

where ω is the natural frequency, and j is the imaginary unit. The N-dimensional mode shape vector $\boldsymbol{\varphi}$ does not vary with time. Substituting Eq. (3-3) into Eq. (3-2) gives:

$$[\boldsymbol{K} - \omega^2\boldsymbol{M}]\boldsymbol{\varphi} = 0 \tag{3-4}$$

which can be interpreted as a set of N homogeneous algebraic equations. The nontrivial solutions of Eq. (3-4) are:

$$\det(\boldsymbol{K} - \omega^2 \boldsymbol{M}) = 0 \tag{3-5}$$

Eq. (3-5) is known as the characteristic equation or frequency equation. The *N* roots of Eq. (3-5) determine the *N* natural frequencies $\omega_n (n = 1,2, \dots N)$ of vibration. When a natural frequency ω_n is known, Eq. (3-4) can be solved for the corresponding vector $\boldsymbol{\varphi}_n$. The displacement response of the system can then be obtained as:

$$\begin{aligned} \boldsymbol{u}(\mathrm{t}) &= \sum_{n=1}^{N} \boldsymbol{\varphi}_n (C_n \exp(j\omega_n t) + C'_n \exp(-j\omega_n t)) \\ &= \sum_{n=1}^{N} A_n \boldsymbol{\varphi}_n \cos(\omega_n t - \gamma_n) \\ &= \sum_{n=1}^{N} q_n(t) \boldsymbol{\varphi}_n \end{aligned} \tag{3-6}$$

where C_n, C'_n and A_n are the amplitudes and γ_n is the phase for the *n*th mode. The symbol $q_n(t)$ represents the generalized coordinate of the *n*th mode and indicates the *n*th mode response $A_n \sin(\omega_n t - \gamma_n)$ in this case.

In practice, the floor structures are represented by discrete systems, implying that *N* is a finite number. However, the value of *N* is usually very large, since the bandwidths of actuators and sensors cannot response to the highest frequency modes and also the highest modes are hard to be excited in a physical structure. The number of modes contributed to the responses are assumed to be *M* such that:

$$\boldsymbol{u}(\mathrm{t}) = \sum_{n=1}^{M} q_n(t) \boldsymbol{\varphi}_n \tag{3-7}$$

where $M \ll N$. The structural displacements and/or velocities and/or accelerations are measured at various physical points by sensors. If *S* sensors are used, Eq. (3-7) can be re-written as:

$$\boldsymbol{u}_s(\mathrm{t}) = \sum_{n=1}^{M} q_n(t) \boldsymbol{\varphi}_{sn} \tag{3-8}$$

where $\boldsymbol{u}_s(\mathrm{t})$ and $\boldsymbol{\varphi}_{sn}$ are *S*-dimensional vectors and the parameters of modal shape $\boldsymbol{\varphi}_{sn}$ are the values corresponding to that at the same sensor locations of $\boldsymbol{\varphi}_n$.

Then a modal filter is applied to the measured response data $\boldsymbol{u}_s(\mathrm{t})$ to extract the modal coordinate responses of interest. In order to extract the modal response of the *i*th mode, a modal filtering vector $\boldsymbol{\psi}_i$ is sought which has the following characteristics:

$$\boldsymbol{\psi}_i^{\mathrm{T}}\boldsymbol{\varphi}_{sn} = 0 \qquad i \neq n$$
$$= 1 \qquad i = n \tag{3-9}$$

which is equivalent to generating a weighted average of the responses measured at *S* locations on the structure such that:

$$\begin{aligned}\boldsymbol{\psi}_i^{\mathrm{T}}\boldsymbol{u}_s(\mathrm{t}) &= \boldsymbol{\psi}_i^{\mathrm{T}}\sum_{n=1}^{M} q_n(t)\boldsymbol{\varphi}_{sn} \\ &= \boldsymbol{\psi}_i^{\mathrm{T}}\boldsymbol{\varphi}_{si}q_i(t) \\ &= q_i(t)\end{aligned} \tag{3-10}$$

The above discussion holds for the damped case as well, both proportional and non-proportional [58].

It should be noted that the modal filtering vectors $\boldsymbol{\psi}_i$ $(i = 1{,}2 \ldots \mathrm{M})$ are very sensitive to the modal shape $\boldsymbol{\varphi}_{sn}$, therefore it is of great significance to obtain an accurate mode shape $\boldsymbol{\varphi}_{\mathrm{n}}$ before calculating the modal filtering coefficients. Selecting sensor locations to obtain the optimal $\widehat{\boldsymbol{\varphi}}_{sn}$ is not an easy task. There are as many as $N!/(S!\,(N-S)!)$ ways to choose *S* sensor locations from a possible *N* candidates. The strategy to find an optimal sensor placement will be studied in Chapter 5.

3.2 Modal direct velocity feedback control

As discussed above, after modal filtering, the filtered mode can be approximately seemed as a single-degree-of-freedom system, as:

$$m_i\ddot{q}_i(t) + c_i\dot{q}_i(t) + k_iq_i(t) = f_{ci}(t) + f_{di}(t) \tag{3-11}$$

where m_i, c_i and k_i are the modal mass, modal damping coefficient and modal stiffness of the *i*th mode, respectively, $f_{ci}(t)$ is the modal control force and $f_{di}(t)$ is the modal disturbance. If the dynamics of the actuator are not considered in the real system, the Modal Direct Velocity Feedback (MDVF) control strategy can be a natural choice due to its readily established implementation. The MDVF control indicates that the control force for the *i*th mode $f_{ci}(t)(i = 1{,}2 \ldots)$ is defined to be proportional to the velocity of the *i*th response $\dot{q}_i(t)$ obtained by utilizing the modal filtering to the dynamic response $\boldsymbol{u}_{\mathrm{s}}(\mathrm{t})$ measured by sensors, as:

$$f_i(t) = -\beta_i\,\dot{q}_i(t) \tag{3-12}$$

where β_i is the gain for the *i*th mode. In this case the system is "collocated in modal space" with the associated "nice characteristics" such as guaranteed stability associated with conventional "collocated in physical space" systems. By using this controller, this characteristic exists even if the sensors and actuators are actually not physically collocated. Substituting the expression for control force into Eq. (3-11) gives:

$$m_i\ddot{q}_i(t) + c_i\dot{q}_i(t) + k_iq_i(t) = -\beta_i\,\dot{q}_i(t) + f_{di}(t) \tag{3-13}$$

Transforming the control force term to the left hand side, Eq. (3-13) becomes:

$$m_i\ddot{q}_i(t) + (c_i + \beta_i)\dot{q}_i(t) + k_iq_i(t) = f_{di}(t) \tag{3-14}$$

which means that the damping ratio of the target mode would be increased. Therefore, the control force for multiple modes, denoted by $f(t)$, is calculated by:

$$f(t) = f_1(t) + f_2(t) + \cdots = \left(-\beta_1\,\dot{q}_1(t)\right) + \left(-\beta_2\,\dot{q}_2(t)\right) + \cdots \tag{3-15}$$

The response reduction effect for each mode is achieved by choosing optimal sufficiently large value of the control gain β_i. However, dynamics of actuator or other dynamic components involved in the system cannot be ignored during the real-time control process, therefore the amplitude and phase of the response $\dot{q}_i(t)$ for each mode would be changed. Although the altered amplitude can be compensated by adjusting the value of β_i for each mode, the phase change might degrade the performance of this control strategy by reducing the stability margins as well as possible damping to be introduced. Hence, a modified MDVF controller designed to increase the closed-loop system stability and to make the system more amenable to the introduction of significant damping is needed. In Chapter 6 and Chapter 7, designed techniques would be introduced to compensate for the phase lags caused by the dynamic components for each control mode.

3.3 Control spillover and observation spillover

For a structural vibration control problem, it is expected to control a large DOF system with a much smaller order controller because of the computing power limitations and modelling error, which would restrict the control to a few critical modes C ($C < M$). These critical modes to be controlled are chosen based on the system performance requirements and are not necessarily the lowest few frequency modes in the spectrum. In order to examine the effects of control spillover and observation spillover, it is assumed that C is the number of the critical modes considered to be controlled of a floor system and the rest (R=$M - C$) of the modes are the residual (uncontrolled) modes which will lead to control and observation spillover [66], [67]. The control force:

$$F(x,t) = \sum_{i=1}^{L} \delta(x - x_i)f_i(t) \tag{3-16}$$

is generated by L force actuators located at points x_i ($i = 1,2 \ldots, L$), and the measured S sensor responses at points z_j ($j = 1,2 \ldots, S$) are expressed as either displacement:

$$y_j(t) = u(z_j, t) \qquad j = 1, \ldots, S \tag{3-17}$$

or velocity:

$$y_j(t) = \dot{u}(z_j, t) \qquad j = 1, \ldots, S \tag{3-18}$$

Then the equations of motion for an N-DOF structural system are written as (neglecting damping):

$$\boldsymbol{M}\ddot{\boldsymbol{u}} + \boldsymbol{K}\boldsymbol{u} = \boldsymbol{F} \tag{3-19}$$

From Eq. (3-7), the solution of Eq. (3-19) can be partitioned into a controlled part and a residual part of displacements as:

$$\boldsymbol{u}(x,t) = \boldsymbol{u}_C(x,t) + \boldsymbol{u}_R(x,t) \tag{3-20}$$

where the controlled part is:

$$\boldsymbol{u}_C(x,t) = \sum_{i=1}^{C} q_i(t)\boldsymbol{\varphi}_{\mathrm{i}}\,(t) \tag{3-21}$$

The modal coordinates $q_i(t)$ of the controlled modes form a vector $\boldsymbol{q}_C(t)$ and together with the velocity vector $\dot{\boldsymbol{q}}_C(t)$ form the state:

$$\boldsymbol{v}_C(t) = [\,\boldsymbol{q}_C^T(t), \qquad \dot{\boldsymbol{q}}_C^T(t)]^T \tag{3-22}$$

Similarly:

$$\boldsymbol{v}_R(t) = [\,\boldsymbol{q}_R^T(t), \qquad \dot{\boldsymbol{q}}_R^T(t)]^T \tag{3-23}$$

is the state of the residual part. Substituting of Eqs. (3-22) and (3-23) into Eqs. (3-16) and (3-19), $\boldsymbol{v}_C(t)$ and $\boldsymbol{v}_R(t)$ satisfy:

$$\dot{\boldsymbol{v}}_C(t) = \boldsymbol{A}_C\boldsymbol{v}_C(t) + \boldsymbol{B}_C\boldsymbol{f}(t) \tag{3-24}$$

$$\dot{\boldsymbol{v}}_R(t) = \boldsymbol{A}_R\boldsymbol{v}_R(t) + \boldsymbol{B}_R\boldsymbol{f}(t) \tag{3-25}$$

where $\boldsymbol{f}(t) = [f_1(t), \ldots, f_M(t)]^T$ is the control input vector, and the system parameters are expressed as:

$$\boldsymbol{A}_C = \begin{bmatrix} \boldsymbol{0} & \boldsymbol{I} \\ -\boldsymbol{\Lambda}_C & \boldsymbol{0} \end{bmatrix} \qquad \boldsymbol{A}_R = \begin{bmatrix} \boldsymbol{0} & \boldsymbol{I} \\ -\boldsymbol{\Lambda}_R & \boldsymbol{0} \end{bmatrix}$$

$$\boldsymbol{B}_C = \begin{bmatrix} \mathbf{0} \\ \boldsymbol{B}'_C \end{bmatrix} \qquad \boldsymbol{B}_R = \begin{bmatrix} \mathbf{0} \\ \boldsymbol{B}'_R \end{bmatrix}$$

where $\boldsymbol{\Lambda}_C$ and $\boldsymbol{\Lambda}_R$ are the diagonal matrices with entries of the controlled modal frequencies $\omega_1, \dots, \omega_C$ and $\omega_{C+1}, \dots, \omega_M$, respectively, and $\boldsymbol{B}'_C, \boldsymbol{B}'_R$ are the matrices whose rows are the controlled and residual mode shapes $\boldsymbol{\varphi}_{\mathrm{i}}(x)$ at the actuator locations x_i, which are:

$$\boldsymbol{B}'_C = \begin{bmatrix} \varphi_1(x_1) & \cdots & \varphi_1(x_M) \\ \vdots & \ddots & \vdots \\ \varphi_C(x_1) & \cdots & \varphi_C(x_M) \end{bmatrix} \qquad \boldsymbol{B}'_R = \begin{bmatrix} \varphi_{C+1}(x_1) & \cdots & \varphi_{N+1}(x_M) \\ \vdots & \ddots & \vdots \\ \varphi_M(x_1) & \cdots & \varphi_M(x_M) \end{bmatrix}$$

The sensor output vector:

$$\boldsymbol{y}(\boldsymbol{t}) = [y_1(t), \dots, y_S(t)]^T$$

satisfies:

$$\boldsymbol{y}(\boldsymbol{t}) = \boldsymbol{C}_C \boldsymbol{v}_C(t) + \boldsymbol{C}_R \boldsymbol{v}_R(t) \tag{3-26}$$

where, if displacement sensors are used:

$$\boldsymbol{C}_C = [\boldsymbol{C}'_C \quad \mathbf{0}] \qquad \boldsymbol{C}_R = [\boldsymbol{C}'_R \quad \mathbf{0}]$$

or, if velocity sensors are used:

$$\boldsymbol{C}_C = [\mathbf{0} \quad \boldsymbol{C}'_C] \qquad \boldsymbol{C}_R = [\mathbf{0} \quad \boldsymbol{C}'_R]$$

in either case:

$$\boldsymbol{C}'_C = \begin{bmatrix} \varphi_1(z_1) & \cdots & \varphi_C(z_1) \\ \vdots & \ddots & \vdots \\ \varphi_1(z_S) & \cdots & \varphi_C(z_S) \end{bmatrix} \qquad \boldsymbol{C}'_R = \begin{bmatrix} \varphi_{C+1}(z_1) & \cdots & \varphi_M(z_1) \\ \vdots & \ddots & \vdots \\ \varphi_{C+1}(z_S) & \cdots & \varphi_M(z_S) \end{bmatrix}$$

Recall that the controller introduced in Sec. 3.2 is achieved by ignoring the residual mode system (3-25), and an adequate control performance can be provided if the matrices $\boldsymbol{B}'_R$ and $\boldsymbol{C}'_R$ are both zero. This is not the case for most of control systems and their effects (to which the term ‘spillover’ is affixed) can be detrimental. The control forces excite the residual modes by the term $\boldsymbol{B}_R \boldsymbol{f}(t)$, which are termed the control spillover, while the sensor measurements are contaminated through the residual modes by the term $\boldsymbol{C}_R \boldsymbol{v}_R(t)$, which are termed the observation spillover, see Figure 3.1.

If the observation spillover is zero ($\boldsymbol{C}_R = \mathbf{0}$) and the modal direct velocity feedback control introduced in Sec. 3.2 is used, implying that $\boldsymbol{f}(t) = \boldsymbol{G}_C \boldsymbol{v}_C(t)$ in which $\boldsymbol{G}$ is the control gain matrix, the residual mode system of Eq. (3-25) is:

$$\dot{\boldsymbol{v}}_R(t) = \boldsymbol{A}_R \boldsymbol{v}_R(t) + \boldsymbol{B}_R \boldsymbol{G}_C \boldsymbol{v}_C(t) \tag{3-27}$$

or, equivalently:

$$\ddot{\boldsymbol{q}}_R(t) + \boldsymbol{\Lambda}_R \boldsymbol{q}_R(t) = \boldsymbol{B}_R \boldsymbol{G}_C \boldsymbol{v}_C(t) \tag{3-28}$$

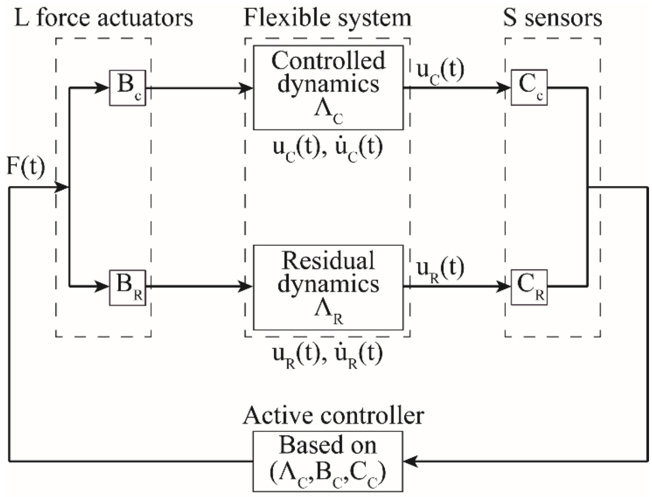

Figure 3.1 Control and observation spillover

Eq. (3-28) implies that the residual system with no damping is driven by $\boldsymbol{v}_C$ and any control spillover ($\boldsymbol{B}_R \neq \boldsymbol{0}$) would cause unwanted vibrations of the residual modes, and that the control spillover can degrade the system responses through residual modes, but it cannot destabilize the system when observation spillover is absent.

On the other hand, if the observation spillover is present and the modal direct velocity feedback control is used, the control force is expressed by $\boldsymbol{f}(t) = \boldsymbol{G}_C(\boldsymbol{v}_C(t) + \boldsymbol{v}_{spill}(t))$, in which $\boldsymbol{v}_{spill}(t)$ means the control mode responses contaminated with residual mode responses through $\boldsymbol{C}_R$ and $\boldsymbol{B}_R$. The composite closed-loop system becomes:

$$\dot{\boldsymbol{v}}_C(t) = (\boldsymbol{A}_C + \boldsymbol{B}_C \boldsymbol{G}_C)\boldsymbol{v}_C(t) + \boldsymbol{B}_C \boldsymbol{G}_C \boldsymbol{v}_{spill}(t) \tag{3-29}$$

$$\dot{\boldsymbol{v}}_R(t) = (\boldsymbol{A}_R + \boldsymbol{B}_R \boldsymbol{G}_{spill})\boldsymbol{v}_R(t) + \boldsymbol{B}_R \boldsymbol{G}_C \boldsymbol{v}_C(t) \tag{3-30}$$

Therefore, when observation spillover and control spillover are present, the poles of the closed-loop system are functions of the parameters of $\boldsymbol{C}_R$ with the stating values of poles ($\boldsymbol{A}_C + \boldsymbol{B}_C \boldsymbol{G}_C$) and $\boldsymbol{A}_R$.

It should be noted that even for a small perturbations of the original poles instabilities can occur, especially for the poles of $\boldsymbol{A}_R$ which are usually lie near the imaginary axis of the *s*-plane and have an insufficient stability margin. For the poles of $\boldsymbol{A}_C + \boldsymbol{B}_C \boldsymbol{G}_C$, it is not likely that the system becomes unstable for small spillover since they have been designed with a substantial stability. Although it is not always the case that the effects of control and observation spillovers would cause instability depending on the parameters $\boldsymbol{B}_C, \boldsymbol{B}_R, \boldsymbol{C}_C, \boldsymbol{C}_R$, all modal controllers have the possibility to produce instabilities unless observation spillover can be eliminated. Two obvious ways of reducing the effects of spillover are arranging the locations of actuators and sensors and using signal filters. Both of these two methods will be adopted in later Chapters.

3.4 Effects of actuator and filter dynamics

To simplify the explanation, all of the actuator and sensor dynamics have been ignored during the analysis, and it also has been assumed that the controller is perfectly implemented without the need for high or low pass filters. Accelerometers are usually used to measure the vibration of structures and they can be chosen such that a relatively flat frequency response within the bandwidth of interest, therefore their dynamics can be safely ignored. However, this is not the case for other dynamic components in reality and the existence of these dynamics can significantly influence both performance and stability of the resultant controller. Their effects on the structural system are discussed below.

3.4.1 Effects of actuator dynamics

In many civil engineering structures, it is often the case that there is no fixed frame of reference against which an actuator can react, therefore inertial actuators are generally used [68], [69]. The inertial actuator generates control forces through acceleration of a moving mass to the structure on which it is placed. Its behavior is described as a linear second order model as shown in Figure 3.2 [25].

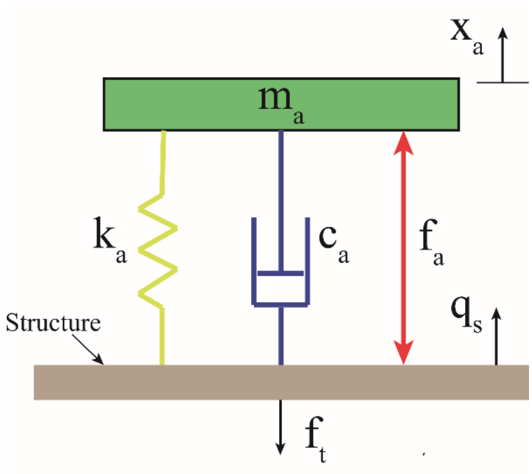

Figure 3.2 Inertial actuator model

It is assumed the filtered ith mode can be treated as a SDOF after applying modal filtering as Eq. (3-11). By transforming both side of Eq. (3-11) into its Laplace domain, it can be expressed as:

$$m_i s^2 q_i(s) + c_i s q_i(s) + k_i q_i(s) = F(\mathrm{s}) \tag{3-31}$$

Then the transfer function (TF) between the modal displacement and the modal force can be represented as:

$$G_i(s) = \frac{1/m_i}{s^2 + 2\xi_i \omega_i s + \omega_i^2} \tag{3-32}$$

where ξ_i, ω_i are the modal damping ratio and modal frequency of ith mode. The actuator control force $f_a(\mathrm{t})$ proportional to the input voltage of ith mode, based on Sec. 3.2, can be generated by scaling it with a constant gain g_i:

$$f_a(\mathrm{t}) = g_i v_i(t) \tag{3-33}$$

From Figure 3.2, using the displacements of the inertial mass and the structure x_a and q_s ($q_s = q_i$), respectively, the transmitted force from the actuator to the structure can be expressed in the Laplace domain as:

$$F_t(\mathrm{s}) = F_a(\mathrm{s}) + (c_a s + k_a)(Q_s(s) - X_a(s)) \tag{3-34}$$

where $F_t(\mathrm{s}), F_a(\mathrm{s}), X_a(s)$ and $Q_s(s)$ are the Laplace transforms of $f_t(\mathrm{t}), f_a(\mathrm{t}), x_a(t)$ and $q_s(t)$, respectively. At the same time, the transmitted force acts on the inertial mass so that:

$$F_t(\mathrm{s}) = m_a s^2 X_a(s) \tag{3-35}$$

Substituting Eq. (3-35) into Eq. (3-34), the following expression can be derived for the inertial mass displacement:

$$X_a(s) = \frac{1}{m_a s^2 + c_a s + k_a} F_a(\mathrm{s}) + \frac{c_a s + k_a}{m_a s^2 + c_a s + k_a} Q_s(s) \tag{3-36}$$

Substituting Eqs. (3-36) and (3-33) into Eq. (3-35), the transmitted force to the structure can be written as:

$$\begin{aligned} F_t(\mathrm{s}) &= \left(\frac{m_a s^2}{m_a s^2 + c_a s + k_a} g_i\right) V(s) + \left(\frac{m_a s^2 (c_a s + k_a)}{m_a s^2 + c_a s + k_a}\right) Q_s(s) \\ &= G_a(s) V(s) + G_r(s) Q_s(s) \end{aligned} \tag{3-37}$$

in which $V(s)$ is the Laplace transform of $v_i(t)$, $G_a(s)$ is the TF of the actuator when the mode displacement $q_i(s)$ is zero, and $G_r(s)$ is the sensitivity of the transmitted force to the mode movement. Eq. (3-37) can be expressed by the block diagram shown in Figure 3.3(a), in which the TF of modal structure $G(s)$ of Eq. (3-32) is considered.

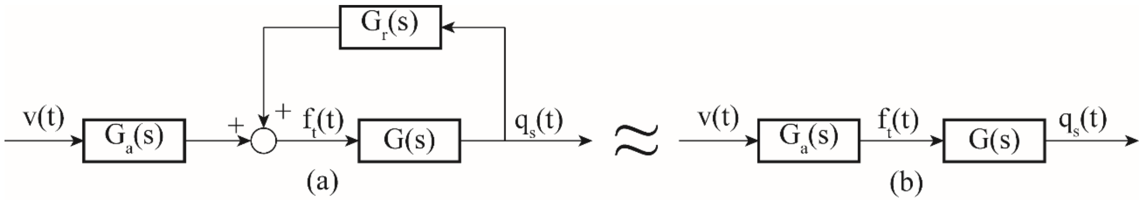

Figure 3.3 Decoupling between actuator and modal dynamics

From Figure 3.3(a), the TF between the modal displacement $Q_s(s)$ and the control voltage $V(s)$ is:

$$\frac{Q_s(s)}{V(s)} = G_a(s)\frac{G(s)}{1 + G(s)G_r(s)} \tag{3-38}$$

Where the term $G(s)G_r(s)$ can be written as:

$$G(s)G_r(s) = \frac{1}{m_i s^2 + c_i s + k_i}\frac{m_a s^2(c_a s + k_a)}{m_a s^2 + c_a s + k_a} \tag{3-39}$$

Since the modal mass m_i is much larger than the mass of actuator in civil engineering structure, it is obvious to get $m_a/m_i \approx 0$ such that $\mathrm{G}(s)\mathrm{G}_r(s) \approx 0$. Then Eq. (3-38) can be simplified as:

$$\frac{Q_s(s)}{V(s)} = G_a(s)G(s) \tag{3-40}$$

The block diagram of Eq. (3-40) is shown in Figure 3.3(b). Eq. (3-40) implies that the transmitted force generated by the actuator to the structure can be considered independent of the structural movement. The actuator dynamics $G_a(s)$, which is the TF between the transmitted force and control voltage, can be expressed as:

$$G_a(s) = \frac{F_t(\mathrm{s})}{V(s)} = \frac{m_a s^2}{m_a s^2 + c_a s + k_a} g_i = \frac{g_i s^2}{s^2 + 2\xi_a \omega_a s + \omega_a^2} \tag{3-41}$$

in which ξ_a and ω_a are the damping ratio and natural frequency of the actuator, respectively. Hence, if a control signal calculated by the controller is provided to the actuator, not only the amplitude but also the phase of the original signal is altered.

3.4.2 Effects of low pass and high pass filters

Both a low pass filter and a high pass filter are necessary during AVC implementation. A low pass filter is required to avoid spillover effects of the higher modes introduced in Sec. 3.3. A high pass filter is also required to avoid numerical issues associated with integration of acceleration signals to velocity as well as to reduce the stroke saturation effects caused by the dynamics of actuator, as described in Sec. 2.1. Therefore, it is of great importance to study the effects of the dynamics of these filters to the control system.

Filters can be divided into analog filters and digital filters, and the digital filter will be used in this study because of its better performance, not only in the time domain such as the step response but also in the frequency domain like the ripple and roll-off performance [70].

The finite impulse response (FIR) filter is one category of digital filter which is implemented through convolution, such as the Wiener and matched filters. Although these filters can achieve perfect performance for specific applications, it is not possible to apply a FIR filter in real-time control because of its heavy computational burden of convolution. In comparison, the infinite impulse response (IIR) filter works much faster, and can provide an acceptable level of performance.

The IIR filter is also called a recursive filter, implying that it is carried out through the recursive method. The algorithm of the recursive method is in the form of:

$$\begin{aligned} y[n] = a_0x[n] + a_1x[n-1] + a_2x[n-2] + a_3x[n-3] + \cdots \\ +b_1y[n-1] + b_2y[n-2] + b_3y[n-3] \end{aligned} \tag{3-42}$$

where $x[n], x[n-1], x[n-2], x[n-3]$ are the input signals at sampling time $n, n-1, n-2, n-3$, and $y[n], y[n-1], y[n-2], y[n-3]$ are the output signals at sampling time $n, n-1, n-2, n-3$. The coefficients "a" and "b" values that define the IIR filter are called the recursion coefficients. Eq. (3-42) implies that each point in the output signal is calculated by multiplying the values from the input signal by the "a" parameters, multiplying the previously calculated output signals by the "b" parameters, and adding them together. In practice, it is not possible to use more than a dozen recursion coefficients because the filter will become unstable.

The Chebyshev filter is often used as one of IIR filters for its ability of achieving a faster roll-off by allowing ripple in the frequency domain. As the ripple increase (not preferable), the roll-off becomes sharper (favorable). When the ripple is designed to 0%, the filter is called the Butterworth filter. There are four parameters to design a Chebyshev filter: (1) a high pass or low pass response, (2) the cut-off frequency, (3) the percent ripple in the passband and (4) the number of poles.

For a two-pole low pass Butterworth filter, it is designed by placing two poles evenly around the left-half of the circle on the *s*-plane, as shown in Figure 3.4. The radius of the circle is the cut-off frequency.

Since no zero exists in Figure 3.4, the TF of this filter can be written as:

$$H(s) = \frac{1}{(s-p_1)(s-p_2)} \tag{3-43}$$

where p_1 and p_2 are the two poles of the filter.

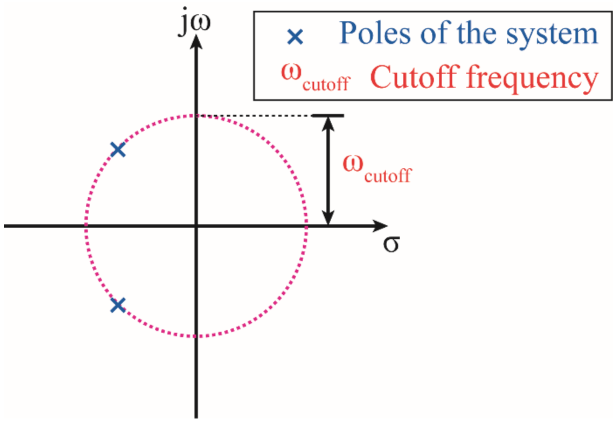

Figure 3.4 The Butterworth *s*-plane

Since a digital filter is considered here, it is necessary to convert the filter from the *s*-domain into the *z*-domain using the technique called the bilinear transform. The bilinear transform changes $H(\mathrm{s})$ into $H(\mathrm{z})$, by the substitution of:

$$s \rightarrow \frac{2(1-z^{-1})}{T(1+z^{-1})} \tag{3-44}$$

that is replacement of each s in the $H(s)$ with the above equation, and $T = 2\tan(0.5) = 1.093$. Therefore, the TF in the *z*-domain becomes:

$$H(z) = \frac{a_0 + a_1 z^{-1} + a_2 z^{-2}}{1 - b_1 z^{-1} - b_2 z^{-2}} \tag{3-45}$$

where “*a*” and “*b*” are the recursion coefficients shown in Eq. (3-42). For the design of a two-pole high pass Butterworth filter, it is simply changing the “*a*” and “*b*” coefficients of the low pass filter with the same cut off frequency using the technique called the spectral inversion, which keeps the “*b*” coefficients be unchanged and modifies the “*a*” coefficients by:

$$\begin{aligned} a_0 &= 1 - a_0 \\ a_1 &= -a_1 - b_1 \\ a_2 &= -a_2 - b_2 \end{aligned} \tag{3-46}$$

From Eq. (3-45), it is known that both the low pass filter and high pass filter are linear second order models, which are similar to the model of the actuator. Figure 3.5 and Figure 3.6 show the performance of two-pole Butterworth low pass and high pass filters with a cut-off frequency of $0.2\omega_{Ny}$, where ω_{Ny} is the Nyquist frequency, which is a half of the sampling frequency. It is obvious that the dynamics of these filters will change the amplitude as well as the phase of the original signal.

For the higher-order Butterworth filters, the process of design is similar to the two-pole case. However, since the phase change will become extremely large for a higher order filter and two-pole Butterworth filters perform well in the structural control region, the two-pole low pass and high pass filters (or bandpass filter) will be used in the ensuing chapters.

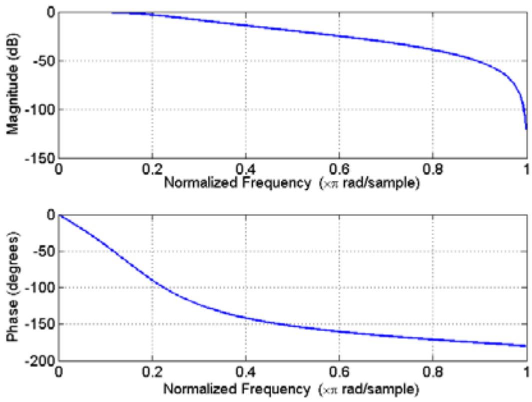

Figure 3.5 Two-pole Butterworth low pass filter

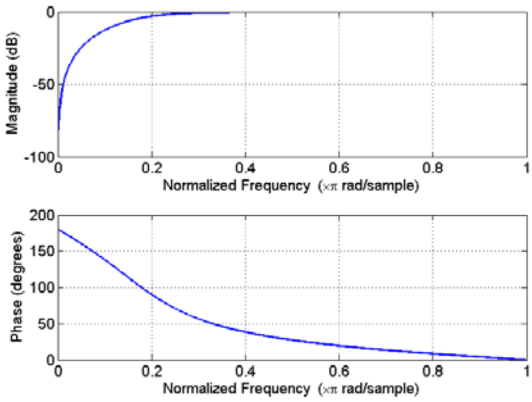

Figure 3.6 Two-pole Butterworth high pass filter

3.5 Types of delays

In the real-time active control tests, there are several inevitable time delays and lags that can be divided into three main categories: communication delays, computing time delays, and delays of dynamic components. These types of delays are described in this section.

3.5.1 Communication delays

Since the real-time active control is implemented as a closed-loop system, a continuous exchange of information among all of the components required to conduct the test (i.e., computer, digital signal processor (DSP) and data acquisition system) is needed and therefore communication delays obviously affect the system dynamics. The main communication delays are caused by:

1. The time required to pass the acceleration responses measured by accelerators to the data acquisition system.
2. The time required to digitize the continuous signals to discrete time digital signals with a time interval through Analog-to-Digital Conversion (ADC).
3. The time required to pass the digitized signals from data acquisition system to DSP and send back the control signals to the data acquisition system.
4. The time required to convert the digital signals to continuous signals through Digital-to-Analog Conversion (DAC).
5. The time required to send the continuous control signals to actuators.

These delays become especially important when conducting remote control through the internet since the network delays are random and can be very large. The communication delays can be assumed as a constant time delay during the real-time active control tests.

3.5.2 Computing time

The processor in the controller calculates the modal accelerations from the measured accelerations and the modal velocities by numerical time integration, and the control outputs based on the calculated modal velocities. This time required to calculate the actuator outputs at the next time step becomes especially significant for an adaptive controller and large model control (several modes need to be controlled). The computing time can also be seemed as a constant delay.

3.5.3 Delay of dynamic components

As discussed in Sec. 3.4, in real-time active control tests, the dynamic coupling of the structures with other dynamic components is particularly important, resulting in a phase lag between the command signal and the realization by the actuator. Typically, the phase lag can be modelled as a pure time delay and the time lag due to the dynamic components depends on the response frequency; therefore, this phase lag cannot be regarded as a constant time delay.

In fact, the total effects of these time delays and/or phase lags might reduce the stability margins and the possible damping to be introduced. In the implementation of the control strategy to the controller, all of these delays should be considered during the control system design.

3.6 Summary

This chapter provides background information regarding the model based active control, which will be used in the controller design in the ensuing chapters.

The modal filtering (MF) method is first reviewed. The modal filtering vectors are very sensitive to the modal shapes, therefore it is of great significance to identify accurate mode shapes prior to the calculation of the modal filtering vectors.

The simple modal direct velocity feedback controller, in which the control force for the *i*th mode is calculated as the modal velocity multiplied by a positive control gain, is presented. It performs well if dynamic components can be neglected. However, dynamics of the actuator or other dynamic components involved in the system cannot usually be ignored during the real-time control process and therefore improvement should be considered.

A review of the control spillover and observation spillover effects to the control system follows. If the observation spillover does not exist, although the control spillover can degrade the system response through the residual modes, it does not contribute to destabilization of the system. On the other hand, if both of the observation and control spillover exist, the combined effect of spillover can lead to closed-loop instabilities especially in the residual modes with insufficient stability margins.

Then, the effects of the actuator dynamics, the filter dynamics and the actuator-specimen interaction are presented. It has been demonstrated that the force transmitted from the actuator to the structure can be considered independent of the structural movement since the mass of the actuator is considerably smaller than the modal mass of floor. Also, it is shown that the dynamic characteristics of the actuator and the band pass filter can affect both magnitude and phase of the control signal.

Finally, the sources of time delays and lags are reviewed. All of these delays should be considered during the control system design such that a good control performance can be achieved.

Chapter 4 System for Active Control Testing

In order to allow execution of real-time AVC testing, a testing system consisting of the real-time-oriented hardware and software for high speed computation and communication, with high performance actuators and sensors has been designed. This system is used throughout study developed in this dissertation to experimentally evaluate the proposed methods and algorithms. Descriptions of the system architecture, components and tests conducted to characterize their performance are presented in this chapter.

4.1 System architecture

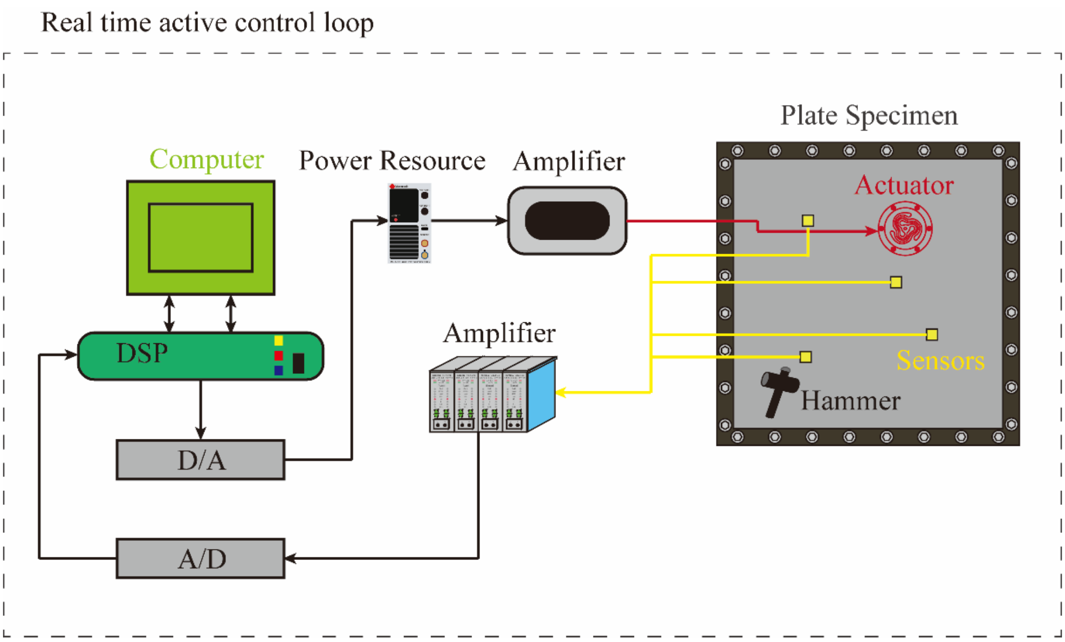

Figure 4.1 Schematic of system for real-time active control testing

Figure 4.1 shows the schematic of the testing system, which includes a hammer to generate impulsive loadings, an electromagnetic actuator connected with a power resource and an amplifier to produce the control force, four acceleration sensors to provide acceleration feedback through amplifiers, a computer to exchange data with a DSP (digital signal processor), which is used for real-time control algorithm development, and digital-to-analog (D/A) and analog-to-digital (A/D) converters. The DSP system is based on TMS320C6713 processor (Texas Instruments).

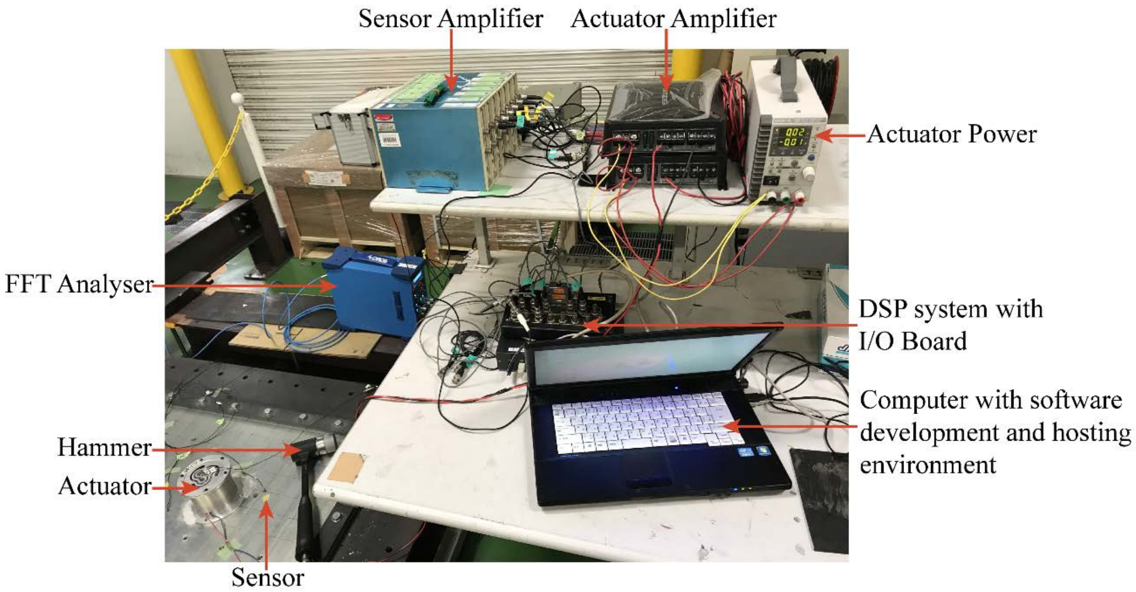

Figure 4.2 Experimental setup (system for real-time active control)

4.2 System components

Figure 4.2 shows the main components of the active control testing system and Figure 4.3 shows a detailed view of the components on the specimen. This testing equipment is developed at the testing facility of Sumitomo Riko Co. Ltd. in Komaki city in Japan.

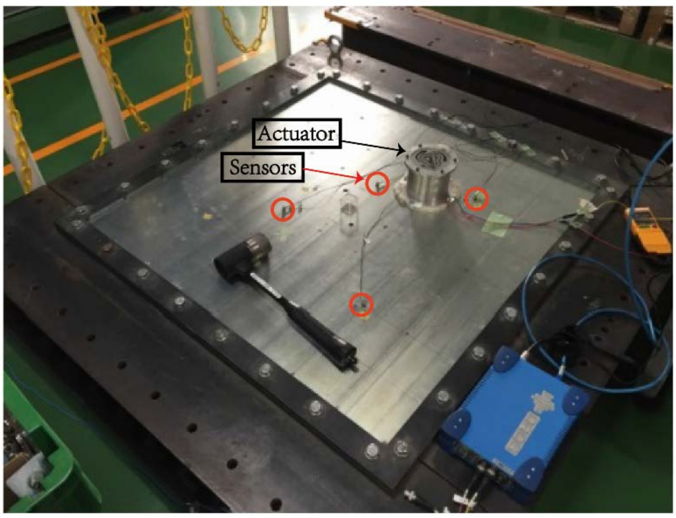

Figure 4.3 Experimental setup (on the plate)

Descriptions of the components of the real-time active control testing system are as follows:

4.2.1 Test specimen

A series of verification experiments are conducted on the steel plate shown in Figure 4.3, which is regarded as the floor model. The specimen consists of a 840mm×840mm steel plate with a thickness of 4.5mm. All four edges are connected to sufficiently rigid steel beams with bolt-clamp connection.

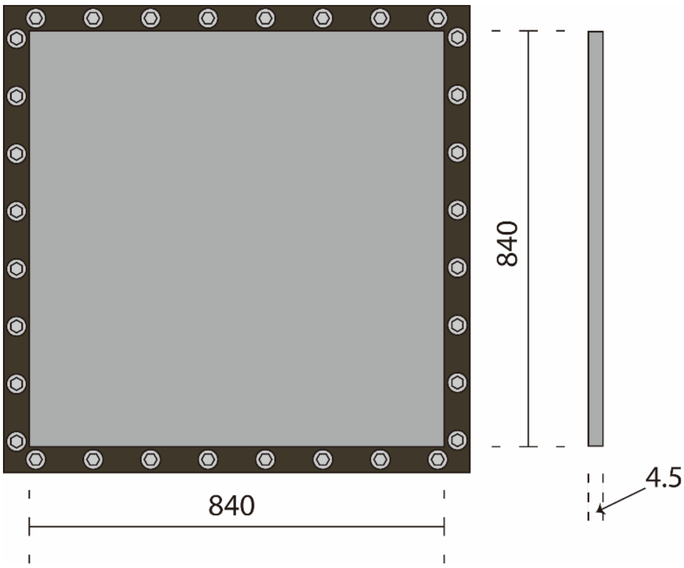

Figure 4.4 Dimensions of steel plate model (mm)

Dimensions and material properties of the steel plate are presented in Figure 4.4 and Table 4.1, respectively.

Table 4.1 – Material properties of steel plate

	Steel plate specimen
Young's modulus [N/mm^2]	2.06×10^5
Mass density [g/cm^3]	7.85
Poisson's ratio	0.27

4.2.2 Actuator and sensor

An electromagnetic actuator, which is manufactured by Sumitomo Riko Co. Ltd. for the development project, is used to provide the active control force. The appearance and dimension of the actuator are shown in Figure 4.5. The actuator consists of an inertial mass attached to a high performance magnet which is surrounded by a current-carrying solenoidal coil, as shown in Figure 4.6. The weight and stroke length of the inertial mass are 1.8kg and ±8mm, respectively. The actuator is connected to an analog amplifier and a power resource to generate the control force as shown in Figure 4.2.

Figure 4.5 Electromagnetic actuator

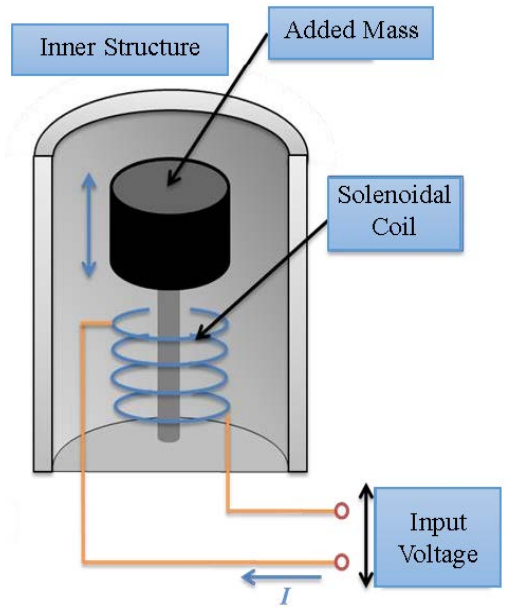

Figure 4.6 Components inside the actuator

The piezoelectric accelerometers are used in the tests to measure the vibrations of the steel plate. Specifications of the accelerometers are shown in Table 4.2. Strain in the piezoelectric materials generates electrical charge and then the electrical charge is converted into a voltage in a suitable range. The piezoelectric accelerometer consists of a mass which is connected to the floor structure through the piezoelectric material which acts as an extremely stiff spring. This mass-spring system has its own resonant frequency which must be well above the frequency range of interest. Acceleration in the floor structure can then produce an inertial force in the piezoelectric material, which will be proportional to the acceleration. The appearance and dimension of the accelerometer are shown in Figure 4.7.

Accelerometers can be mounted on the floor model via a variety of methods, such as using glue, magnets or beeswax. Since attaching the accelerometers with magnets and beeswax have the advantage that the sensing location can be moved with ease, this method is used in this study.

Table 4.2 – Sensor specifications

Mass	Frequency Range	Resonance Frequency	Temperature Range	Static Capacity
1.2g	1~25000Hz	70kHz	-50~+160 °C	410pF

Figure 4.7 Sensor used in the test

4.2.3 DSP and data communication system

A PC connected with the DSP system based on a parallel processing DSK board based on the Texas Instrument TMS320C6713 processor is used to carry out the real-time active control. An input-output board that contains 6 input (A/D) channels and 8 output (D/A) channels is employed to convert the signals from analog to digital, and digital to analog, respectively, both having a resolution of 16 bits. All of the input and output channels have a voltage capacity range of +/-10V, providing a minimum resolution of 0.3mV on the ADC. Figure 4.8 shows the DSP system used in the test. Access to the input and output channels is provided by the board connector panels that allow the signal cables to be connected via BNC ports.

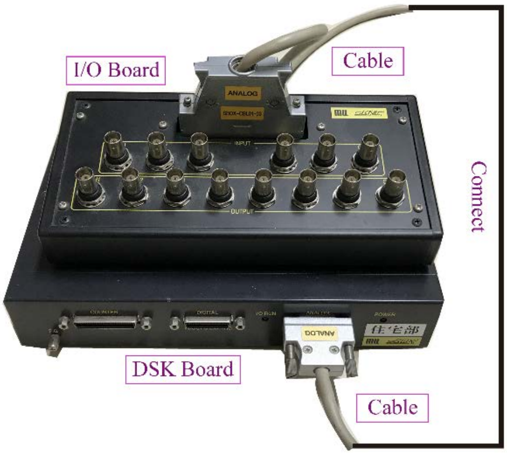

Figure 4.8 DSP system

4.2.4 Impulse hammer

The impulsive force for the active control testing is generated by striking the test object with the force-instrumented hammer shown in Figure 4.9. The length of the hammer is 37cm and the head diameter is 5.1cm.

Figure 4.9 Impulse hammer

The hammer consists of an Integrated Circuit Piezoelectric (ICP) force sensor mounted on the striking end of the hammer head. The sensing element works to transfer impulsive force into electrical signal for measurement. An impact tip is installed on the striking end of the hammer and it functions to transfer the force of impact to the ICP sensor and to protect the sensor face from damage.

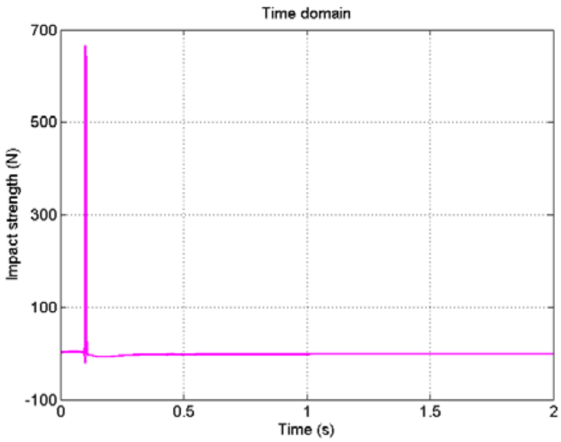

Figure 4.10 Impulsive response in the time domain

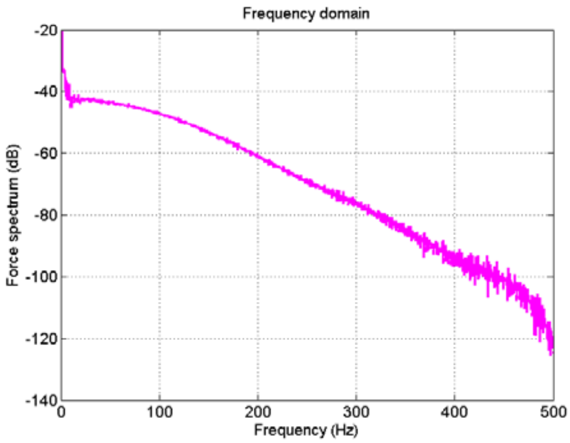

Figure 4.11 Impulsive response in the frequency domain

The hammer can generate a nearly constant spectral values over a broad frequency range and is therefore capable of exciting all of resonances of the specimen in that range. The force impulse in the time domain and frequency domain on a stiff mass for the hammer are shown in Figure 4.10 and Figure 4.11, respectively.

For more information about the hardware introduced above and the associated amplifiers, see Table 4.3.

Table 4.3 – Website for all the hardware products

Actuator	https://www.sumitomoriko.co.jp/index.php
Actuator Amplifier	http://pioneer.jp/carrozzeria/archives/products/gm_d6400_6100/
Sensor	http://svmeas.rion.co.jp/download/catalog/PV-90B
Sensor Amplifier	http://svmeas.rion.co.jp/products/10008/UV160009
DSP system	http://www.mtt.co.jp/dsp/sbox_index.html
Hammer	https://www.toyo.co.jp/pcb-pf/hammer.php

4.2.5 Software

The development environment for the algorithms used for the real-time active control is Code Composer Studio (CCS) development environment, as shown in Figure 4.12. All the algorithms are programmed into CCS using C language. In real-time active control testing, the output voltages to be imposed to the actuator are not known in advance. To prevent damage of the steel plate specimen and the actuator, limits of the absolute value of boundary outputs are set to prevent occurrence of excessive voltage. At each real-time step, the actuator output values are compared to the user-defined allowable values, and if any of these values is exceeded, the pre-defined value is used as the output.

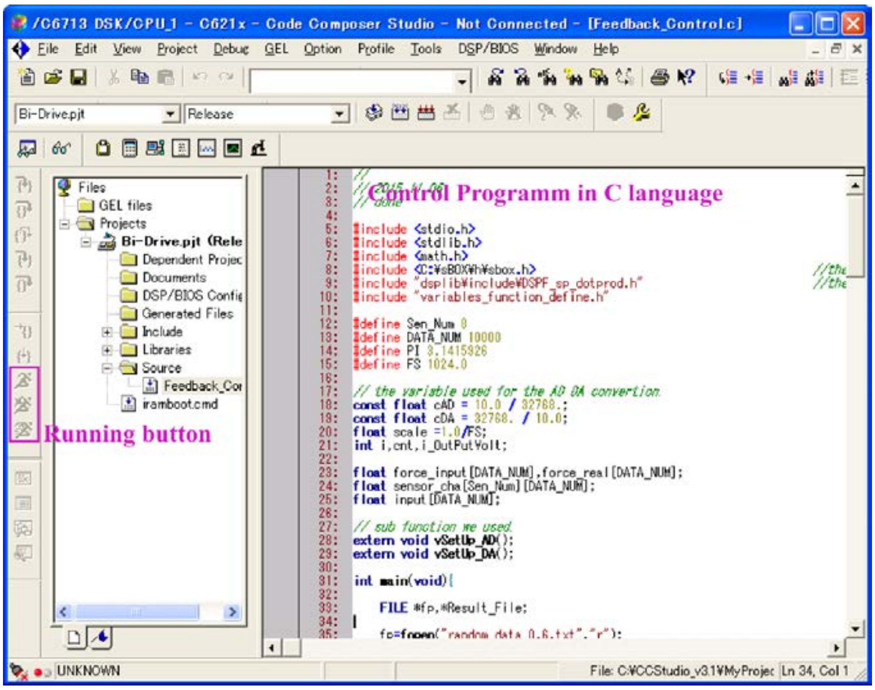

Figure 4.12 CCS interface

4.3 Modal testing of steel plate

It is necessary to establish an accurate model of the steel plate specimen for development of the active control algorithm based on modal filtering. The modal testing was carried out to identify the lowest modes of floor vibration. The identified mode shapes of the specimen can be used in the selection of the optimal sensor and actuator placement for the real-time control and implementation of the modal filtering technique. The identified mode frequencies can be utilized in the development of the modal phase compensation techniques. The modal tests were carried out in 4 hours without the adverse effects of extraneous excitation on the measurements.

4.3.1 Equipment

The modal testing was performed using the hammer described in Sec. 4.2.4 as the excitation source. The excitation forces were measured through the ICP sensor installed inside the hammer and sent to signal analyser.

The structural responses were measured using the piezoelectric accelerometers described in Sec. 4.2.2, which were mounted on the steel plate with beeswax.

The digital excitation and measurement signals were collected using the OR30 Series Multi-job FFT Analyser (http://www.toyo.co.jp/mecha/products/detail/oros-fft.html), which has 16 input channels. The analyser provided immediate calculation of frequency response functions (FRFs) so that the quality of the signals can be assessed as the modal testing progressed. The effective signals were recorded and stored on the analyser for the structural parameter estimation performed afterwards.

4.3.2 Methodology

A square 9×9 grid mesh was defined to specify 81 test points (sensor location candidates) on the surface of the steel plate, as shown in Figure 4.13. The testing proceeded by knocking the steel plate at Point 21 using the hammer, the response accelerometers were located at eight test points and FRF measurements were made. Then the seven accelerometers were moved to another set of seven locations while the location of the other one reference sensor was retained at its original location and again the FRF measurements were made. The approximate impulsive loading was adjusted through the reference sensor. This process is repeated until the acquisition of all of the 81 FRFs was completed. The frequency range of the recording was set between 0Hz and 200Hz during the modal testing.

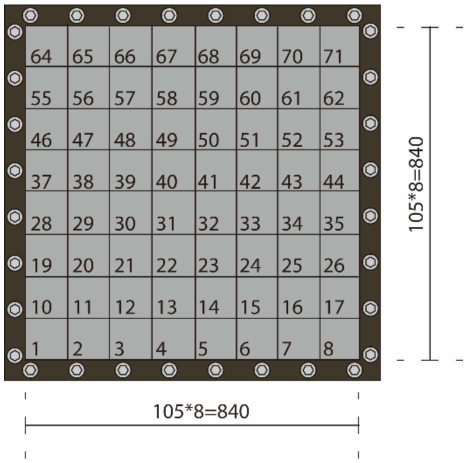

Figure 4.13 Point mesh on the steel plate

After the acquisition of 81 set FRF data, modal parameter estimation was conducted to determine the vibration modes of the steel plate. It took only a short time for the parameter estimation if the acquired data were of sufficient quality and if there were no points that required repeated measurement.

The rational fraction polynomial method with global fitting [71]–[73] was utilized to achieve the modal estimation. In this method, the global frequency and damping are estimated as the first step, and these data were then used to estimate the modal shapes in the second step, therefore this method provided more accurate parameter estimates than simultaneously estimating the modal frequency, damping and mode shape for each mode in each measurement.

The modal estimation was carried out using the commercial software “ME’scope” (http://systemplus.co.jp/product/mescope/index.html).

4.3.3 Results

The first five modes of vibration (modal natural frequencies, modal damping ratios and mode shapes) estimated from the measured FRF data are shown in Figure 4.14, Table 4.4 and Table 4.5.

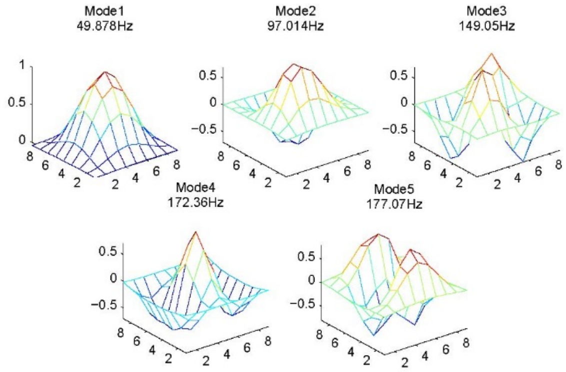

Figure 4.14 Identified modal frequencies and mode shapes

Table 4.4 – Identified modal frequencies and damping ratios

	Mode 1	Mode 2	Mode 3	Mode 4	Mode 5
Frequency	49.88Hz	97.01Hz	149.05Hz	172.36Hz	177.07Hz
Damping ratio	0.0108	0.0052	0.0035	0.0029	0.0036

Table 4.5 – Relative mode shape values

	Mode 1	Mode 2	Mode 3	Mode 4	Mode 5
Point 1	-0.0148	-0.0226	0.0011	-0.0049	0.0017
Point 2	-0.0103	-0.0051	0.0117	-0.0193	0.0307
Point 3	-0.0034	0.0156	0.0241	-0.0291	0.0652
Point 4	0.0004	0.0236	0.0166	-0.0256	0.0837
Point 5	0.0038	0.0264	-0.0004	-0.0243	0.0919
Point 6	0.0055	0.0261	-0.0186	-0.0297	0.0913
Point 7	0.0039	0.0193	-0.0234	-0.0338	0.0655
Point 8	0.0033	0.0118	-0.0188	-0.0284	0.0374
Point 9	0.0027	0.0065	-0.0124	-0.0196	0.0103
Point 10	-0.0127	-0.0040	0.0141	-0.0584	-0.0100
Point 11	0.0205	0.1417	0.2550	-0.2315	0.1004
Point 12	0.0931	0.3637	0.5228	-0.2962	0.3437
Point 13	0.1594	0.4697	0.4416	-0.1201	0.6320
Point 14	0.1896	0.4348	0.0514	0.0095	0.7949
Point 15	0.1601	0.2976	-0.3383	-0.1075	0.6748
Point 16	0.1026	0.1591	-0.4692	-0.2936	0.3934
Point 17	0.0370	0.0524	-0.2517	-0.2478	0.1242
Point 18	0.0071	0.0057	-0.0318	-0.0815	-0.0095
Point 19	-0.0118	0.0106	0.0239	-0.0939	-0.0249
Point 20	0.0919	0.3302	0.4946	-0.4605	-0.0057
Point 21	0.2927	0.7894	0.9990	-0.5408	0.2452
Point 22	0.4770	0.9983	0.8569	-0.0706	0.6951
Point 23	0.5521	0.8727	0.0922	0.2730	0.9868

	Mode 1	Mode 2	Mode 3	Mode 4	Mode 5
Point 24	0.4775	0.5674	-0.6817	-0.0319	0.8140
Point 25	0.3081	0.2641	-0.9415	-0.5337	0.3353
Point 26	0.1150	0.0771	-0.5233	-0.5030	0.0287
Point 27	0.0125	0.0058	-0.0441	-0.1246	-0.0339
Point 28	-0.0135	0.0166	0.0156	-0.1154	-0.0443
Point 29	0.1553	0.3758	0.3633	-0.5738	-0.3476
Point 30	0.4738	0.8531	0.7264	-0.5568	-0.4756
Point 31	0.7368	0.9831	0.6090	0.2086	-0.1672
Point 32	0.8520	0.7317	0.0452	0.7357	0.0727
Point 33	0.7521	0.3416	-0.5723	0.2686	-0.0926
Point 34	0.4835	0.0608	-0.7709	-0.5393	-0.4214
Point 35	0.1883	-0.0129	-0.4397	-0.6007	-0.3574
Point 36	0.0126	0.0043	-0.0390	-0.1458	-0.0604
Point 37	-0.0196	0.0165	-0.0025	-0.1203	-0.0526
Point 38	0.1765	0.2476	-0.0296	-0.5372	-0.5257
Point 39	0.5589	0.5013	-0.0580	-0.4235	-0.8966
Point 40	0.8707	0.4077	-0.0673	0.4573	-0.7218
Point 41	0.9997	0.0503	-0.0405	0.9984	-0.5273
Point 42	0.8789	-0.3234	-0.0617	0.4494	-0.7353
Point 43	0.5741	-0.3819	-0.1044	-0.3969	-0.9509
Point 44	0.2105	-0.1858	-0.0727	-0.5343	-0.5984
Point 45	0.0096	0.0013	-0.0184	-0.1391	-0.0721
Point 46	-0.0227	0.0117	-0.0236	-0.1213	-0.0391
Point 47	0.1416	0.0685	-0.4243	-0.5467	-0.2696
Point 48	0.4601	0.0468	-0.8358	-0.5420	-0.3624
Point 49	0.7262	-0.2178	-0.6764	0.2044	-0.0817
Point 50	0.8372	-0.6418	-0.0370	0.6716	0.0907
Point 51	0.7748	-0.8020	0.3906	0.2553	-0.3272
Point 52	0.4861	-0.7403	0.5756	-0.5034	-0.5444

	Mode 1	Mode 2	Mode 3	Mode 4	Mode 5
Point 53	0.1787	-0.3243	0.2816	-0.5591	-0.4127
Point 54	0.0086	-0.0014	0.0008	-0.1397	-0.0666
Point 55	-0.0288	0.0079	-0.0235	-0.1030	-0.0178
Point 56	0.0767	-0.0266	-0.4832	-0.4878	0.0593
Point 57	0.2823	-0.1725	-0.9623	-0.5954	0.3529
Point 58	0.4709	-0.4567	-0.7760	-0.1204	0.7654
Point 59	0.5396	-0.7845	-0.0158	0.2093	0.9439
Point 60	0.3536	-0.8283	0.5475	-0.2189	0.7722
Point 61	0.2817	-0.7456	0.7559	-0.6224	0.1786
Point 62	0.1031	-0.3021	0.3737	-0.5143	-0.0563
Point 63	0.0035	0.0040	0.0091	-0.1187	-0.0430
Point 64	-0.0348	0.0048	-0.0162	-0.0667	0.0010
Point 65	0.0046	-0.0286	-0.2526	-0.2585	0.1374
Point 66	0.0851	-0.1194	-0.5078	-0.3581	0.3982
Point 67	0.1595	-0.2591	-0.4087	-0.2115	0.6689
Point 68	0.1782	-0.3918	-0.0121	-0.1060	0.7580
Point 69	0.1443	-0.4420	0.3265	-0.2437	0.6083
Point 70	0.0848	-0.3366	0.3949	-0.3759	0.3136
Point 71	0.0265	-0.1264	0.1952	-0.2683	0.0779
Point 72	-0.0032	0.0161	0.0058	-0.0650	-0.0183
Point 73	-0.0402	0.0027	0.0002	-0.0193	0.0086
Point 74	-0.0341	-0.0017	-0.0082	-0.0337	0.0385
Point 75	-0.0284	-0.0055	-0.0150	-0.0430	0.0680
Point 76	-0.0217	-0.0105	-0.0154	-0.0444	0.0926
Point 77	-0.0148	-0.0133	-0.0025	-0.0417	0.1009
Point 78	-0.0114	-0.0120	0.0104	-0.0436	0.0943
Point 79	-0.0103	0.0006	0.0111	-0.0364	0.0654
Point 80	-0.0097	0.0149	0.0073	-0.0239	0.0355
Point 81	-0.0089	0.0309	-0.0004	-0.0009	0.0047

Based on the results of the modal testing, the total number of the modes within the bandwidth of interest are selected to be five. In the subsequent steps of the investigation, the $1\text{st}{\sim}3\text{rd}$ modes of the plate are chosen as the control modes, and the $4\text{th}{\sim}5\text{th}$ modes are considered as the residual modes, which will be used to analyse the spillover effects. More details will be shown in the next chapter.

4.4 System characterization

When conducting real-time active control experiments, information on the dynamic responses of the testing components is essential for the control algorithm development. Effects associated with actuator dynamics and time delays must be properly determined in advance. In this section, experimental identification of the actuator dynamics and time delays are conducted.

4.4.1 Actuator dynamics

In order to understand the behavior of the actuator over a wide range of frequencies, the TF $G_a(s)$ from the input voltage (V) to the measured actuator force (N) was determined using a binary random excitation as input, as shown in Figure 4.15. The actuator force was measured by placing an accelerometer on the top of the actuator mass and obtained by multiplying the measured acceleration by the weight of the actuator mass. The output accelerations are shown in Figure 4.16. The data were captured at a sampling rate of 1000Hz for 5 seconds.

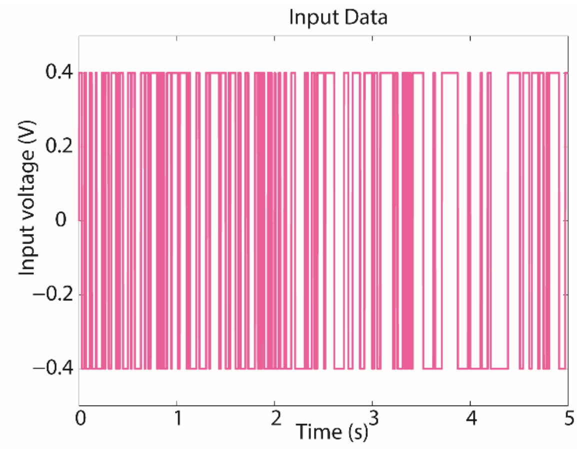

Figure 4.15 Input binary random data

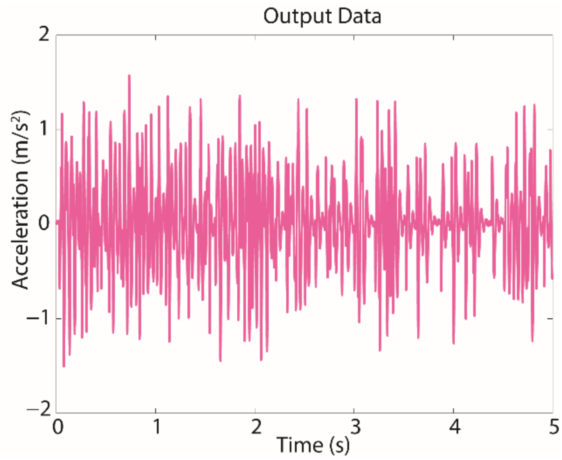

Figure 4.16 Output acceleration

The data set was divided into two parts; the first half data were used to estimate the actuator model while the second half data were used to detect the degree of fitting of the estimated model. The former was carried out through the Instrument Variable (IV) method as long as the number of the poles and zeros are known, while the latter was achieved through simulating the response of the estimated model and comparing the result with the measurement.

These were done using the System Identification Toolbox in MATLAB. The obtained actuator model was:

$$G_a(s) = \frac{F_t(s)}{V(s)} = \frac{12.228s^3 + 15091s^2 - 2.73e^4 s - 5.7174e^6}{s^3 + 381.17s^2 + 3.7852e^4 s + 4.7259e^6} \tag{4-1}$$

Transfer Eq. (4-1) to the zero-pole form gives:

$$G_a(s) = \frac{12.228(s - 18.45)(s + 20.57)(s + 1232)}{(s^2 + 2 * 0.295 * 123.85s + 123.85^2)(s + 308.1)} \tag{4-2}$$

It can be found that there are two zeros near the origin in Eq. (4-2). The dynamics of the actuator can be regarded as a linear second-order system described in Sec. 3.4.1 cascaded with a system of the term $(s + 1232)/(s + 308.1)$, which is added to account for the dynamic property of the actuator. The natural frequency and damping ratio of the actuator are estimated to be 19.71Hz and 0.2950, respectively. The bode diagram of the actuator system and the experimental data are shown in Figure 4.17.

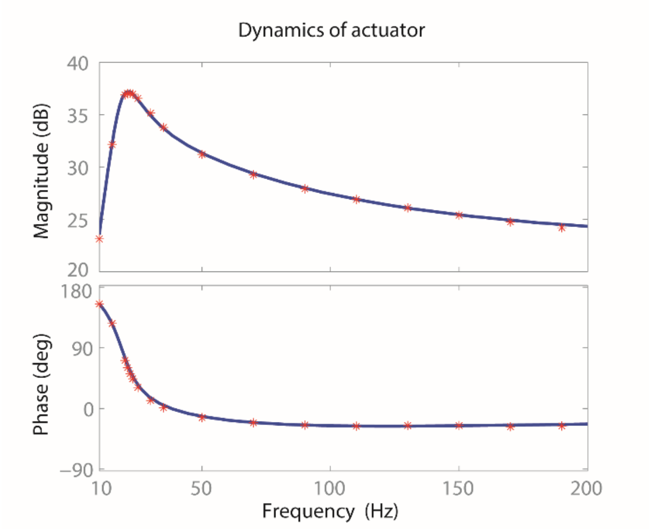

Figure 4.17 Frequency response of actuator: (*) experimental (—) model

Ideally, one would expect an actuator system with a phase lag of zero over the entire control frequency range. In usual cases, this behavior is not possible. At all the identified modes of the steel plate including the first mode at the natural frequency of 49.88Hz, non-zero phase lags present as indicated by the phase plot.

4.4.2 Time delays

Except for the actuator time lags, there are several other time delays and lags exist during the real-time active control experiment. Possible sources of these delays and lags are as follows:

- Sampling rate of the controller

- Computation time
- A/D converter for measured signals
- D/A converter for command signals
- Communication delays of cables
- Low pass and high pass filter time lags

A series of tests were performed to quantify these time delays. The communication delays caused by cables was assumed to be negligible.

For the first test, the DSP system was set to run with a sampling time of 1msec (sampling rate of 1000Hz). A sinusoidal function with a frequency of 50Hz and an amplitude of 0.05V was generated, sent out to the D/A interface, and instrumented by the A/D interface by connecting the interfaces with a cable. This test considered the total delays associated with the D/A and A/D converters. Figure 4.18 shows the results of this test. As can be observed, the delays are approximately 1msec (one time step).

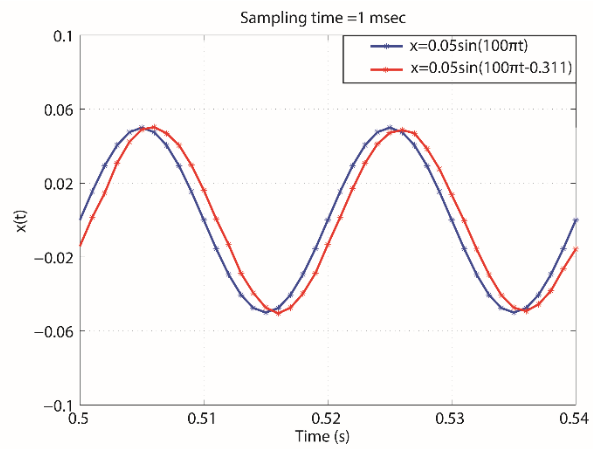

Figure 4.18 Time delays generated by A/D-D/A

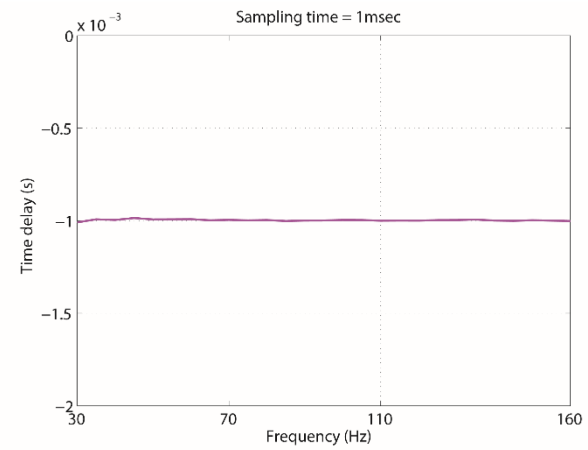

Figure 4.19 A/D-D/A time delays of different frequencies

The tests with the identical procedure were also conducted in the frequency range between 30Hz and 160Hz to examine the A/D-D/A delays at various frequencies. The results are shown in Figure 4.19. It is obvious that the A/D-D/A time delays do not depend on frequency and therefore can be regarded to be constant.

The effect of the sampling rate on the time delay was studied using the same sinusoidal signal as the first test (50 Hz and 0.05V). The sampling rate was changed from 500Hz to 5000Hz with a frequency interval. It can be seen from Figure 4.20 that as the sampling rate increases, the time delays caused by A/D-D/A decreases (keep one time step). In the following tests, the sampling rate of 1000Hz is chosen for consistency with the previous tests.

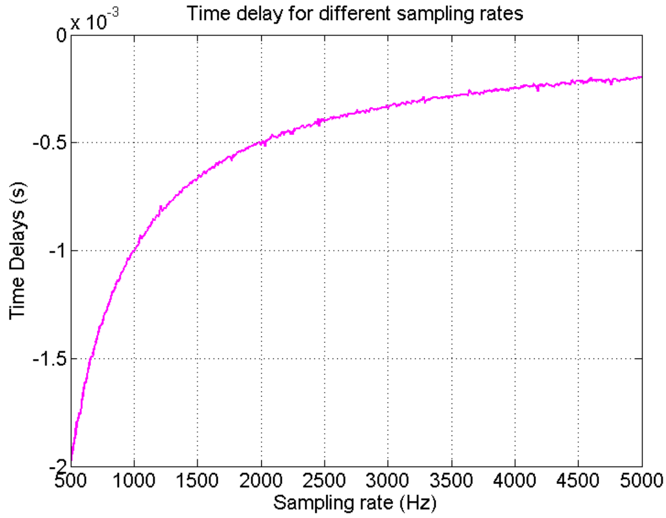

Figure 4.20 Effect of sampling rate

The delay time due to calculation of the DSP system used in the tests was measured. Using the model identical to the one used for the real active three modes control of floor vibration testing, as described in Chapter 8, a computational burden is provided to the DSP system by running a code to simulate the response. Figure 4.21 shows the measured signal that includes the delays associated with the converters and computation time, and the signal that only includes the A/D-D/A delays. As can be observed, the total time delays are estimated to be the same for the two signals. Therefore, the computation time can be neglected during the real-time control tests.

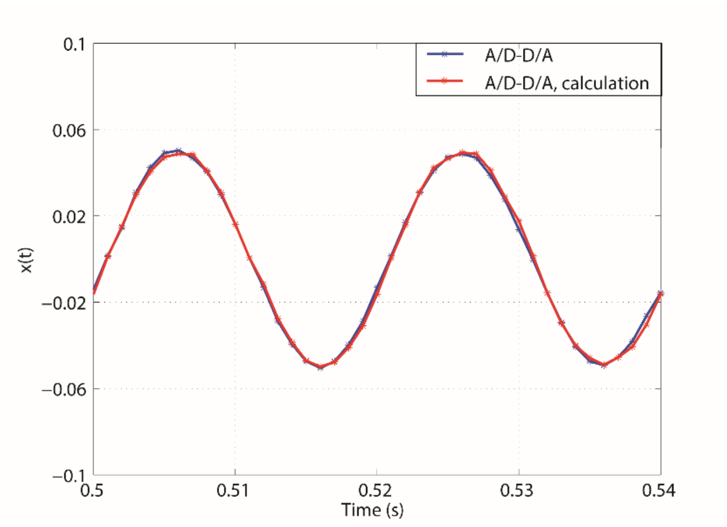

Figure 4.21 Effect of calculation delay

The time lags associated with the actuator was measured. The measurement procedure is as follows: the same sinusoidal wave was generated on the DSP system, the signal was sent to the D/A interface to activate the actuator and the measured acceleration signal was captured by the A/D interface. The acceleration is measured by attaching an accelerometer on the top of the actuator mass. Since the amplitude of the measured signal was significantly larger than 0.05V, the amplitude was scaled to 0.05V for phase comparison. The results are shown in Figure 4.22, which includes the command signal (blue line), the measured A/D-D/A signal (red line) and measured A/D-D/A-actuator signal (green line). The time delay caused by A/D-D/A and the actuator is approximately 1.7msec. Therefore the time delay of the actuator for 50Hz sinusoidal input is 0.7msec.

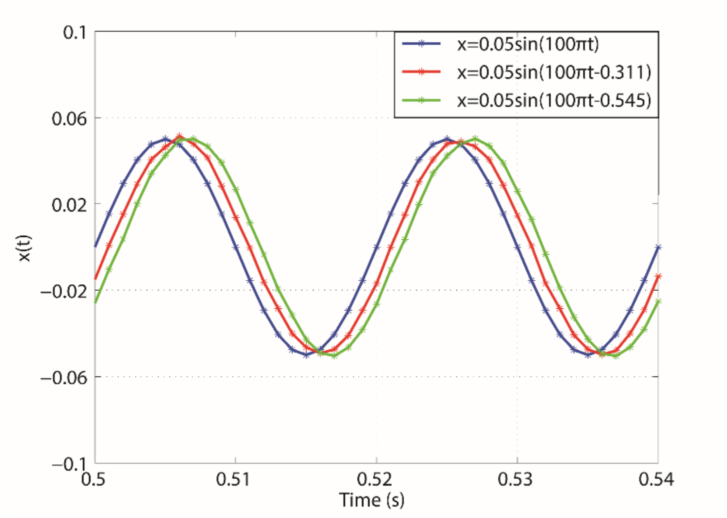

Figure 4.22 Effect of actuator delay

Finally, the time lags caused by low pass filter and high pass filter were measured. Two-pole Butterworth filters described in Sec. 3.4.2 were used in the tests. The cut-off frequency for high pass filter was set to 10Hz, while the cut-off frequency for low pass filter was 200Hz. The same signal was generated on the DSP system, sent out the D/A interface, and captured by the A/D interface, then the low pass filter or the high pass filter was applied on the captured signal. The results are shown in Figure 4.23 and Figure 4.24, which include the command signal (blue line), the measured A/D-D/A signal (red line) and measured A/D-D/A-high pass or low pass filtered signal (green line). From Figure 4.23, it can be observed that the total time delays caused by A/D-D/A and the high pass filter are approximately 0.085msec, which means that the high pass filter provides a lead time to the measured signal. The lead time of the high pass filter for the 50Hz sinusoidal signal is 0.915msec. The total time delays caused by A/D-D/A and low pass filter is approximately 2msec, as can be seen from Figure 4.24. Therefore, the time delay of the low pass filter for the 50Hz sinusoidal signal is 1msec.

It should be noted that the time delays of the actuator and the filters were measured using only the 50Hz sinusoidal signal. The time delays for other sinusoidal signals will not the same as the 50Hz case, which can be explained by comparison of Figure 3.5, Figure 3.6 and Figure 4.17.

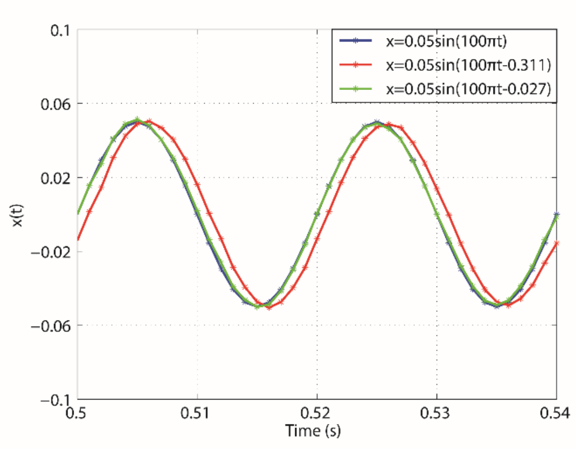

Figure 4.23 Effect of high pass filter

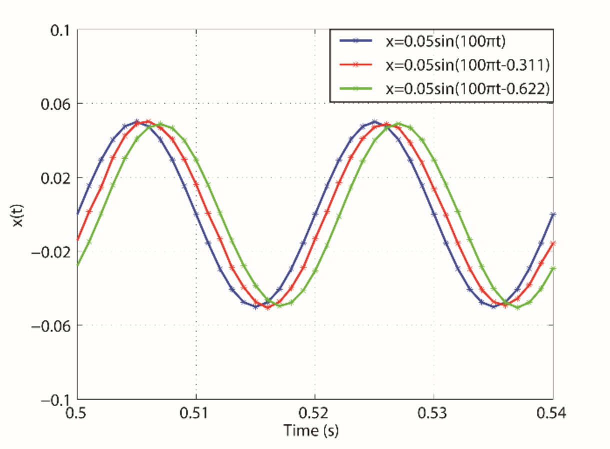

Figure 4.24 Effect of low pass filter

It can be concluded from the measurement results that the main sources of delays in the present real-time testing system are the A/D-D/A converters, dynamics of actuators and filters.

4.5 Selection of sampling rate

It can be observed from Figure 4.20 that the value of sampling rate significantly affects the A/D-D/A time delays, and several other factors must be considered when choosing the sampling rate for satisfactory execution of a real-time active control experiment. These factors include accurate integration of the filtered modal response from acceleration to velocity, maintaining smoothness of the control signal and effective use of the two-pole Butterworth filters. Based on a series of trial-and-error testing, the sampling rate for the modal filtering-based active control is selected to be 1000Hz.

4.6 Summary

A testing system that combines real-time hardware and software with high performance actuators and sensors is assembled for real-time active control experiments. The testing system is used throughout the whole active control experiments.

Modal testing of the plate specimen and the actuator is conducted. Five modes are identified in the natural frequency range less than 200Hz. The lowest three modes are to be controlled and the other two modes are considered as the residual modes in the investigation developed in the ensuing chapters.

Time delays/lags are critical parameters in the real-time active control experiments. Experimental measurements to quantify these parameters show that the time lags/delays associated with the A/D-D/A converters, dynamics of actuators and filters are the dominant factors, while computing time and delays related to communication are, in general, relatively small.

Chapter 5 Optimal Sensor and Actuator Placement

A new approach to optimal placement of sensors and actuators for suppressing vibration of floor panels using the modal filtering technique is presented. As discussed in Sec. 3.3, limitation of the model-based methods is related to the spillover effects caused by the neglected modes. In this chapter, a sensor and actuator placement determination procedure is developed so that enhancement of the separation performance of the modelled modes and reduction of the spillover effect of the truncated modes in modal filtering are achieved at the same time by combining the minimum spillover method, effective independence method (EFI) and modal assurance criterion (MAC). Performance of the proposed procedure is investigated by conducting verification tests on the rectangular steel plate, and the sensor placement determined by the proposed approach achieves preferable results than other two sensor placement cases. The effectiveness of the proposed approach is also verified by state feedback control for individual modes.

5.1 Introduction

The optimal sensor placement (OSP) in mechanical systems and structures has become a popular and frequently discussed topic in the past decades. Applications cover a variety of areas such as modelling, identification, fault detection, health monitoring and active control of such systems [74]–[81]. On the other hand, the optimal actuator placement (OAP) is frequently used in the area of active control and investigated in association with the OSP. The goal of OSP and OAP is to determine where sensors or actuators are to be installed so that the configuration fulfils the requirements.

For the case of active control of human induced vibration of floors, since Direct-Output Feedback controllers are usually adopted, sensor and actuator placement for the application of modal filtering based active control have not been deeply developed. In Sec. 3.1, it has been shown that there are as many as $N!/(S!\,(N-S)!)$ candidates to choose S sensor locations from a possible N candidates if the modal filtering technique is utilized, therefore it is not an easy task to select the sensor placement to achieve the optimal modal filtering matrix [51].

For successful application of the MF technique for floor system vibration control, the placement of sensors and actuators to reduce the associated noise and spillover effects and to enhance the performance of the system as well as its fatigue durability is of great significance [82]. While the number of sensors should be greater or equal to the total number of the modes considered in modal filtering, use of a large number of sensors is not recommended for the economic and aesthetic considerations. For the case of dynamic response control of a system with classical damping, it is possible to point out the following four issues that should be considered in determining the sensor placements.

1) Observability: the sensors should be located in the vicinity of the anti-nodes of the natural modes to be measured.
2) State estimate ability [19]: the covariance matrix of the estimate errors should be as small as possible with the effect of white noise in the measurement signal by the sensors.
3) Orthogonality: this property is considered to ensure the principle of modal filtering to rigorously hold and to enhance robustness against the error of modal shape estimation.
4) Observation spillover: since it is not practical and not necessary to model all the modes, a few number of lower modes or modes in the bandwidth of interest are considered to be controlled by this method. However, the neglected modes are still present in the system and the truncation of the modes may cause a spillover effect when the system is subjected to disturbance excitations or control forces, as described in Sec.3.3. The spillover observed by the sensors should be as small as possible to avoid instability caused by the truncated modes [66], [67], [83].

There are two issues for the optimal actuator placement.

1) Controllability: the actuators should be located in the vicinity of the anti-nodes of the natural modes to be controlled.
2) Control spillover: parallel to the observation spillover, the control spillover generated by actuators should be as small as possible to avoid instability caused by the truncated modes.

The objective of the study described in this chapter is to develop a sensor and actuator placement procedure to deal with the above problems. The minimum spillover method, the effective independence method and the modal assurance criterion used as background techniques are introduced in Sec. 2. The proposed sensor and actuator placement method that enhances the separation performance of the modelled modes and reduces the spillover effects of the neglected modes is developed in Sec. 3. Some results of experimental tests are discussed in Sec. 4.

5.2 Preliminaries

5.2.1 The minimum spillover method

As introduced in Sec. 3.1, the MF technique is based on the idea of coordinate transformation, where the signal measured by the sensors can be expressed as a linear combination of sinusoidal responses in multiple natural vibration modes. Sensors can be placed randomly on the meshed point of finite elements, while the mode shape of the individual meshed points for each mode can be obtained from either FEM or modal testing. From Eq. (3-6), the physical responses measured by sensors can be expressed as:

$$\boldsymbol{u}(\mathrm{t}) = \sum_{n=1}^{N} A_n \boldsymbol{\varphi}_n \cos(\omega_n t - \gamma_n) = \sum_{n=1}^{N} q_n(t) \boldsymbol{\varphi}_n \tag{5-1}$$

where $\boldsymbol{u}(\mathrm{t})$ is the responses measured by sensors represented as a vector, *N* is the number of natural modes to be considered, A_n is the real amplitude, $\boldsymbol{\varphi}_n$ is the modal shape vector, γ_n is the phase, ω_n is the natural angular frequency and *n* denotes that the variable is for the *n*th mode. The symbol $q_n(t)$ represents the generalized coordinate of the *n*th mode that represents the *n*th mode response $A_n \cos(\omega_n t - \gamma_n)$ in this case.

The number of the modes *N* is assumed to be a finite integer. Let us assume that the number of the controlled modes be M such that $M < N$. In this case, the responses $\boldsymbol{u}(\mathrm{t})$can be divided into a controlled part and a residual part [84], [85], as discussed in Sec. 3.3, which can be expressed in a matrix-form:

$$\{u\} = [\varphi_m]\{q_m\} + [\varphi_{um}]\{q_{um}\} \tag{5-2}$$

where $\{u\}$ is an S-dimensional vector, S is the number of sensors such that $S \geq M$, the size of the matrix $[\varphi_m]$ is $S \times M$, that of $[\varphi_{um}]$ is $S \times (N - M)$, $\{q_m\}$ is an M-dimensional vector and $\{q_{um}\}$ is an $(N - M)$-dimensional vector.

From Eq. (5-2):

$$\{q_m\} = ([\varphi_m]^T[\varphi_m])^{-1}[\varphi_m]^T\{u\} - ([\varphi_m]^T[\varphi_m])^{-1}[\varphi_m]^T[\varphi_{um}]\{q_{um}\} \tag{5-3}$$

Note that $([\varphi_m]^T[\varphi_m])^{-1}[\varphi_m]^T)$ is the generalized inverse of the modal matrix $[\Psi_m]$ [86]. The second term on the right hand side of Eq. (5-3) is referred to as the residual part. If the spillover effects are sufficiently small and negligible, Eq. (5-3) can be expressed as:

$$\{q_m\} = ([\varphi_m]^T[\varphi_m])^{-1}[\varphi_m]^T\{u\} \tag{5-4}$$

In order for $\{q_m\}$ to be acceptably expressed by Eq. (5-4), the modal shape matrix $[\varphi_{um}]$ included in the residual part should be altered by adjusting the sensor placement. The observation spillover term $\{\Delta\}$ is defined as the residual part with the negative sign:

$$\{\Delta\} = ([\varphi_m]^T[\varphi_m])^{-1}[\varphi_m]^T[\varphi_{um}]\{q_{um}\} = [\varphi_{spill}]\{q_{um}\} \tag{5-5}$$

Minimization of the observation spillover can be achieved by using the norm of the spillover term $\{\Delta\}$ as the objective function [87]:

$$\|\Delta\|^2 = \{q_{um}\}^T[\varphi_{spill}]^T[\varphi_{spill}]\{q_{um}\} = \{q_{um}\}^T[\varphi_{spi}]\{q_{um}\} \tag{5-6}$$

For any $\{q_{um}\}$, the following inequality holds:

$$\lambda_{min}([\varphi_{spi}]) \leq \frac{\{q_{um}\}^T[\varphi_{spi}]\{q_{um}\}}{\{q_{um}\}^T\{q_{um}\}} \leq \lambda_{max}([\varphi_{spi}]) \tag{5-7}$$

where $\lambda_{min}([\varphi_{spi}])$ and $\lambda_{max}([\varphi_{spi}])$ are the minimum and maximum eigenvalues of $[\varphi_{spi}]$, respectively. In order to minimize the spillover effect, sensors must be arranged to achieve the minimum value of $\lambda_{max}([\varphi_{spi}])$, which means that the sensor placement is to be determined using the following objective function [88]:

$$J_{spi} = \lambda_{max}([\varphi_{spi}]) \rightarrow minimize \tag{5-8}$$

Note that the presence of noise in the measurement signals is not assumed in the formulation. Orthogonality of the modal matrix $[\varphi_m]$ is not assumed in this approach either. Also, since an enormous number of possible sensor locations have to be considered in the algorithm in practice, computational efficiency is required in the determination procedure of the optimal sensor location to achieve the minimum of the objective function J_{spi}.

The minimum spillover method can also be developed for searching the optimal actuator placement. As discussed in Sec. 3.3, if the observation spillover effects exist, the filtered modal responses are contaminated by the residual modes, and because the modal direct velocity feedback controller is used, the control forces will excite the residual modes, which are referred to as the control spillover effects. If the number of actuators is assumed to be N_{ac}, the modal control forces of the control modes $\{f_{mc}\}$ and the residual modes $\{f_r\}$ can be expressed as:

$$\{f_{mc}\} = [B_c]\{V\} \tag{5-9}$$

And:

$$\{f_r\} = [B_r]\{V\} \tag{5-10}$$

where $\{f_{mc}\}$ and $\{f_r\}$ are M-dimensional and $(N-M)$-dimensional vectors, respectively. $\{V\}$ is the control force generated by the actuators represented as an N_{ac}-dimensional vector. The size of the mode shape matrix $[B_c]$ is $N_{ac} \times M$, and that of $[B_r]$ is $N_{ac} \times (N-M)$.

From Eq. (5-9):

$$\{V\} = ([B_c]^T[B_c])^{-1}[B_c]^T\{f_{mc}\} \tag{5-11}$$

where $[B_c]^T[B_c])^{-1}[B_c]^T$ is the generalized inverse of the modal matrix $[B_c]$. Substitution of Eq. (5-11) into Eq. (5-10) yields:

$$\{f_r\} = [B_r]([B_c]^T[B_c])^{-1}[B_c]^T\{f_{mc}\} \tag{5-12}$$

The control spillover term $\{\Delta_c\}$ is defined as:

$$\{\Delta_c\} = [B_r]([B_c]^T[B_c])^{-1}[B_c]^T = \left[B_{spill}\right] \tag{5-13}$$

A small control spillover effect can be achieved by altering the position of actuators. As discussed in the observation spillover, minimization of the control spillover can be achieved by using the norm of the spillover term $\{\Delta_c\}$ as the objective function:

$$||\Delta_c||^2 = \{f_{mc}\}^T\left[B_{spill}\right]^T\left[B_{spill}\right]\{f_{mc}\} = \{f_{mc}\}^T\left[B_{spi}\right]\{f_{mc}\} \tag{5-14}$$

For any $\{f_{mc}\}$, the following inequality holds:

$$\lambda_{min}(\left[B_{spi}\right]) \leq \frac{\{f_{mc}\}^T\left[B_{spi}\right]\{f_{mc}\}}{\{f_{mc}\}^T\{f_{mc}\}} \leq \lambda_{max}(\left[B_{spi}\right]) \tag{5-15}$$

where $\lambda_{min}(\left[B_{spi}\right])$ and $\lambda_{max}\left(\left[B_{spi}\right]\right)$ are the minimum and maximum eigenvalues of $\left[B_{spi}\right]$, respectively. The actuator placement is determined using the following objective function:

$$J_{spiac} = \lambda_{max}\left(\left[B_{spi}\right]\right) \rightarrow minimize \tag{5-16}$$

5.2.2 The effective independence method (EFI)

The EFI was proposed by Kammer [89]–[93] to address the sensor placement problem of using the data collected from the sensors to validate the finite element model of an on-orbit large space structure (LSS). This is achieved by placing the sensors on the LSS such that the data measured during an on-orbit vibration experiment will provide independent tested mode shapes and frequencies that can be used to make a comparison with FEM modal parameters using test-analysis correlation techniques. The FEM can be updated to accurately represent the real structure and therefore used in structural dynamics analysis and system control.

In the EFI, based on the pre-launch FEM, a set of target modes is selected so that the set include all the modes that are strongly excited by the actuator at the location of configuration. An initial candidate set of the sensor locations is also selected. The candidate sensor locations are ranked according to their contribution to the linear independence of the target modal partitions in an iterative manner. The trace and determinant of the related Fisher information matrix are maximized by this method, leading to improved estimates of the concerned modes in the presence of white noise. The candidate solution is narrowed iteratively by removing the sensor locations that contribute the least of all the position sensor locations to the linear independence of the target modal partitions.

If the initial candidate sensor set is assumed to be L and N target modes are excited by the actuator, from Eq. (5-1), the output of each sensor candidate with additive white noise can be written as:

$$\{u_L\} = [\varphi_L]\{q_N\} + \{\varepsilon\} = \boldsymbol{H}(q_N) + \{\varepsilon\} \tag{5-17}$$

where the symbol $\boldsymbol{H}$ represents the process measurement and $\{\varepsilon\}$ is a stationary Gaussian white noise vector with zero mean and a variance of $[\psi_0^2]$. For simplification of the analysis, it is assumed that the noise is uncorrelated and has the same statistical properties for all sensors. For an efficient unbiased estimator, the covariance matrix of the estimate error can be expressed as:

$$\begin{aligned} \mathrm{E}[(\boldsymbol{q}_N - \widehat{\boldsymbol{q}}_N)(\boldsymbol{q}_N - \widehat{\boldsymbol{q}}_N)^T] &= \left[\left(\frac{\partial \boldsymbol{H}}{\partial \boldsymbol{q}_N}\right)[\psi_0^2]^{-1}\left(\frac{\partial \boldsymbol{H}}{\partial \boldsymbol{q}_N}\right)\right]^{-1} \\ &= \left[\frac{1}{[\psi_0^2]}[\varphi_L]^T[\varphi_L]\right]^{-1} \\ &= \boldsymbol{Q}^{-1} \end{aligned} \tag{5-18}$$

in which $\widehat{\boldsymbol{q}}_N$ is the unbiased estimator of $\boldsymbol{q}_N$, and $\boldsymbol{Q}$ is the Fisher information matrix. Maximizing $\boldsymbol{Q}$ is assumed to lead to the best state estimate of $\boldsymbol{q}_N$. From Eq. (5-18), the Fisher information matrix is given as:

$$\boldsymbol{Q} = \frac{1}{[\psi_0^2]}[\varphi_L]^T[\varphi_L] = \frac{1}{[\psi_0^2]}\,\boldsymbol{A}_0 \tag{5-19}$$

Therefore, minimization of the estimate error is equal to maximizing a suitable norm of the matrix $\boldsymbol{A}_0$, which is called the Fisher information matrix as well. It is suggested that the trace norm should be used as the most useful and meaning full matrix norm in a physical sense and the determinant of the Fisher information matrix achieves its maximum among all the linear unbiased estimators, if the modal estimate is the best.

The Fisher information matrix $\boldsymbol{A}_0$ can be expressed as the formation of contribution of each degree of freedom to the mode shapes:

$$\boldsymbol{A}_0 = \sum_{i=1}^{L} \{\varphi_L^{iT}\}\{\varphi_L^{i}\} = \sum_{i=1}^{L} \boldsymbol{A}_i \tag{5-20}$$

where $\{\varphi_L^i\}$ is the ith row of the modal partition $[\varphi_L]$ corresponding to the ith degree of freedom or the ith candidate of sensor location. From Eq. (5-20), it can be observed that as each degree of freedom adding or subtracting from the candidate set, information is added or subtracted from the Fisher information matrix $\boldsymbol{A}_0$. The method is proposed by removing those sensor candidates that do not contribute significantly to the Fisher information matrix $\boldsymbol{A}_0$. The first step of the procedure is to find the solution of the eigenvalue equation:

$$[[\varphi_L]^T[\varphi_L] - \boldsymbol{\lambda}\mathbf{I}]\boldsymbol{\Psi} = 0 \tag{5-21}$$

where the N columns in $[\varphi_L]$ are the target modes which are assumed to be linearly independent for the initial total candidate sensor set such that the $N \times N$ matrix $\boldsymbol{A}_0$ is positive definite, and $\boldsymbol{\lambda}$ is the diagonal eigenvalue matrix, $\boldsymbol{\Psi}$ is the matrix consisting of the orthogonal eigenvectors such that $\boldsymbol{\Psi^T}\boldsymbol{A}_0\boldsymbol{\Psi} = \boldsymbol{\lambda}$ and $\boldsymbol{\Psi^T}\boldsymbol{\Psi} = \mathbf{I}$. Since the vectors of the columns of $\boldsymbol{\Psi}$ are orthogonal, they represent N orthogonal directions in an N-dimensional space. Defining the product:

$$\boldsymbol{G} = [[\varphi_L]\,\boldsymbol{\Psi}] \ \odot [[\varphi_L]\,\boldsymbol{\Psi}] \tag{5-22}$$

where the symbol $\odot$ represents the term-by-term matrix multiplication, each row of the matrix $\boldsymbol{G}$ contains the square of the components of the rows of $[\varphi_L]$ in terms of the coordinate system defined by the columns of $\boldsymbol{\Psi}$. Therefore the ith component of a column represents the contribution of the ith sensor location to the associated eigenvalue. Post-multiplying $\boldsymbol{G}$ by the inverse of the matrix $\boldsymbol{\lambda}$ gives that:

$$\boldsymbol{F}_E = [[\varphi_L]\,\boldsymbol{\Psi}] \ \odot [[\varphi_L]\,\boldsymbol{\Psi}]\boldsymbol{\lambda^{-1}} \tag{5-23}$$

This means that each direction is now of equal importance. Note that the ith component in the jth column of the $L \times N$ matrix $\boldsymbol{F}_E$ represents the fractional contribution of the ith sensor location of the jth eigenvalue. Matrix $\boldsymbol{F}_E$ is called the fractional eigenvalue distribution. Adding all the components of each row of $\boldsymbol{F_E}$ gives:

$$\boldsymbol{E}_D = [\sum_{j=1}^{N} \boldsymbol{F}_{E1j} : \sum_{j=1}^{N} \boldsymbol{F}_{E2j} : \sum_{j=1}^{N} \boldsymbol{F}_{E3j} : \ldots : \sum_{j=1}^{N} \boldsymbol{F}_{ELj}] \tag{5-24}$$

where $\boldsymbol{F}_{Eij}$ is the jth component in the ith row of matrix $\boldsymbol{F_E}$. The summation $\sum_{j=1}^{N}\boldsymbol{F}_{Eij}$ can be regarded as the fractional contribution of the ith sensor location to the linear independence of the modal shape $\boldsymbol{\varphi}_L$. Vector $\boldsymbol{E}_D$ is referred to as the effective independence distribution of the candidate sensor location.

The effective independence distribution vector $\boldsymbol{E}_D$ can also be formulated as the diagonal of the matrix:

$$\boldsymbol{E}_D = [\varphi_L]\boldsymbol{\Psi}\boldsymbol{\lambda}^{-1}\boldsymbol{\Psi}^{T}[\varphi_L]^T \tag{5-25}$$

And therefore can be written as:

$$\boldsymbol{E}_D = [\varphi_L]([\varphi_L]^T[\varphi_L])^{-1}[\varphi_L]^T \tag{5-26}$$

Then the procedure is employed to sort the elements of the E_D vector and to remove the smallest component corresponding to a candidate sensor location. The vector E_D is updated based on the new modal shape matrix, and the process is repeated iteratively until the number of remaining sensor locations reaches to a pre-defined value.

Note that the purpose of EFI is to maximize information on the designated modes through the optimal configuration of sensors, while the spillover caused by the truncated modes is not considered.

5.2.3 Modal assurance criterion (MAC)

The development of the MAC originated from the need for a quality indicator for experimental modal vectors which are estimated from measured frequency response functions [94]. It was used to check the orthogonality between different modal vectors and therefore can be used here to check the orthogonality of different modal filtering vectors.

The MAC is defined as a scalar value representing the degree of consistency (linearity) between modal shape vectors [95]. For two modal shape vectors Ψ_a and Ψ_b, the MAC value is defined by:

$$MAC(\Psi_a, \Psi_b) = \frac{\left|{\Psi_a}^H \Psi_b\right|^2}{\|\Psi_a\|^2 \|\Psi_b\|^2} \tag{5-27}$$

The modal assurance criterion takes on values in the range between zero - representing mutual orthogonality of modal shape vectors, and unity – representing linear dependence of the two vectors. Therefore, the sensor placement with the greatest degree of independence can be found by solving the optimization problem for the following objective function:

$$J_{mac} = \sum_{a=1}^{M-1} \sum_{b=a+1}^{M} MAC(\Psi_a, \Psi_b) \rightarrow minimize \tag{5-28}$$

where M is the total modes to be considered. The sensor placement for which the sum of $MAC(\Psi_a, \Psi_b)$ for all different a and b achieves the minimum is supposed to be closest to the one that satisfies the mutual orthogonality condition.

5.3 Procedure of determination of optimal sensor and actuator placement

5.3.1 Problem statement

In the case of floor vibration, possible sensor and actuator location candidates are assumed to be the hypothetical rectangular grid points on the floor surface with a sufficiently fine mesh size. The values of the modal shape of the plate representing the floor are treated as vector components corresponding to the grid points, and the plate is approximated as a MDOF system. Therefore, the number of sensor and actuator placement candidates is equal to the number of the grid points of the plate, denoted by L. Since the value of L can be enormous in practice, the number of modes to be considered N is assumed to be divided into two parts-the control modes and the residual modes, as in Eq. (5-2). If the number of control modes is assumed to be M, $N-M$ is the number of residual modes. For the purpose of filtering out all the control modes, usually $S \geq M$ should be satisfied, where S is the number of sensors. The actuator used to generate the control force is assumed to be N_{ac}. As stated in Sec. 5.1, state estimate ability, orthogonality, observability as well as observation spillover should be considered in determining the sensor placement for the use of modal filtering, while controllability and control spillover effects should be considered for the actuator placement.

5.3.2 Sensor placement

Based on the number of sensors S that are used for the modal filtering implementation, the problem can be divided into a small number of sensors and a large number of sensors cases.

5.3.2.1 Case of small number of sensors

As the first step, EFI is used for the state estimate ability as well as decreasing the number of sensor placement candidates. The number of sensor candidates is then reduced from a large set L to a pre-defined number P by removing those candidates which contribute least to the state estimate ability of the control modes based on Eq. (5-26) in an iterative manner. The value of P is specified to be sufficiently small for the use of the minimum spillover method.

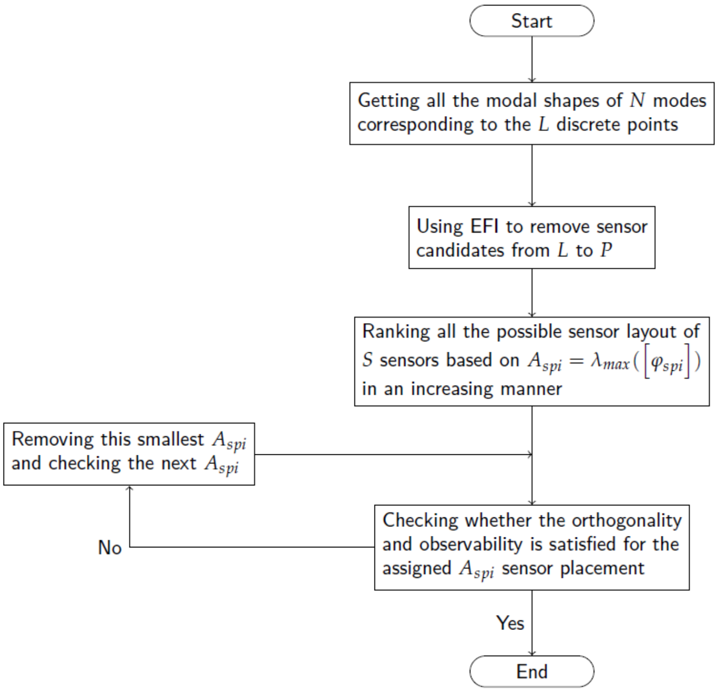

Figure 5.1 Flow chart of small number sensor placement design

Then for the P candidate positions and S sensors, all the possible sensor placements are ranked by the minimum spillover method in the order of the severity of spillover, implying the value of $A_{spi} = \lambda_{max}([\varphi_{spi}])$ in Eq. (5-7) in an increasing manner. It is possible to rank all of the sensor placement because a small number of sensors are assumed, the total number of possible sensor placement is equal to $P!/(S!\,(P-S)!)$.

In the final step, observability and orthogonality are checked for the smallest $\lambda_{max}([\varphi_{spi}])$ sensor placement, and the index A_{mac} is defined by $A_{mac} = \sum_{a=1}^{M-1}\sum_{b=a+1}^{M} MAC(\Psi_a, \Psi_b)$ here. If A_{mac} is sufficiently small and the system is observable, the sensor placement is the optimal one. Otherwise, if A_{mac} is greater than the tolerance value such as 0.1, this sensor placement is discarded and the next smallest sensor placement is examined and calculated by the same procedure until an acceptable value of A_{mac} is obtained. If A_{mac} is sufficiently small, it is likely to that the observability is also satisfied. The flow chart of the proposed design for choosing the optimal small number sensor placement is shown in Figure 5.1.

5.3.2.2 Case of large number of sensors

If a large number of sensors is assumed, it is not possible to rank the spillover effect of all the possible sensor placement, requiring a large amount of computation as well as computer memories. The Genetic Algorithm (GA) will be used to search for the optimal sensor placement that satisfy the observability, orthogonality and spillover requirement. The GA is a search method based on the mechanics of natural genetics and survival-of-the-fittest and the GA used here is very similar to the algorithm that can be found in the standard literature on this topic [75], [78], [96]–[99]. A brief introduction of GA is presented in Appendix A.

The first step is the use of EFI for the state estimate ability and decreasing the number of sensor placement candidates, similar to the case of small number of sensors. The number of sensor candidates is reduced from a large number L to a pre-defined number P.

Next step is to apply the GA to the remaining P sensor placement candidates. Once the population of genomes of each generation is set, an initial population of binary strings can be randomly created. Each of these binary strings represents one possible sensor placement solution to the search problem. Then the binary strings are converted to their decimal equivalents and each solution is tested its fitness using the objective function. In this research, the fitness function is defined as:

$$\mathrm{J}_{fitness} = C_1 * \lambda_{max}\left(\left[\varphi_{spi}\right]\right) + C_2 * \sum_{a=1}^{M-1} \sum_{b=a+1}^{M} MAC(\Psi_a, \Psi_b)$$

where C_1 and C_1 are positive weight scalars. It is obvious that the algorithm acts towards minimizing this fitness measure. After the fitness $\mathrm{J}_{fitness}$ of the entire population are calculated, the elite (best performance) candidate is recorded, and the three genetic operations of selection, crossover and mutation are applied to the original binary strings to generate the next generation. Then the binary string of the elite member is selected to replace any one of the new population. The same process is conducted to the next generation and an optimal or sub-optimal sensor placement can be found after all the generation are finished. The flow chart of the proposed design using GA is shown in Figure 5.2.

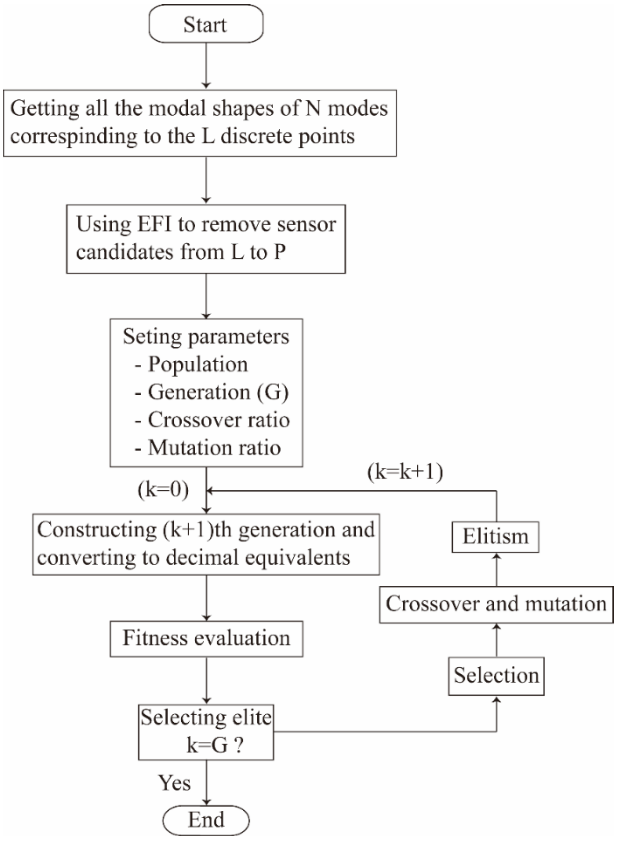

Figure 5.2 Flow chart of sensor placement optimization using genetic algorithm

The solution is said to be sub-optimal because GA is operated in a random manner. It is believed that the sub-optimal solution is close to the optimal one. The entire process of GA can run several times and the sensor placement with the minimum $J_{fitness}$ can be treated as the final optimal one.

5.3.3 Actuator placement

Same as the sensor placement methods, the EFI method is firstly used to reduce the actuator placement candidate from the total number of the grid points L to a pre-defined number P. This removes the candidates which contribute least to excite the control modes such that controllability can be guaranteed.

Then for the P candidate locations and N_{ac} actuators, the minimum spillover method is utilized for all the possible actuator placement and the one with the minimum $J_{spiac} = \lambda_{max}([B_{spi}])$ is treated as the optimal actuator placement. The flow chart of the proposed optimal actuator placement is shown in Figure 5.3.

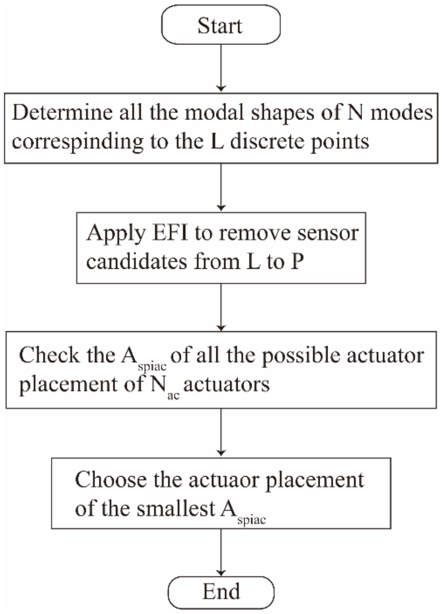

Figure 5.3 Flow chart of actuator placement design

5.4 Verification test: case of small number of sensors

5.4.1 Test setup and experimental identification

The sensor placement approach is applied to a steel plate specimen as described in Sec. 4.2.1. The system is shown in Figure 4.3. The system consists of a 840mm×840mm steel plate with a thickness of 4.5mm. Dimensions of the steel plate specimen are shown in Figure 4.4. A square 9×9 grid mesh is defined to specify $L = 81$ sensor location candidates on the surface of the steel plate, as shown in Figure 4.13.

Experimental identification of the steel plate has been conducted to obtain the natural frequencies, modal damping ratios and mode shape vectors for the 81 grid mesh points described in Sec.4.3.2. The frequency range of recording is between 0Hz and 200Hz. The identified results are shown in Figure 4.14, Table 4.4 and Table 4.5.

Based on the results of experimental identification, the total number of the modes to be considered is selected to be 5, implying that $N = 5$. The 1st~3rd modes are chosen as the modelled modes, i.e. $M = 3$, and the 4th~5th modes are considered as the residual modes, for which the spillover effect are to be minimized. The total number of the sensors used for the modal filtering of the first three modes is 4, implying that $S = 4$, and one actuator is used to generate the control force, that is $N_{ac} = 1$.

5.4.2 Optimal sensor placement

The results of each step in the procedure described in Sec. 5.3.2.1 are shown here. The modal matrix $\boldsymbol{\Psi}$ evaluated at the L grid points, such that $\boldsymbol{\Psi}^{\boldsymbol{T}}\boldsymbol{\Psi} = \boldsymbol{I}$ can be obtained by modal identification of the plate, as shown in Table 4.5. Therefore the 81 degrees of freedom are selected as the total candidate set of the sensor locations. The initial analysis ranks the importance of each sensor location within the 81 candidate set to the first three control modes. The vector $\boldsymbol{E}_D$ that contains the effective independence for each sensor location calculated by Eq. (5-26). The effective independence values for the initial candidate sensor set within $\boldsymbol{E}_D$ are sorted from the highest to the lowest values, and the plot is shown in Figure 5.4. The largest value is 0.1546, implying that no single sensor position is dominantly influential to the independence of the target control modes. However, it can be observed that 30 sensor positions out of 81 grid points are of almost no significance to the independence and, therefore, can be eliminated from the sensor set during the first iteration.

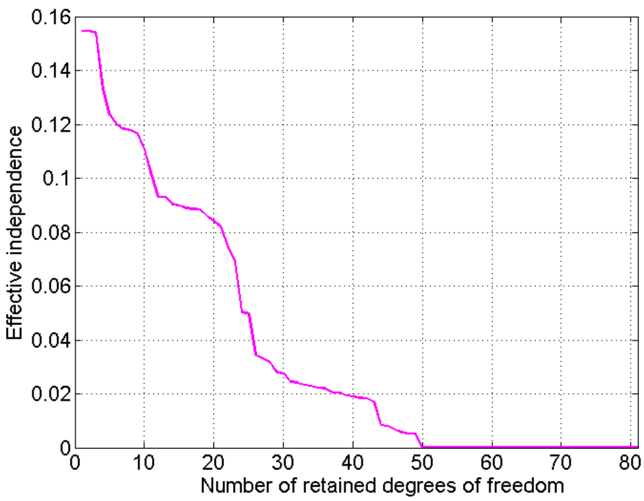

Figure 5.4 Effective independence distribution for 81-DOF candidate sensor set and three target modes

After several iterations, the number of sensor locations is reduced from 81 to a predefined value $P = 41$. The remaining P points are shown as blue circles in Figure 5.5. It can be seen that the contribution of the points near the clamped edges to the linear independence of the target first three modes is less significant and effects on the state estimation are comparatively minor.

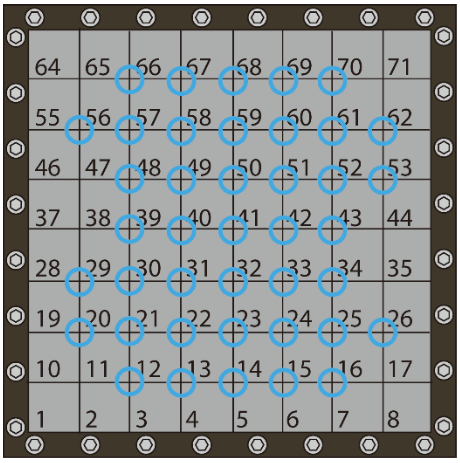

Figure 5.5 Sensor candidates after EFI

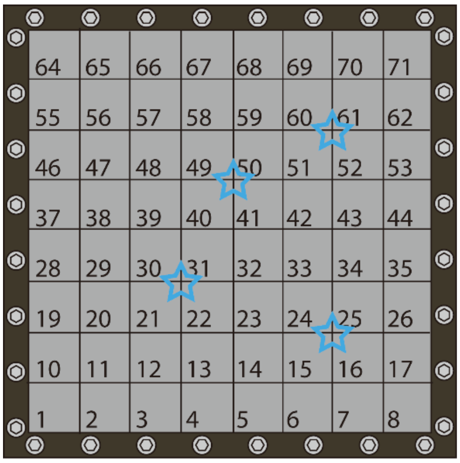

Figure 5.6 Optimal sensor placement

Next, all the possible sensor placement of four sensors within 41 point candidates are ranked in an increasing manner based on the value of A_{spi}, as described in Sec. 5.2.1. The sensor placement for the smallest $\mathrm{A}_{spi} = 0.0705$ is the case of sensor points 16, 31, 51, 60. However, since the value of $A_{mac} = \sum_{a=1}^{2}\sum_{b=a+1}^{3} MAC(\Psi_a, \Psi_b)$ is 0.6373, which is significantly larger than the tolerance value $\mathrm{A}_{maclim} = 0.1$, this sensor placement is not the optimal one.

By checking the next smallest sensor placement and comparing the value of A_{mac} with the tolerance value A_{maclim} until $A_{mac} \leq A_{maclim}$ is satisfied, the final optimal sensor placement is found to be the case of sensor points 25, 31, 50 and 61 with $A_{spi} = 0.0948$ and $A_{mac} = 0.056$. The locations of the 4 sensors of the optimal placement are shown in Figure 5.6. The MAC values for this sensor placement is shown in Table 5.1.

5.4.3 Performance of modal filtering

In order to evaluate the performance of the modal filtering with the optimal sensor placement, three cases are considered. Case A: the optimal sensor placement with $A_{spi} = 0.0948$ and $A_{mac} = 0.056$. Case B: a large spillover and small consistency sensor placement, such that $A_{spi} = 30.2283$ and $A_{mac} = 0.0776$. Case C: another large consistency and small spillover sensor placement, such that $A_{spi} = 0.0965$ and $A_{mac} = 0.7461$. The illustration of the sensor placement for Case B and Case C are shown in Figure 5.7 and Figure 5.8, respectively. The MAC values for these two cases are shown in Table 5.1.

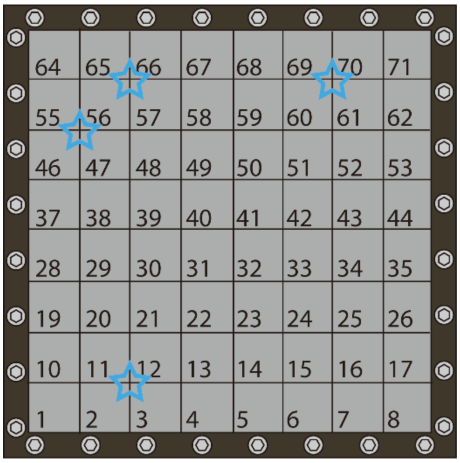

Figure 5.7 Case B sensor placement

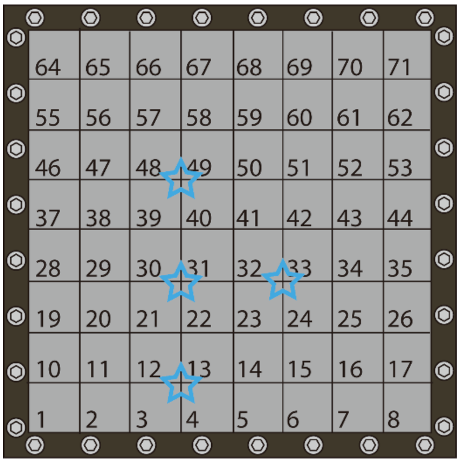

Figure 5.8 Case C sensor placement

Table 5.1 – MAC values

Case A - Optimal layout

MAC	1st	2nd	3rd
1st	1	0.0012	0.0447
2nd	0.0012	1	0.0098
3rd	0.0447	0.0098	1

Case B - Large spillover layout

MAC	1st	2nd	3rd
1st	1	0.0063	0.0001
2nd	0.0063	1	0.0712
3rd	0.0001	0.0712	1

Case C - Large consistency layout

MAC	1st	2nd	3rd
1st	1	0.3591	0.0722
2nd	0.3591	1	0.3147
3rd	0.0722	0.3147	1

The Fourier spectra of the modal filtering output using Eq. (5-3) for the three cases are shown in Figure 5.9 through Figure 5.11 with a sampling rate of 1000Hz. The natural frequencies of the modes are indicated with red arrow symbols. It can be observed in Case A that all the first three modes are filtered out and the spillover of the 4^{th} and 5^{th} modes are small, implying that all of the first three modes are observed and the modal filtering for the optimal sensor placement enhances the target natural mode response while the other two residual modes are effectively reduced. Note that the spillover effect still exists here and refinement of the mesh (large L) is needed to achieve further reduction of the spillover effect.

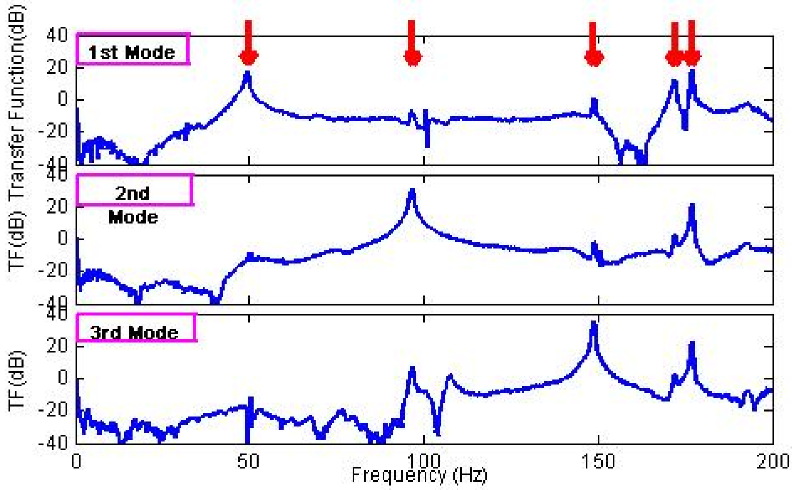

Figure 5.9 Transfer function for MF output (Case A)

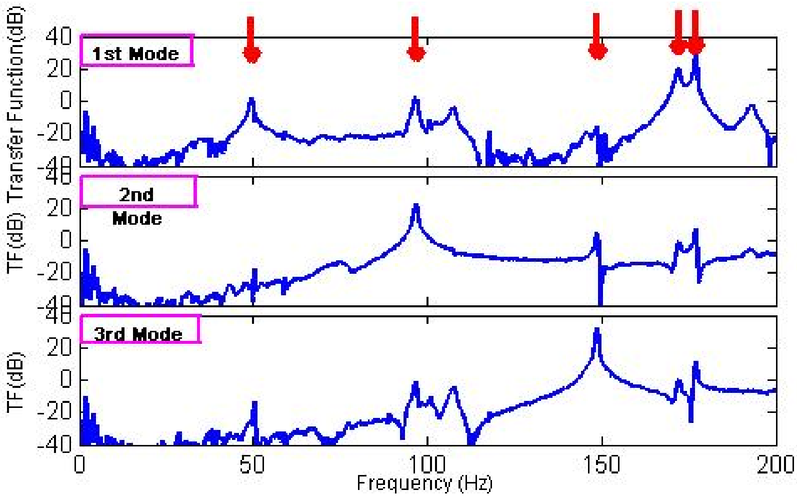

Figure 5.10 Transfer function for MF output (Case B)

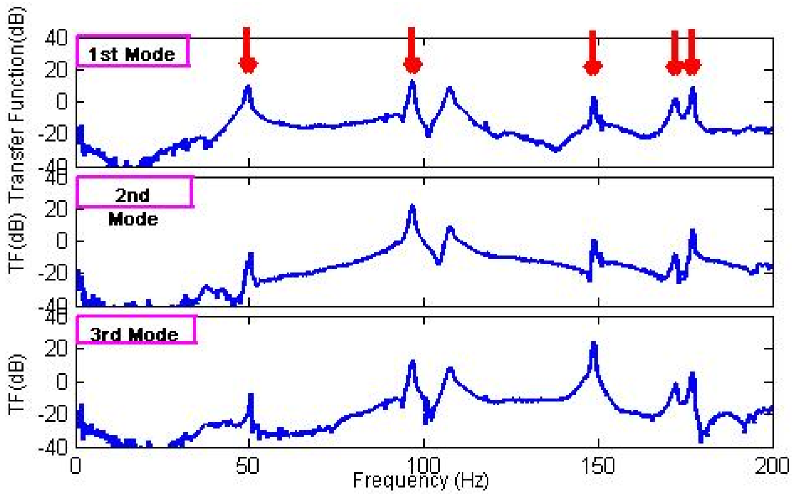

Figure 5.11 Transfer function for MF output (Case C)

In Case B, not only the spillover effect for the first mode is far greater than Case A but also the separation performance for the first mode is poor, while the performance of the modal filtering is excellent for the 2nd and 3rd mode. The inferior effect for the first mode is caused by the poor observation quality of the 1st mode, while the good performance for the 2nd and 3rd modes are the consequence of the high value of A_{spi}, see Figure 5.7. All the four sensors are located near the nodes of the 1st mode.

In Case C, although the spillover effect is small as in Case A, the separation performance of modal filtering is very poor, especially for the 1st and 3rd modes. This result is explained by the relatively large value of A_{mac}.

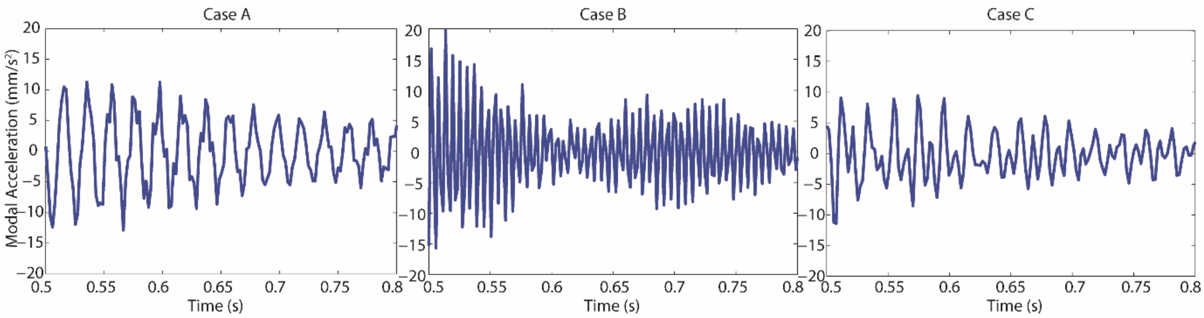

Figure 5.12 First mode modal acceleration

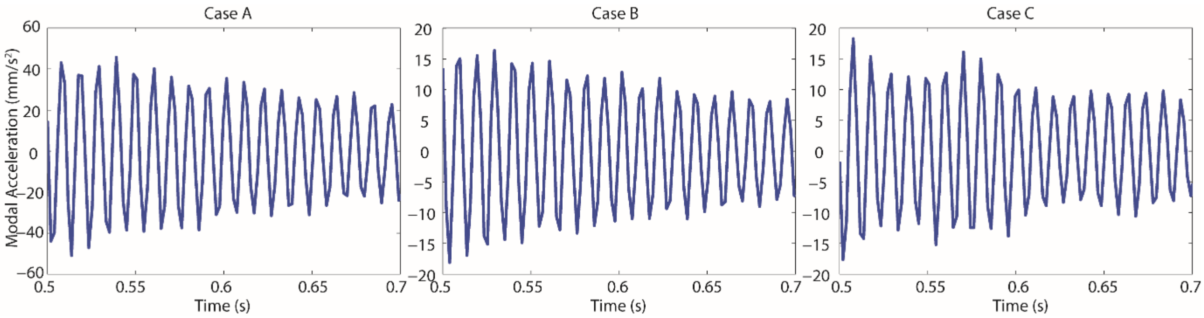

Figure 5.13 Second mode modal acceleration

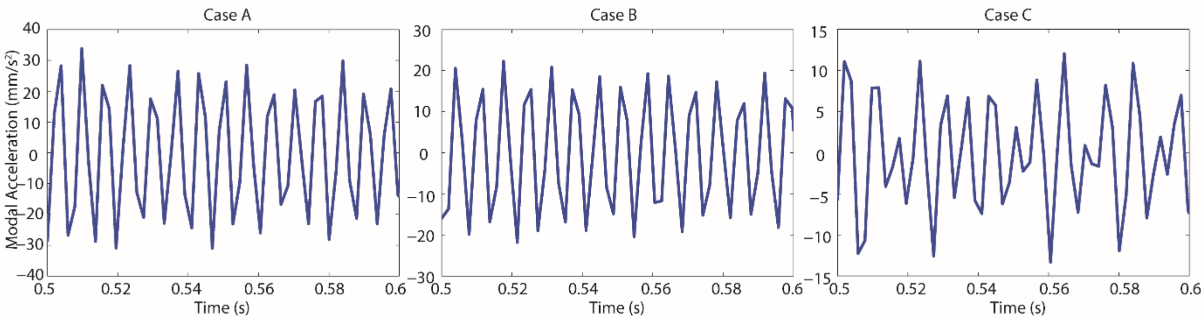

Figure 5.14 Third mode modal acceleration

Figure 5.12 through Figure 5.14 show the performance of the filtering for the lowest three modes in the time domain. The natural frequencies of the three modes ranged from 0Hz to 200Hz. It can be observed that only Case A is successful in separating the three mode responses. For Case B, since the high spillover effect of the 4th and 5th modes is involved in the first mode, it is difficult to observe the first mode responses from Figure 5.12. In contrast to the first mode, good performance can be found in Figure 5.13 and Figure 5.14, in which the second and third mode responses are reasonably filtered out. Thus, a sensor placement with high value of A_{spi} does not mean that all of the modes cannot be separated by this method.

5.4.4 Actuator placement

As described in Sec. 5.3.3, EFI is used to remove the candidate actuator points which contain least information to the control modes to obtain 10 candidate actuator points (a pre-defined number) out of 81 grid points. The remaining 10 points are shown as red circles in Figure 5.15. Since only one actuator is used in this test, the spillover effects of the actuator can be checked through the modal participation of the residual modes on these 10 points using Table 4.5. A point located between 51 and 52 is found to have a large participation on the control modes and small participation on the residual modes. The actuator is determined to be located at this point near the node of the 4th mode. The optimal placement of the sensors and the actuator is shown in Figure 5.16.

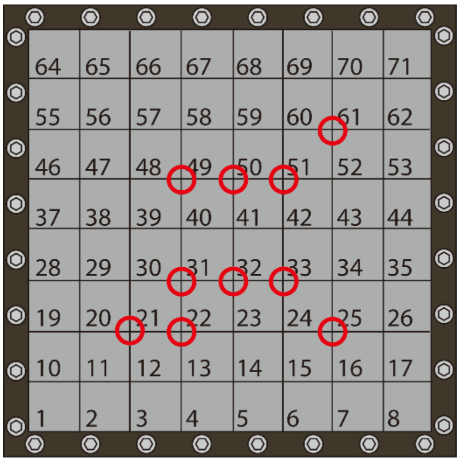

Figure 5.15 Actuator candidates after EFI

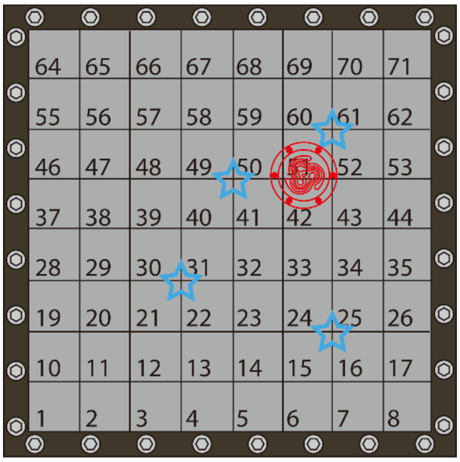

Figure 5.16 Optimal sensor and actuator placement

5.4.5 Active control using optimal sensor placement

The performance of MF using the optimal sensor and actuator placement under real-time active control is shown in this section. The control strategy used in the tests is described in Chapter 6 and Chapter 7.

For all of the control tests, the hammer described in Sec. 4.2.4 is used to repeatedly apply impact loads to point 21. The piezoelectric accelerometers and the electromagnetic actuator introduced in Sec. 4.2.2 are used for measurement of the steel plate vibration and generation of control forces, respectively.

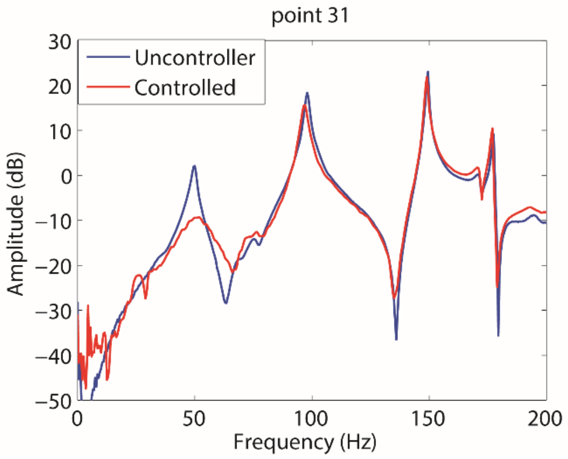

Figure 5.17 Test result: first mode control at Point 31

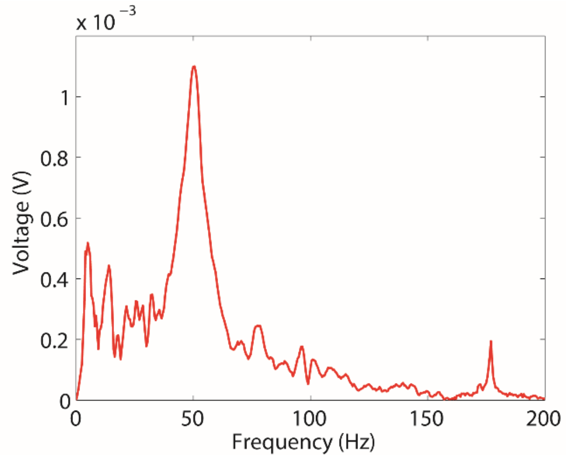

Figure 5.18 Test result: actuator voltage for first mode control

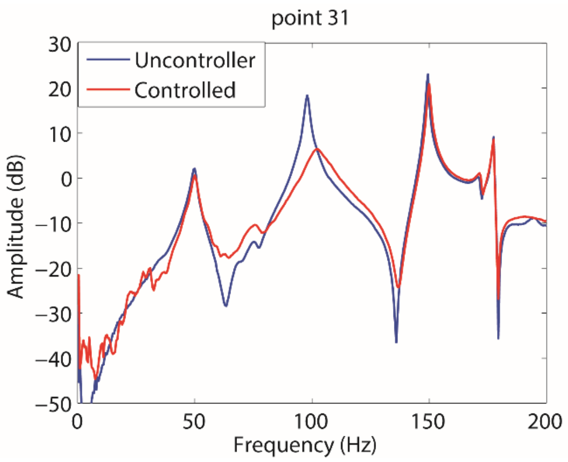

Figure 5.19 Test result: second mode control at Point 31

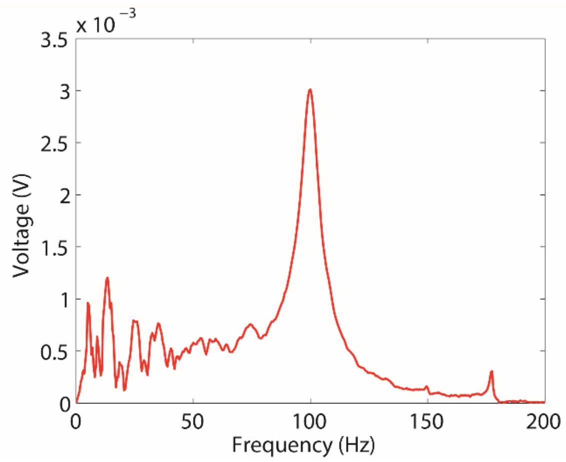

Figure 5.20 Test result: actuator voltage for second mode control

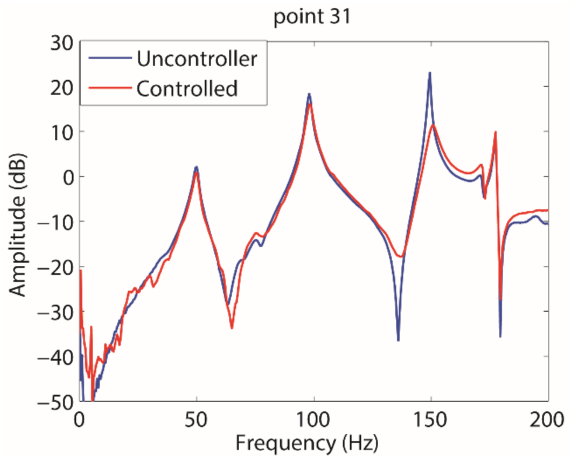

Figure 5.21 Test result: third mode control at Point 31

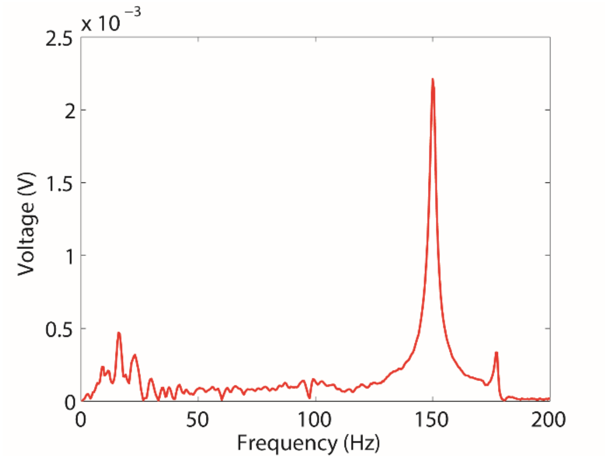

Figure 5.22 Test result: actuator voltage for third mode control

The proposed sensor and actuator placement method is verified by single-mode control tests. The results are shown in Figure 5.17, Figure 5.19 and Figure 5.21, in which the transfer functions between the excitation force and the acceleration response at Point 31 for the cases with and without active control are compared. The corresponding input voltages to the actuator are shown in Figure 5.18, Figure 5.20 and Figure 5.22. It can be seen that an effective modal filtering of the desired modes are achieved. Also, the spillover effect of the 4th and 5th modes with small amplitudes can be observed in these plots.

5.5 Summary

In order to develop an effective active control technique for reducing human-induced vibration and noise of building floors, a procedure for the optimal sensor and actuator placement applicable to active control of plate vibration is proposed. The aim of the proposed procedure is to provide a solution to the problems of ensuring the state estimate ability, minimization of the spillover effect, consideration for orthogonality of the natural vibration modes and system observability. Effectiveness of the proposed procedure and achieved control performance are examined by a series of verification tests using a rectangular steel plate and the optimal sensor and actuator placement determined by the procedure.

The procedure for the proposed sensor placement approach is effective in the reduction of the spillover effect of the residual modes and in the enhancement of the separation performance of the modelled modes. First, the effective independence (EFI) method removes the sensor location candidates with small contribution to the state estimate of the controlled modes, and then for the case of a the small number of sensors, the minimum spillover method is used to rank all the possible sensor placements in the order of severer spillover effects, and finally the sensor placement with the minimal spillover effects, and the least off-diagonal MAC values is chosen as the optimal one. For the case of large number of sensors, application of the genetic algorithm (GA) is proposed to estimate the optimal sensor placement considering minimum spillover effects and MAC values.

A procedure for the optimal actuator placement approach is also proposed. In the first step, the effective independence method is used to remove the candidate actuator points with less influence on the control modes, then the minimum spillover method is used to determine the final actuator placement which provides the least control spillover effects.

Effectiveness of the sensor placement by the proposed method is verified by comparison with other two cases. Orthogonality and spillover effect are the important factors for the successful separation of desired modes. It is found that the separation of the first mode fails while the separation of the other modes are successful for the case of high spillover indicator A_{spi}.

Control tests also showed the effectiveness of the modal filtering in mode-by-mode floor vibration control if the sensor and actuator placement is determined by the proposed procedure.

Chapter 6 Phase-lead Velocity Feedback Control

With the determination of the optimal sensor and actuator placement and application of the modal filtering to the sensor measurements excited by human-induced impact loadings, each separated mode can be regarded as a SDOF system. It has been shown in the previous chapter that the control system may involve a large phase delay of the actuator force from the input signal, which can strongly influence the dynamics of the control system. In fact, the conventional modal direct velocity feedback controller for each filtered mode may go into system instability without attaining effective increase of modal damping if a large phase delay exists [24]. This chapter describes an independent modal space design process based on modal direct velocity feedback control with a phase-lead compensator, which is referred to as the independent modal space phase-lead velocity feedback (PLVFB) controller. The phase-lead compensator is designed using the root locus method to enhance the stability margins and increase the damping of each filtered mode [100]. Figure 6.1 shows the schematic block diagram of the PLVFB active control for a mode. The main purpose of this chapter is to lay a theoretical foundation for the use of the phase-lead compensator to compensate the phase delays. Verification experiments using the steel plate specimen are conducted and the test results show that effective reduction of the vibration level is successfully achieved.

6.1 Model of dynamic testing system

This section presents a model of the floor-actuator system. The model includes mathematical representation of three components of the testing system, including the SDOF modal of test specimen, the actuator model and the constant delay caused by DSP.

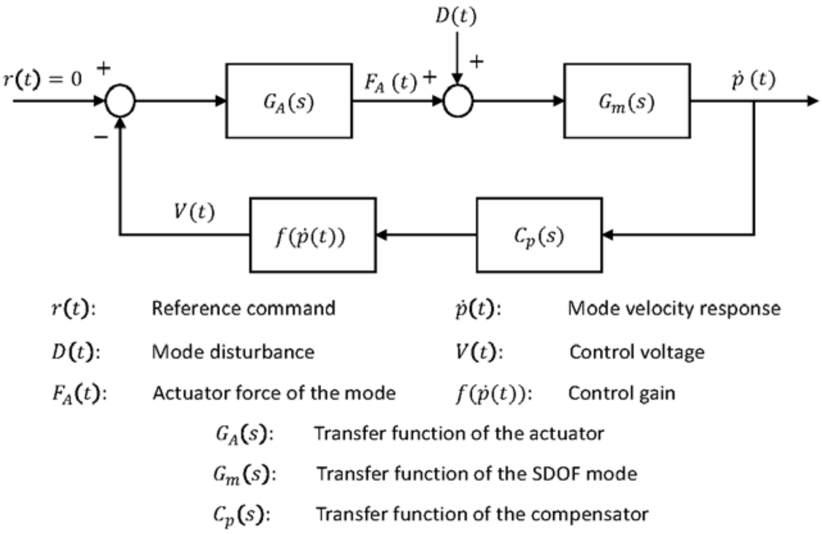

Figure 6.1 Schematic of control of a mode

6.1.1 SDOF model of test specimen

It has been shown in Chapter 5 that after applying modal filtering to the sensor measurements, the separated responses can be approximately seemed as that of individual SDOF systems. The filtered mode *m* of the specimen, therefore, has its own dynamic characteristics, which can be described using the following equation of motion:

$$m_m \ddot{q}_m(t) + c_m \dot{q}_m(t) + k_m q_m(t) = F_A(t) \tag{6-1}$$

where m_m, c_m and k_m are the modal mass, modal damping coefficient and modal stiffness, respectively, of the mode *m*, and $F_A(t)$ is the force applied to the mode by the actuator. The transfer function relating the output velocity with the control force is obtained by taking the Laplace transform of Eq. (6-1), and is given by the following equation:

$$G_m(s) = \frac{\dot{q}_m(s)}{F_A(s)} = \frac{s}{m_m s^2 + c_m s + k_m} \tag{6-2}$$

where s is the Laplace variable. Since the modal natural frequency ω_m and the modal damping ratio ζ_m are obtained in advance through model testing as described in Sec. 4.3, Eq. (6-2) can also be written as:

$$G_m(s) = \frac{\dot{q}_m(s)}{F_A(s)/m} = \frac{s}{s^2 + 2\zeta_m \omega_m s + \omega_m^2} \tag{6-3}$$

6.1.2 Actuator dynamics

As described in Sec. 3.4.1, the behavior of the actuator can be approximately expressed as a linear second order model as shown in Figure 3.2 and the transfer function between the transmitted force and the control voltage can be expressed as:

$$G_{a1}(s) = \frac{F_t(s)}{V(s)} = \frac{K_a s^2}{s^2 + 2\xi_a \omega_a s + \omega_a^2} \tag{6-4}$$

where K_a is the amplifier gain, ζ_a and ω_a are the damping ratio and natural frequency of the actuator, respectively.

However, based on the experimental identification of the actuator in Sec. 4.4.1, another first order term $\mathrm{G}_{c1} = \frac{s+\mu}{s+\varepsilon}$ appears to account for the dynamic property of the actuator. Therefore, the dynamics of the actuator is expressed as a third order transfer function:

$$G_a(s) = G_{a1}(s)\mathrm{G}_{c1}(s) = \frac{K_a s^2 (s+\mu)}{(s^2 + 2\xi_a \omega_a s + \omega_a^2)(s+\varepsilon)} \tag{6-5}$$

6.1.3 Constant delay

It has been shown in Sec. 4.4.2 that the delay caused by the A/D-D/A interfaces is one of the main sources of time delays, which is in fact a constant delay. The other two sources are the actuator and the band pass filter. The transfer function for a pure time delay is given as:

$$G_{pure}(s) = e^{-\tau s} \tag{6-6}$$

where τ is referred to as the time delay. Generally, control system design techniques require a rational transfer function, and for this purpose, the Padé approximation for dead time is often used. The Padé's first-order approximation is:

$$G_{pure}(s) = e^{-\tau s} \approx \frac{1 - \frac{\tau}{2}s}{1 + \frac{\tau}{2}s} = \frac{1 - Ts}{1 + Ts} \tag{6-7}$$

where $T = \tau/2$.

Therefore, if no other dynamic components are involved, the feedback control system for the *m*th mode using the modal direct velocity feedback control with a constant gain *K* can be illustrated as in Figure 6.2.

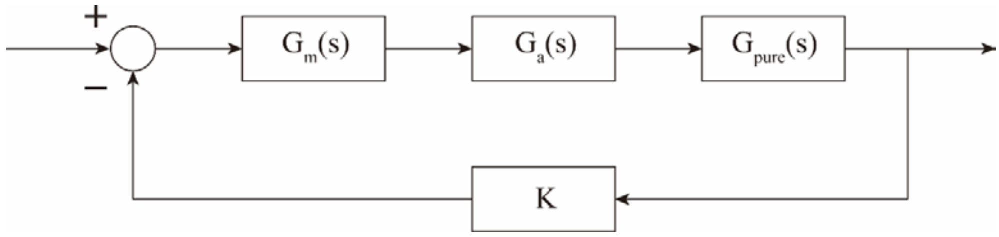

Figure 6.2 Initial feedback control for actuator-floor system of mode *m*

The transfer function of the closed-loop control system, therefore, can be written as:

$$G_{sys}(s) = \frac{G_m(s)G_a(s)G_{pure}(s)}{1 + KG_m(s)G_a(s)G_{pure}(s)} \tag{6-8}$$

6.2 Effects of time delays

In this section, the effects of constant time delays to a SDOF system is examined in order to explain why the time delay is a significant concern in the feedback control system. Since a SDOF system is considered, the influence of time delays caused by other dynamic components can also be regarded as a part of the pure constant time delays for simplicity, as shown in Figure 6.3. As an example, it is assumed that the natural frequency and damping ratio of mode m are 50Hz and 0.03, respectively, and therefore the transfer function for $G_m(s)$ is given as:

$$G_m(s) = \frac{\dot{q}_m(s)}{F_A(s)/m} = \frac{s}{s^2 + 18.84s + 98596} \tag{6-9}$$

In the discussion that follows, the effects of time delays on the stability margin and the damping ratio of the SDOF system with a modal direct velocity feedback controller is derived from the specific transfer function of Eq. (6-9).

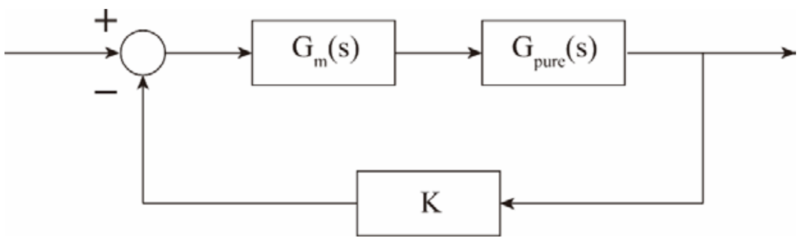

Figure 6.3 Simplified feedback control system with time delays

6.2.1 Stability margin

A feedback control system must be stable as a basic requisite for satisfactory control. The definition of BIBO stability is: “an unconstrained linear system is said to be stable if the output response is bounded for all bounded inputs [101]." And it is well known that a feedback control system is stable if all the roots of its characteristic equation have negative real parts, which means the poles of the system are to the left of the imaginary axis on the complex s-plane. The characteristic equation for the feedback control system shown in Figure 6.3 can be written as:

$$1 + G_m(s)G_{pure}(s)K = 0 \tag{6-10}$$

Substitution of Eqs. (6-3) and (6-7) into Eq. (6-10) yields:

$$1 + \frac{Ks}{s^2 + 2\zeta_m\omega_m s + \omega_m^2}\frac{1 - Ts}{1 + Ts} = 0 \tag{6-11}$$

Rearranging Eq. (6-11) in a polynomial equation results in:

$$Ts^3 + (2\zeta_m\omega_m T - KT + 1)s^2 + (K + \omega_m^2 T + 2\zeta_m\omega_m)s + \omega_m^2 = 0 \tag{6-12}$$

Generally, it is difficult to solve the roots of Eq. (6-12). Thus, classical Routh's stability criterion is often used to identify the stability of the control system [100]. This criterion of stability does not require calculation of the actual values of the roots of the characteristic polynomial equation, while it is a method to know if any root is to the right of the imaginary axis. A brief introduction of Routh's stability criterion is shown in Appendix B.

As the first step, it is necessary to check whether all of the coefficients in the characteristic equation is positive. Since T and K are positive values, the following condition must be satisfied:

$$2\zeta_m\omega_m T - KT + 1 > 0 \tag{6-13}$$

Next, if all of the coefficients are positive, the Routh array can be calculated and the results are shown in Table 6.1.

From Routh's stability criterion, the necessary and sufficient condition for all roots to have negative real parts is that all of the elements in the first column of the Routh array are positive.

Table 6.1 – Routh array of characteristic equation

Row 1	T	$K+\omega_m{}^2T+2\zeta_m\omega_m$
2	$2\zeta_m\omega_m T-KT+1$	$\omega_m{}^2$
3	$\dfrac{(2\zeta_m\omega_m T-KT)(K+\omega_m{}^2T+2\zeta_m\omega_m)+(K+2\zeta_m\omega_m)}{2\zeta_m\omega_m T-KT+1}$	0
4	$\omega_m{}^2$	0

Therefore, another condition that the system must satisfy is:

$$(2\zeta_m\omega_m T - KT)(K + \omega_m^2 T + 2\zeta_m\omega_m) + (K + 2\zeta_m\omega_m) > 0 \tag{6-14}$$

It is obvious that if $K \leq 2\zeta_m\omega_m$, Eqs. (6-13) and (6-14) will be unconditionally satisfied. However, if $K > 2\zeta_m\omega_m$, there will be a trade-off between T and K. From Eq. (6-14), it can be found that as the value of T increases, the margin of stability reduces, because the system is only stable for a lower value of K. For the transfer function of the SDOF system of Eq. (6-9), the characteristic equation is:

$$Ts^3 + (18.84T - KT + 1)s^2 + (K + 98596T + 18.84)s + 98596 = 0 \tag{6-15}$$

And the Routh array of the characteristic equation is shown in Table 6.2.

From Table 6.2, the following two conditions must be satisfied for a stable feedback control system:

$$18.84T - KT + 1 > 0 \tag{6-16}$$

$$(18.84T - KT)(K + 98596T + 18.84) + (K + 18.84) > 0 \tag{6-17}$$

From Eq. (6-16),

$$K < \frac{1 + 18.84T}{T} \tag{6-18}$$

Table 6.2 – Routh array of the characteristic equation for the specific mode

Row 1	T	K+98596T+18.84
2	18.84T-KT+1	98596
3	$\frac{(18.84T-KT)(K+98596T+18.84)+(K+18.84)}{18.84T-KT+1}$	0
4	98596	0

The plot of T verse K is shown in Figure 6.4. In this case, the area under the curve is the stable region, while that above the curve is the unstable region. It can be observed that as the value of the time delay T increases, the limitation of the control gain K for a stable system decreases. The similar conclusion can be achieved for the condition of Eq. (6-17), as shown in Figure 6.5. The final stable region is the intersection of the stable regions of both two conditions.

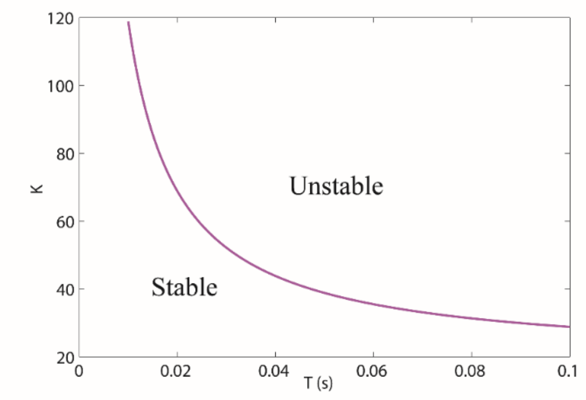

Figure 6.4 T-K plot for condition 1

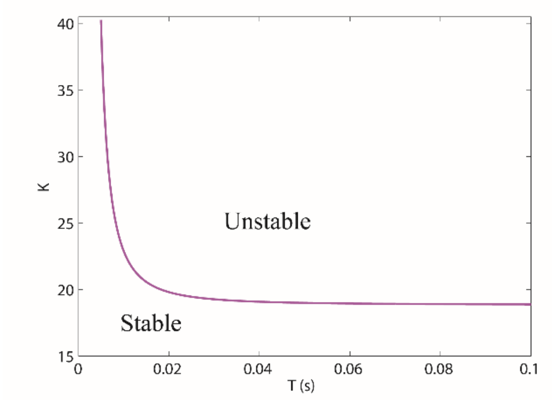

Figure 6.5 T-K plot for condition 2

6.2.2 Damping ratio

As shown in Sec. 3.2, the purpose of use of the modal direct velocity feedback controller is to increase the damping ratio of each mode to be controlled. Consider the block diagram shown in Figure 6.3. If no time delay exists, the characteristic function of the closed-loop system is given as:

$$1 + KG_m(s) = \frac{s^2 + (2\zeta_m\omega_m + K)s + \omega_m^2}{s^2 + 2\zeta_m\omega_m s + \omega_m^2} \tag{6-19}$$

Then the transfer function for the closed-loop system can be written as:

$$G_{sys1}(s) = \frac{G_m(s)}{1 + KG_m(s)} = \frac{s}{s^2 + (2\zeta_m\omega_m + K)s + \omega_m^2} \tag{6-20}$$

which means that the damping ratio is increased from ζ_m to $\zeta_m + K/2\omega_m$.

On the other hand, if there is a time delay component within the closed-loop system, how will it affect the damping ratio with the same value of K? In this case, the characteristic function of the closed-loop system is:

$$1 + KG_m(s)G_{pure}(s) = \frac{Ks(1 - Ts) + (s^2 + 2\zeta_m\omega_m s + \omega_m^2)(1 + Ts)}{(s^2 + 2\zeta_m\omega_m s + \omega_m^2)(1 + Ts)} \tag{6-21}$$

Therefore, the transfer function for the closed-loop system can be derived as:

$$G_{sys}(s) = \frac{s(1 - Ts)}{(s^2 + (2\zeta_m\omega_m + K)s + \omega_m^2) + Ts(s^2 + (2\zeta_m\omega_m - K)s + \omega_m^2)} \tag{6-22}$$

It is obvious that the first term of the denominator of Eq. (6-22) is the same as the denominator of Eq. (6-20), the effect of the time delay on the damping ratio of the whole feedback control can be detected from the second term of the denominator in Eq. (6-22), in which the damping ratio decreases.

Assuming the SDOF system descried in Eq. (6-9), and the constant control gains of $K = 10$ and $K = 30$, the impulse responses of the feedback control system for different time delays $T = 0$, $T = 0.005$ and $T = 0.01$ are shown in Figure 6.6 and Figure 6.7, respectively.

For $K = 10$, it is observed from Figure 6.6 that as the time delay increases, the damping ratio of the system decreases. The same situation occurs for the case of $K = 30$ as shown in Figure 6.7, while the system becomes unstable when $T = 0.01$. This is explained by the roots of Eq. (6-17) for those parameter values become negative values, and the stability condition given by Routh's stability criterion is not satisfied.

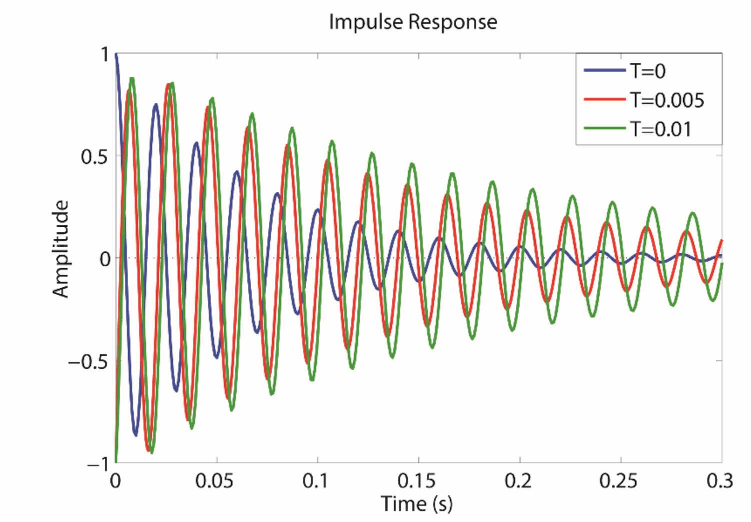

Figure 6.6 Impulse responses of different delay times for K=10

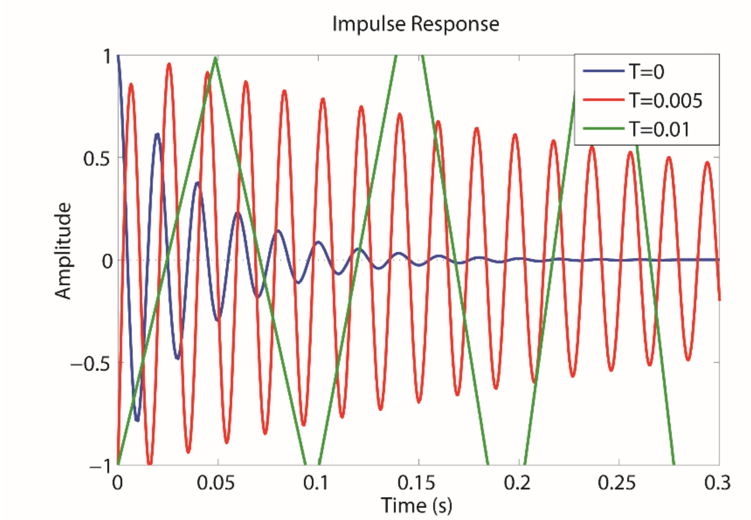

Figure 6.7 Impulse responses of different delay times for K=30

6.3 Experimental identification of $G_a - G_{pure}$ model

In this section, the numerical model of the actuator dynamics and other time delay elements is experimentally identified using the measurements of the dynamic behavior of the system. It is expected that this model can accurately express the time delays caused by the actuator and the DSP system. The resulting model allows use of the root locus technique for phase-lead compensator design in the next section.

Assuming a linear behavior, the transfer function G_A, from the command voltage generated on the DSP system to the measured acceleration multiplied by the weight of the actuator mass can be determined. This is achieved by generating a random excitation as the DSP computation command, sending out through the D/A interface, activating the actuator and the response is captured by the sensor and the measured signal is provided to the A/D interface. The actuator is mounted on the steel plate during the test so that the effects of the actuator-floor interaction described in Sec. 3.4.1 are considered. The response and outputs of the system components are instrumented at a sampling rate of 1000Hz for 5 seconds. The command input and the acceleration output are shown in Figure 6.8 and Figure 6.9, respectively.

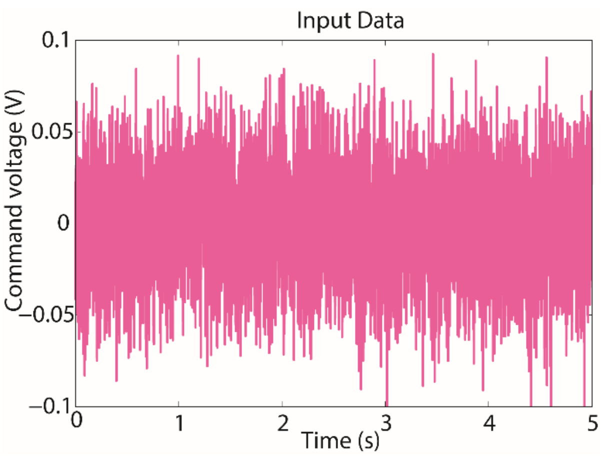

Figure 6.8 Input random data

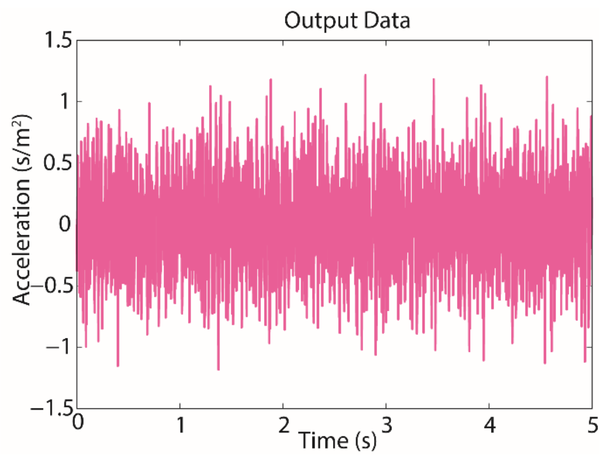

Figure 6.9 Output acceleration

Similar to the actuator model identification described in Sec. 4.4.1, the Instrument Variable (IV) method was utilized if the number of poles and zeros are known. For the estimation, MATLAB environment was used. When a fourth-order model for the G_A dynamics is assumed, the resulting transfer function is:

$$G_A(s) = \frac{-0.008225s^4 + 3.655s^3 + 1.39e^4s^2 - 8.333e^4s - 5.735e^6}{0.00065s^4 + 1.258s^3 + 421.6s^2 + 4.217e^4s + 4.957e^6} \quad (6\text{-}23)$$

which has four poles and four zeros. Transferring Eq. (6-23) to the zero-pole form yields:

$$G_A(s) = \frac{12.654(s-23.45)(s+17.57)(s+1100)(1-0.00065s)}{(s^2+2*0.295*123.85s+123.85^2)(s+323.18)(1+0.00065s)} \quad (6\text{-}24)$$

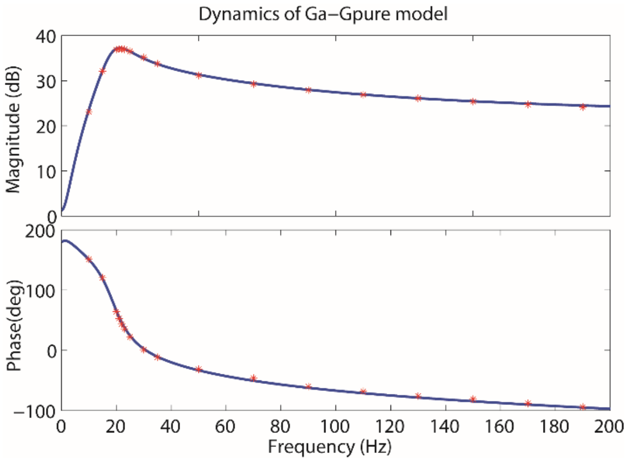

Figure 6.10 Frequency response of G_A system: (*) experimental (—) model

It can be found from Eq. (6-24) that two zeros out of the four zeros are located in the vicinity of the origin. From Sec. 4.4.2, the total time delay caused by the actuator-plate interaction, A/D-D/A interfaces, signal communication and computation etc. is estimated to be 0.0013s. As can be expected, comparison of Eq. (6-24) with Eq. (4-2) indicates that the dynamics of G_A is approximately equal to the dynamics of the actuator G_a cascaded with the pure term G_{pure} of Eq. (6-7) with $T = 0.00065$. The dynamics of the actuator is still involved through the term $(s^2 + 2 * 0.29 * 123.85s + 123.85^2)$. Therefore, G_A is referred to as the transfer function of the generalized actuator. The bode diagram of the estimated G_A model and the measured data are shown in Figure 6.10 for the range of 10~200Hz. As can be observed, the four-pole four-zero model provides a good fit for the amplitude and phase of the system. Since the main purpose of the G_A model is to reflect the phase characteristics within 0-150Hz frequency range (the lowest three modes), the fourth-order model is considered to be sufficient for the phase-lead compensator design, which will be introduced in the next section.

6.4 Phase-lead compensator design

In order to further enhance the control performance of MDVF controller, it is efficient to develop a modified MDVF controller designed to increase the closed-loop system stability and to make the system more amenable to the introduction of significant damping for each mode to be controlled. Toward this goal, a compensator should be introduced to compensate for the phase delays caused by the dynamic components for each control mode.

6.4.1 Preliminaries

For compensator design, the dynamics of the generalized actuator of Eq. (6-24) is approximately expressed as a linear fourth-order system with the following transfer function relating the control force with the command input voltage:

$$G_A(s) = (\frac{K_A s^2}{s^2 + 2\zeta_A \omega_A s + \omega_A^2})(\frac{s+\mu}{s+\varepsilon})(\frac{1-Ts}{1+Ts}) \tag{6-25}$$

in which K_A is the gain, ζ_A and ω_A are the damping ratio and natural frequency of the actuator, respectively. A filter element expressed by the pole at $-\varepsilon$ and zero at $-\mu$ is added to account for the dynamic property of the actuator. T is the half of the time delays caused by the DSP system and other components.

A phase lead compensator C_p is considered here for the purpose of increasing the stability and damping of the modes to be controlled. The following two assumptions are made for the design of the compensator:

1) The spillover effects of truncated modes are neglected, implying that each mode can be treated as a SDOF system.
2) The natural frequency of the actuator ω_A is sufficiently below the natural frequency of the mode ω_m.

6.4.2 Compensator Design

The root locus method is used for the compensator design. The root locus of a feedback system is to represent the possible locations of its closed-loop poles for varying values of a certain system parameter in the graphical way on the complex s-plane [100]. The points which are part of the root locus must satisfy the phase condition, while the value of the parameter for a certain point of the root locus is obtained using the magnitude condition. A brief introduction of the root locus method is shown in Appendix B.

The system parameter is the control gain K, and the phase-lead compensator design is achieved only use the information of $K = 0$.

Based on assumption 1), the transfer function relating the output velocity with the control force of mode *m* of floor can be written in Eq. (6-3). In order to improve the performance of the modal direct velocity feedback controller, the phase-lead compensator is applied to the mode velocity measurement signal as:

$$C_p(s) = \frac{s+\delta}{s}, \delta \leq 0 \tag{6-26}$$

where δ is a non-positive constant parameter. Therefore, the block diagram of the phase-lead velocity feedback control for each mode can be expressed as shown in Figure 6.1. The modal velocity is assumed to be the measured signal in Figure 6.1. If the structural acceleration is used as the measurement signal in the feedback control, an integrator component must be inserted to obtain the modal velocity.

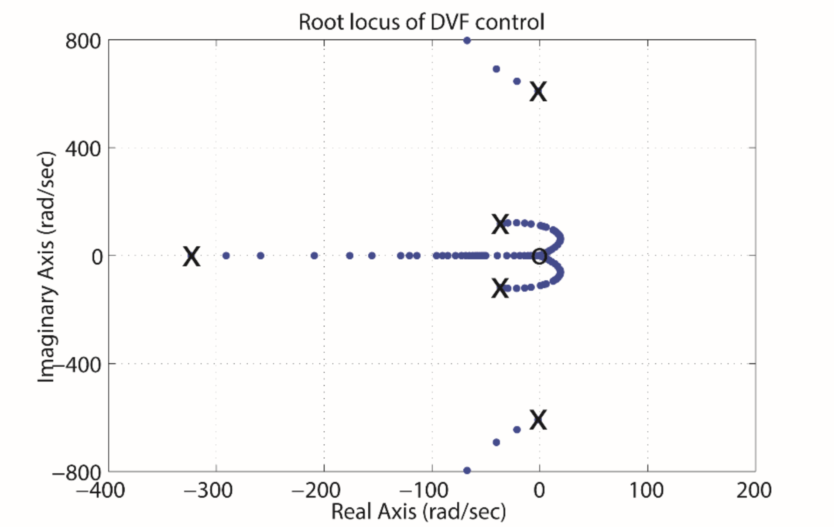

Figure 6.11 Root locus of DVF $(\times)$ poles (o) zeros

A typical root locus for the DVF controller is shown in Figure 6.11. An example of the mode with a natural frequency of 97Hz and a damping ratio of 0.003 is assumed. In this example, the specified mode is represented by a pair of low damped poles and a zero at the origin, while the actuator dynamics is represented by a pair of high-damped poles and two zeros at the origin. The natural frequency and damping ratio of the actuator are assumed to be 20Hz and 0.29, respectively, K_A is 12.65, ε is 323.18, $\mu = 1100$ and $T = 0.005$. As can be observed from the figure, the assumption 2) is satisfied by the natural frequency of the actuator is less than a half of 97Hz. It can also be observed that as the control gain increases, the damping ratio of this mode does not proportionally grow.

The advantages of the application of the phase-lead compensator described in Eq. (6-26) can be described as follows. The parameter δ is chosen so that [24]:

1) Substantially improves the relative stability of the mode.
2) Decreases the angles with respect to the negative real axis to increase the mode damping.
3) Increases the distance to the origin to allow increasing natural frequency.

Among many possible values for δ, the design value is determined based on the departure angle at zero gain of the locus. The departure angle of the locus of the poles corresponding to the specified mode must point toward the negative direction of the real axis to satisfy the conditions 1) ~ 3). Using the argument equation of the closed-loop characteristic equation, the following equation must be satisfied for any specific point on the trajectory:

$$\sum_{i=1}^{n_z} \angle(s_1 + z_i) - \sum_{j=1}^{n_p} \angle(s_1 + p_j) = \pm(2k+1)\pi \quad k \in \mathbb{N} \tag{6-27}$$

where n_z and n_p are the number of zeros and poles, respectively, $\angle(s_1 + z_i)$ is the angle of the vector drawn from ith zero and $\angle(s_1 + p_j)$ is the angle of the vector drawn from the jth pole. Then by letting s_1 be a point close to one of the poles of the mode, the departure angle can be determined.

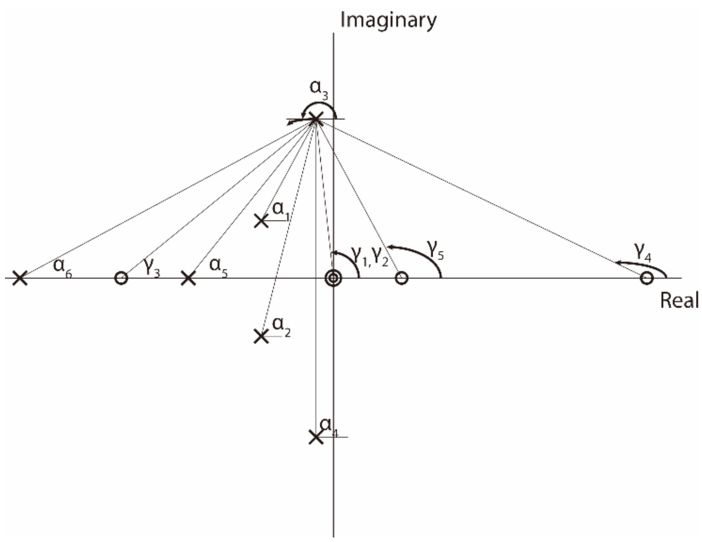

Figure 6.12 Departure angle of the locus corresponding to the specified mode (×) poles (o) zeros

If the zeros and poles of the phase compensated system are as shown in Figure 6.12, Eq. (6-27) for the transfer function of Eq. (6-8) can be rewritten as:

$$\begin{aligned}(\gamma_1 + \gamma_2 + \gamma_3 + \gamma_4 + \gamma_5) - (\alpha_1 + \alpha_2 + \alpha_3 + \alpha_4 + \alpha_5 + \alpha_6)\\ = \pm(2\mathrm{k}+1)\pi \quad k \in \mathbb{N}\end{aligned} \tag{6-28}$$

Since the damping of the mode to be controlled are considerably low in most cases, $\zeta_m \approx 0$, and it can reasonably be assumed that $\gamma_1 = \gamma_2 \approx \pi/2$. $\alpha_4 = \pi/2$. Then Eq. (6-28) becomes:

$$\begin{aligned}\gamma_3 + \gamma_4 + \gamma_5 - (\alpha_1 + \alpha_2 + \alpha_3 + \alpha_5 + \alpha_6)\\ = \left(\pm 2\mathrm{k}\pi + \frac{\pi}{2}\right) or \left(\pm 2\mathrm{k}\pi + \frac{3\pi}{2}\right) \quad k \in \mathbb{N}\end{aligned} \tag{6-29}$$

Based on Eqs. (6-3), (6-7) and (6-25), the parameters can be calculated as:

$$\alpha_1 = \text{atan}(\frac{\omega_m}{\zeta_m \omega_A} - \frac{\sqrt{1-\zeta_A^2}}{\zeta_A}) \tag{6-30}$$

$$\alpha_2 = \text{atan}(\frac{\omega_m}{\zeta_m \omega_A} + \frac{\sqrt{1-\zeta_A^2}}{\zeta_A}) \tag{6-31}$$

$$\alpha_5 = \text{atan}(\frac{\omega_m}{\varepsilon}) \tag{6-32}$$

$$\alpha_6 = \text{atan}(\omega_m T) \tag{6-33}$$

$$\gamma_3 = \text{atan}(\frac{\omega_m}{\mu}) \tag{6-34}$$

$$\gamma_4 = \pi - \text{atan}(\omega_m T) \tag{6-35}$$

As for α_3, the minimum $\alpha_{3,min}$ and the maximum $\alpha_{3,max}$ values can be specified to satisfy the three conditions described above, such as $\alpha_3 \in (0.95\pi,\ 1.05\pi)$. Then the minimum and maximum bounding values of γ_5 can be obtained as:

$$\gamma_{5,min} = -\frac{\pi}{2} + (\alpha_1 + \alpha_2 + \alpha_5 + \alpha_6 + \alpha_{3,min}) - (\gamma_3 + \gamma_4) \tag{6-36}$$

$$\gamma_{5,max} = -\frac{\pi}{2} + (\alpha_1 + \alpha_2 + \alpha_5 + \alpha_6 + \alpha_{3,max}) - (\gamma_3 + \gamma_4) \tag{6-37}$$

where it is assumed that $k = 1$. By combining Eqs. (6-36) and (6-37) with $\gamma_5 \in (\pi/2, \pi)$, the variation set of γ_5 is derived as:

$$\gamma_5 \in (\max\left(\frac{\pi}{2}; \gamma_{5,min}\right), \min(\pi; \gamma_{5,max})) \tag{6-38}$$

On the other hand, from Eqs. (6-3) and (6-26), the angle γ_5 is obtained as:

$$\gamma_5 = \pi - \text{atan}(\frac{\omega_m}{-\delta}) \tag{6-39}$$

Combining Eqs. (6-38) and (6-39), the corresponding variation set of $\delta \in (\delta_{min},\ \delta_{max})$ can be determined. The final value δ must be chosen from this set to complete the phase-lead compensator. Substituting the parameters of the actuator and the floor mode into Eqs. (6-30) ~ (6-39), it can be found that $\gamma \in (2.4576, 2.7718)$ and $\delta \in (-1571.1,\ -747.0431)$. The root locus plot of the proposed phase-lead velocity feedback control for the cases such that δ are chosen to be -1571.1, -747.0431 and -1000 are shown in Figure 6.13, Figure 6.14 and Figure 6.15, respectively. With the application of the compensator, the performance of the specified mode is significantly improved compared with the conventional MDVF controller. By appropriate choice of the control gain, the mode damping can be increased for the specified mode. The procedure introduced above then can be used for all the modes to be controlled with the modal filtering technique.

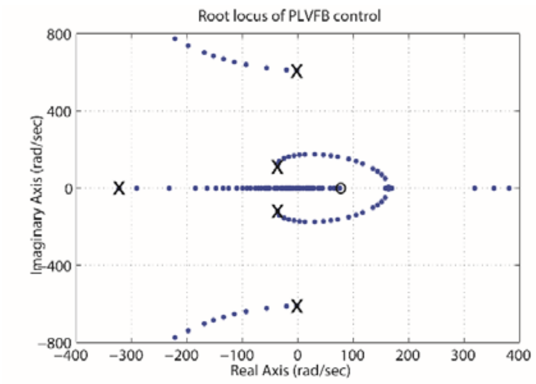

Figure 6.13 Root locus of PLVFB $(\times)$ poles (o) zeros δ=-747.0431

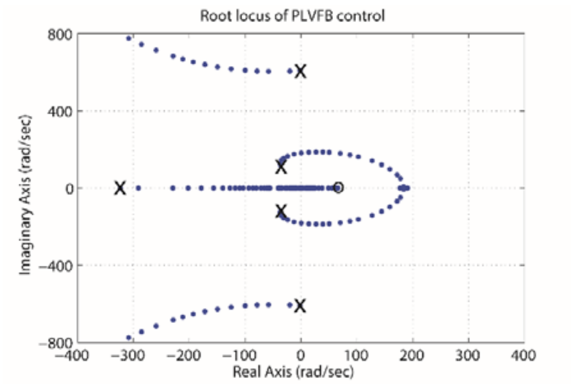

Figure 6.14 Root locus of PLVFB $(\times)$ poles (o) zeros δ=$-1.5711e+03$

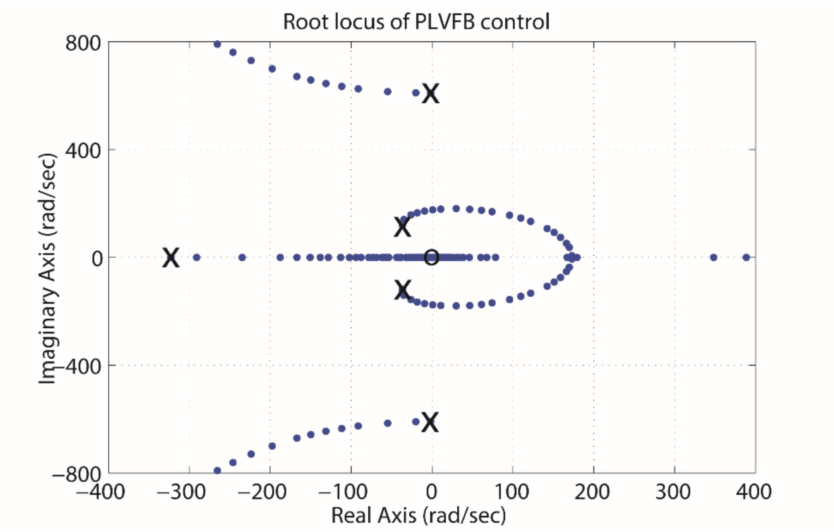

Figure 6.15 Root locus of PLVFB $(\times)$ poles (o) zeros δ=-1000

It should be pointed out that from Eq. (6-38), it is assumed that γ_5 should be smaller than π, otherwise the calculated range for δ cannot satisfy the specified range of α_3. However, if the time delays are very large, the calculated γ_5 will be larger than π. In this situation, the counterpart phase lag compensator must be used to improve the performance of the control system. The design process is the same as the procedure described above, except that $\delta > 0$.

6.4.3 Design process

Based on all the analysis described in the preceding sections, the whole control scheme for the independent modal space phase-lead velocity feedback control can be summarized by the following steps:

1) Experimentally identify the dynamics of the floor and the generalized actuator. For the floor, it is expected to determine the modal frequencies, modal damping ratios

and mode shapes of individual modes which are in the frequency range of interest. For the generalized actuator, it is expected to identify the model that can express the phase dynamics exhibited by the actuator and other dynamic components as accurate as possible.

2) Determine the number of modes to be controlled and the number of sensors and actuators to be used.
3) Determine the locations of the sensors and actuators based on the procedure described in Chapter 5 and calculate the modal filtering coefficients.
4) Design the phase-lead compensator for each mode to potentially increase the modal damping and robustness with respect to stability and performance following the steps described in Sec. 6.4.2.
5) Design the control gain for each mode to be controlled according to stability condition and control performance of the whole floor system. Non-linear actuator saturation must also be considered when choosing the control gains.

6.5 Verification test

In this section, a series of verification tests of the proposed phase-lead velocity feedback control scheme using the steel plate test specimen subjected to impact loads are described, and its control efficiency is discussed. A typical example of the controller design process is illustrated through the verification test, and the experimental control performance enhancement achieved by the proposed control scheme is investigated by the comparison between the test result of PLVFB and the result using the conventional modal direct velocity feedback (MDVF) controller.

Step 1 to 3 of the design process of Sec. 6.4.3 are introduced in Secs. 5.4.1 and 6.3, and a brief review is given herein.

For the first step, the modal frequencies, modal damping ratios and mode shapes are shown in Table 4.4 and Table 4.5, in which five modes in the frequency range between 0Hz and 200Hz are identified. The transfer function for the generalized actuator is identified as Eq. (6-24).

Next, the lowest three modes are considered to be controlled, and four sensors and one actuator are used for the active control implementation.

For the third step, the placement of sensors and actuator is determined as shown in Figure 5.16. The corresponding modal filtering coefficients are shown in Table 6.3.

Table 6.3 – Modal filtering coefficients

	Point 25	Point 31	Point 50	Point 61
Mode 1	0.4092	0.4940	0.7527	0.1485
Mode 2	0.0945	0.7133	-0.5006	-0.4813
Mode 3	-0.7532	0.4025	-0.2336	0.4650

6.5.1 Controller design

The purpose of this sub-section is to design the compensator $C_p(s)$ for the lowest three modes of the steel plate following the procedure described in Sec. 6.4.2.

For the first mode, the modal frequency and modal damping are 48.88Hz and 0.0108, respectively. Since two zeros of the actuator are close to the origin–one on the left side and one on the right side of the complex plane, and $\gamma_1 + \gamma_2 \approx \pi$, $\alpha_4 = \pi/2$. The values of α_1, α_2, α_5, α_6, γ_3 and γ_4 can be determined using Eqs. (6-30) ~ (6-35) and the results are 1.5676, 1.5635, 0.7599, 0.1970, 0.2723 and 2.9446, respectively. If $\alpha_3 \in (0.95\pi,\ 1.05\pi)$, from Eqs. (6-36) to (6-39), it can be calculated that $\gamma_1 \in (2.5992, 2.9134)$ and $\delta_1 \in (-509.6, -266.3)$.

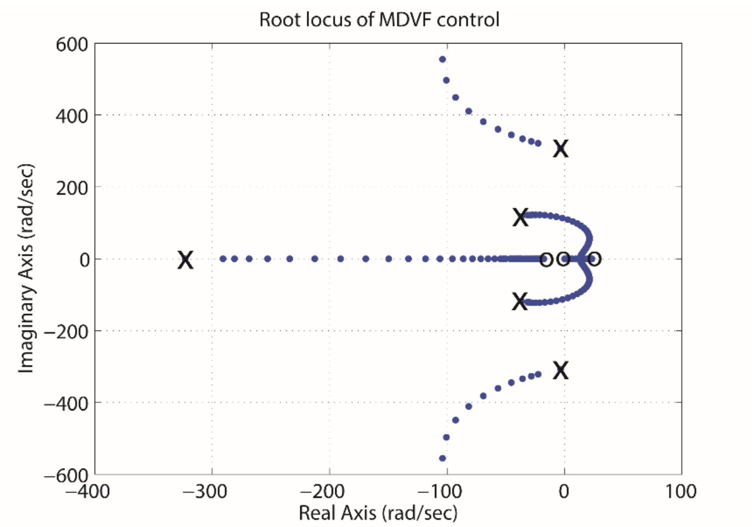

Figure 6.16 Root locus using DVF for the first mode

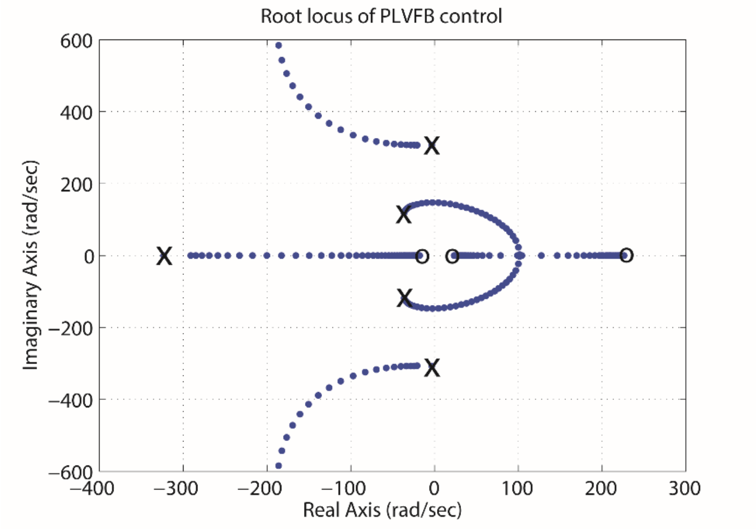

Figure 6.17 Root locus using PLVFB for the first mode

In this example, $\delta_1 = -226.3$ is selected as the parameter for the compensator. The root loci using MDVF and PLVFB controllers for the first mode SDOF system are plotted as Figure 6.16 and Figure 6.17, respectively. Since a small amount of phase lag caused by the generalized actuator is involved, the difference between these two root locus figures is insignificant. Therefore, it is expected that the simple modal direct velocity feedback controller can be used to control the first mode of the steel plate.

For the second mode, the modal frequency and modal damping are 97.01Hz and 0.0052, respectively. Same as the first mode, $\gamma_1 + \gamma_2 \approx \pi$ and $\alpha_4 \approx \pi/2$. The values of α_1, α_2, α_5, α_6, γ_3 and γ_4 are 1.5699, 1.5695, 1.0833, 0.3772, 0.5060 and 2.7644, respectively. From Eqs. (6-36) to (6-39), it can be found that $\gamma_2 \in (2.7432, 3.0574)$ and $\delta_2 \in (-7221.7,\ -1448.3)$.

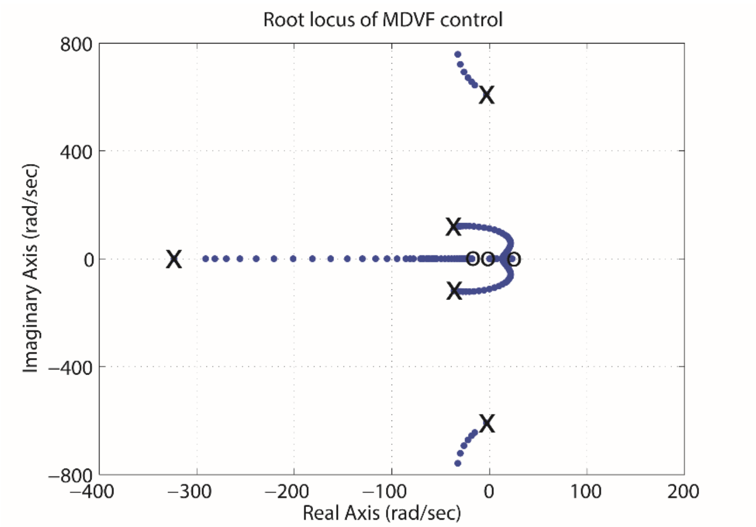

Figure 6.18 Root locus using DVF for the second mode

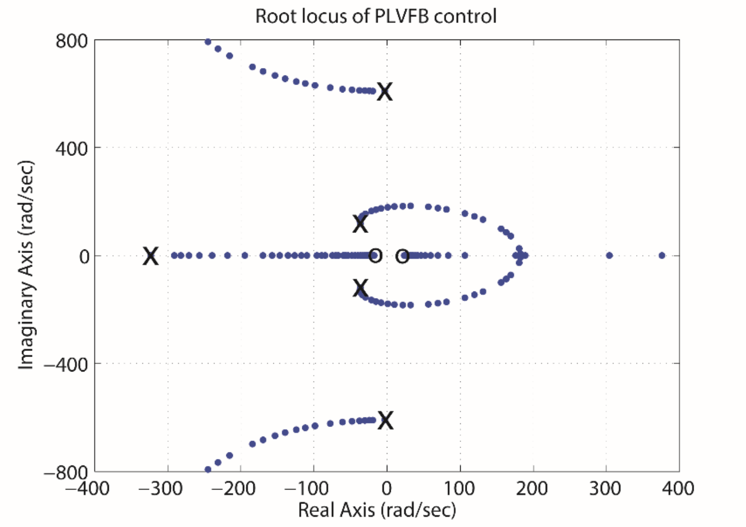

Figure 6.19 Root locus using PLVFB for the second mode

The parameter of the phase-lead compensator $\delta_2 = -1448.3$ is selected for this mode. The root loci for using MDVF and PLVFB controllers for this mode are plotted in Figure 6.18 and Figure 6.19, respectively. It is obvious that the performance of the second mode is significantly improved using the PLVFB controller compared with the MDVF controller. By appropriate choice of the control gain, the mode damping is expected to be increased for this mode using the PLVFB controller. The control results will be shown later.

For the third mode, the modal frequency and modal damping are 149.05Hz and 0.0035, respectively. The process is the same as the previous two modes. First, $\gamma_1 + \gamma_2 \approx \pi$ and $\alpha_4 = \pi/2$. $\alpha_1 = 1.5704$, $\alpha_2 = 1.5703$, $\alpha_5 = 1.2385$, $\alpha_6 = 0.5468, \gamma_3 = 0.7053$ and $\gamma_4 = 2.5948$. Based on these values, it can be calculated that $\gamma_3 \in (3.0396, 3.1416)$ and $\delta_3 \in (-inf, -9151.7)$.

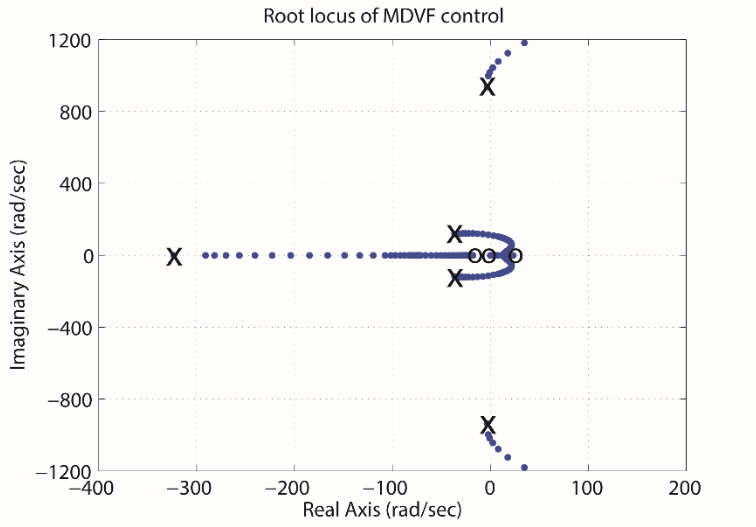

Figure 6.20 Root locus using DVF for the third mode

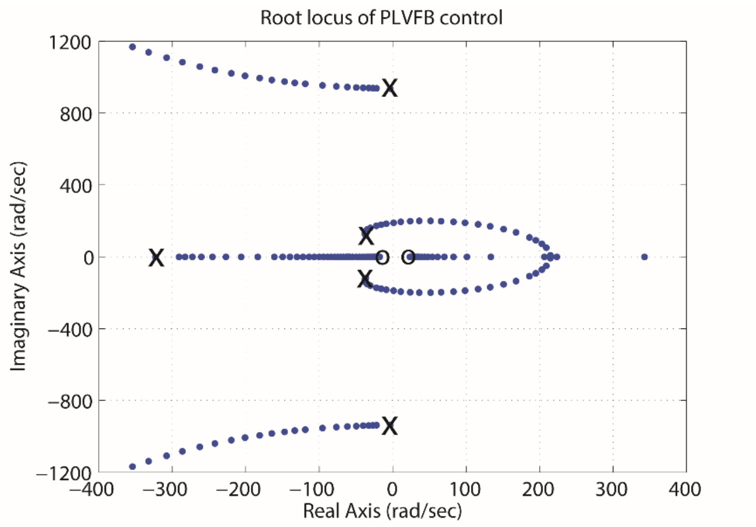

Figure 6.21 Root locus using PLVFB for the third mode

In this case, δ_3 is chosen as -9151.7. Figure 6.20 and Figure 6.21 show the root loci for the MDVF controller and PLVFB controller, respectively. Since a large amount phase lag is involved, the modal damping ratio of the third mode will not increase, but rather decreases as the control gain increases if the MDVF controller is used. Therefore the use of the PLVFB controller for the real-time active control is expected to be effective.

The final step for the control process is tuning the control gains for the three control modes. Using the test system the control gains are tuned by a repetitive procedure, in which the vibration of the plate induced by an impact load by the hammer is measured by the sensors, and the values of the gains of control modes are incrementally increased, until the system becomes unstable. When instabilities occur, the tuning process is completed. The reasonable gains can be determined as the ones used in the latest stable case.

6.5.2 Impact loading test

6.5.2.1 Modal direct velocity feedback control

The performance of the controlled floor using the MDVF control under impact hammer loading is examined first. For the MDVF approach, since acceleration sensors are adopted, integrators should be used to obtain the filtered velocity responses. The filtered velocity responses are then multiplied by control gains directly to generate the control forces. The frequency response functions between the acceleration sensor outputs and the hammer input at points 25, 31, 50 and 61 are compared for the case with and without the active control of single mode.

Firstly, the frequency response functions of the first mode control at four sensor points under different control gains are shown in Figure 6.22 through Figure 6.25. It can be observed that the damping ratio and natural frequency of this mode are increased with the increasing of control gain. Figure 6.26 shows the zoom-in view of the first mode of Point 31 to focus on the changes of frequency and damping ratio. The reason can be explained by the root locus of the first mode with the increasing of control gain, as shown in Figure 6.16. Because of the good performance of modal filtering, the peaks of the second and third modes are not changed, while the peaks of the fourth and fifth modes are increased due to the spillover effects, as shown in Figure 5.9. The effects of the modal filtering become more evident through the control outputs of the DSP system. The frequency response functions between the control outputs and the hammer input are shown in Figure 6.27. From Figure 6.27, it can be detected that as the control gain increases, the peak frequency of the control outputs for the first mode control increases as well, which also explains the reason of the increase of the natural frequency of the first mode shown in Figure 6.26. Furthermore, it can be observed from Figure 6.22 through Figure 6.25 that the control performance at the four points are consistent with each other, which conformed the global control characteristics of the model-based feedback controller.

Figure 6.28 through Figure 6.31 show the frequency response functions of the second mode control at four sensor points under different control gains. Significant changes of the damping ratio cannot be seen from these figures while the natural frequency of this mode is considerably increased. Figure 6.32 shows a zoom-in view of the second mode where the natural frequency and damping ratio are changing with the increasing of control gain. This is due to the large phase difference caused by the actuator and DSP hardware. From Figure 6.33, it can also be found that even though the control energy is large for the second mode, the damping ratio of this mode cannot be sufficiently increased because of the phase delay. This phenomenon can also be explained through the root locus of the second mode control, as shown in Figure 6.18. However, it is observed from Figure 6.28 through Figure 6.31 that the peaks of the first mode and the third mode are not significantly changed, which is owing to the good performance of the modal filtering method.

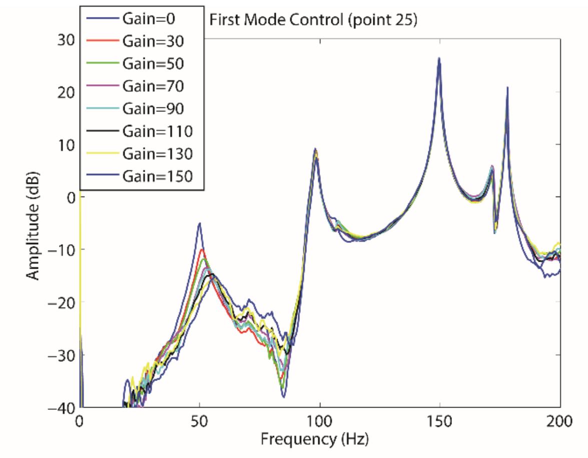

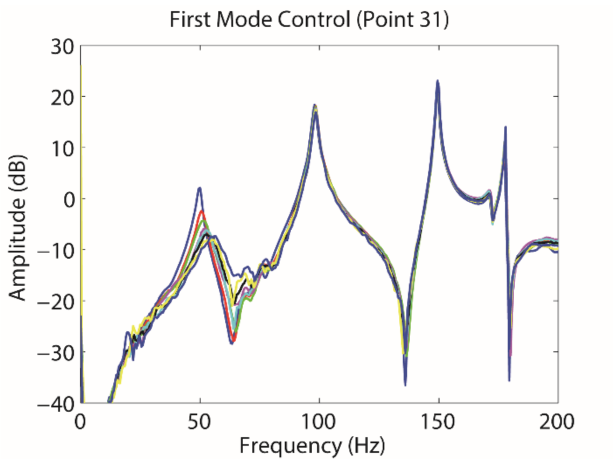

Figure 6.22 First mode control using MDVF for different control gains (Point 25)

Figure 6.23 First mode control using MDVF for different control gains (Point 31)

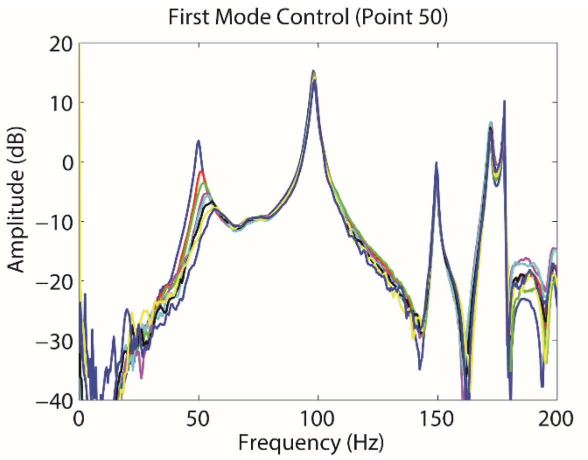

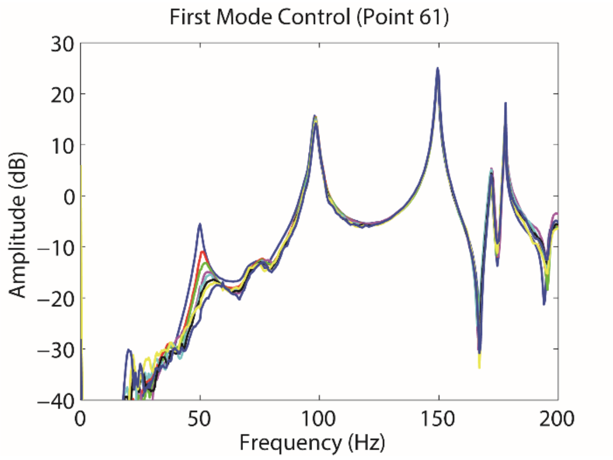

Figure 6.24 First mode control using MDVF for different control gains (Point 50)

Figure 6.25 First mode control using MDVF for different control gains (Point 61)

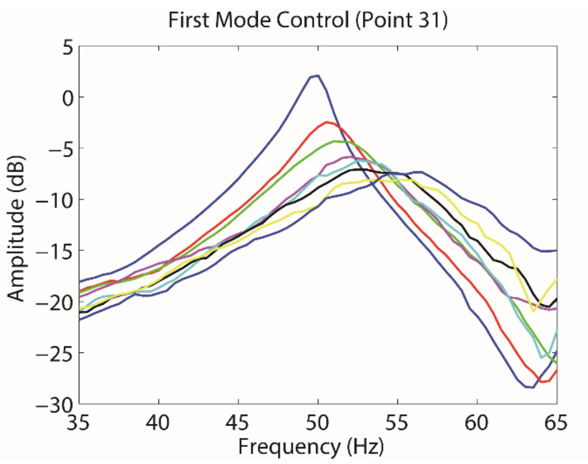

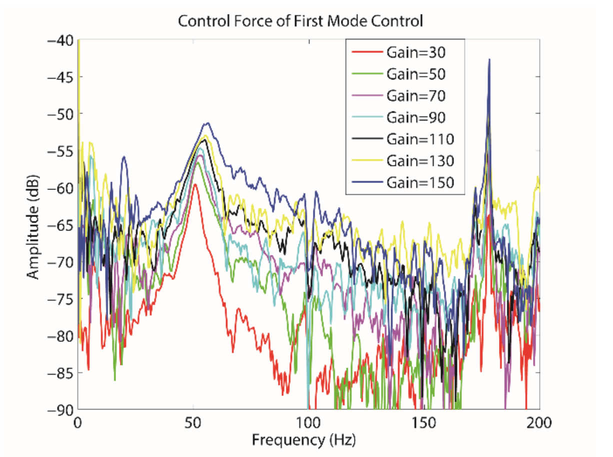

Figure 6.26 First mode control (Point 31)

Figure 6.27 Control force outputs for different control gains

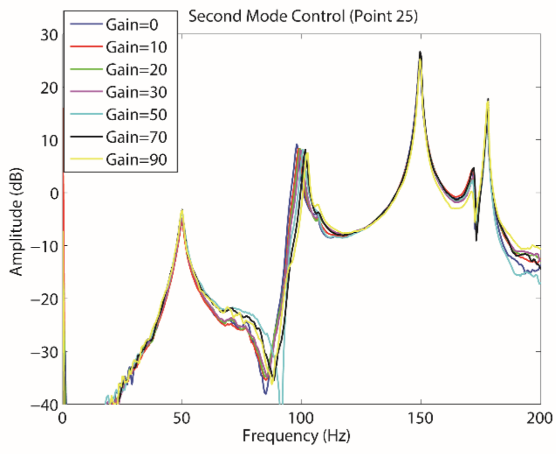

Figure 6.28 Second mode control using MDVF for different control gains (Point 25)

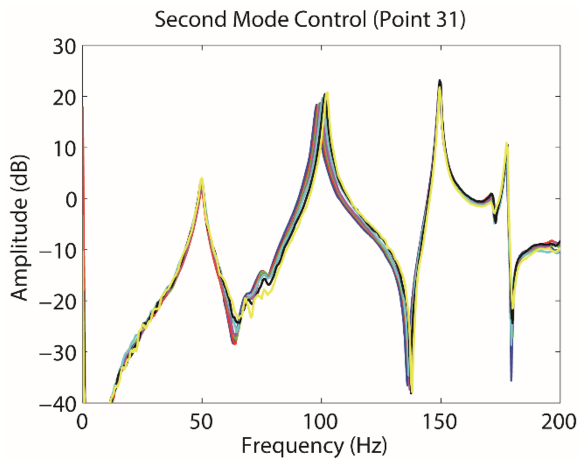

Figure 6.29 Second mode control using MDVF for different control gains (Point 31)

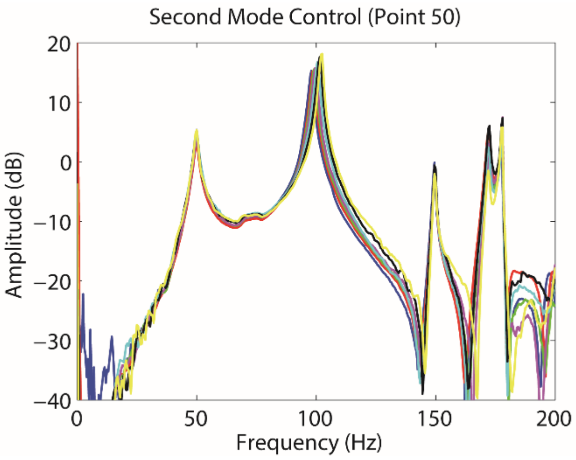

Figure 6.30 Second mode control using MDVF for different control gains (Point 50)

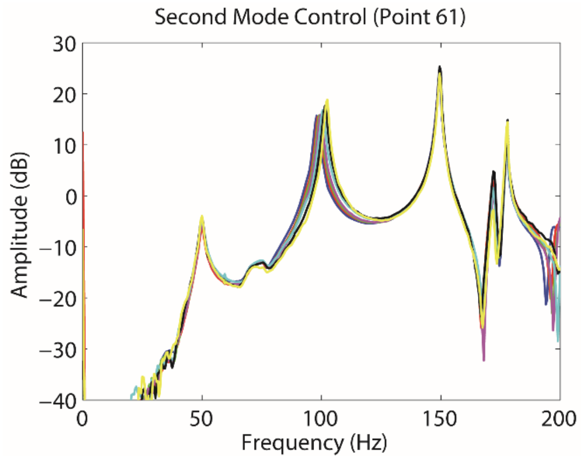

Figure 6.31 Second mode control using MDVF for different control gains (Point 61)

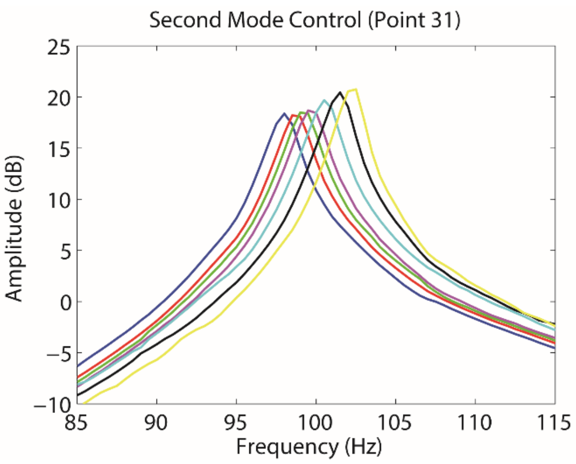

Figure 6.32 Second mode control (Point 31)

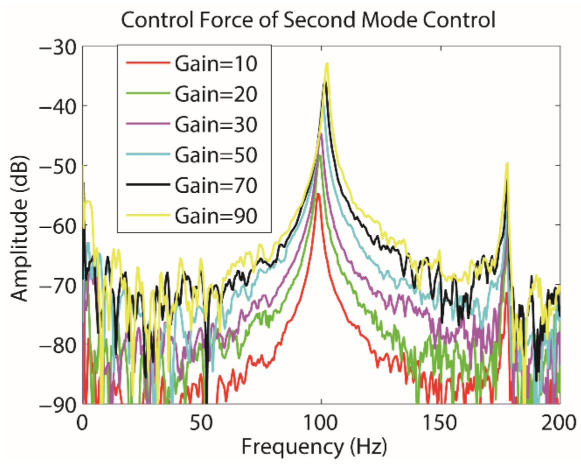

Figure 6.33 Control force outputs for different control gains

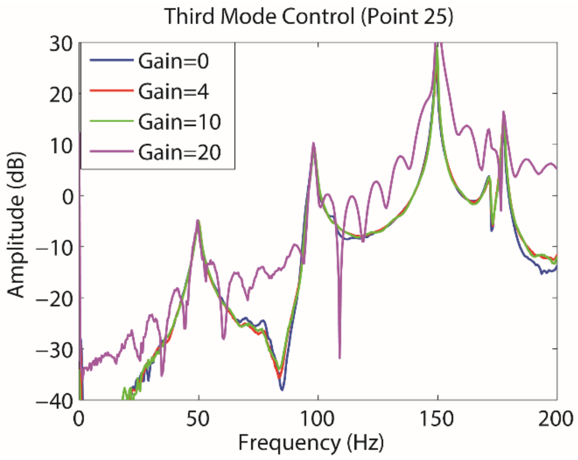

Figure 6.34 Third mode control using MDVF for different control gains (Point 25)

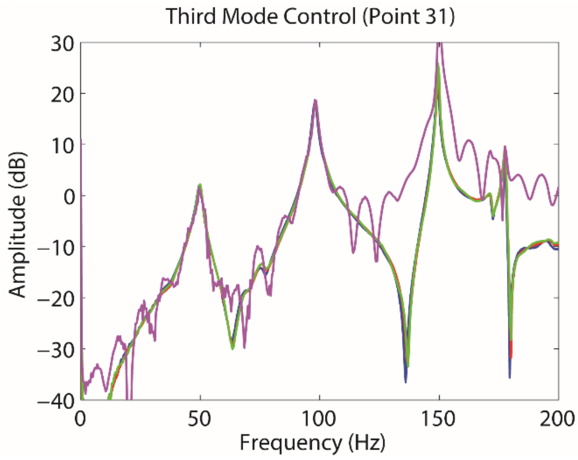

Figure 6.35 Third mode control using MDVF for different control gains (Point 31)

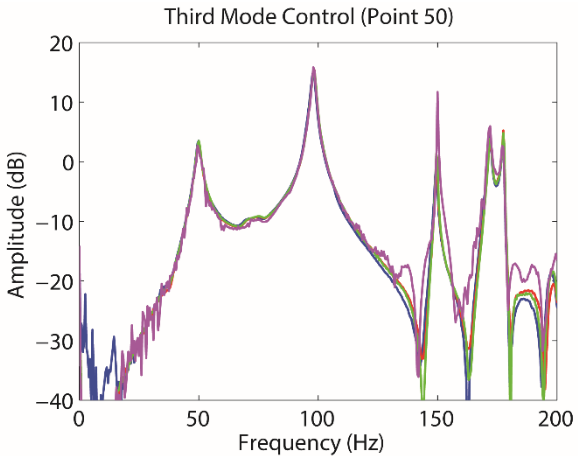

Figure 6.36 Third mode control using MDVF for different control gains (Point 50)

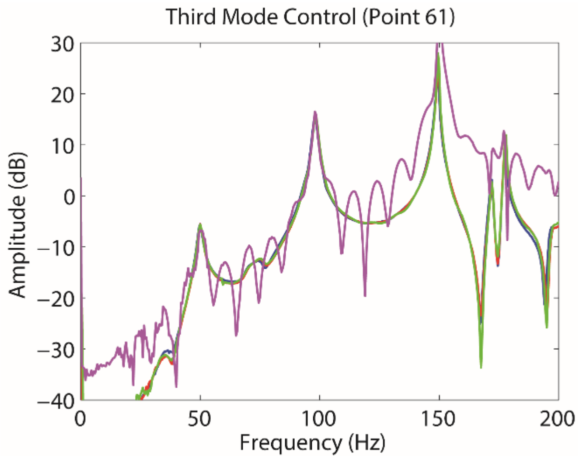

Figure 6.37 Third mode control using MDVF for different control gains (Point 61)

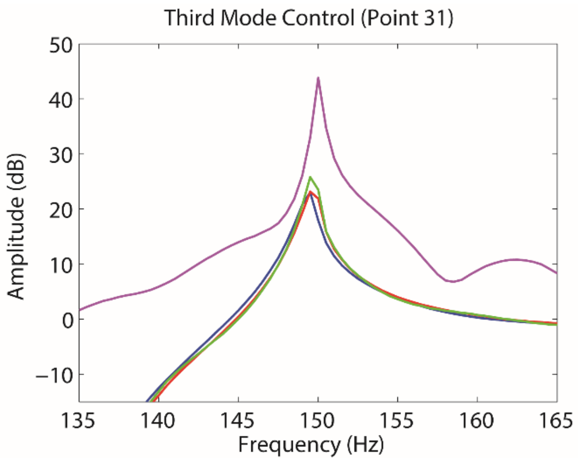

Figure 6.38 Third mode control (Point 31)

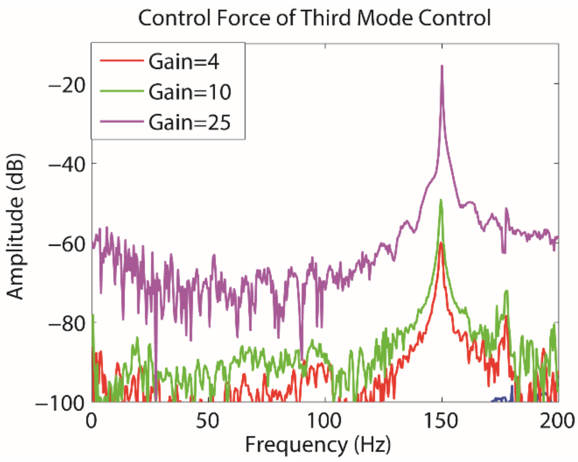

Figure 6.39 Control force outputs for different control gains

Finally, the frequency response functions of the third mode control at four sensor points under different control gains are examined, as shown in Figure 6.34 through Figure 6.37. Figure 6.38 and Figure 6.39 show the zoom-in view of the third mode peak change and DSP control outputs, respectively. Similar to the second mode MDVF control case, the damping ratio of the third mode is not increased, but rather decreased due to the large phase delay, and the system became instable when the control gain is increased further. The performance is well estimated from the root locus of shown in of Figure 6.20. It can also be observed that the peaks of the first mode and the second mode do not significantly change.

6.5.2.2 PLVFB control of single mode

From Sec. 6.5.2.1, it is known that a good control performance of the first mode can be achieved using the simple MDVF control, and the damping ratio was sufficiently increased. However, the performance of the MDVF controller is not excellent for the second and third modes control, and it is found that the modal frequencies of both modes increased while the modal damping ratios did not increase as that of the first mode. The reason can be explained from the root locus of these three modes without phase lead compensation. In order to improve the control performance, phase-lead compensators of Eq. (6-26) must be used.

The test results for the first mode control using three different δ within the calculated range are shown in Figure 6.40, in which the frequency response functions of the three control cases are compared with the case without active control of Point 31. The control gains for the three cases are chosen for the purpose of achieving the same amplitude. It can be seen from this figure that the damping ratios of all the three cases are increased while the natural frequencies are changing in different ways. This can also be explained through the root locus of this mode when the phase-lead compensator is utilized, since the distance between the poles of mode and the origin represents the natural frequency, with the increase of the control gain, the poles of the system move in different manners when different phase-lead compensators are used.

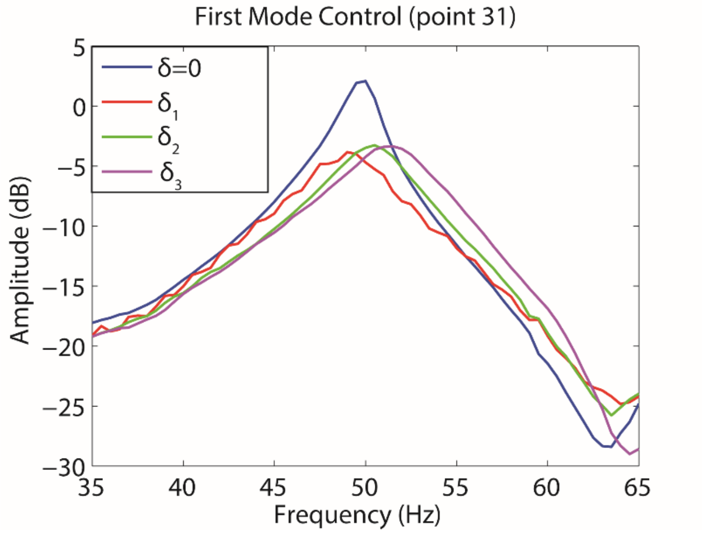

Figure 6.40 First mode control using selected phase-lead parameters

Figure 6.41 and Figure 6.42 show two cases of the PLVFB control for the first mode of the plate for increased control gains. The compensator parameter δ in case 1 is larger than that of case 2. It can be observed that as the control gain increases, the natural frequency of the first mode remarkably increases for case 1 compared with case 2, while more significant increase of the damping ratio for case 2 is achieved compared with case 1.

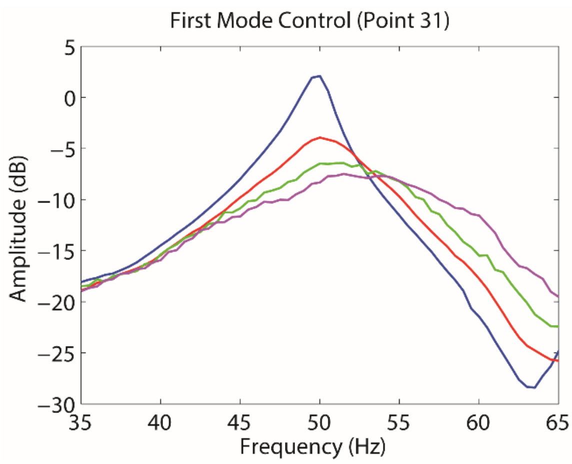

Figure 6.41 PLVFB control of the first mode (case 1)

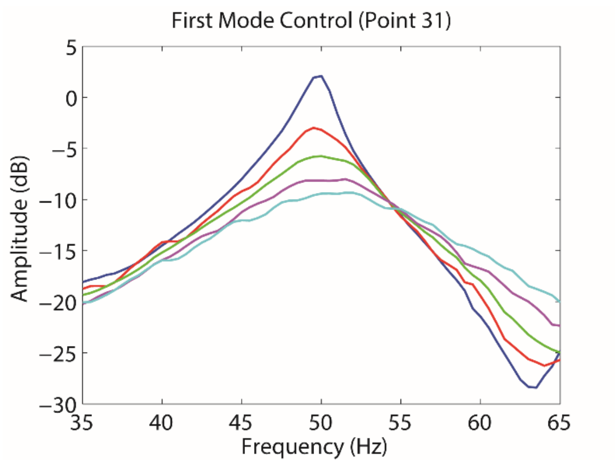

Figure 6.42 PLVFB control of the first mode (case 2)

Figure 6.43 shows the performance for the second mode control using three different compensator parameters δ. It is found that the control performance is significantly improved compared with the control results using the MDVF controller. For different parameters δ, the natural frequency and damping ratio will change in different manners, which can be estimated from the root locus of the poles of the mode.

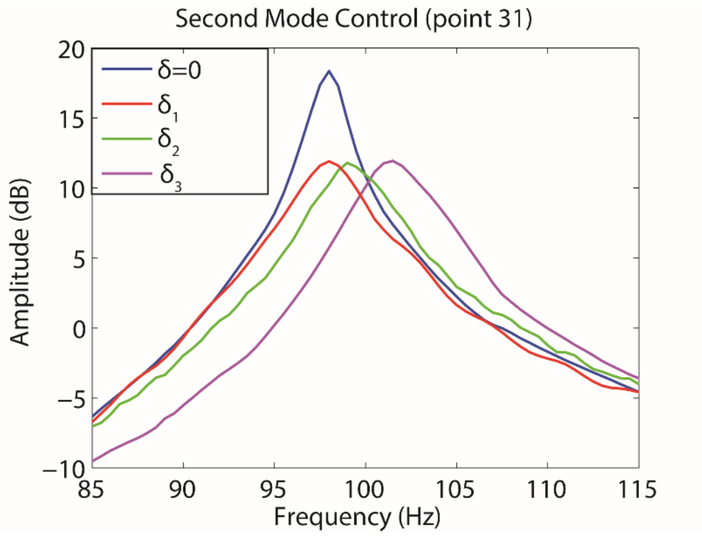

Figure 6.43 Second mode control using selected phase-lead parameters

Same as the first mode control, Figure 6.44 and Figure 6.45 show two cases of the PLVFB control for the second mode for increased control gains, where the compensator parameter δ in case 1 is larger than that of case 2. It can be observed that both of the two cases are capable of sufficiently increasing the damping ratio of the second mode.

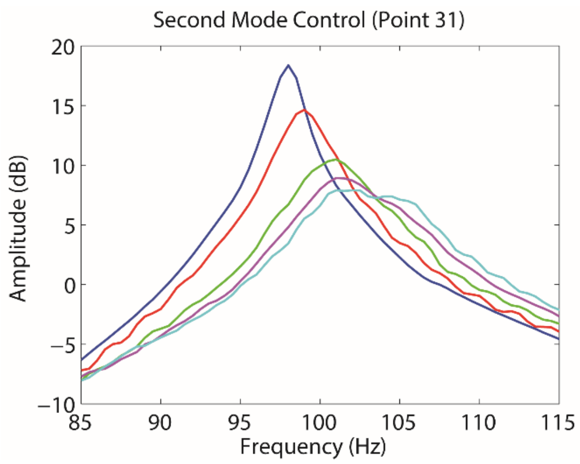

Figure 6.44 PLVFB control of the second mode (case 1)

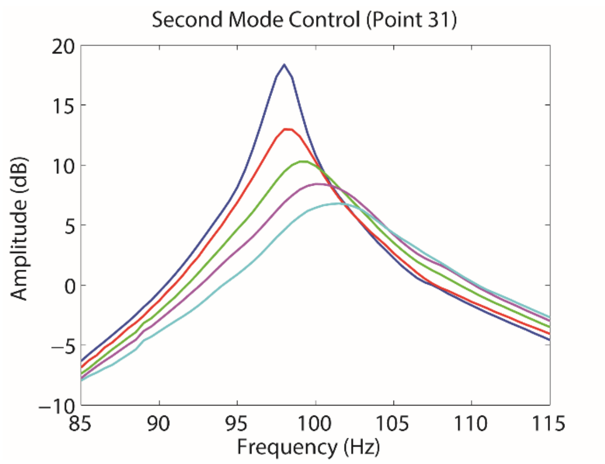

Figure 6.45 PLVFB control of the second mode (case 2)

Finally, the PLVFB controller is applied on the third mode control application. Figure 6.46 shows the performance for this mode control using three different compensator parameters δ. Similar to the control performance for the second mode, it is noticed that the control performance is significantly improved compared with the MDVF controller counterpart. Figure 6.47 shows the case of using PLVFB controller for the third mode with increased control gains. It can be observed that the damping ratio is considerable increased as the control gain increases.

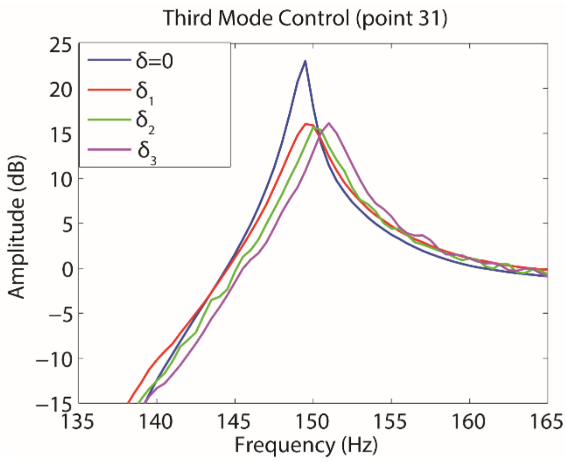

Figure 6.46 Third mode control using selected phase-lead parameters

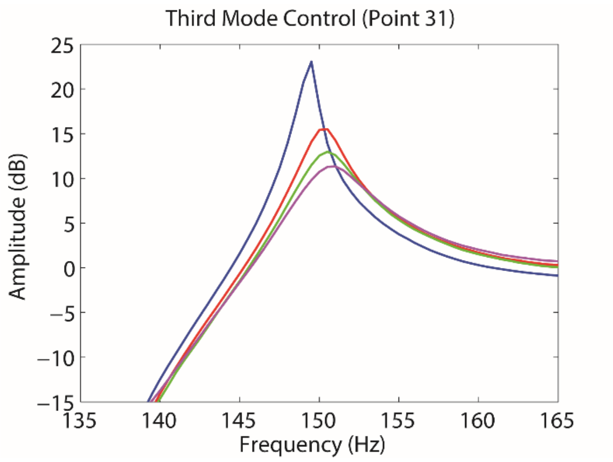

Figure 6.47 PLVFB control of the third mode

6.5.2.3 PLVFB control of multiple modes

The final experiments are conducted for the cases of using PLVFB controller to suppress the vibration of multiple modes. A high pass filter with a cut-off frequency of 10Hz is used to avoid the low frequency noise. Since the high pass filter will introduce phase lead to the control modes, it will not degrade the control performance. Because of the global control characteristic of the model based controllers, only the control results of Point 31 are shown.

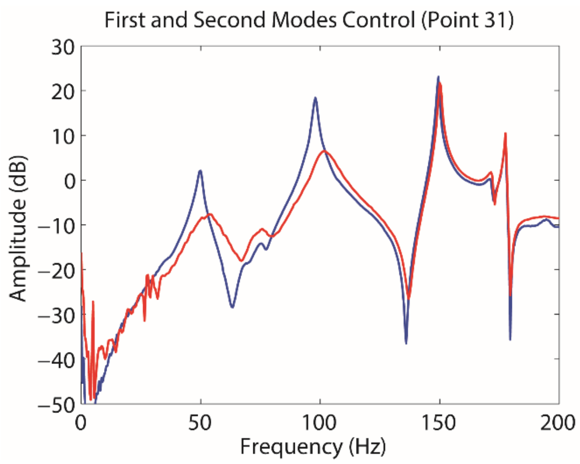

Figure 6.48 Test result: lowest two modes control at Point 31

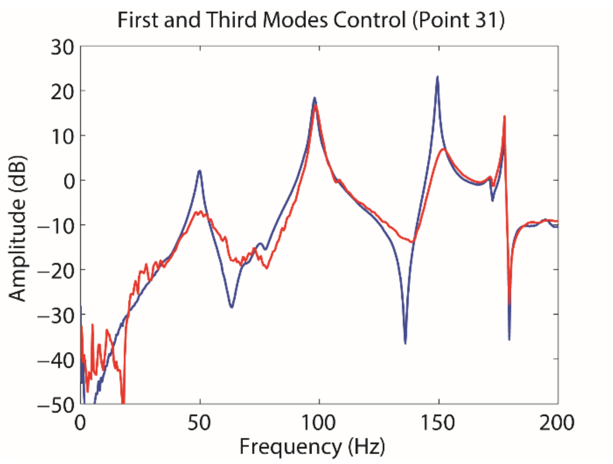

Figure 6.49 Test result: first and third modes control at Point 31

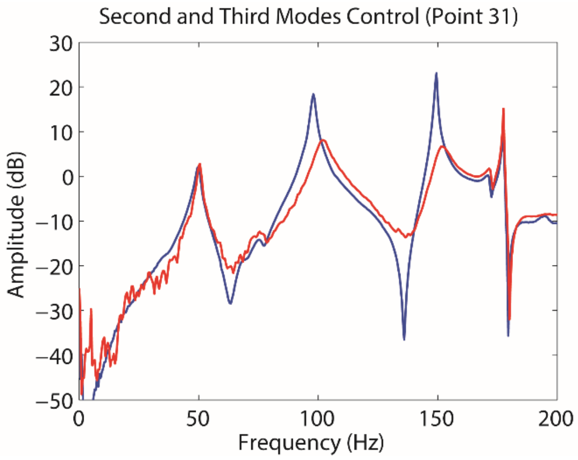

Figure 6.50 Test result: second and third modes control at Point 31

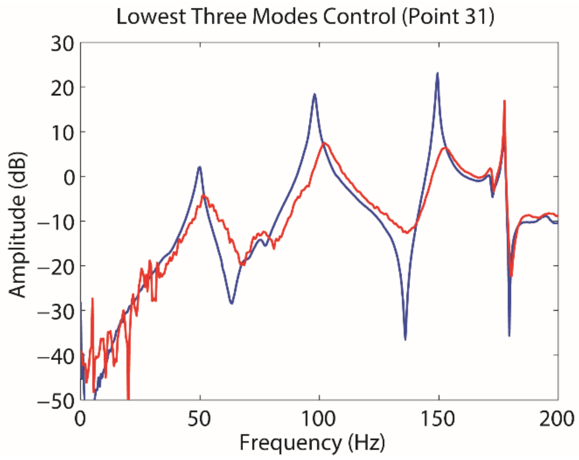

Figure 6.51 Test result: lowest three modes control at Point 31

Figure 6.48 shows the test result of control of the lowest two modes, in which the frequency response functions of Point 31 between sensor outputs and hammer inputs are compared for the case with and without active control. It is observed that the modal frequencies and damping ratios of the lowest two modes increases without affecting the modal properties of the third mode due to the high performance of the PLVFB controller and the modal filtering technique. Figure 6.49 and Figure 6.50 show the results of the first and third modes control and second and third modes control, respectively.

Figure 6.51 shows the control results of the lowest three modes for the cases with and without active control of Point 31. Significant reduction of peaks in the lowest three modes shown in the figure indicates that the independent modal control enables the system to increase the modal damping of each controlled mode to effectively reduce the vibration of the steel plate. Since the actuator is placed in the vicinity of the node of the 4th mode shape, the change of the peak response of this mode is not significant. On the other hand, the increase of the peak of the 5th mode response is a strong indication of the spillover effect.

6.6 Summary

The independent modal space phase-lead velocity feedback controller was presented in this chapter in the context of cancellation of floor vibration. The motivation of the development is that the traditional modal direct velocity feedback (MDVF) controller may not be a good choice if a large phase delay exists.

Firstly, the effects of time delays are examined in order to explain the problem of time delay in the feedback control system. It is found that large time delays would reduce the stability margins and the possible damping for each of the control mode.

Then a numerical model of the dynamics of the actuator and time delay due to other components which is referred to as the generalized actuator system, is identified using experimental measurements of the dynamic behavior of the system. This model can accurately express the time delays caused by the actuator and the DSP hardware.

Next, the phase-lead compensator technique, which is in fact introducing a first order compensator to the control system, is proposed in order to achieve significant stability enhancement and damping for the control modes. The root locus method is used to calculate the phase-lead compensator parameters for individual control modes.

Finally, an active control system designed based on the proposed control scheme is tested on the steel plate. The control tests using the MDOF controller are conducted for individual modes control. Because of the large phase delay involved, the performance of the MDOF controller is not excellent. Then the phase-lead compensators for individual control modes are designed and introduced to the system. The test results show that significant reduction of the responses are achieved in the control modes.

Up to present, only the modes within 0-200Hz are considered. However, higher modes above 200Hz are present and may degrade the control performance during the active control if their influence is ignored in the control system. Figure 6.52 shows an example of the control force outputs from the DSP system when the first mode is controlled using the PLVFB controller. It is observed that the modes above 200Hz are intensely excited and in fact the amplitudes of these modes will increase as the control gain for the first mode control increases. Therefore, if the control gain is large, the system may become unstable because of the poles of the higher modes move to the right hand side of the *s*-plane.

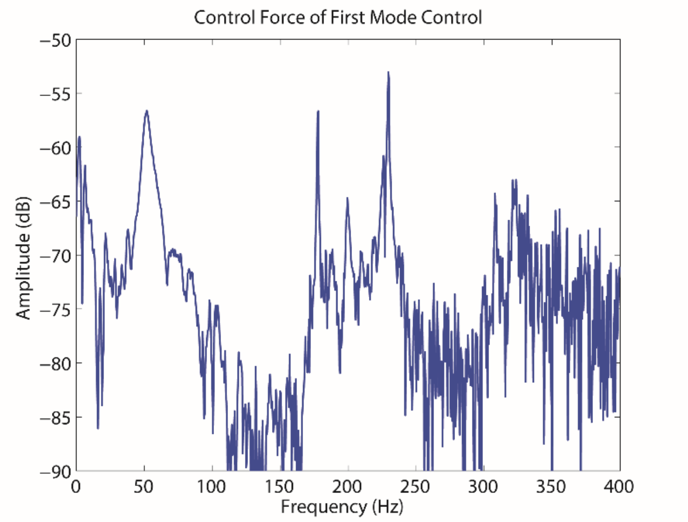

Figure 6.52 Control force outputs for first mode control using PLVFB controller

One possible solution is the use of the optimal sensor placement technique described in Chapter 5. For this purpose, the higher modes above 200Hz must be accurately identified and then considered as the residue modes. However, it has been shown in Chapter 5 that the spillover effects of the residue modes cannot be completely eliminated unless they are considered as the control modes. In that case, more sensors should be used. Furthermore, it is difficult to suppress the spillover effects using a small number of sensors if a large number of modes are considered as the residue modes.

Another possible solution is the application of the low pass filter to attenuate the signals in the frequency range higher than the cut-off frequency. However, the low pass filter will introduce more poles into the whole system, and therefore will introduce more phase delay. On the other hand, from Figure 6.52, it should also be noted that a high pass filter is need to attenuate the signals in the low frequency range due to numerical issues associated with integration of acceleration signals to velocity. Furthermore, use of high pass filter can avoid the stroke saturation described in Sec. 2.1 and therefore make the system more stable.

It is possible to design the phase-lead compensators when low pass and high pass filters are applied. However, the process is complicated and the dynamic components involved in the whole control system must be accurately identified for the compensator design. Based on the theoretical fundamentals of the PLVFB controller presented in this chapter, a more practical and accurate method will be introduced in the next chapter for the purpose of phase compensation without any information of the dynamic components.

Chapter 7 Compensation for Time Delays

The effects of time delays on the performance of real-time control using MDVF controller for each control mode were analysed in detail in the previous chapter, and a phase-lead compensator was developed using root locus method based on a generalized actuator model. However, there are disadvantages of the root-locus based method. First, application of the root locus technique becomes more complicated if the high pass and low pass filters are involved, since a higher order model must be identified to represent the phase dynamics of all the components including the filters. Second, it may be difficult to choose a proper parameter δ from a range of allowable values for each mode so that all the control modes be well-behaved based on the same criterion. Finally, model identification becomes time consuming, complicated and error prone with the increase of the dynamic components in the real-time control.

In this chapter, new phase compensation techniques are proposed. The associated controller associated with these techniques is referred to as the phase compensated velocity feedback control (PCVFB). All the time delays caused by the dynamic components for each control mode will be compensated in this study. Phase compensation can be implemented by a simple weighted linear combination of integration with the target modal control signal itself, which is similar to the proportional-integral (PI) technique. The only information needed for the implementation is the modal frequency. As long as the modal frequency of the control mode is known, the PI parameters can be searched in an automatic way such that not only the phase but also the magnitude can be compensated.

7.1 PI compensation

The idea of PI compensation comes from the phase-lead compensator introduced in the previous chapter. Recall that the transfer function for the phase-lead compensator is written as:

$$C_p(s) = \frac{v_{cf}}{v_f} = \frac{s+\delta}{s}, \delta \leq 0 \tag{7-1}$$

where v_f is the modal velocity and v_{cf} is the compensated modal velocity. Transformation of Eq. (7-1) from the Laplace domain to the time domain yields:

$$v_{cf}(t) = v_f(t) + \delta \int_0^t v_f(\tau)\, d\tau \tag{7-2}$$

In order to keep the amplitudes of these two modal velocities equal, a scaler parameter β is multiplied to the right-hand side of Eq.(7-2):

$$v_{cf}(t) = \beta v_f(t) + \beta\delta \int_0^t v_f(\tau)\, d\tau \tag{7-3}$$

Therefore, the PI compensator can be written as:

$$v_{cf}(t) = a v_f(t) + b \int_0^t v_f(\tau)\, d\tau \tag{7-4}$$

Figure 7.1 shows a schematic block diagram of the configuration for the phase compensated velocity feedback control of mode *m*.

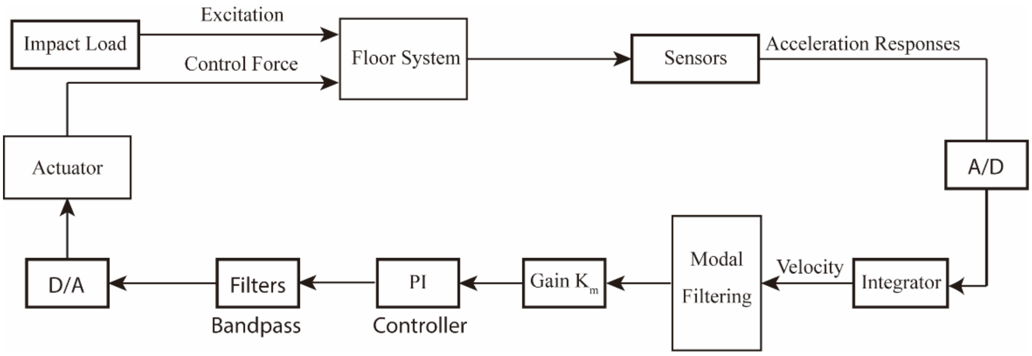

Figure 7.1 Phase compensated velocity feedback control of the *m*th mode

The purpose of the PI compensation is to compensate all the time delays caused by the dynamic components, such as the actuator, A/D-D/A interfaces and bandpass filters. The issue is the method to adjust the PI parameters a_m and b_m for each mode without any knowledge of the transfer functions of these dynamic components.

7.2 PCVFB controller design

In this section, the proposed procedure of PI parameter search is described. The PI parameters a_j and b_j are obtained by a set of real-time experiments prior to the real-time control. In order to search for the value of these parameters, the following four assumptions are introduced here:

1) The digital signal processing (DSP) system has the ability to generate signals by itself to activate the actuator.
2) The sinusoidal signals are used in the PI parameter search and the phase compensation procedure.
3) The delayed control force can be detected by the sensor mounted on the mass of the actuator.
4) All the components in the control loop are linear time invariant systems.

The DSP system used in the phase compensation and active control has six input channels and eight output channels that satisfy the assumption 1). In the ensuing subsections, two phase compensation techniques are introduced. Both methods can successfully search the PI parameters.

7.2.1 Standard phase compensation

According to the assumption 2), a sinusoidal signal $y = B\sin(\omega t)$, which can be regarded as the modal velocity, where B is the amplitude (selected randomly) and ω is the frequency of the mode that need to be controlled, is supposed to be generated and provided from Output Channel 1. While the sinusoidal signal is monitored through the Input Channel 1, the signal is provided to the feedback control loop to activate the actuator. For the measurement of the control force, the acceleration of the actuator mass is measured as the amplifier output of the accelerometer mounted on the mass detected with Input Channel 2. The system concept is shown in Figure 7.2. The green lines represent the digital processing inside the DSP system and the red lines represent analogue signal cable connection.

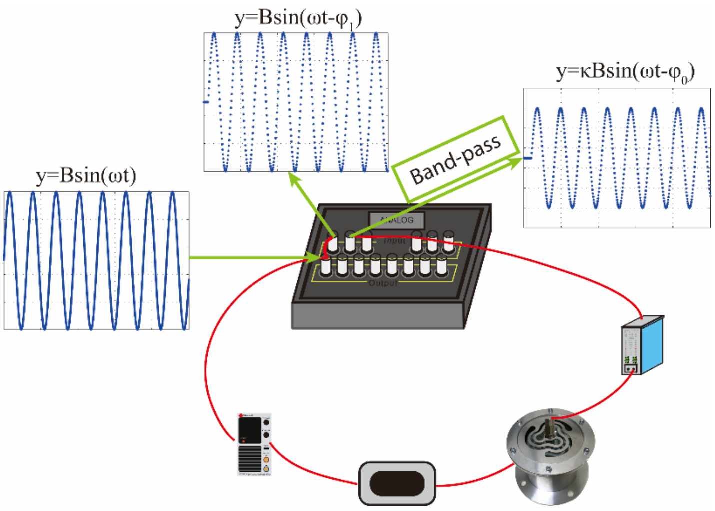

Figure 7.2 Signal before phase compensation

Assuming that the physical signal is expressed by $y = B\sin(\omega t)$, the instrumented signal received through Input Channel 1 eventually has a phase lag φ_1 , which can be expressed as $y = B\sin(\omega t - \varphi_1)$. The signal instrumented through Input Channel 2 and filtered can be written as $y = \kappa B\sin(\omega t - \varphi_0)$, in which φ_0 is the phase lag from the physical signal, and κ is the factor of the amplitude change. The phase delay $\varphi_0 - \varphi_1$ is regarded to be caused by the bandpass filter and actuator dynamics.

In order to compensate the phase lag φ_0, a PI manipulation using two parameters a and b is then applied to the signal from Input Channel 1, so that the measured signal by input channel 2 is expected as same as the original physical signal $y = B\sin(\omega t)$. The process is shown in Figure 7.3.

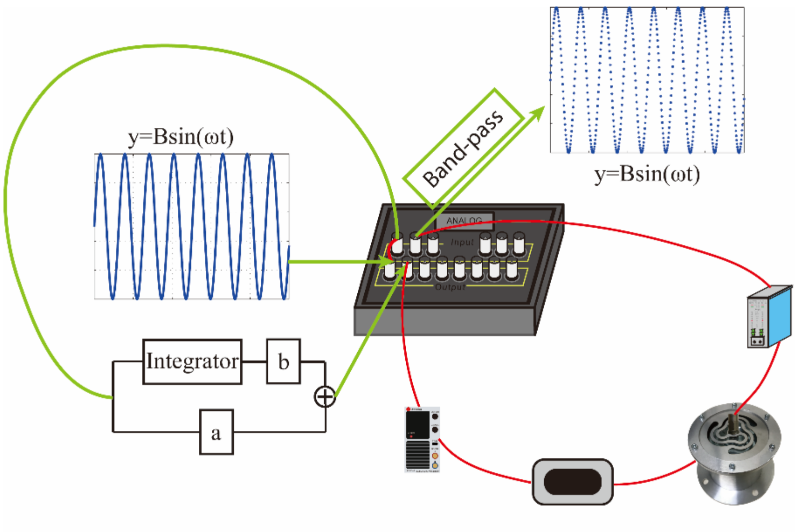

Figure 7.3 Signal after phase compensation

Two techniques to automatically search for the appropriate values of the parameters a and b are developed. The only information required is the modal frequencies of the control modes. The proposed techniques do not require any accurate model of the actuator nor information regarding other dynamic components of the control system.

As the first step, the discrete time data of the measured signal is expressed as sinusoidal signals with the offset A_{off}, amplitude A_{amp}, frequency ω and phase φ by:

$$y = A_{off} + A_{amp}\sin(\omega t + \varphi) \tag{7-5}$$

in which ω should be set equal to the natural frequency of the mode to be controlled because of the linear time invariant characteristics of the system as assumed in assumption 4). The identification of the other three parameters A_{off}, A_{amp} and φ is achieved by nonlinear parameter fitting with the Lebenberg-Marquardt algorithm (LMA) [102]. Appendix C shows a brief introduction of the LMA. The identified A_{off} can be subtracted from the measured signal during tests to obtain unbiased signal to be used in the ensuing signal processing. This operation is trivial and A_{off} will not be mentioned in the discussion that follows.

The process of the standard phase compensation is shown as follows:

Step 1: A sinusoidal signal with amplitude A, expressed by $y = A\sin(\omega t)$, is assumed to be generated at the Output Channel 1 for a short duration of time. Therefore, the signal measured at Input Channel 1 is $y = A\sin(\omega t - \varphi_1)$. Meanwhile, the signal measured at Input Channel 2, including the dynamics of the bandpass filter and the actuator, is expressed as $y = B\sin(\omega t - \varphi_0)$. The amplitude B, and the phase lags $\varphi_1$and φ_0 are identified by LMA.

Step 2: A sinusoidal signal with the identified amplitude B, expressed by $y = B\sin(\omega t)$, is then generated at Output Channel 1 for a short duration of time. The same process as Step 1 is applied, and the signals are measured at Input Channel 1 and Input Channel 2 as $y = B\sin(\omega t - \varphi_1)$ and $y = C\sin(\omega t - \varphi_0)$, respectively.

Step 3: The signal $y = B\sin(\omega t)$ is assumed as the target signal, in order to obtain $y = B\sin(\omega t)$ at Output Channel 2, the signal that should be generated at Output Channel 2, from Step 1, is $y = A\sin(\omega t + \varphi_0)$. The parameters a and b should satisfy the following equation:

$$a * B\sin(\omega t - \varphi_1) + \mathrm{b} * \mathrm{Int}\big(B\sin(\omega t - \varphi_1)\big) = A\sin(\omega t + \varphi_0) \tag{7-6}$$

where $\mathrm{Int}\big(B\sin(\omega t - \varphi_1)\big)$ denotes the integration of signal $B\sin(\omega t - \varphi_1)$. Substitution of $\mathrm{Int}\big(B\sin(\omega t - \varphi_1)\big) = -B\cos(\omega t - \varphi_1)/\omega$ into Eq. (7-6) yields:

$$a * B\sin(\omega t - \varphi_1) - \frac{b * B}{\omega}\cos(\omega t - \varphi_1) = A\sin(\omega t + \varphi_0) \tag{7-7}$$

From the basic sine and cosine of sum identities, $a * B = A\cos(\varphi_0 + \varphi_1)$ and $-b * \frac{B}{\omega} = A\sin(\varphi_0 + \varphi_1)$. Therefore, the parameters a and b are found to be:

$$a = \frac{A\cos(\varphi_0 + \varphi_1)}{B} \tag{7-8}$$

$$b = -\frac{A * \omega\sin(\varphi_0 + \varphi_1)}{B} \tag{7-9}$$

Table 7.1 – Theoretical procedure of phase compensation

Procedure	Output Channel	Input Channel 1	Input Channel 2
Step 1	$y = A\sin(\omega t)$	$y = A\sin(\omega t - \varphi_1)$	$y = B\sin(\omega t - \varphi_0)$
Step 2	$y = B\sin(\omega t)$ (Target)	$y = B\sin(\omega t - \varphi_1)$	$y = C\sin(\omega t - \varphi_0)$
Calculate a and b by Eqs. (7-8) and (7-9).			
Step 3	$y = A\sin(\omega t + \varphi_0)$		$y = B\sin(\omega t)$

Table 7.1 shows the corresponding mathematical expressions for the signals in the procedure.

Step 4: The actuator is connected to Output Channel 2. The PI compensation scheme using the computed a and b is applied to the assumed input $y = B\sin(\omega t)$, and the resulting signal is generated at Output Channel 2 for a short duration of time to excite the actuator. Because of inherent nonlinear characteristics in the control system and the difference between the ideal integrator and the implemented integrator (with intentionally added high pass characteristics to remove the DC bias from the output), the measured signal at Input Channel 2, in general, will not be exactly equal to $y = B\sin(\omega t)$, and turns out to be, say, $y = B_1\sin(\omega t - \varphi_2)$, where B_1 is the amplitude and φ_2 is the phase lag. Replacing φ_0 with $\varphi_0 + \varphi_2$ and B with B_1, the updated values of the parameters a and b are computed by Eqs. (7-8) and (7-9). This process is repeated until the conditions $\varphi_2 = 0$ and $B_1 = B$ are acceptably satisfied. The final a and b are used to the phase compensation.

Step 5: The procedure Step 1 through Step 4 is repeated for all the control modes to find the PI parameters a and b for each mode.

7.2.2 Modified phase compensation

Due to the transient nature of the response generated by individual dynamic components as well as unexpected outside disturbances, the sinusoidal signals obtained by curve fitting, with the signal measured from Input Channel 2 and filtered with the bandpass filter may be different every time even for the same input signal. Therefore, it may take several times of repetition in Step 4 until the convergence of the parameters a and b is achieved.

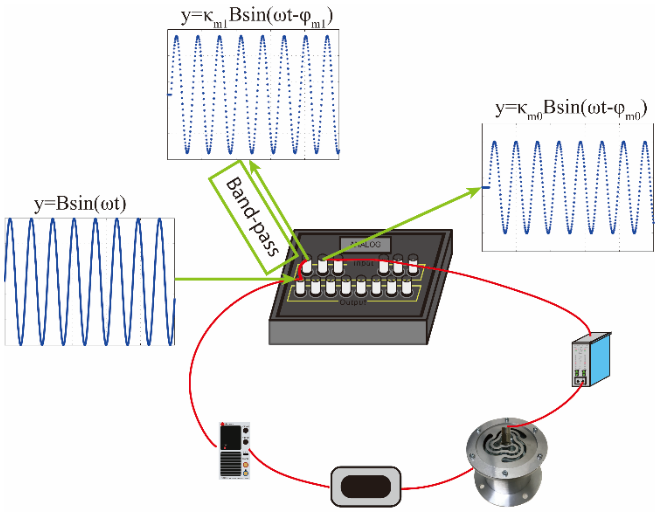

Figure 7.4 Signal before phase compensation (modified)

In order to circumvent the problem of such a situation, a modified version of the phase compensation procedure incorporating the bandpass filtering of the response measurement signal is developed. The details of this modified procedure are described as following:

The assumed process is shown in Figure 7.4. A sinusoidal signal $y = B\sin(\omega t)$ is generated at Output Channel 1, while the sinusoidal signal is monitored through the Input Channel 1, which is $y = B\sin(\omega t - \varphi_1)$. This signal at Output Channel 1 is connected to the actuator, and the actuator mass acceleration measurement signal is connected to Input Channel 2. It is assumed that the measurement signal at Input Channel 2 is expressed by $y = \kappa_{m0} B\sin(\omega t - \varphi_{m0})$, where κ_{m0} is a constant to represent the amplitude factor, and φ_{m0} is a phase lag. Then, the monitored signal of Input Channel 1 is manipulated with a bandpass filter and the filtered signal is assumed to be expressed by $y = \kappa_{m1} B\sin(\omega t - \varphi_{m1})$, where κ_{m1} is a constant, and φ_{m1} is a phase lag.

The process is shown in Figure 7.5. If the bandpass filter is applied to the measured signal at Input Channel 1, the total phase delay is expected to be $\varphi_{m0} + \varphi_{m1} - \varphi_1$. In order to compensate this delay, the PI manipulation scheme with the parameters a and b is applied to the signal measured at Input Channel 1, and the resulting signal is generated at Output Channel 2, which is connected to the actuator. In this case, the measured signal at Input Channel 2 is expected to be $y = \frac{B}{\kappa_{m1}}\sin(\omega t + \varphi_{m1} - \varphi_1)$. The procedure to find the parameters a and b such that the measured signal at Input Channel 2 be $y = \frac{B}{\kappa_{m1}}\sin(\omega t + \varphi_{m1} - \varphi_1)$ can be described as follows:

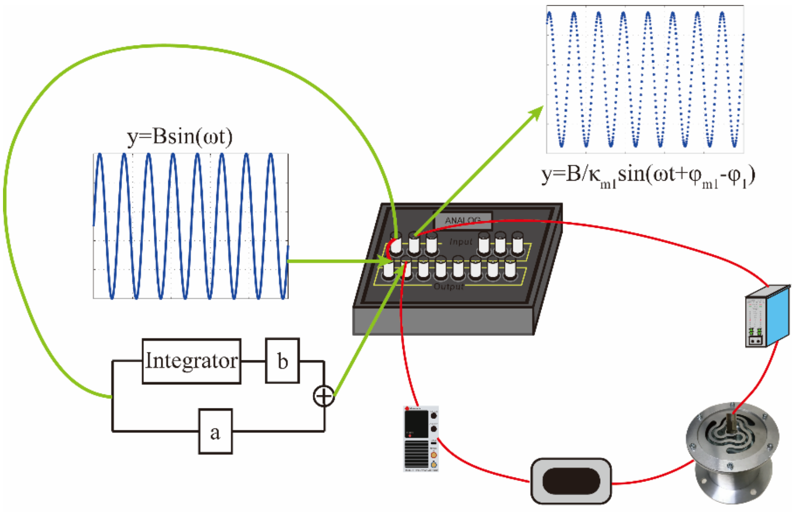

Figure 7.5 Signal after phase compensation (modified)

Step 1: A sinusoidal signal with the amplitude A, expressed as $y = A\sin(\omega t)$, is assumed to be generated by the Output Channel 1, which is connected to the actuator, for a short duration of time. Then the signals measured at Input Channel 1 and Input Channel 2 are $y = A\sin(\omega t -$

$\varphi_1)$ and $y = B\sin(\omega t - \varphi_{\mathrm{m0}})$, respectively. The signal $y = A\sin(\omega t - \varphi_1)$ goes through a pre-defined bandpass filter and the resulting signal is $y = \kappa_{m1} A\sin(\omega t - \varphi_{\mathrm{m1}})$. The amplitude B, the scalar κ_{m1} and the phase lags φ_1, φ_{m0} and φ_{m1} are identified by LMA.

Step 2: A sinusoidal signal with amplitude B, expressed as $y = B\sin(\omega t)$, is then generated at Output Channel 1 for the short duration of time. The signals measured by Input Channel 1 and Input Channel 2 are $y = B\sin(\omega t - \varphi_1)$ and $y = C\sin(\omega t - \varphi_{\mathrm{m0}})$, respectively.

Step 3: The signal $y = B\sin(\omega t)$ is assumed as the target signal. In order to obtain the signal $y = \frac{B}{\kappa_{m1}}\sin(\omega t + \varphi_{m1} - \varphi_1)$ at Input Channel 2, the signal that should be generated at Output Channel 2 is $y = \frac{\varphi}{\kappa_{m1}}\sin(\omega t + \varphi_{m0} + \varphi_{m1} - \varphi_1)$. The parameters a and b are to be determined to satisfy:

$$a * B\sin(\omega t - \varphi_1) + b * \mathrm{Int}\big(B\sin(\omega t - \varphi_1)\big) = \frac{A}{\kappa_{m1}}\sin(\omega t + \varphi_{\mathrm{m0}} + \varphi_{m1} - \varphi_1) \tag{7-10}$$

Substitution of $\mathrm{Int}\big(B\sin(\omega t - \varphi_1)\big) = -\mathrm{B}\cos(\omega t - \varphi_1)/\omega$, into Eq. (7-6) yields:

$$a * B\sin(\omega t - \varphi_1) - \frac{b * B}{\omega}\cos(\omega t - \varphi_1) = \frac{A}{\kappa_{m1}}\sin(\omega t + \varphi_{\mathrm{m0}} + \varphi_{m1} - \varphi_1) \tag{7-11}$$

From the basic sine and cosine of sum identities, $a * B = \frac{A}{\kappa_{m1}}\cos(t_{\mathrm{m0}} + \varphi_{m1})$ and $-b * \frac{B}{\omega} = \frac{A}{\kappa_{m1}}\sin(\varphi_{\mathrm{m0}} + \varphi_{m1})$. Therefore:

$$a = \frac{A\cos(\varphi_{\mathrm{m0}} + \varphi_{m1})}{B\kappa_{m1}} \tag{7-12}$$

$$b = -\frac{A * \omega\sin(\varphi_{\mathrm{m0}} + \varphi_{m1})}{B\kappa_{m1}} \tag{7-13}$$

Step 4: The actuator is connected to Output Channel 2. The PI compensation scheme using the computed *a* and *b* is applied to the assumed input $y = B\sin(\omega t)$, and the resulting signal is generated at Output Channel 2 for a short duration of time to excite the actuator. The measured signal at Input Channel 2 in Step 3, in general, will not be exactly equal to $y = \frac{B}{\kappa_{m1}}\sin(\omega t + \varphi_{m1} - \varphi_1)$ due to the nonlinearity and transient nature of the response, and turns out to be, say, $y = \frac{B_1}{\kappa_{m1}}\sin(\omega t + \varphi_{m1} - \varphi_1 - \varphi_2)$, where B_1 is the amplitude and φ_2 is the phase lag. Replacing φ_1 with $\varphi_1 + \varphi_2$ and B with B_1, the updated values of parameters *a* and *b* are computed by Eqs. (7-12) and (7-13). This process is repeated until the conditions $\varphi_2 = 0$

and $B_1 = B$ are acceptably satisfied. The final a and b are used as the parameters in the phase compensation.

Step 5: The procedure Step 1 through Step 4 are repeated for all the control modes to find the PI parameters a and b for each mode.

7.2.3 Examples

Some example tests are shown to illustrate the previously described procedures. In the example tests, the actuator is attached on a rigid fixed base.

7.2.3.1 Standard procedure case

It is assumed that a structure to be controlled has a modal natural frequency of 50Hz. The cut-off frequencies for the high pass filter and low pass filter are 10Hz and 200Hz, respectively. The sampling rate used in the DSP system is 1000Hz.

As the first step, a signal $y = 0.03\sin(100\pi t)$ is generated at the Output Channel 1 for 0.2s and the measured signal at Input Channel 1 is shown in Figure 7.6. The actuator response to the signal of the Output Channel 1, measured at Input Channel 2 is shown in Figure 7.7. The filtered actuator response measurement signal is shown Figure 7.8. Note that the LMA works very well to regress the discrete signals even with the presence of transient responses. Based on the results of LMA, the identified response amplitude and phase lags are $\mathrm{B} = 0.0597\mathrm{V}$, $\varphi_1 = 0.3125\mathrm{rad}$ and $\varphi_0 = 0.5414\mathrm{rad}$.

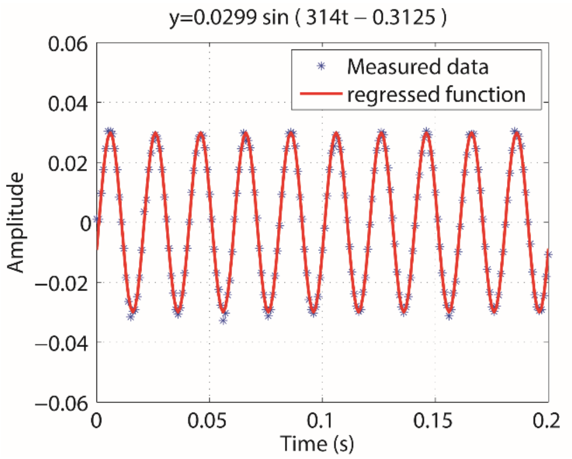

Figure 7.6 Step 1 – input channel 1 (standard)

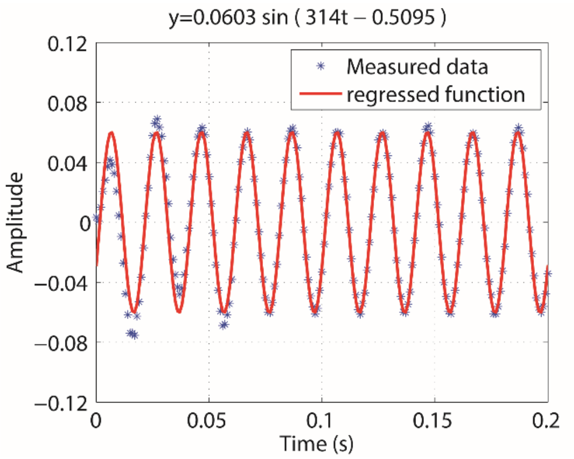

Figure 7.7 Step 1 – input channel 2 (standard)

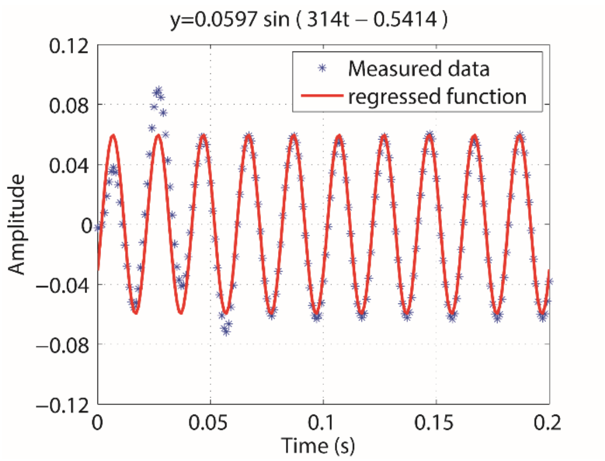

Figure 7.8 Step 1 – filtered data (standard)

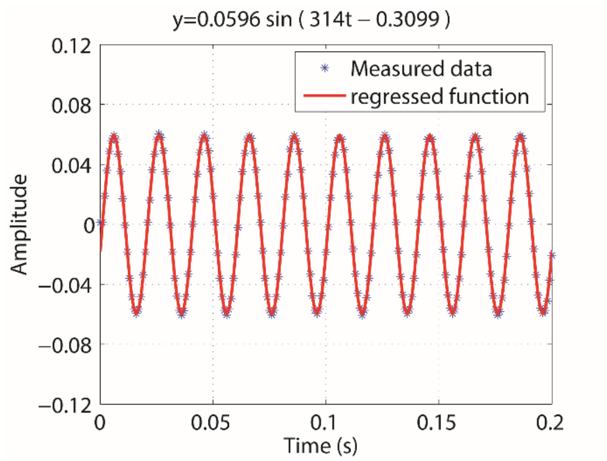

Figure 7.9 Step 2 – input channel 1 (standard)

In Step 2, the signal $y = 0.0597\sin(100\pi t)$ is generated at Output Channel 1 for the same duration of 0.2s. The signal measured at Input Channel 1 is shown in Figure 7.9. It is found that the phase lag $\varphi_1 = 0.3099$ identified by LMA are almost equal to $\varphi_1 = 0.3125$ obtained in Step 1. In Step 3, firstly, discrete time integration of the measured signal obtained in Step 2 is computed, as shown in Figure 7.10. The values of PI parameters a and b can be calculated using Eqs. (7-8) and (7-9). Then the result of PI compensation with the determined parameters is obtained, as shown in Figure 7.11.

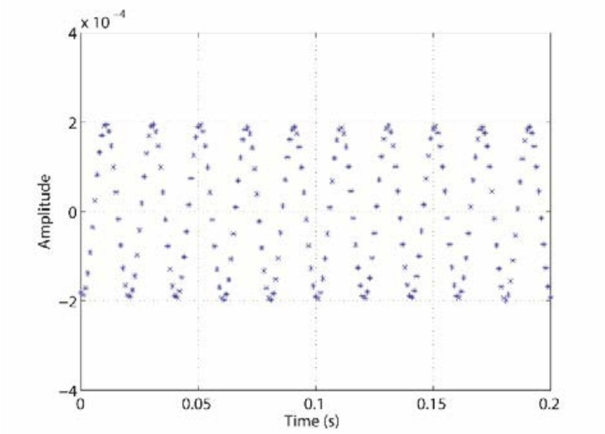

Figure 7.10 Step 3 – Integrated data (standard)

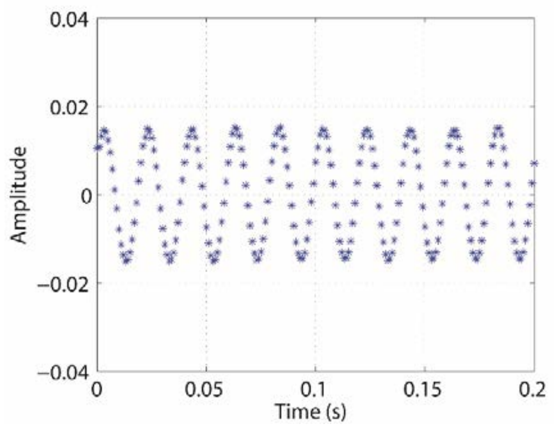

Figure 7.11 Step 3 – Synthesized data after PI (standard)

The result of PI compensation is provided to the actuator. The measured actuator response is filtered with the bandpass filter (10-200Hz). The output of the bandpass filter is shown in Figure 7.12.

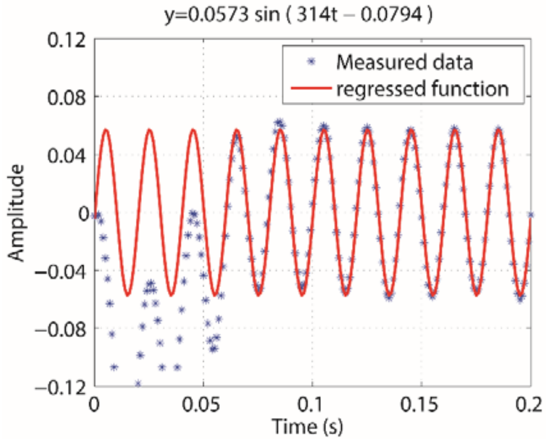

Figure 7.12 Step 3 – filtered data (standard)

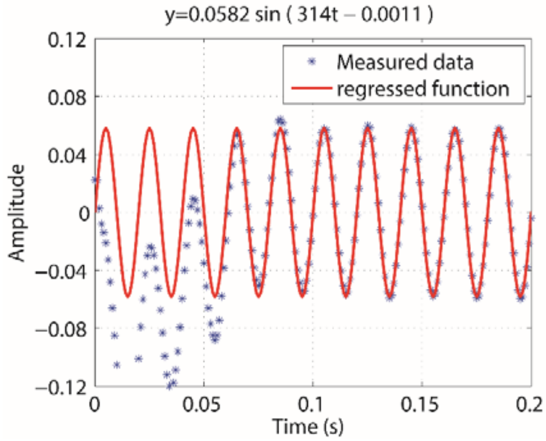

Figure 7.13 Step 4 – filtered data (standard)

From Figure 7.12, it is found that there still exists a phase lag of 0.0794rad. The final results of the repetition in Step 4 are shown in Figure 7.13, where the phase lag becomes as small as 0.0011rad. The PI parameters are calculated as $a = 0.37$ and $b = -115.21$.

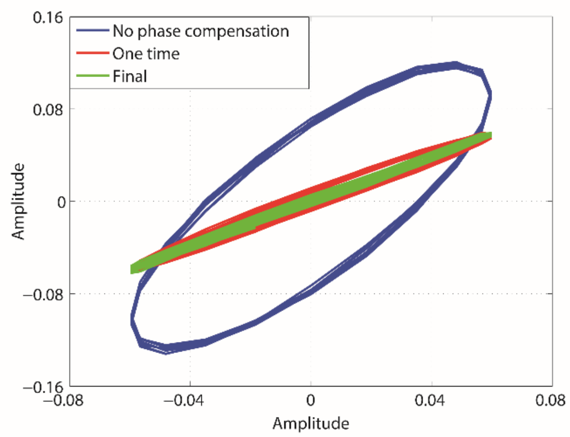

Figure 7.14 Lissajous curves

The plot of the Lissajous curve between the target and filtered actuator response signals is an ellipse with a phase difference involved in two signals, while the curve becomes a straight line when the phase difference is zero. The Lissajous curves for no phase compensation, phase compensation with one-time parameter calculation and the phase compensation with final parameters are shown in Figure 7.14. It is observed that the curve for the final phase compensation case becomes almost a straight line.

7.2.3.2 Modified procedure case

A controlled mode with a natural frequency of 50Hz is also assumed. The cut-off frequencies for the high pass filter and low pass filter are 10Hz and 200Hz, respectively. The sampling rate in the DSP system is 1000Hz.

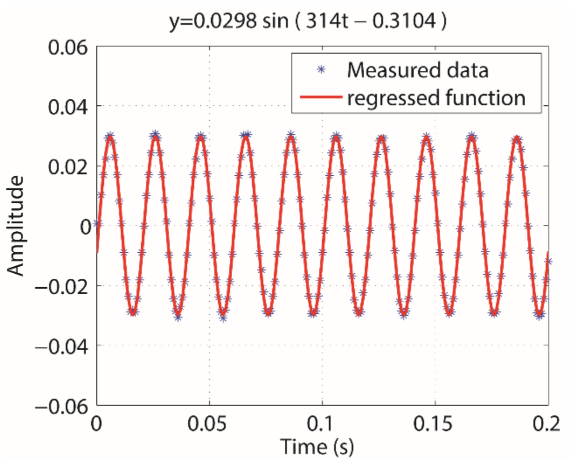

Figure 7.15 Step 1 – input channel 1 (modified)

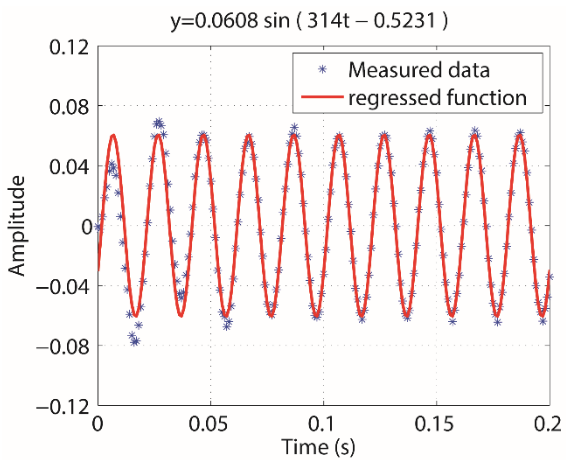

Figure 7.16 Step 1 – input channel 2 (modified)

As the first step, a signal $y = 0.03\sin(100\pi t)$ is generated at Output Channel 1 for 0.2s. The signal measured at Input Channel 1 is shown in Figure 7.15. The measured signal of the actuator response is shown in Figure 7.16. The Input Channel 1 signal processed with the bandpass filter is shown in Figure 7.17.

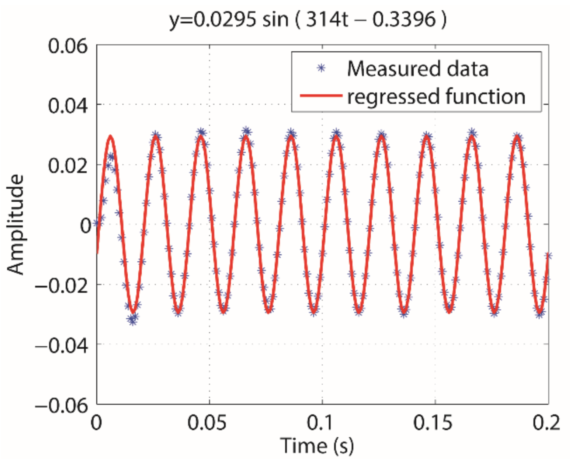

Figure 7.17 Step 1 – filtered data (modified)

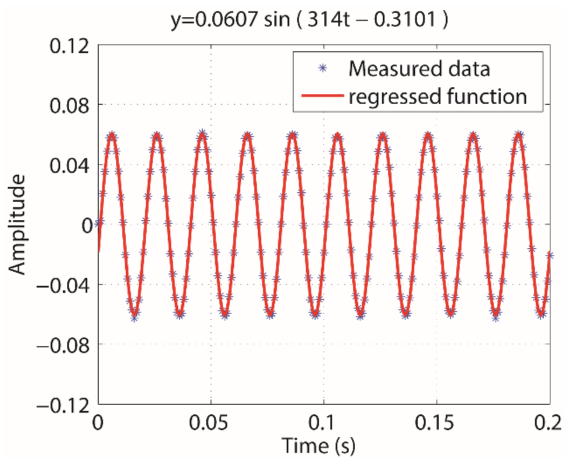

Figure 7.18 Step 2 – input channel 1 (modified)

Based on the results of LMA, identified amplitude parameters and time delays are $\mathrm{B} = 0.0608\mathrm{V}$, $\kappa_{m1} = 0.099, \varphi_1 = 0.3104\mathrm{rad}, \varphi_{\mathrm{m1}} = 0.3396\mathrm{rad}$ and $\varphi_{\mathrm{m0}} = 0.5231\mathrm{rad}$. The total phase lag $(\varphi_{m0} + \varphi_{m1} - \varphi_1)$ is 0.5523rad, which is almost equal to the total phase lag $\varphi_0 = 0.5414\mathrm{rad}$ for the standard case.

In Step 2, the signal $y = 0.0608\sin(100\pi t)$ is generated at Output Channel 1 for 0.2s. The measured signal at Input Channel 1 is shown in Figure 7.18.

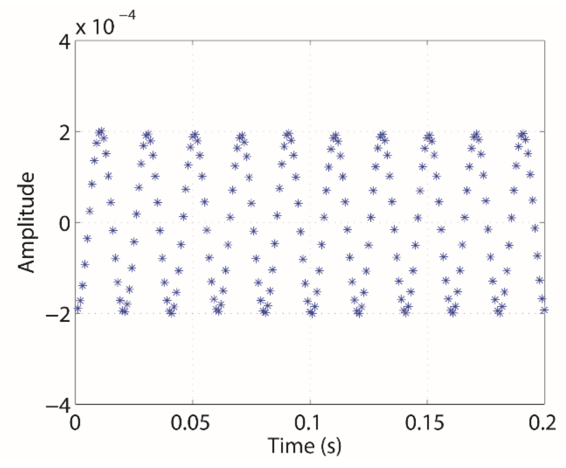

Figure 7.19 Step 3 – Integrated data (modified)

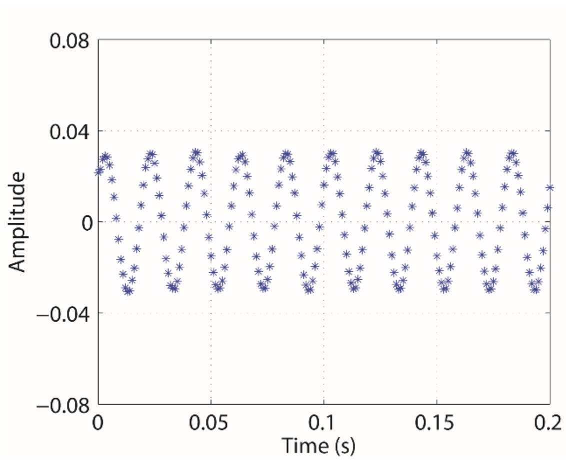

Figure 7.20 Step 3 – Synthesized data after PI (modified)

In Step 3, discrete time integration of the measured signal obtained in Step 2 is computed first, as shown in Figure 7.19. The values of the PI parameters *a* and *b* are calculated using Eqs. (7-12) and (7-13). The result of PI compensation is shown in Figure 7.20.

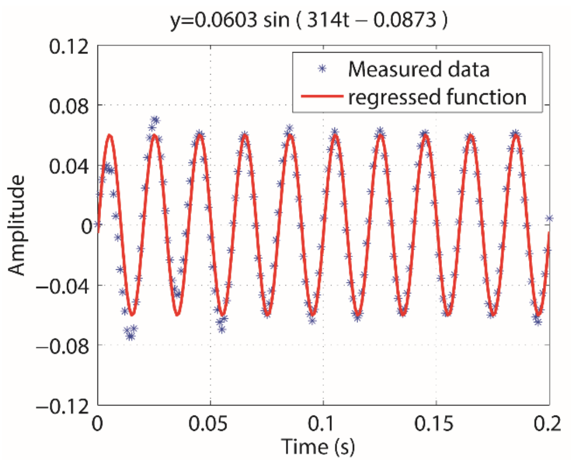

Figure 7.21 Step 3 – input channel 2 (modified)

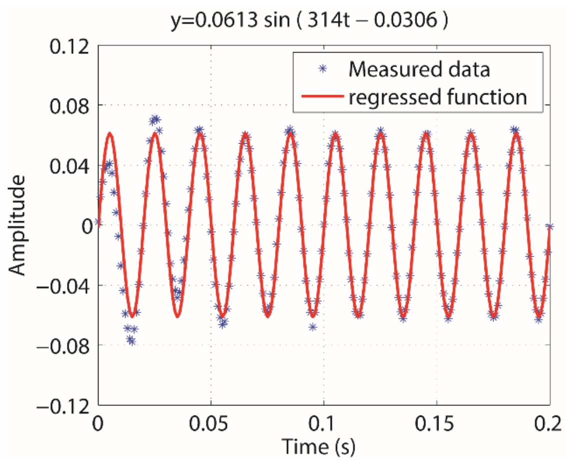

Figure 7.22 Step 4 – input channel 2 (modified)

The result of PI compensation is provided to the actuator. The measured actuator response at Input Channel 2 is shown in Figure 7.21.

Base on the algorithm of the modified phase compensation, the measured signal at Input Channel 2 is expected to have a phase lag of $\varphi_{\mathrm{m}1} - \varphi_1 = 0.0292$rad, while it is found that there still exists a phase lag of $0.0873 - 0.0292 = 0.0581$rad, as shown in Figure 7.21. The final results of the repetition in Step 4 are shown in Figure 7.22, where the phase lag becomes as small as 0.0014rad. The PI parameters are calculated as $a = 0.36$ and $b = -116.78$.

From the example tests, it is verified the PI parameters can be successfully determined by both of the phase compensation techniques. The standard phase compensation procedure is straightforward and comprehensible. The calculation involved in this method is simple as well. Furthermore, the Lissajous curve can be directly used to check the accuracy of the result. On the other hand, if the original signal is processed by high order dynamic component, a severe effect of transient response may be involved in the processed signal as shown in Figure 7.12, and this effect may degrade the applicability of the LMA. The modified phase compensation is advantageous in improved stability owing to division of the dynamic component into two parts for the PI parameter search, although the calculation is more complicated and the Lissajous curve cannot be directly used to check the results.

7.2.4 Phase control

In the above analysis, the time delay caused by the dynamic components is compensated using the proposed phase compensation techniques. Therefore, the damping ratio of the control mode is expected to be increased without significantly affecting the natural frequency with the MDVF control. However, it is preferable to introduce a small amount of time lag such that the modal frequency be increased because increase of modal frequency and modal damping is known to be effective in reducing the settling time of the said mode. The phase compensation techniques can also be used for this purpose.

If the time delay to be introduced to the control mode is φ_{lag} ($\varphi_{lag} > 0$), the total compensated phase in Figure 7.2 will be $\varphi_0 - \varphi_{lag}$, as shown in Figure 7.23. If the same PI manipulation is applied to the target signal to compensate the time lag $\varphi_0 - \varphi_{lag}$, the measurement signal at Input Channel 2 is expressed by $y = B\sin(\omega t - \varphi_{lag})$, as shown in Figure 7.24.

The standard and modified phase compensation techniques described in Sec. 7.2.1 and Sec. 7.2.2 can be used for the PI parameter search.

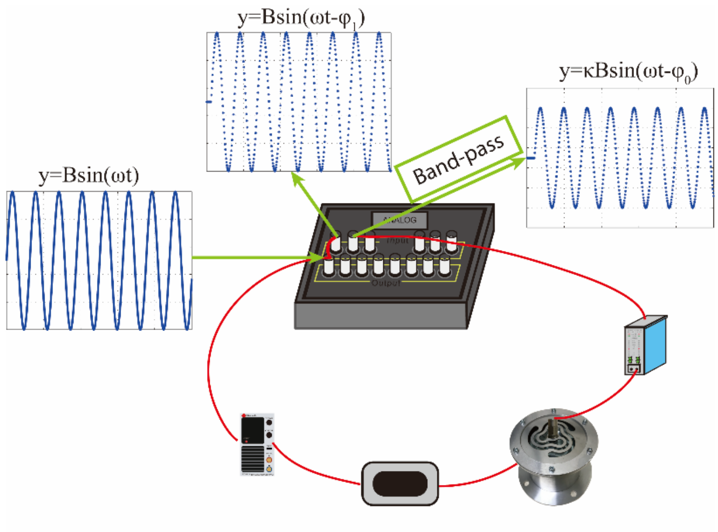

Figure 7.23 Signal before phase compensation (phase control)

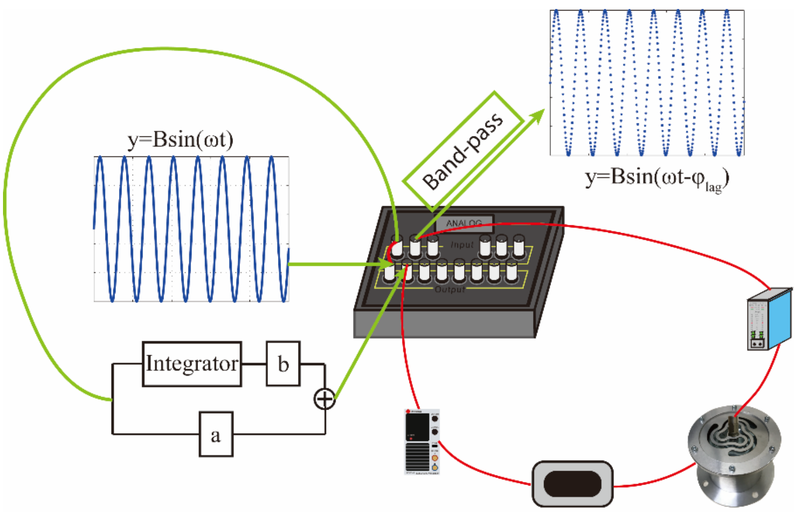

Figure 7.24 Signal after phase compensation (phase control)

7.3 Design process

The steps of the procedure to apply the independent modal space phase compensated velocity feedback control can be summarized follows:

1) Identify the dynamic properties of the floor and to determine the modal frequencies, modal damping ratios and mode shapes of individual modes which are in the frequency range of interest. Based on the information, select the cut-off frequencies for the band-pass filters.

2) Determine the number of modes to be controlled and the number of sensors and actuators to be used.
3) Determine the locations of the sensors and actuators based on the procedure described in Chapter 5 and calculate the modal filtering matrix.
4) Determine the PI parameters for all the control modes and actuators using the techniques described in Sec. 7.2. It is recommended to use the modified phase compensation if a number of high-order dynamic components are involved.
5) Tune the control gains according to the stability condition and control performance. Non-linear actuator saturation must be considered when choosing the control gains as well.

7.4 Verification test

This section presents the design and practical implementation of the PCVFB control system based on the process described in Sec. 7.3 for the steel plate test setup.

The identified modal frequencies, modal damping ratios and mode shapes of the five modes in the frequency range between 0Hz and 200Hz are already shown in Table 4.4 and Table 4.5. The cut-off frequencies for the high pass filter and low pass filter are 20Hz and 200Hz, respectively. The determined coefficients for the two-pole Butterworth bandpass filter are shown in Table 7.2. (Step 1))

Table 7.2 – Coefficients for the bandpass filter

	a_0	a_1	a_2	b_1	b_2
High-pass	0.915	-1.830	0.915	1.823	-0.837
Low-pass	0.207	0.413	0.207	0.370	-0.196

As Step 2), the 1st, 2nd and 3rd modes are selected to as the modes to be controlled, and four sensors and one actuator are used for the active control implementation. During the phase compensation tests, one more sensor is used to measure the response of the actuator.

Following Step 3), the placement of sensors and actuator is determined as shown in Figure 5.16. The corresponding modal filter coefficients are shown in Table 6.3.

7.4.1 Controller design

In this sub-section, the PI parameters *a* and *b* for the lowest three modes of the steel plate are identified following the procedure described in Sec. 7.2.

The actuator is attached on the steel plate during the PI parameter search. Since the modal frequencies has already been obtained, the PI parameters can be determined in an automatic manner. The results with and without the bandpass filter are shown in Table 7.3 and Table 7.4, respectively.

Table 7.3 – PI parameters (without bandpass)

	Mode 1	Mode 2	Mode 3
a	0.5341	0.2428	-1.0993
b	-206.74	-630.56	-377.67

Table 7.4 – PI parameters (bandpass)

	Mode 1	Mode 2	Mode 3
a	0.7985	-0.2537	-1.2028
b	-107.47	-739.54	832.45

It should be noted that the parameters a and b are both negative for the third mode without bandpass filter and the second mode with the bandpass filter. It implies that the phase lags between the target signal and the actuator response are larger than $\pi/2$ in these cases, based on Eqs. (7-8) and (7-9). For a similar reason, the phase lag is larger than π for the third mode with the bandpass filter.

The final step for the controller setup is tuning the control gains for the three control modes using a repetitive procedure, in which the vibration of the plate induced by an impact load by the hammer is measured, and the values of the gains of the control modes are incrementally increased, until the system becomes unstable. When instabilities occur, the tuning process is completed. The reasonable gains can be determined as the ones used in the latest stable case.

7.4.2 Impact loading test

7.4.2.1 Modal direct velocity feedback control with bandpass filter

In this section, the control performance of the MDVF controller with the bandpass filter is investigated. For simplification, only the control results of Point 31 will be shown. Refer to Figure 6.22 through Figure 6.39 regarding the test results on the reduction effects of the MDVF controller without bandpass filtering.

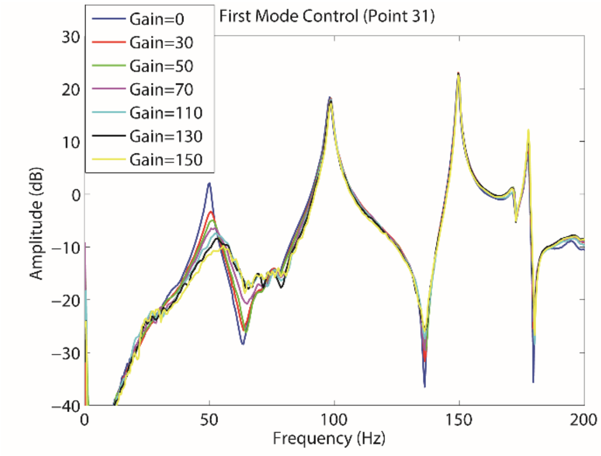

Figure 7.25 First mode control using MDVF with bandpass filter for different control gains (Point 31)

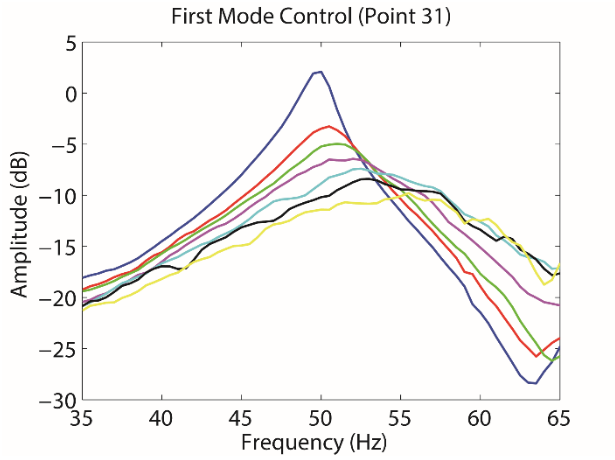

Figure 7.26 First mode control (Point 31)

The frequency response functions of the first mode control are shown in Figure 7.25. Figure 7.26 shows the zoom-in view of the first mode (from 35Hz to 65Hz) and the changes of the modal frequency and damping ratio. Firstly, it can be observed that the damping ratio and natural frequency of the first mode increased with the increase of the control gain. By comparison of Figure 7.26 with Figure 6.26, the first mode natural frequency in Figure 7.26 does not change as much as that in Figure 6.26. This improved result is the effect of bandpass filter, which provides a phase lead to the first mode (the phase lead caused by the high pass filter is larger than the phase lag caused by the low pass filter). Figure 7.27 shows the spectrum of the corresponding DSP outputs. Because of the use of the two-pole Butterworth low pass filter with a cut-off frequency of 200Hz, the spillover effect of the seventh (230Hz) mode is decreased compared with the case without the low pass filter, as shown in Figure 6.52. However, it can be observed that the spillover effect is still significant. For a better control performance, it is expected either to use a lower cut-off frequency or to choose a higher-pole Butterworth low pass filter. From Figure 7.27, it can also be found that the low frequency noise is significantly decreased because of the use of the high pass filter.

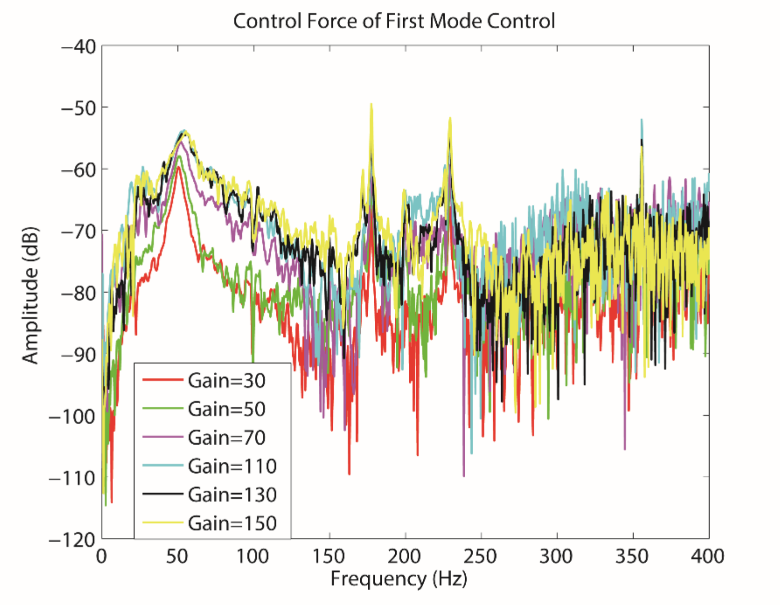

Figure 7.27 Spectra of control force outputs for different control gains (first mode)

Figure 7.28 shows the frequency response functions of the second mode control under different control gains and Figure 7.29 shows the corresponding zoom-in view of the second mode. Since the bandpass filter (the phase lead caused by the high pass filter is smaller than the phase lag caused by the low pass filter) introduces additional time delays to this mode, it is observed that the natural frequency increases while the damping ratio decreases as the control gain increases. This result indicates a poor control performance.

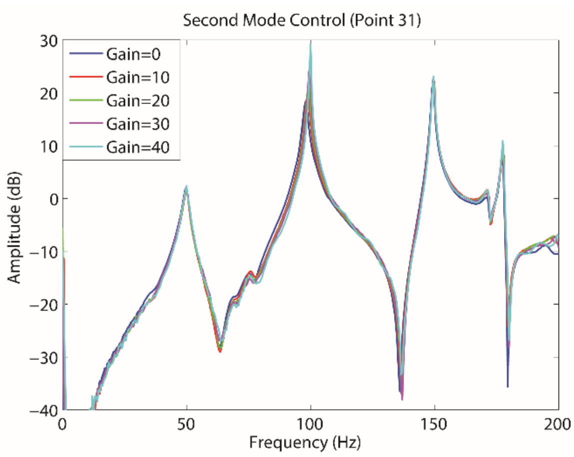

Figure 7.28 Second mode control using MDVF with bandpass filter for different control gains (Point 31)

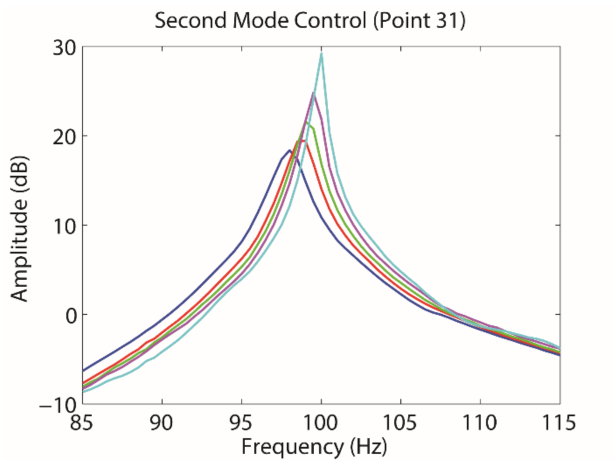

Figure 7.29 Second mode control (Point 31)

Figure 7.30 gives the spectrum of the DSP outputs of the second mode control. It can be observed that the spillover effects of the higher modes are minor.

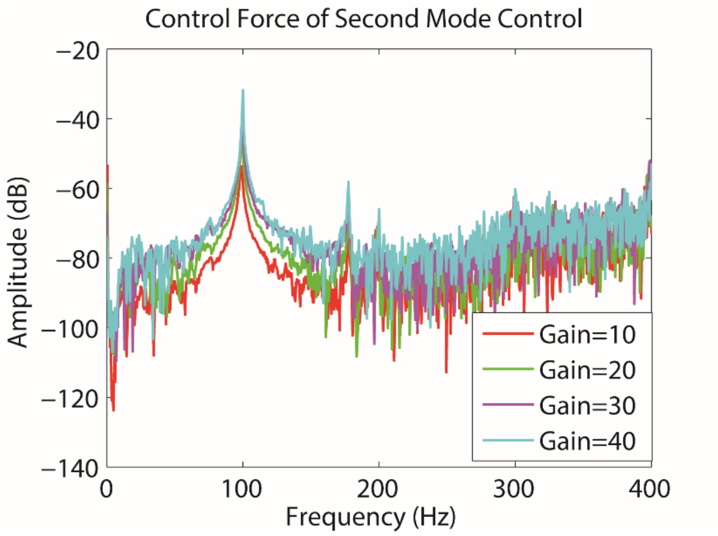

Figure 7.30 Spectra of control force outputs for different control gains (second mode)

Finally, the frequency response functions of the third mode control are shown in Figure 7.31. Figure 7.32 and Figure 7.33 show the zoom-in view of the third mode and the spectra of the corresponding DSP control outputs, respectively. As the bandpass filter (the phase lead caused by the high pass filter is smaller than the phase lag caused by the low pass filter) introduces a large phase delay to this mode, the damping ratio of the third mode reduces, and the system became unstable even when the control gain remains small. Application of the phase compensation technique is expected to be effecting in improving the control performance of the third mode. Also, it can be observed that the spillover effects of higher modes are very small in Figure 7.33.

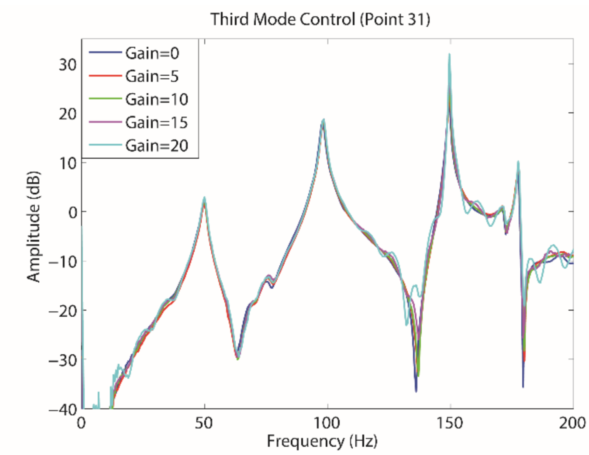

Figure 7.31 Third mode control using MDVF with bandpass filter for different control gains (Point 31)

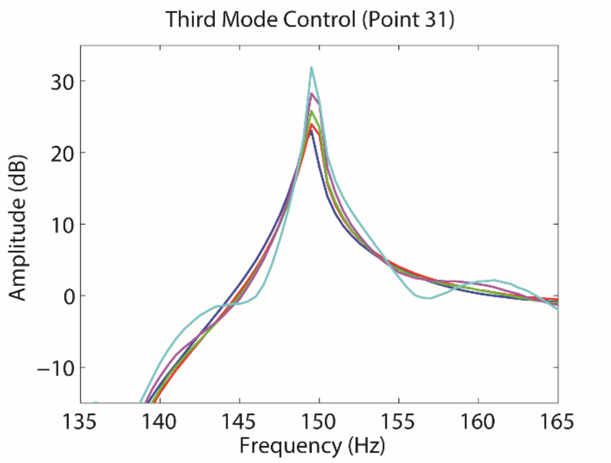

Figure 7.32 Third mode control (Point 31)

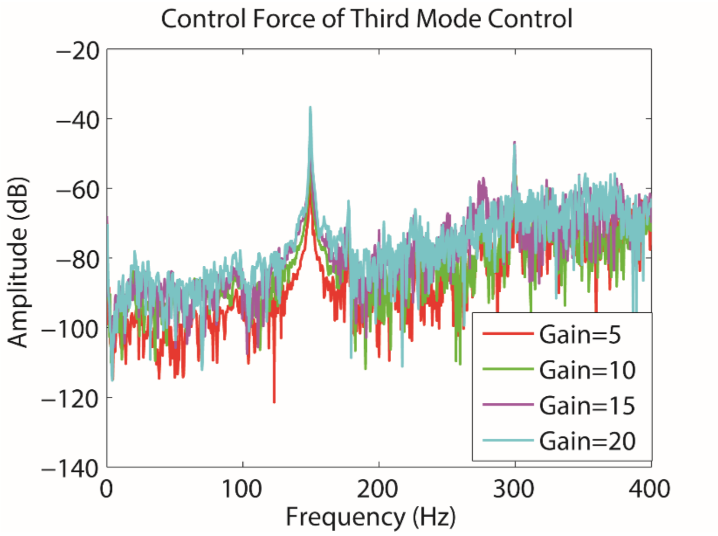

Figure 7.33 Spectra of control force outputs for different control gains (third mode)

These test results reveal that the traditional MDVF controller can successfully control only the first mode, while the performance of the second and third modes control is poor. Therefore, it is imperative to use the phase compensation technique in order to achieve a good control performance for all the control modes.

7.4.2.2 PCVFB control without bandpass filter

In this section, the tests of control using the PCVFB controller without bandpass filter is described. The PLVFB controller described in Chapter 6 is applied, and the phase-lag feedback controller is used for the third mode. The determined PI parameters for these tests are shown in Table 7.3.

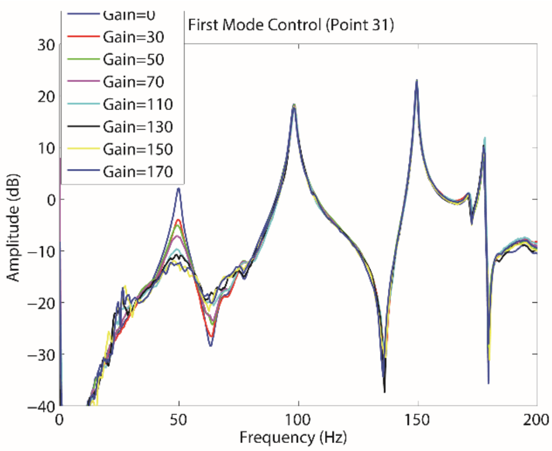

Figure 7.34 First mode control using PCVFB for different control gains (Point 31)

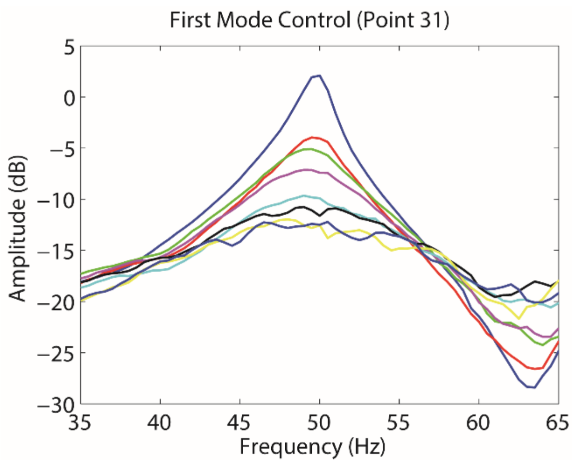

Figure 7.35 First mode control (Point 31)

Figure 7.34 shows the spectrum of the response at Point 31 when the PCVFB controller is applied for the first mode control and Figure 7.35 shows the zoom-in view of the first mode. As can be expected, the damping ratio of this mode considerably increased while the natural frequency does not significantly change as the control gain increases. By comparison of Figure 7.35 with Figure 6.26 and Figure 7.26, it can be noticed that the increase of the damping ratio is more efficient when using the PCVFB controller than the other two cases The root loci of the closed loop control systems also suggest the efficiency of PCVFB controller in enhancing the damping without significantly affecting the natural frequency.

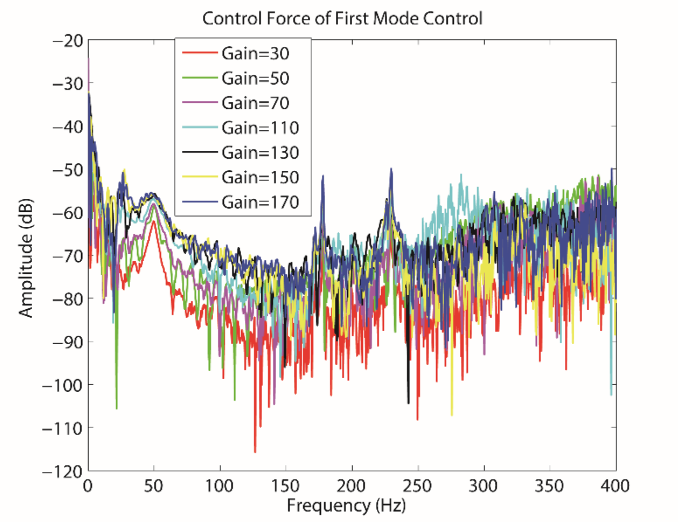

Figure 7.36 Spectra of control force outputs for different control gains (first mode)

The amplitude spectra of the DSP control outputs are shown in Figure 7.36. It can be observed that not only the spillover of the higher modes but also the low frequency noise is significant if the bandpass filter is not applied. A peak at around 20Hz can be seen and is found to become higher as the control gain increases. This is because the poles corresponding to the actuator move to left as the gain increases, and they eventually come close to the imaginary axis of the *s*-plane. If a higher control gain is adopted, stroke saturation or even system unstable is likely to be induced.

The results of the second mode control test are shown in Figure 7.37 and Figure 7.38. As can be anticipated, the control performance of the second mode is significantly improved and the amplitude of the peak of the second mode reduced by greater than 10dB.

The amplitude spectra of the DSP control outputs for the second mode control are shown in Figure 7.39. Similar to the first mode control case, significant low frequency noise is found. The control performance may be affected by the low frequency noise.

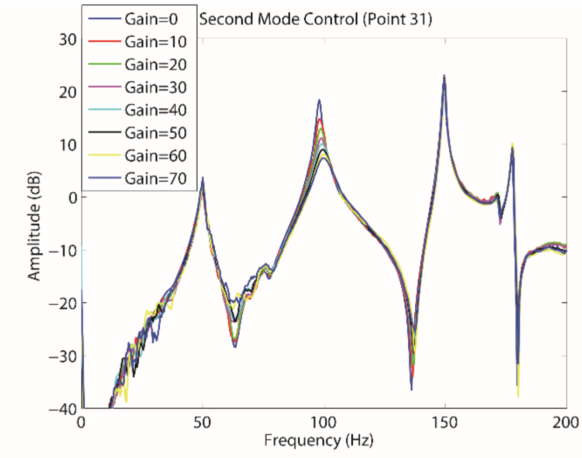

Figure 7.37 Second mode control using PCVFB for different control gains (Point 31)

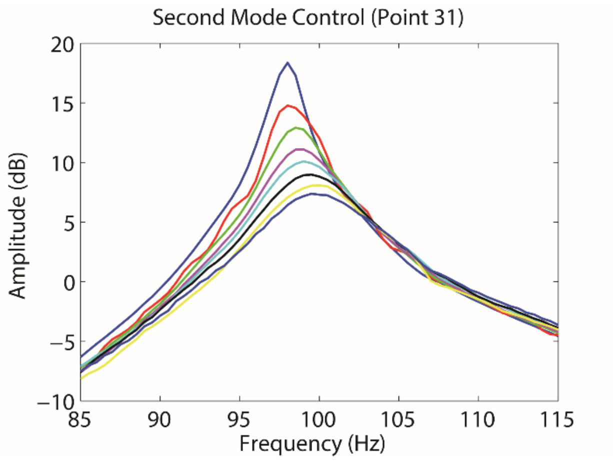

Figure 7.38 Second mode control (Point 31)

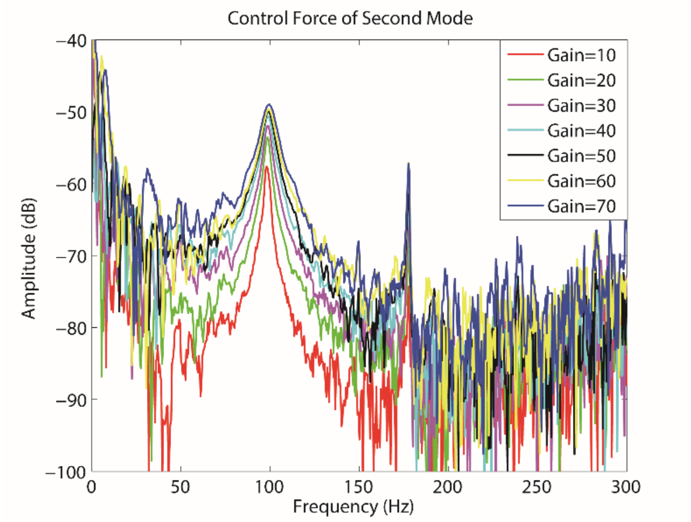

Figure 7.39 Spectra of control force outputs for different control gains (second mode)

Figure 7.40 and Figure 7.41 show the results of the third mode control using the PCVFB controller, and Figure 7.42 shows the corresponding DSP control outputs. Since the spillover of the seventh (230Hz) mode is severer than the spillover effects shown in Figure 7.33, use of the low pass filter is effective in reducing the spillover effects of the seventh mode. A high pass filter is also required to mitigate the effect of low frequency noise.

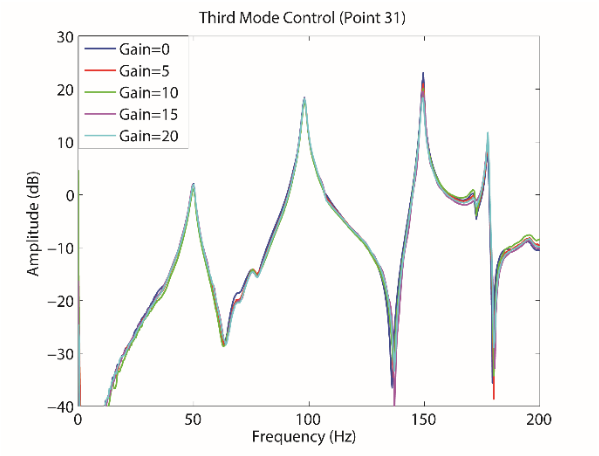

Figure 7.40 Third mode control using PCVFB for different control gains (Point 31)

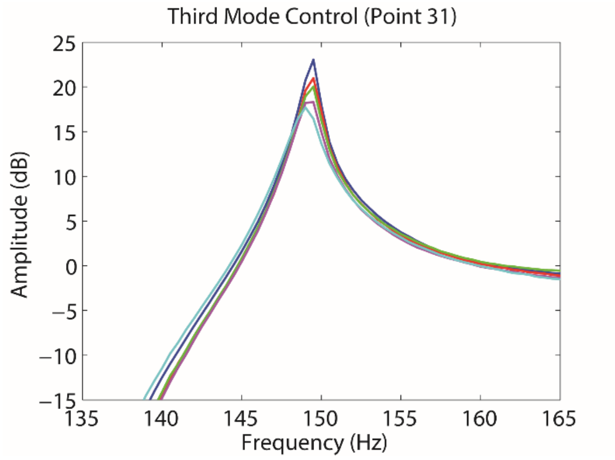

Figure 7.41 Third mode control (Point 31)

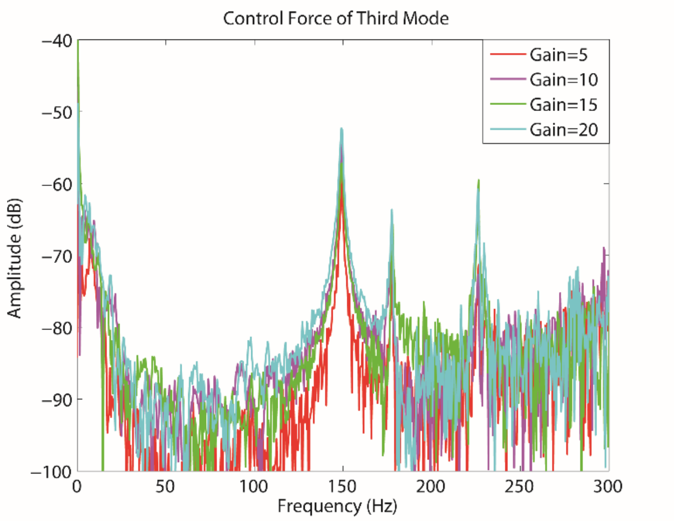

Figure 7.42 Spectra of control force outputs for different control gains (third mode)

From the above experiments, it is verified that the phase compensation technique perform well to compensate the time delays caused by the dynamic components and therefore improve the control performance in a great degree. However, based on the control outputs of the DSP, a bandpass filter is required for a better control performance.

7.4.2.3 PCVFB control with bandpass filter

Now it is time to examine the control performance using the PLVFB controller with bandpass filter. Modified phase compensation technique described in Sec. 7.2.2 is used to search the PI parameters and the results are shown in Table 7.4.

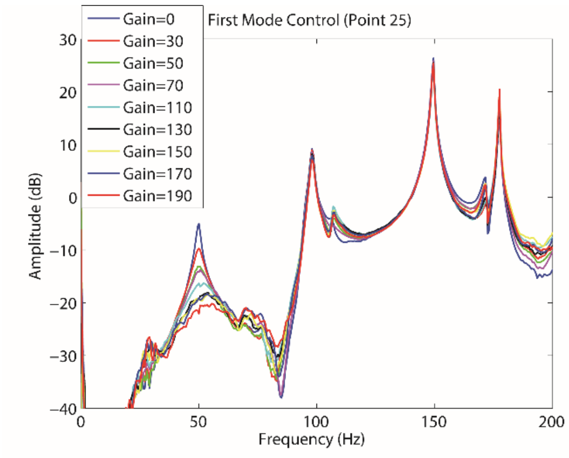

Figure 7.43 First mode control using PCVFB with bandpass filter for different control gains (Point 25)

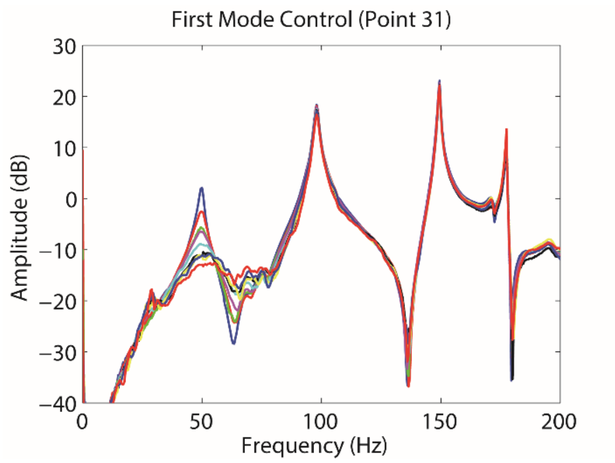

Figure 7.44 First mode control using PCVFB with bandpass filter for different control gains (Point 31)

Figure 7.43 and Figure 7.44 show the spectra of the measured response of Points 25 and 31 for the test of the PLVFB controller with bandpass filter for the first mode, and Figure 7.45 shows the zoom-in view of the first mode. Similar to the results of Sec. 7.4.2.2, the damping ratio of this mode is effectively increased, while the natural frequency is not significantly affected.

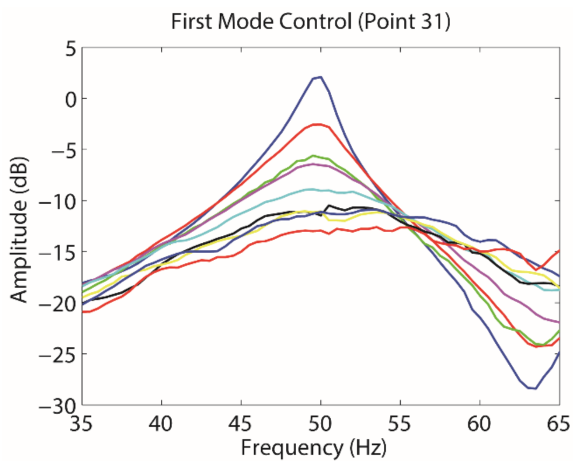

Figure 7.45 First mode control (Point 31)

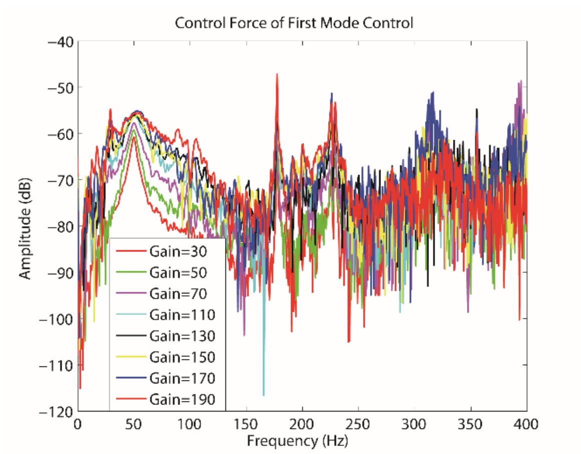

Figure 7.46 Spectra of control force outputs for different control gains (first mode)

Figure 7.46 shows the spectra of the DSP control outputs. Although the peaks of the higher mode responses increase and a peak around 20Hz appears when the gain is increased, the spillover effects and the amplitude of the peak around 20Hz are smaller than the case without bandpass filter. Furthermore, the low frequency noise is successfully reduced by the high pass filter.

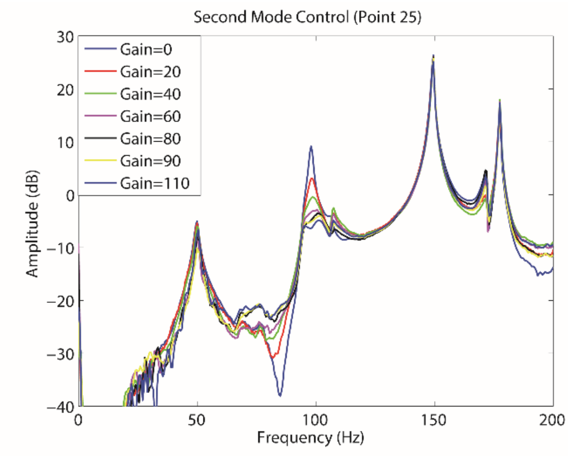

Figure 7.47 Second mode control using PCVFB with bandpass filter for different control gains (Point 25)

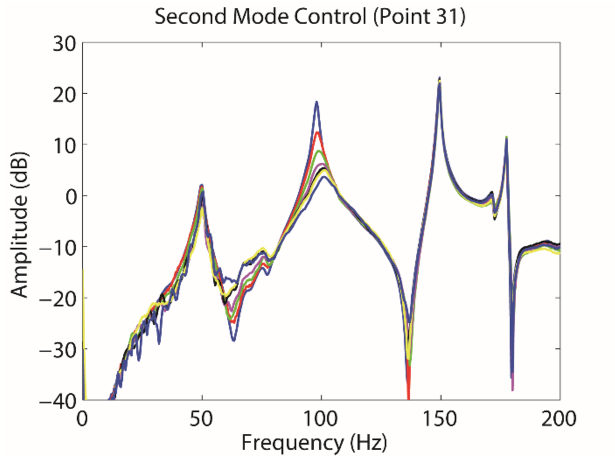

Figure 7.48 Second mode control using PCVFB with bandpass filter for different control gains (Point 31)

Figure 7.47 and Figure 7.48 show the spectra of the response at Points 25 and 31 obtained in the second mode control tests and Figure 7.49 is the corresponding zoom-in view of the second mode peak. Similar to the results of Sec. 7.4.2.2 for the second mode control, the control of the second mode is excellent.

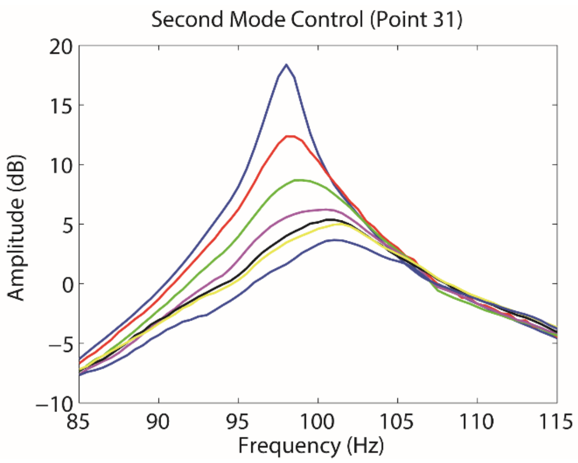

Figure 7.49 Second mode control (Point 31)

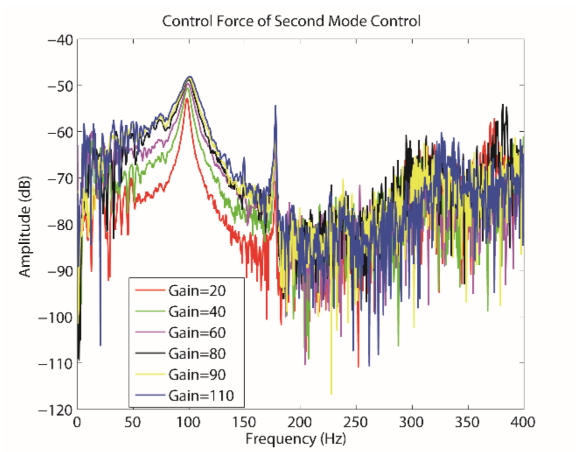

Figure 7.50 Spectra of control force outputs for different control gains (second mode)

As can be seen in the spectra of control output in Figure 7.50, the spillover effects and the low frequency noise are not significant. Superior effect of the bandpass filter is revealed by the comparison of Figure 7.50 with Figure 7.39.

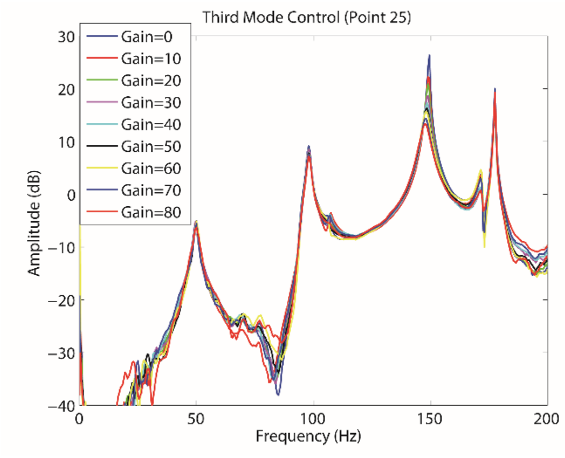

Figure 7.51 Third mode control using PCVFB with bandpass filter for different control gains (Point 25)

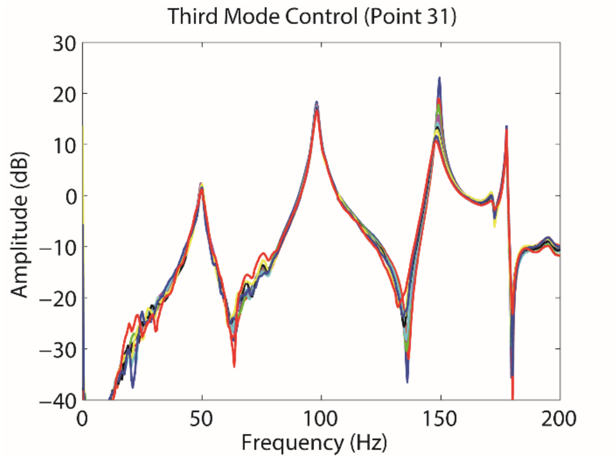

Figure 7.52 Third mode control using PCVFB with bandpass filter for different control gains (Point 31)

Finally, the results of the third mode control using the PCVFB controller with the bandpass filter are shown in Figure 7.51, Figure 7.52 and Figure 7.53.

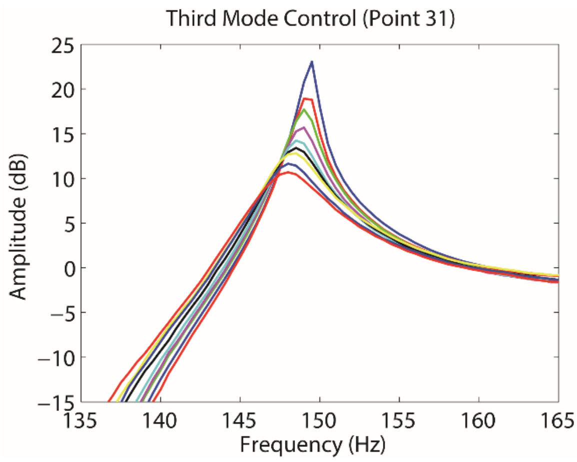

Figure 7.53 Third mode control (Point 31)

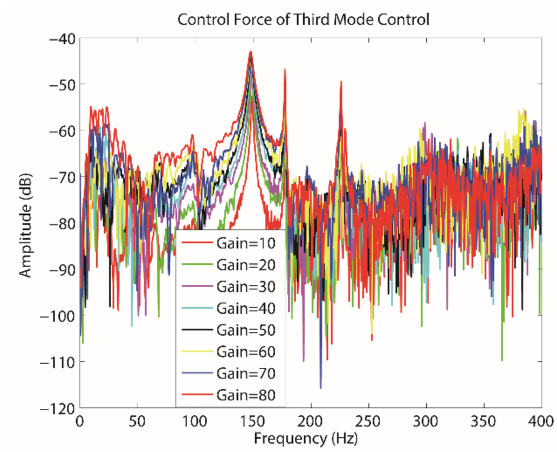

Figure 7.54 Spectra of control force outputs for different control gains (third mode)

The spectra of the control outputs is shown in Figure 7.54. As can be seen in this plot, the spillover effects significantly increase and the peaks of higher modes increase faster than the peak of the third mode as the control gain increases. Although the control performance is acceptable, spillover is more problematic in the third mode control.

7.4.2.4 Multi-mode PCVFB control with bandpass filter

Tests of the PLVFB controller with bandpass filter to suppress the vibration of multiple modes of the plate are described in this subsection.

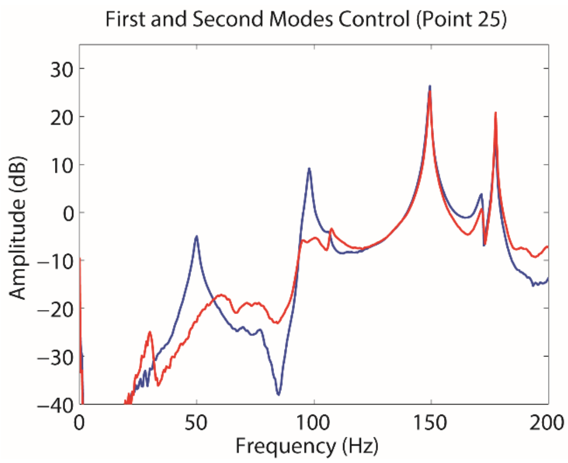

Figure 7.55 Test result: first and second mode control at Point 25

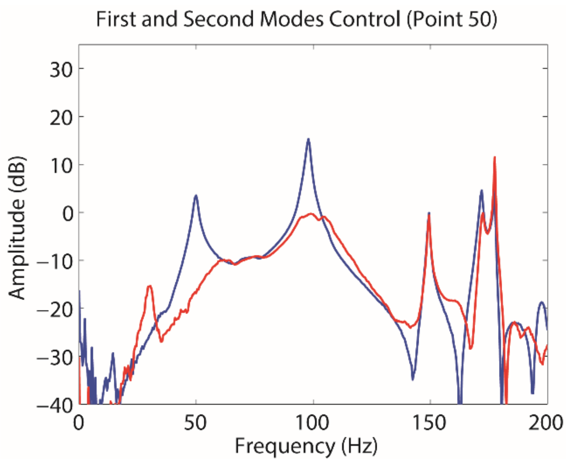

Figure 7.56 Test result: first and second mode control at Point 50

Figure 7.55 and Figure 7.56 show the results of the tests of first and second mode at Points 25 and 50. Successful control of the two modes is shown.

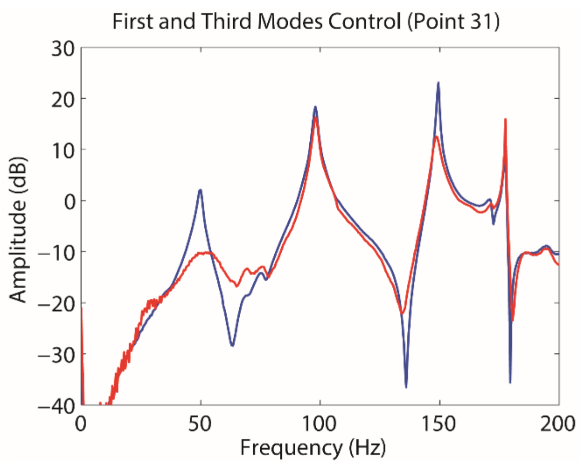

Figure 7.57 Test result: first and third modes control at Point 31

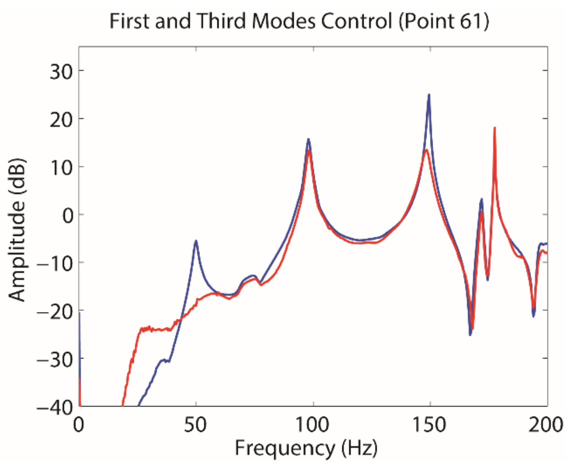

Figure 7.58 Test result: first and third modes control at Point 61

The results of the tests of the first and third mode control at Points 31 and 61 are shown in Figure 7.57 and Figure 7.58.

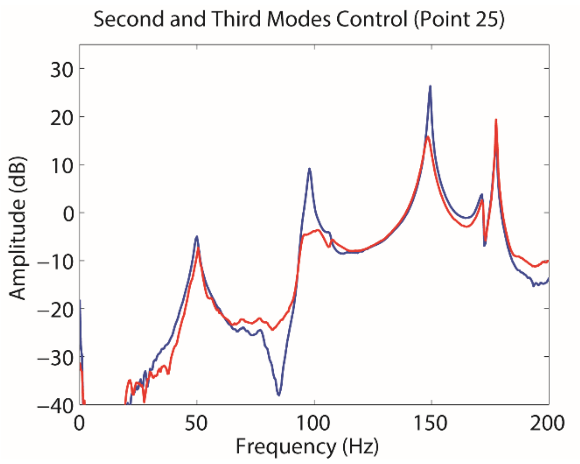

Figure 7.59 Test result: second and third modes control at Point 25

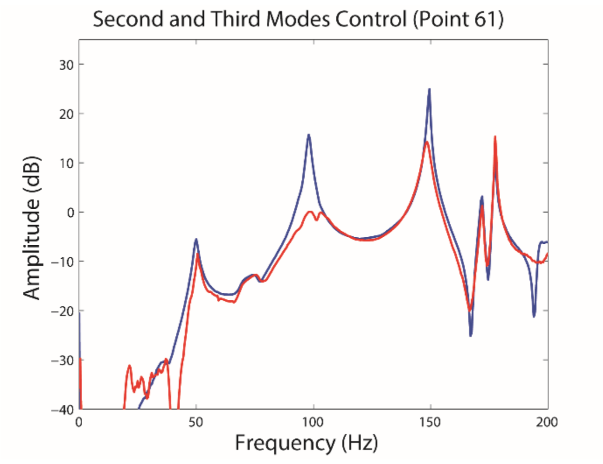

Figure 7.60 Test result: second and third modes control at Point 61

Figure 7.59 and Figure 7.60 show the results of the test of the second and third mode control at Points 25 and 61. Both of the modal damping ratios are increased.

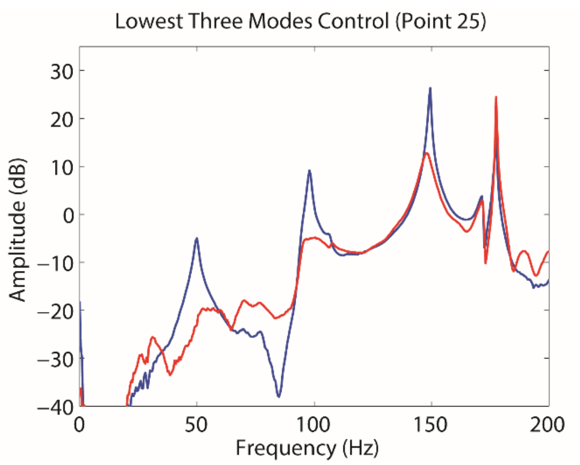

Figure 7.61 Test result: first, second and third mode control at Point 25

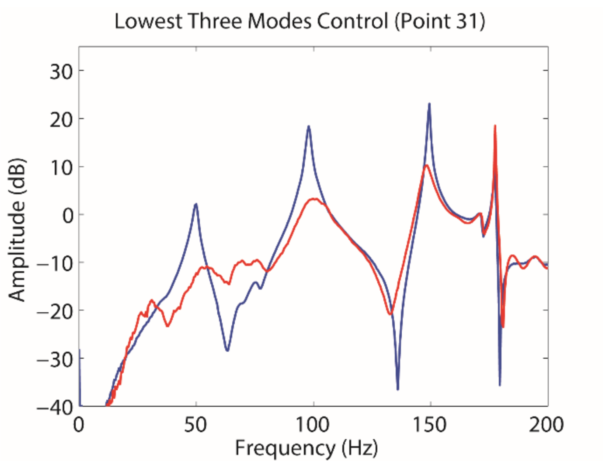

Figure 7.62 Test result: first, second and third mode control at Point 31

Finally, Figure 7.61 and Figure 7.62 show the results of the test of controlling the first, second and third mode control at Points 25 and 31. It is obvious that all of the damping ratios of the modes are increased using the proposed PCVFB controller.

7.5 Summary

In this chapter, PI phase compensation techniques for the actuator and other dynamic components are developed to avoid control system instability and to achieve significant damping for the modes to be controlled with the modal filtering approach.

Two techniques of PI parameter search are proposed – standard phase compensation and modified phase compensation. The standard PI parameter search procedure is advantageous in its straightforward framework, ease of application and allowing accuracy check of the phase compensation by means of the Lissajous curve. The modified procedure incorporating the bandpass filtering of the response measurement signal is more stable than the standard procedure even in the presence of severe transient response caused by higher order dynamic components.

The PI parameters can be automatically determined by the proposed two techniques as long as the modal frequencies of control modes are known. Since little knowledge is required to implement these phase compensation techniques, the methods are suitable for application to complicated control systems, in which identification of all the dynamic components is time consuming and error prone. The control method combined with modal filtering, modal direct velocity feedback control and the phase compensation techniques is referred to as the phase compensated velocity feedback (PCVFB) control.

The control performance of the proposed control scheme is verified by a series of tests using a steel plate as the model of a floor system. First, the performance of the MDOF controller with bandpass filter is found to be poor, because of the large phase delays involved for the second and third modes. The results of the test using PCVFB controller without bandpass filter show that the performance of the PCVFB controller is greatly improved, and its effectiveness is limited by the existence of low frequency noise as well as higher modes spillover effects. The PCVFB controller with bandpass filter is most successful in experimentally achieving remarkable control performance while circumventing the problems of the low frequency noise and the higher mode spillover effects.

Chapter 8 Spatio-Temporal Filtering

In Chapter 6 and Chapter 7, the modal filtering based velocity feedback controllers with a phase-lead term and a phase-compensated term were proposed. The most important work for the successful implementation of these controllers is the modal testing in order to identify the modal frequencies, modal damping ratios and mode shapes. The results of modal testing should be of utmost accuracy such that the modal filtering technique can be used to separate the individual modes. A complete model of the floor is necessary in order to insure control stability and performance for these controllers. For the case of phase-lead controller, a complete and accurate model of the generalized actuator dynamics is also necessary for the control parameter design. In many real world applications, these modelling efforts of the floor and actuator can take the majority work required to develop an active control strategy. For this reason, it is expected to establish a simple and robust active control strategy without requiring extensive and accurate system models. On the other hand, it has been shown that the spillover effects of higher modes cannot be totally eliminated using the MF if a small number of sensors are used, even when the low pass filter is involved. This will degrade the control performance and make the system unstable when large control gains are selected. Therefore, it is also expected to find another MF strategy such that the spillover effects of higher modes for the abstracted mode is minimized. In order to deal with these two problems, the spatio-temporal filtering technique will be investigated and combined with the phase compensation techniques described in the previous chapters to control the vibration of floor structures.

The adaptive spatio-temporal filtering was proposed as a practical and computationally efficient tool for controlling and monitoring the behavior of complex linear systems [41], [52], [56]–[58], [103]. The basic concept of the spatio-temporal filtering is similar to the modal (spatial) filtering: the dynamic response characteristics of a complex system with many structural modes can be decomposed into its fundamental components, so that each component can easily be controlled or monitored independent of the complexities of the rest of the system. Compared with the conventional modal filtering, the adaptive spatio-temporal filtering differs in two aspects:

1. It filters in both space and time is to achieve higher accuracy with fewer sensors.

2. A practical, reference model based approach is used to adaptively calculate spatio-temporal weighting coefficients if the poles of the control modes are known.

Rather than attempting to identify a complete and accurate model of a complex system, only the poles are needed to implement the controller. The spatio-temporal filter attempts to make all of the system response except the modes of interest completely unobservable, dealing with only the modes contributing to the phenomenon – the rest of the system characteristics are not considered any more. Furthermore, it is a robust method that inherently accommodates sensor and actuator failures.

In this chapter, a non-adaptive spatial-temporal filtering combined with phase-compensated modal velocity feedback control without the knowledge of the structure and actuator dynamics is developed. Non-adaptive means that spatio-temporal coefficients are determined before real-time control. In order to achieve this, white noise input is first used to active the actuator, while the vibrations of the floor and the mass of the actuator are detected by sensors at the same time. The spatio-temporal coefficients used to extract desire modes can be calculated based on these data. The phase-compensated modal velocity feedback controller developed in the previous chapter can then be utilized for each of the control mode. Phase lag and spillover effects are considered inherently in this approach.

8.1 Spatio-temporal filtering (STF)

8.1.1 Basic concept

STF is an extension of modal filtering, which utilizes the characteristic that the dynamic response of any real structure is composed of a sum of individual modal responses. In this subsection, the concept of STF will be derived from beginning. The equations of motion for free vibration of an *N*-DOF floor structure system is written as:

$$\boldsymbol{M}\ddot{\boldsymbol{u}} + \boldsymbol{C}\dot{\boldsymbol{u}} + \boldsymbol{K}\boldsymbol{u} = 0 \tag{8-1}$$

where $\boldsymbol{M}$, $\boldsymbol{C}$, $\boldsymbol{K}$ are the mass matrix, stiffness matrix and damping matrix, respectively, of order N. $\boldsymbol{u}$ is the displacement vector. If the damping term is not considered, the *N*-DOF system equations can be written as:

$$\boldsymbol{M}\ddot{\boldsymbol{u}} + \boldsymbol{K}\boldsymbol{u} = 0 \tag{8-2}$$

The free vibration of an undamped structure in one of its natural modes can be expressed mathematically by:

$$\boldsymbol{u} = \boldsymbol{\varphi}e^{i\omega t} \tag{8-3}$$

where ω is the natural frequency, and $\boldsymbol{\varphi}$ is the N-dimensional mode shape vector. Substitution of Eq. (8-3) into Eq. (8-2) yields:

$$[\boldsymbol{K}-\omega^2\boldsymbol{M}]\boldsymbol{\varphi}=0 \tag{8-4}$$

which can be interpreted as a set of N homogeneous algebraic equations. The nontrivial solutions of Eq. (3-4) are:

$$\det(\boldsymbol{K}-\omega^2\boldsymbol{M})=0 \tag{8-5}$$

The N roots of Eq. (8-5) determine the N natural frequencies $\omega_n(\mathrm{n}=1,2,\ldots N)$ of vibration. When a natural frequency ω_n is known, Eq. (8-4) can be solved for the corresponding vector $\boldsymbol{\varphi}_n$. The displacement response of the system can then be obtained as:

$$\begin{aligned}\boldsymbol{u}(\mathrm{t})&=\sum_{n=1}^{N}\boldsymbol{\varphi}_n(C_n\exp(i\,\omega_n t)+C_n'\exp(-i\,\omega_n t))\\&=\sum_{n=1}^{N}A_n\boldsymbol{\varphi}_n\cos(\omega_n t-\gamma_n)\\&=\sum_{n=1}^{N}q_n(t)\boldsymbol{\varphi}_n\end{aligned} \tag{8-6}$$

where C_n, C_n' and A_n are the amplitudes (complex and real) and γ_n is the phase for the *n*th mode. The symbol $q_n(t)$ represents the generalized coordinate of the *n*th mode that represents the *n*th mode response $A_n\sin(\omega_n t-\gamma_n)$ in this case.

Then a modal filter is applied to the measured response data $\boldsymbol{u}(\mathrm{t})$ to extract the modal coordinate response of interest. In order to extract the modal response of the *i*th mode, the modal filtering vector $\boldsymbol{\psi}_i$ is sought which has the following characteristics:

$$\begin{aligned}\boldsymbol{\psi}_i^{\mathrm{T}}\boldsymbol{\varphi}_n&=0 \qquad \mathrm{i}\neq\mathrm{n}\\&=1 \qquad \mathrm{i}=\mathrm{n}\end{aligned} \tag{8-7}$$

Therefore the *i*th modal coordinate response can be derived as:

$$\begin{aligned}\boldsymbol{\psi}_i^{\mathrm{T}}\boldsymbol{u}(\mathrm{t})&=\boldsymbol{\psi}_i^{\mathrm{T}}\sum_{n=1}^{N}q_n(t)\boldsymbol{\varphi}\\&=\boldsymbol{\psi}_i^{\mathrm{T}}\boldsymbol{\varphi}q_i(t)\\&=q_i(t)\end{aligned} \tag{8-8}$$

The above is the same as the derivation of modal filtering coefficients, which uses the information in the spatial domain – mode shapes. The spatio-temporal filter extends the capabilities of the modal filtering by applying temporal information, implying that both information in space and information in time are utilized to filter the global responses.

Recall that in modal filtering, in order to extract the modal coordinate response of interest, the modal vectors, as sampled at the sensor locations, must be linearly independent. This means that at least as many sensors as the independent modes contributing to the measured response are required. If less sensors are utilized, spillover effects caused by the ignored modes may be occurred, as described in Sec. 3.3. Therefore, it is expected to reduce the number of sensors using the temporal information through STF to extract the individual modes successfully.

From Eq. (8-8), $\boldsymbol{\psi}$ is assumed to be the spatial weighting coefficients of the specified mode. The modal coordinate response at time k using modal filtering can be estimated as:

$$\hat{q}_k = \boldsymbol{\psi}^T \boldsymbol{u}_k \tag{8-9}$$

Therefore, an *Nth* order spatio-temporal filter utilizes N past response samples can be defined as:

$$\hat{q}_k = \boldsymbol{\psi}^T \begin{pmatrix} \boldsymbol{u}_k \\ \boldsymbol{u}_{k-1} \\ \cdot \\ \cdot \\ \cdot \\ \boldsymbol{u}_{k-N} \end{pmatrix} \tag{8-10}$$

which in fact introduces a different *Nth* order finite impulse response (FIR) filter on each sensor channel. The FIR filters perform different functions depending on the specific implementation: pole-zero cancellation if spatial resolution alone is insufficient to separate modes; accommodating the relative phase shift between sensors caused by non-proportional damping; and compensation for sensor dynamics.

8.1.2 Reference model

A reference model is introduced for calculating the spatio-temporal weighting coefficients $\boldsymbol{\psi}$ of Eq. (8-10) with limited information of the system. This enables the method to be applied to complex real-world structures.

The framework of the spatio-temporal filter coefficients estimation problem is similar to other estimation problems including an error as a function of the coefficients to be estimated. The parameters are estimated by minimizing the error.

Since discrete-time sampled data systems are assumed in this study, which are widely used for practical applications, the subscript is used to denote the sample number in the ensuing discussion.

An error which is the difference between the true modal coordinate q_k and the modal coordinate estimated by the spatio-temporal filter $\hat{q}_k$ at time k is defined as:

$$e_k = q_k - \hat{q}_k = q_k - \boldsymbol{\psi}^{\boldsymbol{T}} \boldsymbol{U}_{k,N} \tag{8-11}$$

The true modal coordinate q_k, however, is not known. A reference modal coordinate, q_k^r, which is highly correlated with the true modal coordinate may be generated by driving a SDOF reference system constructed from the pole of the mode of interest. The discrete time reference system is:

$$q_{k+1}^r = z_\lambda q_k^r + f_k \tag{8-12}$$

where z_λ is the z-domain pole $z_\lambda = e^{\lambda \Delta t}$, f_k is the driving force. Then the reference modal coordinates are used in Eq. (8-11) instead of the true modal coordinates to calculate the error. The solution problem is to minimize the error over a number of time steps to estimate $\boldsymbol{\psi}$.

Off-line batch method or on-line adaptive method can be employed to minimize the error. For the first step of floor vibration control, off-line method is adopted to search the spatio-temporal weighting coefficients. Through off-line analysis, even if the floor dynamics is not known, pairs of estimated poles can be found and the STF coefficients can then be derived and immediately used for the active control.

8.2 Off-line STF coefficients searching

In modal filtering, the design process is first identifying the dynamic characteristics of the structure using the modal testing technique. Based on the results of structural identification, the number and the placement of sensors and actuators are determined in sequence, and then the controller is designed. Therefore, the structural identification plays the most important role in the modal filtering based controller. However, modal testing is not necessary in the spatio-temporal filtering. It is operated by first determining the number of sensors and actuators, placing the sensors and actuators on the floor, activing the actuators one by one using white noise excitation and recording the responses of the sensors. Based on the excitation and response data, the STF coefficients can be estimated, and finally the controller design can be accomplished for the individual modes. In this section, the process of the off-line search of the STF coefficients is described in details.

8.2.1 Data acquisition

From Eq. (8-10), it is found that if the total number of the STF coefficients is determined, there will be a trade-off between the number of sensors and the number of pass samples. Since the consequence of increasing the number of the pass samples is increase of the amount of computation, while the current DSPs can deal with remarkably immense computation requirement, the number of sensors can be significantly reduced. However, the number of sensors should be greater than the number of modes to be controlled in general, the size of the floor should also be considered in determining the number of sensors. On the other hand, the number of actuators is also determined based on the size of the floor and the number of modes to be controlled such that global response reduction of the floor can be achieved.

Unlike modal filtering, the observation spillover effects caused by residual modes are inherently eliminated in the STF. Based on the discussion in Sec. 3.3, if the observation spillover is zero, the control spillover effect alone would not destabilize the structural system even though it may degrade the system response through residual modes. Therefore, there exists a greater extent of freedom in the placement of sensors and actuators for the STF based control scheme. Depending on the pattern of the floor, the sensors and actuators can be placed randomly, while the observability and controllability characteristics of the sensor and actuator layout must be satisfied. This can be achieved easily through a series of trial-and-error adjustments or the rough results of modal testing.

After determining the number and placement of the sensors and actuators, the data used for the STF coefficient estimation can be taken from the physical floor system to be controlled on site.

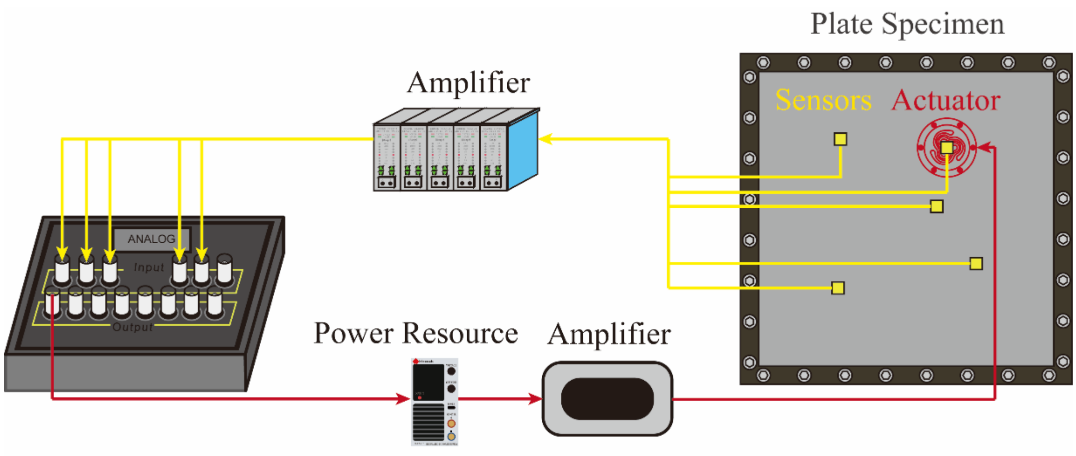

Figure 8.1 Data acquisition system set up

An example of the data acquisition system is shown in Figure 8.1. For simplicity, four sensors and one actuator are placed on the steel plate used as a floor model. One more sensor mounted on the mass of the actuator is used to measure the actuator force (mass acceleration). During the data acquisition test, white noise input is used to active the actuator, while the responses of the floor and the mass of the actuator are measured. If multiple actuators are used, the same procedure can be repeated for individual actuators. The measured data will be used to estimate the STF coefficients of the modes of interest for each actuator.

8.2.2 Data processing

The first step for the coefficient estimation is to find the system poles using the measured excitation (acceleration of the actuator mass) and the measured responses (acceleration of the floor).

There are plenty of methods that can be used to estimate the poles of a structural system, such as the peak picking – half power method [104], the rational fraction polynomial method with global fitting [71]–[73] and the eigensystem realization algorithm (ERA) [105], [106]. In this application, the ERA is adopted for the pole estimation. A brief introduction of the ERA is shown in Appendix D.

As long as the poles of the structural system are obtained, the next step is to estimate the reference modal coordinates q^r for the modes of interest based on Eq. (8-12). Because the reference model is a LTI SDOF system, the Nigam Jennings method can be used here for the q^r estimation [107]. The Nigam Jennings method is introduced in Appendix E.

As the last step, the classical Least Squares filter [108] is applied to the estimation of the STF coefficients based on Eq. (8-11). The theory of Least Square method is presented in Appendix F. After obtaining the STF coefficients, the estimated modal coordinates can be calculated using the estimated STF coefficients.

The flow chart of the proposed STF coefficient estimation is shown in Figure 8.2.

Two indices, Root-Mean-Square (RMS) error and the coefficient of determination R^2 [109], are used to evaluate the fitness of the estimated modal accelerations to the reference modal data.

Root-Mean-Square error:

$$RMSError = \sqrt{\frac{\sum_{i=1}^{n}(\hat{a}_i - a_i)^2}{n}} \tag{8-13}$$

where $\hat{a}_i$ and a_i are the estimated modal accelerations and reference modal accelerations at time step i, respectively, and n is the total time steps.

Coefficient of determination:

$$R^2 = 1 - \frac{\sum_{i=1}^{n}(a_i - \hat{a}_i)^2}{\sum_{i=1}^{n}(a_i - \bar{a}_i)^2} \tag{8-14}$$

where $\bar{a}_i$ is the mean of the reference modal accelerations. For this index, the perfect regression to the reference data corresponds to R^2 value of unity.

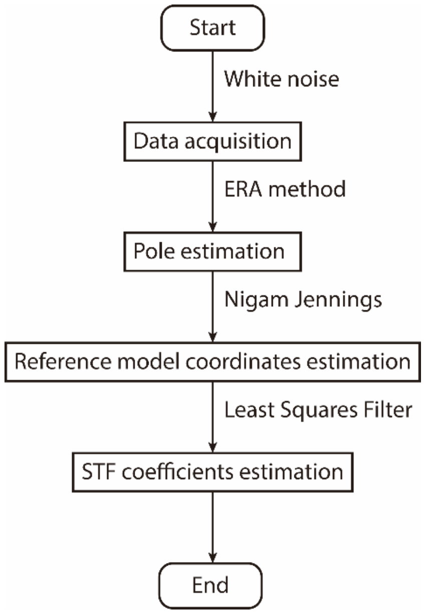

Figure 8.2 Flow chart of STF coefficients estimation

8.3 Performance of STF

In order to examine the performance of STF, a set of experimental data are required. For illustration, the STF coefficients search is demonstrated using the experimental data obtained by the tests using the steel plate specimen.

8.3.1 Standard procedure for STF estimation using experimental data

Five sensors and one actuator are mounted on the plate as shown in Figure 8.3, while one more sensor is used to detect the actuator force. For the data acquisition, the DSP system firstly generates a white noise signal to excite the actuator, and the responses are captured by the sensors and provided to the A/D interface, as shown in Figure 8.1. The data are captured using a sampling rate of 1000Hz for 10 seconds. The command white noise signal is shown in Figure 8.4 and the magnitude plots of the frequency response functions between the five measured floor accelerations and the actuator excitation measured by the mounted sensor between 0Hz and 200Hz are shown in Figure 8.5. Since the actuator is located near the node of the 4th mode as described in the previous Chapters, it can be observed from Figure 8.5 that the response of the 4th mode is minuscule.

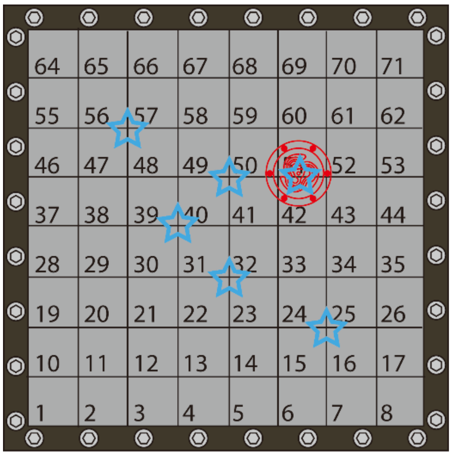

Figure 8.3 Sensor and actuator placement (Case A)

Then the ERA introduced in Appendix D is used to estimate the system poles. The parameters s and r, corresponding to the number of columns and rows in the Hankel matrix, are set to be 200 and 600, respectively. The modal frequencies and modal damping ratios of the identified modes within 200Hz are shown in Table 8.1.

The results are slightly different from the results shown in Table 4.4, which are identified using the rational fraction polynomial method with global fitting. The reason can be attributed to the difference of the environmental temperature between the two tests conducted in autumn and in summer. It is well known that the natural frequencies increase with decreasing temperatures [110].

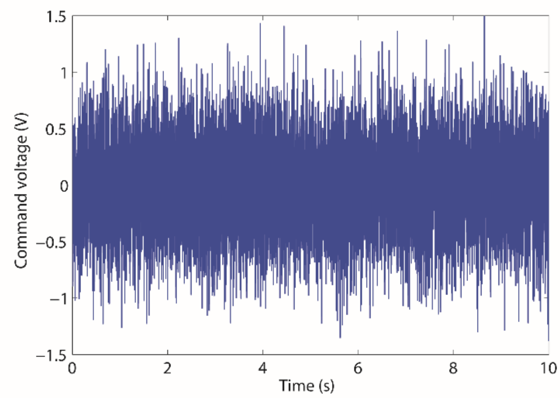

Figure 8.4 Command white noise signal

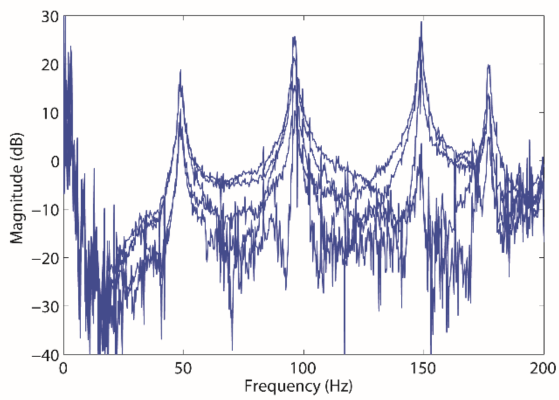

Figure 8.5 Magnitude plots of the frequency response functions

In the next step, the Nigam Jennings method is used to calculate the reference modal coordinates q^r of Eq. (8-12) using Eq. (E-15), where the acceleration $a_{act}(t)$ is the measured actuator mass acceleration. The resulting reference modal accelerations for the first three modes are shown in Figure 8.6.

Table 8.1 – Identified modal frequencies and damping ratios (Case A)

	Mode 1	Mode 2	Mode 3	Mode 4	Mode 5
Frequency	48.81Hz	96.04Hz	148.69Hz	172.02Hz	177.03Hz
Damping ratio	0.0143	0.0044	0.0032	0.0095	0.0027

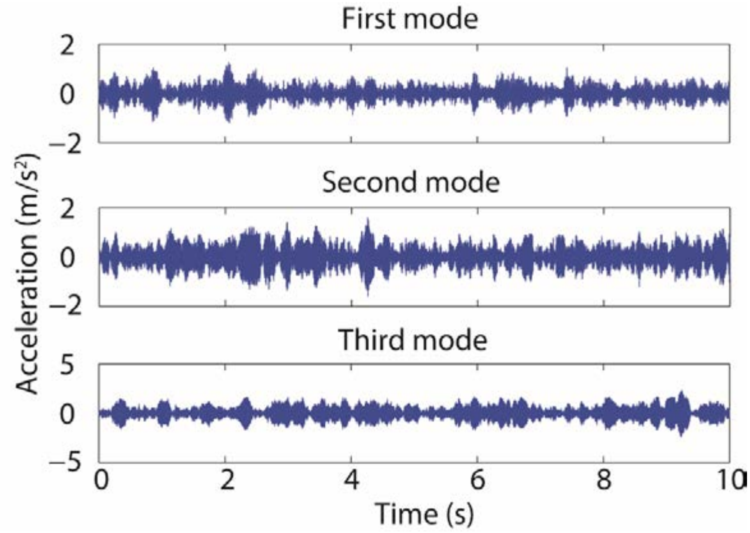

Figure 8.6 The reference modal accelerations

The last step is to estimate the STF coefficients of the three modes using the Least Squares method. If the order of the spatio-temporal filter N is set to 20, the total number of the coefficients for the estimation are 100 for each mode.

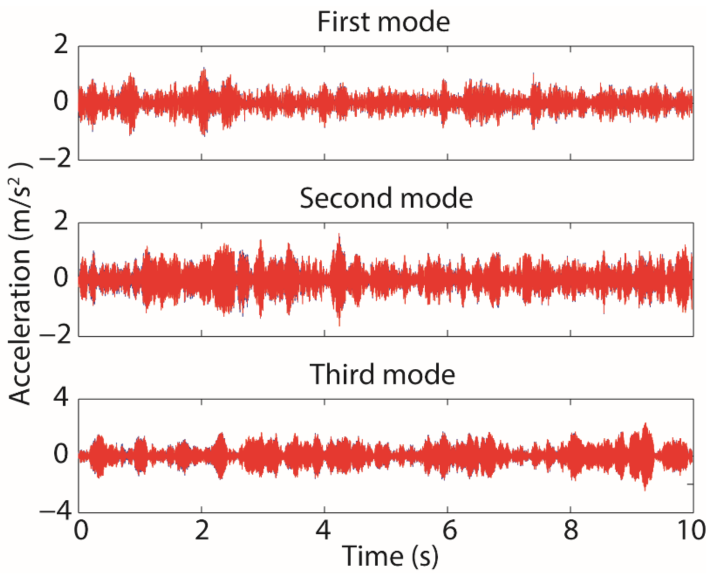

Figure 8.7 Comparison results —reference modal accelerations—estimated modal accelerations

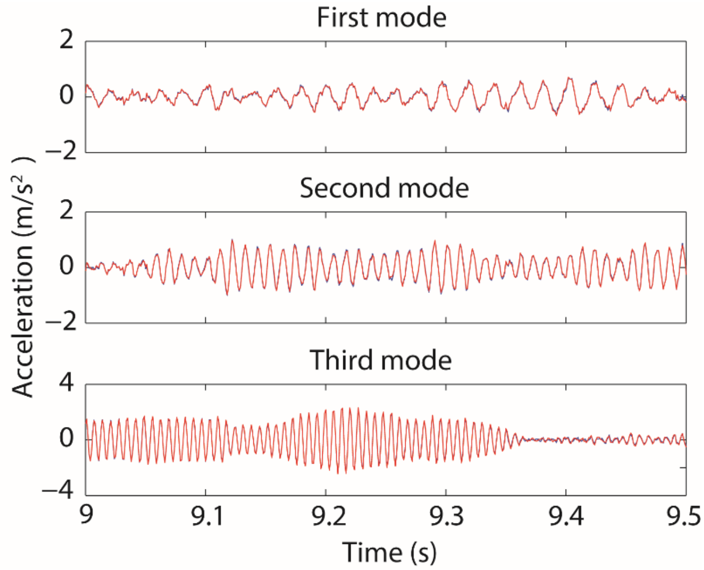

Figure 8.8 Comparison results (9s-9.5s) —reference modal accelerations—estimated modal accelerations

Once the STF coefficients for each mode are obtained by Eq. (F-25), the estimated modal accelerations can be calculated and compared with the reference ones shown in Figure 8.6 to check the effectiveness of the STF coefficients. The comparison results are shown in Figure 8.7 and Figure 8.8.

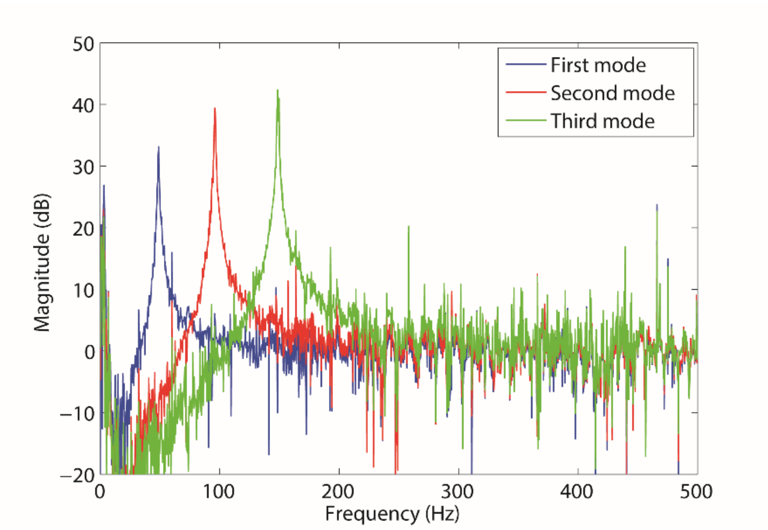

Figure 8.9 Magnitude plots of the frequency response functions of the lowest three modes

The Root-Mean-Square errors of these three modes are 0.0355, 0.0481 and 0.0636, respectively. The coefficients of determination R^2 of these modes are 0.9910, 0.9864 and 0.9812, respectively. These results indicate that the estimated STF coefficients perform well to trace the reference modal coordinates. The magnitude plots of the frequency response functions between the actuator excitation and the estimated modal accelerations of the three modes among 0Hz and 500Hz are shown in Figure 8.9, demonstrating that the STF coefficients are capable of extracting the modes of interest from the experimental data. The spillover effects of the other modes are not observed from Figure 8.9.

The same procedure can be applied to different sets of the STF-based parameters. In the next subsections, the effects of the past sample (temporal) numbers, sensor (spatio) numbers, sensor locations and actuator locations are investigated.

8.3.2 Effects of past sample numbers and sensor numbers

The same experimental data used in the previous subsection is used to investigate the effects of past sample numbers and sensor numbers. Figure 8.10, Figure 8.12 and Figure 8.14 show the relationship between the analyzed Root-Mean-Square errors of the lowest three modes and past sample numbers. Figure 8.11, Figure 8.13 and Figure 8.15 show the relationship between analyzed R^2 values of the lowest three modes and past sample numbers. Five different curves in each figure correspond to the results for different sensor numbers *NS*. (*NS*=1: Point 25; *NS*=2: points 25, 32; *NS*=3: points 25, 32, 40; *NS*=4: points 25, 32, 40, 50; *NS*=5: points 25, 32, 40, 50, 57)

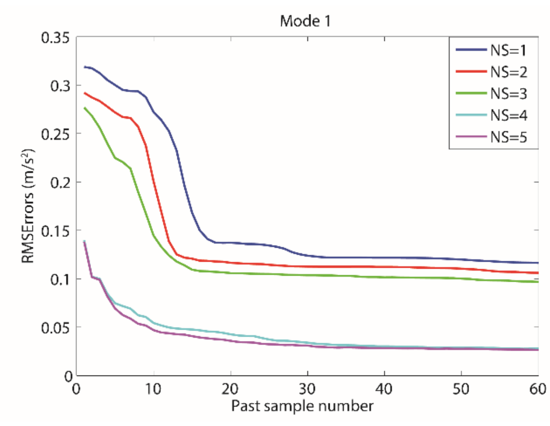

Figure 8.10 RMS Errors of estimated coordinates of different sensor numbers versus past sample numbers (mode 1)

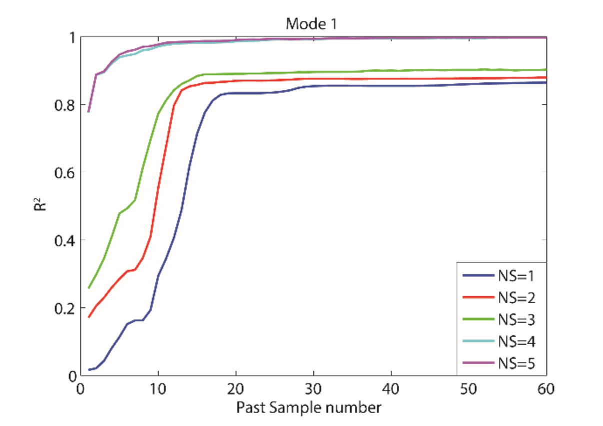

Figure 8.11 R^2 values of estimated coordinates of different sensor numbers versus past sample numbers (mode 1)

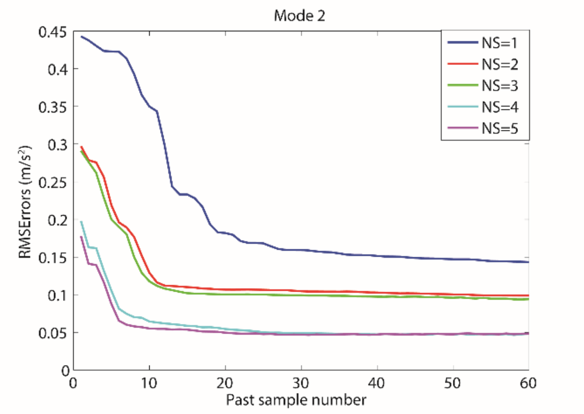

Figure 8.12 RMS Errors of estimated coordinates of different sensor numbers versus past sample numbers (mode 2)

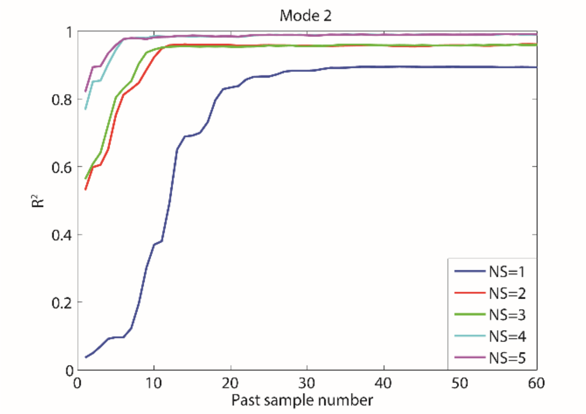

Figure 8.13 R^2 values of estimated coordinates of different sensor numbers versus past sample numbers (mode 2)

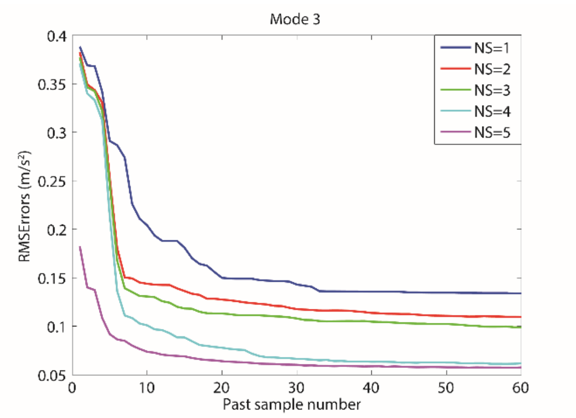

Figure 8.14 RMS Errors of estimated coordinates of different sensor numbers versus past sample numbers (mode 3)

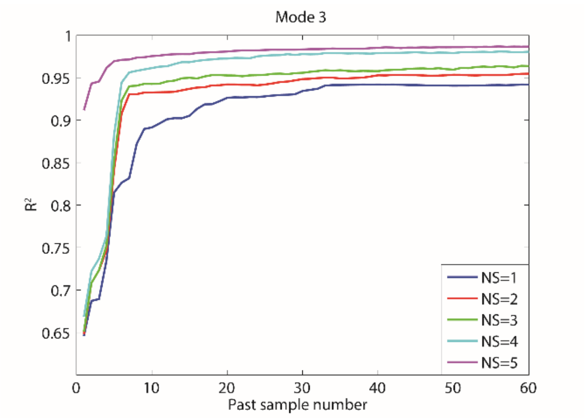

Figure 8.15 R^2 values of estimated coordinates of different sensor numbers versus past sample numbers (mode 3)

As can be seen from these figures, the number of sensors is an important parameter to achieve accurate estimated modal coordinates. As the number of sensors increases, the RMS errors decrease and the R^2 values increase with the same number of past samples. It should be also noted that the performance is almost the same for the four-sensor and five-sensor cases, in which RMS errors becomes small and R^2 values are nearly become unity. Therefore, due to the trade-off between the number of sensors used and the economy consideration, use of a large number of sensors is not necessary.

The number of past samples is another important parameter as can be seen from these figures. A critical value of the number of past samples can be seen in each plot, so that the performance index rapidly decreases or increases to a convergent value at when the number of past samples reaches the critical number. Therefore, the number of past samples should be larger than the critical value and may not be extremely larger than that number. It can also be found that as the number of sensors increases, the critical past sample number decreases. This is an indication of the trade-off between the sensor numbers and the past sample numbers.

Surprisingly, these figures also showed that only one sensor can be used to extract the lowest three modes with an acceptable performance if a large past sample numbers are used, such as $N = 40$. It can be seen from Figure 8.10 to 8.15 that even if $N > 40$ the index values will not significantly change to acheive the nearly best performance. The magnitude plots of the frequency response functions between the estimated modal accelerations of the three modes and the actuator excitation between 0Hz and 500Hz when $NS = 1$ and $N = 40$ are shown in Figure 8.16.

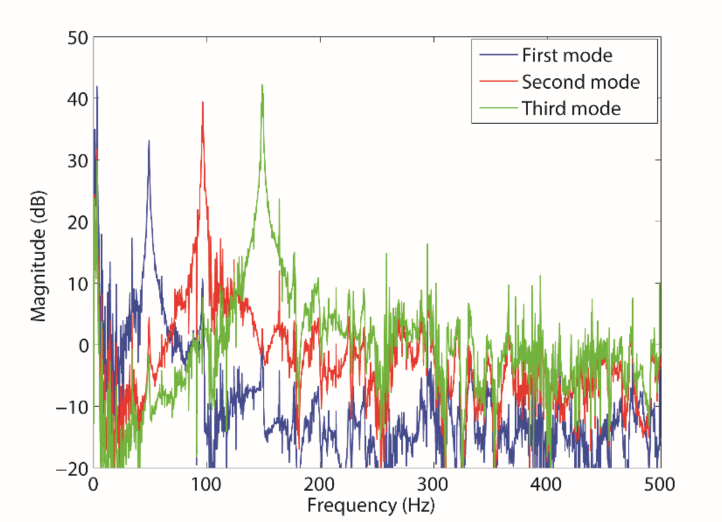

Figure 8.16 Magnitude plots of the frequency response functions of the lowest three modes $NS = 1, N = 40$

8.3.3 Effects of sensor locations

The sensor placement shown in Figure 8.3 is assumed as Case A, in order to analyze the effects of sensor locations, and another two placements, Case B and Case C as shown in Figure 8.17 and Figure 8.18 are considered. In Case B, the sensors are symmetrically arranged on the plate surface, while in Case C, the sensors are arranged on the surface of one half side of the plate. The sensor Point 25 is used in all the three cases. The data quality can be guaranteed if the responses of sensor Point 25 are the same for the three cases. The actuator is placed on the same location as the Case A. The same white noise excitation shown in Figure 8.4 is used to excite the actuator and another two sets of sensor measurements are obtained, and used for the analysis.

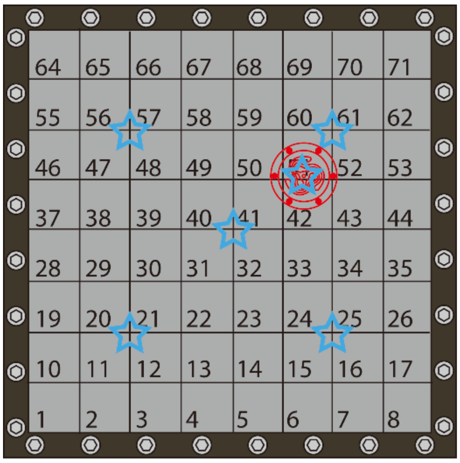

Figure 8.17 Sensor and actuator placement (Case B)

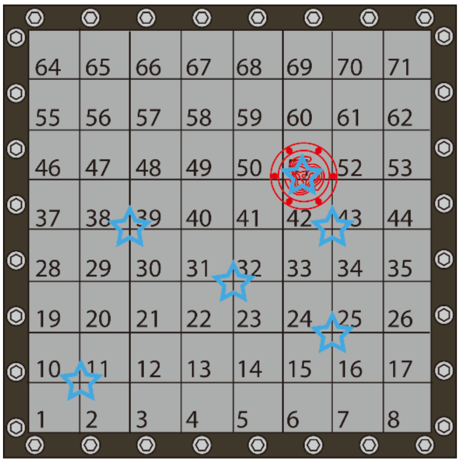

Figure 8.18 Sensor and actuator placement (Case C)

Table 8.2 – Identified modal frequencies and damping ratios (Case B)

	Mode 1	Mode 2	Mode 3	Mode 4	Mode 5
Frequency	48.94Hz	95.34Hz	148.48Hz	171.77Hz	176.94Hz
Damping ratio	0.0136	0.0038	0.0030	0.0054	0.0029

Table 8.3 – Identified modal frequencies and damping ratios (Case C)

	Mode 1	Mode 2	Mode 3	Mode 4	Mode 5
Frequency	49.01Hz	95.47Hz	148.72Hz	171.48Hz	177.03Hz
Damping ratio	0.0135	0.0035	0.0029	0.0036	0.0027

The system poles within 200Hz of the two cases identified with the ERA method are shown in Table 8.2 and Table 8.3. It can be observed that the poles are almost the same for the three cases.

Firstly, the STF performance for the lowest three modes when $NS = 5$, and $N = 20$ are examined for the two cases and compared with the results of the previous case using the two indices. The results are shown in Figure 8.19 and Figure 8.20, and the corresponding magnitude plots of the frequency response functions are shown in Figure 8.21. Figure 8.19 and Figure 8.20 show the performance of Case A and that of Case B are almost the same, while for Case C the performance is slightly inferior. Nonetheless, in all of the three cases, the desired modes are successfully separated, which can be observed in Figure 8.21. It can also be noticed in Figure 8.21 that the peak values of individual modes are the same for the three cases, seemingly because the same excitation of Figure 8.4 are used.

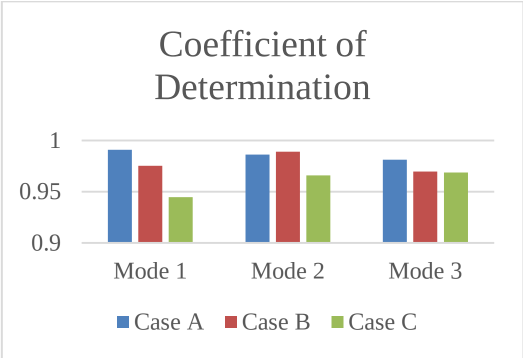

Figure 8.19 Coefficient of Determination comparison among three cases $NS = 5, N = 20$

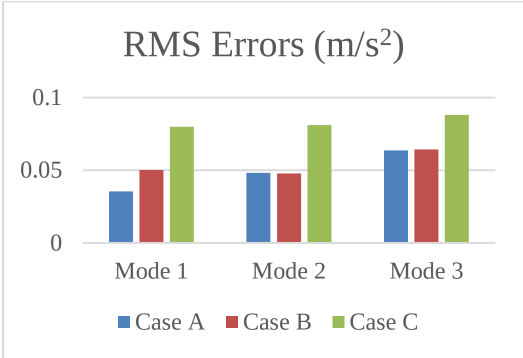

Figure 8.20 RMS Errors comparison among three cases $NS = 5, N = 20$

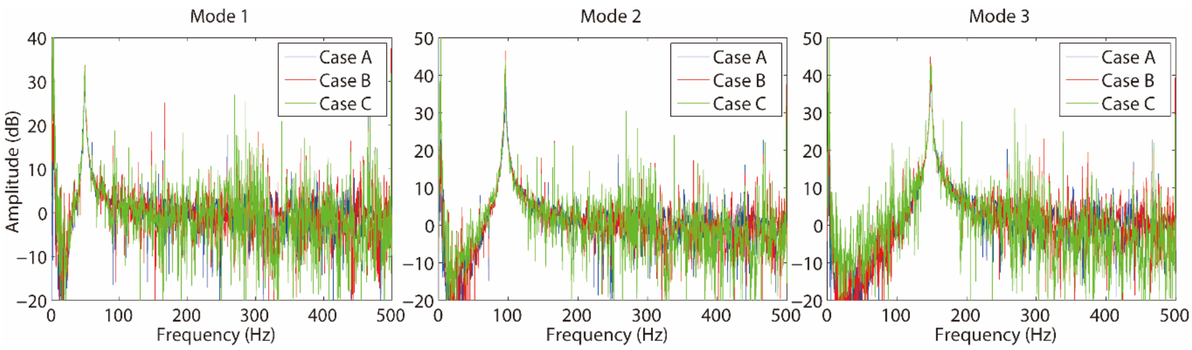

Figure 8.21 Magnitude plots of the frequency response functions of the lowest three modes for three cases $NS = 5, N = 20$

It has been shown in Figure 8.16 that it is possible to extract the modes of interest with one sensor using STF. It is realizable when the sensor is located away from the nodes of the lowest three modes. In order to investigate the possibility when the sensor is located near the node of mode of interest, the sensor measurement of Point 11 of Case C is used. The frequency response function of this point is shown in Figure 8.22, which depicts that the first mode is hardly observed at this point. The STF result of the first mode for $N = 40$ is shown in Figure 8.23, for which $R^2 = 0.2884$ and $\mathrm{RMSError} = 0.2664\ \mathrm{m/s^2}$. From Figure 8.23, it is noticed that the first mode cannot be smoothly extracted from the point which is near the node. The similar phenomenon is seen when Point 41 is used in Case B to extract the third mode. The frequency response function of Point 41 and the corresponding result are shown in Figure 8.24 and Figure 8.25, respectively.

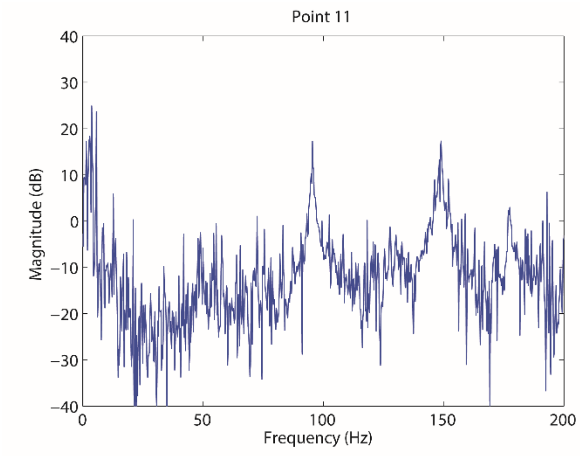

Figure 8.22 Magnitude plot of the frequency response function of point 11

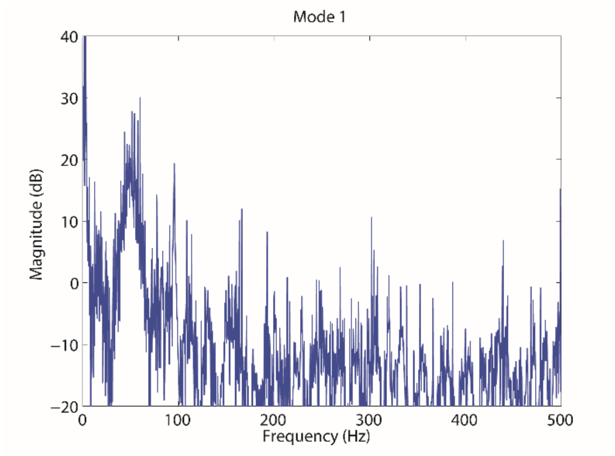

Figure 8.23 Magnitude plots of the frequency response functions of mode 1 $NS = 1, N = 40$ point 11

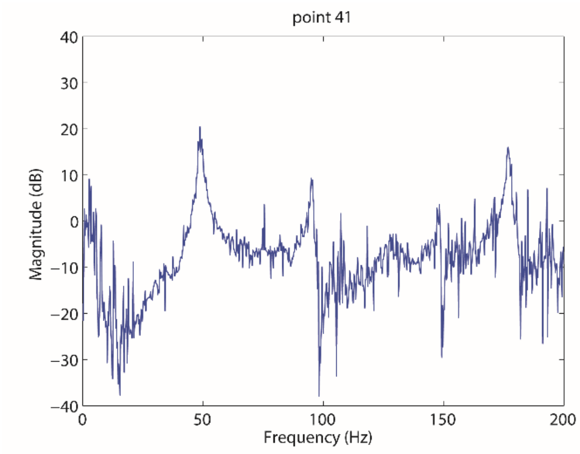

Figure 8.24 Magnitude plot of the frequency response function of point 41

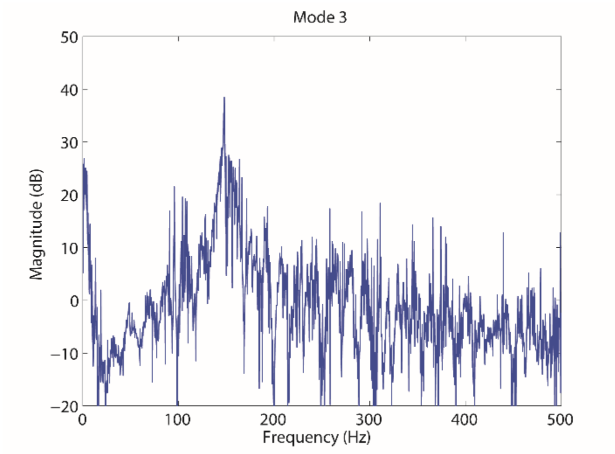

Figure 8.25 Magnitude plots of the frequency response functions of mode 3 $NS = 1, N = 40$ point 41

Therefore, the effective points (EFP) can be defined for the present analysis. Since RMS error is not a dimension-less index, R^2 is used for the definitions that follow. If one mode of a system can be extracted ($R^2 \geq 0.7$) using STF with a sufficiently great N ($N = 40$) from a sensor point, the said point is called as an effective point for the mode. The effective points of the lowest three modes for the three cases are shown in Table 8.4.

Table 8.4 – Effective points of each mode for the three cases

Effective points

	Mode 1	Mode 2	Mode 3
Case A	5	4	4
Case B	5	3	4
Case C	4	5	3

The elite point (ELP) is defined as the sensor point which has the maximum R^2 value among all the sensor sets for the specified mode. The corresponding maximum R^2 value is defined as the elite value (EV). The ELP and EV of the lowest three modes for the three cases when $NS = 5$ are shown in Table 8.5.

Table 8.5 – ELP and EV for the lowest three modes

Elite point

	Mode 1	Mode 2	Mode 3
Case A	50	50	25
Case B	41	61	25
Case C	43	32	25

Elite value

	Mode 1	Mode 2	Mode 3
Case A	0.9425	0.9692	0.9426
Case B	0.9172	0.9657	0.9401
Case C	0.8883	0.9506	0.9514

Thus, the overall performance of individual modes for the three cases (see Figure 8.19) can be regarded as the combination effects of EFP and EV. The sensor placement such that both EFP and EV are high can achieve better STF results. Nonetheless, as has already been mentioned, all of the three modes can be extracted successfully for the three cases if five sensors are used.

8.3.4 Effects of actuator locations

The actuator is located a location between point 51 and 52 as shown in Figure 8.3, and this location turns out to be near the node of the fourth mode, as indicated in Table 4.5. Possibility of extraction of the fourth mode using STF is examined. For Case A, the magnitude plot of frequency response function of the fourth mode with $NS = 5$ and $N = 20$ is shown in Figure 8.26, for which $R^2 = 0.5859$ and $\text{RMSError} = 0.3032\ \text{m/s}^2$. For completeness, the

STF result for mode 5 is shown in Figure 8.27. In this case, the performance indices are $R^2 = 0.9664$ and $\mathrm{RMSError} = 0.0851\ \mathrm{m/s^2}$.

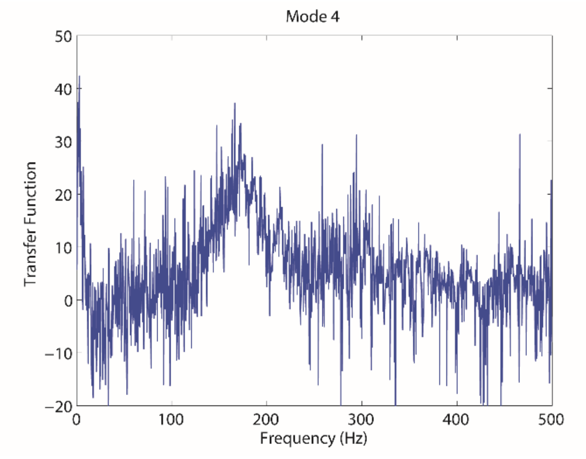

Figure 8.26 Magnitude plot of the frequency response function of mode 4 $NS = 5, N = 20$

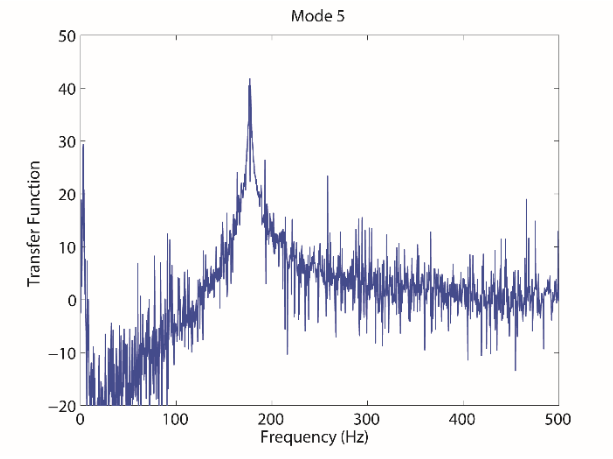

Figure 8.27 Magnitude plot of the frequency response function of mode 5 $NS = 5, N = 20$

Therefore, it can be concluded that extraction of the specified mode is possible (controllable) if the location of the actuator is sufficiently apart from the node of that mode.

8.4 Effectiveness and robustness of STF

In this section, the sensitivity of the STF's effectiveness to an uncertainty in the natural frequency and damping ratio of specified mode is investigated. The experimental data of Case A is used for the analysis.

In the numerical analysis, it is assumed that the poles of the lowest three modes of Table 8.1 estimated by ERA are accurate. Then the modal coordinates (acceleration) estimated from these poles using Nigam Jennings method can be regarded as the reference modal coordinates.

The past sample numbers N is fixed to 60 to ensure the almost best performance for different sensor numbers (see Figure 8.10~Figure 8.15), and the estimated modal coordinates are then obtained for different values of poles around the accurate poles. Five different sensor numbers are considered for comparison.

The RMS error of Eq. (8-13) is used as the performance index which represents the effectiveness of a STF result. It is noted that the STF result providing the smaller value of the RMS Error is regarded to be more effective.

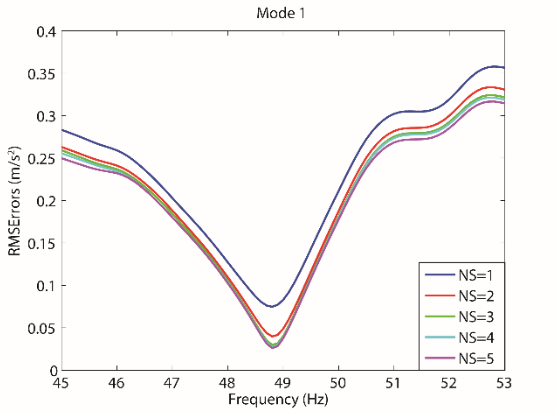

Figure 8.28 Effectiveness of STF in RMS Error versus frequency for different sensor numbers of Mode 1 ($N = 60$ $\beta = 0.0143$)

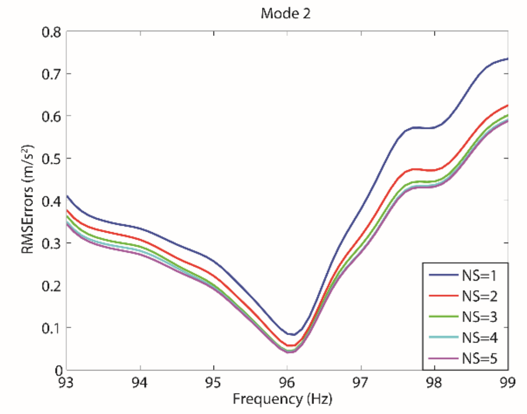

Figure 8.29 Effectiveness of STF in RMS Error versus frequency for different sensor numbers of Mode 2 ($N = 60$ $\beta = 0.0044$)

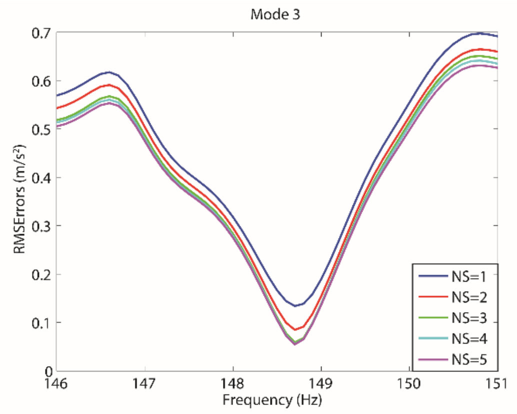

Figure 8.30 Effectiveness of STF in RMS Error versus frequency for different sensor numbers of Mode 3 ($N = 60$ $\beta = 0.0032$)

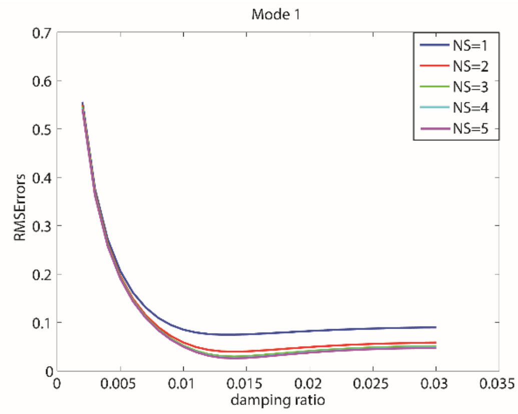

Figure 8.31 Effectiveness of STF in RMS Error versus damping ratio for different sensor numbers of Mode 1 ($N = 60$ $\omega = 48.81$)

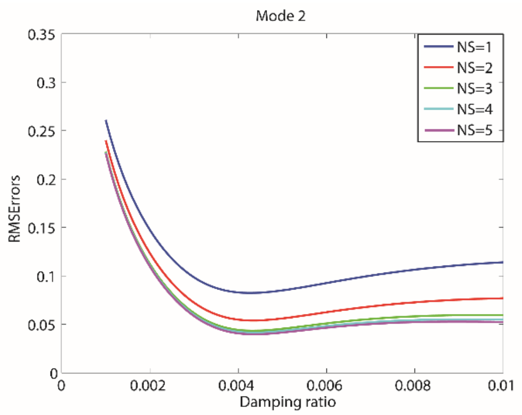

Figure 8.32 Effectiveness of STF in RMS Error versus damping ratio for different sensor numbers of Mode 2 ($N = 60$ $\omega = 96.04$)

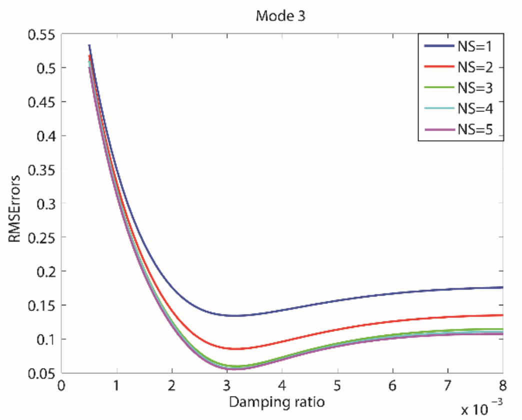

Figure 8.33 Effectiveness of STF in RMS Error versus damping ratio for different sensor numbers of Mode 3 ($N = 60$ $\omega = 148.69$)

Figure 8.28, Figure 8.29 and Figure 8.30 show the relationship between the effectiveness of a STF result or the RMS error and the modal frequency. The modal damping ratios are fixed to the accurate values shown in Table 8.1. The curves for various sensor numbers are shown in each plot.

It can be clearly seen in Figure 8.28, Figure 8.29 and Figure 8.30 that there is the well distinguished optimal frequency such that the RMS Error achieves the minimum. The optimal frequencies correspond to the accurate values shown in Table 8.1. As has been indicated in the previous section, the minimum value of the RMS error can be smaller for large numbers of sensors. It implies that the effectiveness of the STF is enhanced with the increase of the total number of sensors, while the improvement in the effectiveness will be saturated.

Figure 8.28, Figure 8.29 and Figure 8.30 also indicate the robustness against the change or the estimation error in the modal frequencies. As shown in these figures, the STF is not robust when $NS = 1$ in the sense that the error in the modal frequencies tends to increase the RMS Error and hence reduces the effectiveness significantly. On the contrary, the degree of the effectiveness drop of a STF result with large sensor numbers is not significantly different from that of a single sensor case. However, a STF result with large sensor numbers can be more robust by considering the values of effectiveness. Even though the effectiveness of the STF with large sensor numbers is reduced when the modal frequencies are changed within a certain range, it is still capable of extracting the desired modes.

Figure 8.31, Figure 8.32 and Figure 8.33 show the relationship between the effectiveness and the damping ratio. The modal frequencies are fixed to the accurate values shown in Table 8.1. The same conclusion can be achieved as the plot for the modal frequency so that the effectiveness of STF is increased with increase of the total number of sensor although the improvement in effectiveness is limited if larger number of sensors are used. As for the robustness of STF against the change in the damping ratio, it is obvious that within a certain change of the damping ratio, the more sensors are used, the more robust the system is.

Therefore, it is concluded that the STF is more effective and robust against the change in the modal frequency and damping ratio if a large number of sensors are used. However, the effectiveness and robustness are also good even when the number of sensors is small.

8.5 Phase compensated controller design

8.5.1 Phase compensation

From Sec. 8.2, the STF coefficients of the modes to be controlled can be estimated for the individual actuators according to the procedure described in Figure 8.2. Then the modal responses of the control modes can be calculated based on Eq. (8-10). The controller can be designed based on these modal responses. Note that the STF coefficients are estimated from the measurement of actuator force. Therefore, phase lags caused by the DSP system and actuator are involved if the modal direct velocity feedback controller is utilized. This is the same situation as the modal filtering-based case introduced in the previous chapters.

Since the spatio-temporal filter acts like a FIR filter which conducts pole-zero cancellation to extract the modal responses, the observation spillover effects can be ignored during the STF-based controller design. Therefore only the high pass filter is used in order to avoid numerical issues and to remove the low frequency noise during the real-time active control.

Then, the phase compensation methods proposed in Chapter 7 can be utilized to compensate the time delays caused by these dynamic components. The procedure is described in Sec. 7.2, and the modified phase compensation method will be adopted here.

Figure 8.34 shows the schematic block diagram of the phase compensated velocity feedback control of a mode using spatio-temporal filtering.

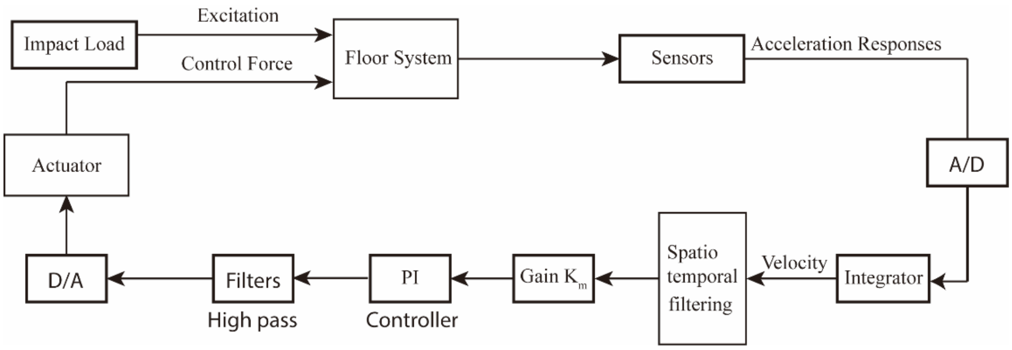

Figure 8.34 Phase compensated velocity feedback control of a mode using STF

8.5.2 Design process

According to the development described in the previous sections, the control scheme for the independent modal space phase compensated velocity feedback control combing with spatio-temporal filtering can be summarized as follows:

1) Determine the number of modes to be controlled and the number of sensors and actuators to be used.
2) Put the sensors and actuators on the floor where the observability and controllability of the control modes can be satisfied.
3) Estimate the STF coefficients of the control modes for individual actuators based on the procedure described in Sec. 8.2.

4) Identify the PI parameters for all the control modes on site by a series of real-time tests using the techniques described in Sec. 7.2. If multiple actuators are used, this step is repeated for all actuators.
5) Design the control gains for the control modes according to stability and performance of the whole floor system. Issues appearing in typical practical situations, including non-linear actuator saturation must also be considered when choosing the control gains.

8.6 Verification test

In order to verify the control efficiency of the proposed STF based phase compensated velocity feedback control scheme, steel plate vibration control tests using the experimental system described in the previous sections were conducted. The design process described in Sec. 8.5.2, was applied to determine the sensor placements and to develop the code installed in the DSP controller. The test results and its control efficiency is discussed in this section.

8.6.1 STF based control for different sensor placement

To investigate the effects of sensor placement on the control efficiency, the three configurations, Case A, Case B and Case C shown in Figure 8.3, Figure 8.17 and Figure 8.18 are used in the verification tests. Since the sensor Point 25 is commonly included in all the three cases, it is regarded as the reference point and the responses at this point are compared among three cases.

The actuator is placed on the same location as mentioned in Sec. 8.3.3, and the identical white noise excitation signal shown in Figure 8.4 is used. As has been described to discuss the result using three sensor placement cases in Figure 8.21, the control performance evaluated by the response at the reference point does not depend on the sensor placement, provided that the control gain is the same.

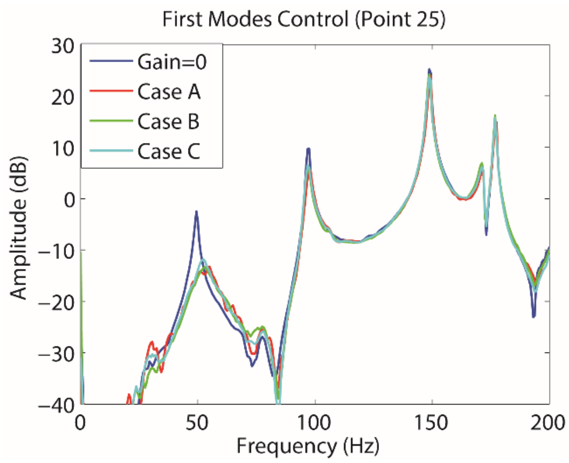

Figure 8.35 First mode control of the three cases with the same control gain

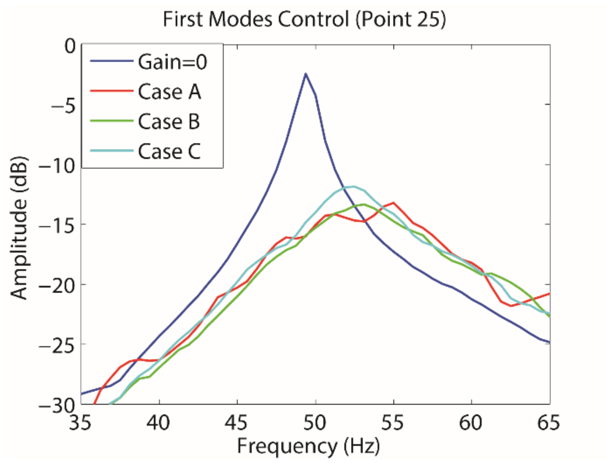

Figure 8.36 First mode control (Point 25)

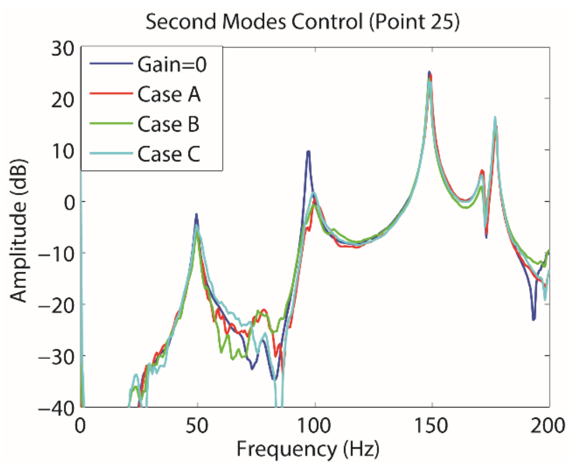

Figure 8.37 Second mode control of the three cases with the same control gain

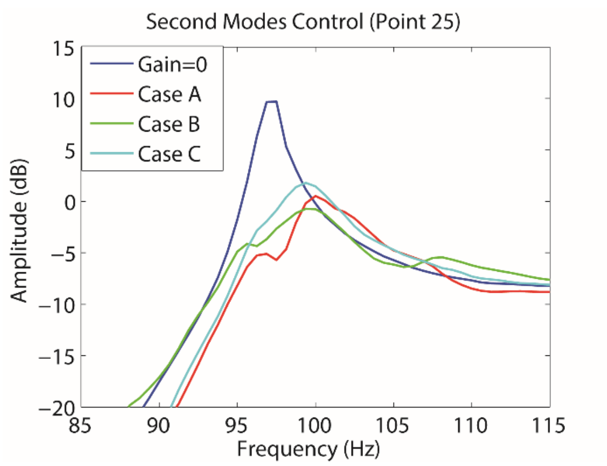

Figure 8.38 Second mode control (Point 25)

The control results for the first mode and second mode are shown in Figure 8.35 through Figure 8.38, among which Figure 8.36 and Figure 8.38 are the zoom-in views of these two modes. It can be observed that the response of the first two modes are successfully reduced by approximately 10dB in both cases, and the equal control performance is obtained with the same control gain. This means that the effectiveness of the STF based controllers are not affected by sensor placement. This is a great advantage of the STF approach in practical application it is often the case that there exists strict restriction on the locations of the sensors to be installed.

In the following control tests, the performance of STF based controller is thoroughly investigated using the ‘optimal’ sensor and actuator placement to compare the control results with those obtained in the previous chapters.

8.6.2 STF based phase-lead controller

First of all, the number of past samples used is chosen as 20, and then the STF coefficients for the lowest three modes are estimated by the procedure described in Sec. 8.2. The values of ELP, EP and EV for this sensor placement are shown in Table 8.6.

Table 8.6 – EP, ELP and EV for the lowest three modes

	Mode 1	Mode 2	Mode 3
EP	3	4	3
ELP	50	61	25
EV	0.9358	0.9543	0.9382

The bandpass filter shown in Table 7.2 is used in the STF based controller. The use of a low pass filter can also be favorable in avoiding higher modes spillover effects.

The phase lead compensators introduced in Chapter 6 is effective in frequency increase and damping enhancement. In order to implement phase lead compensators, the technique proposed in Sec. 7.2.4 is used. The control performance of the lowest two modes are highlighted in this section for demonstration of the global control characteristics of the STF based controller. The control results of the third mode will be given in the next section.

Figure 8.39 through Figure 8.43 show the results for the first mode control. Obviously, as the control gain increases, the damping ratio of the first mode increases without influencing the response of other modes within 300Hz. This is a desirable result expected to STF based controllers.

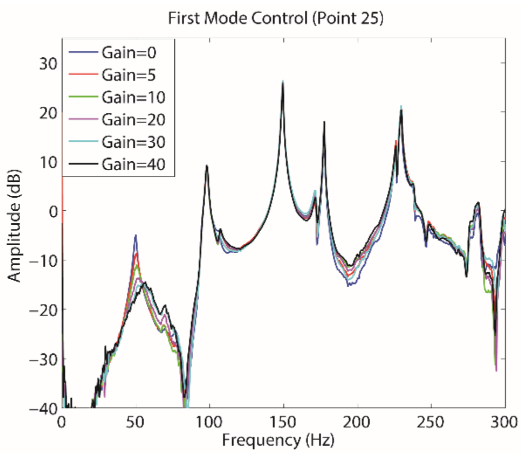

Figure 8.39 First mode control using STF based phase-lead controller for different control gains (Point 25)

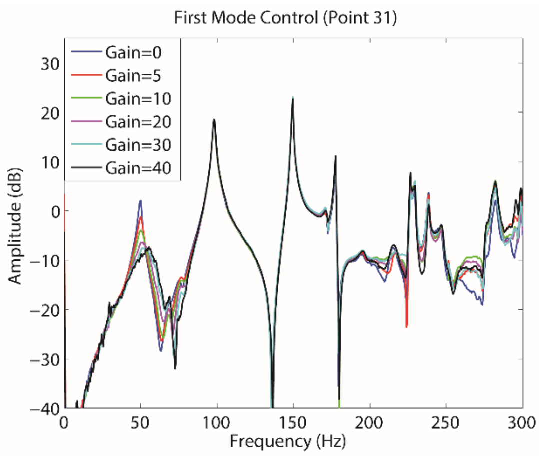

Figure 8.40 First mode control using STF based phase-lead controller for different control gains (Point 31)

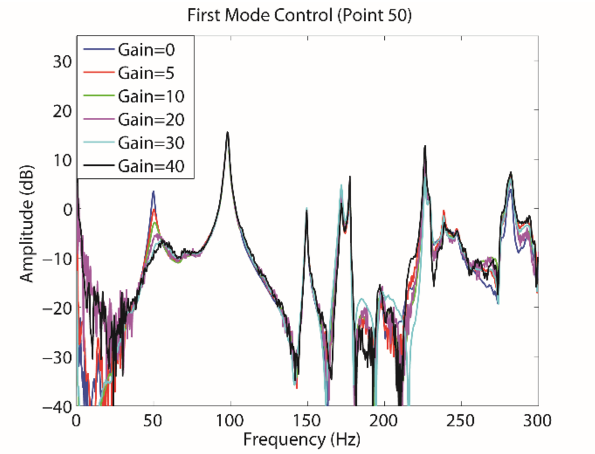

Figure 8.41 First mode control using STF based phase-lead controller for different control gains (Point 50)

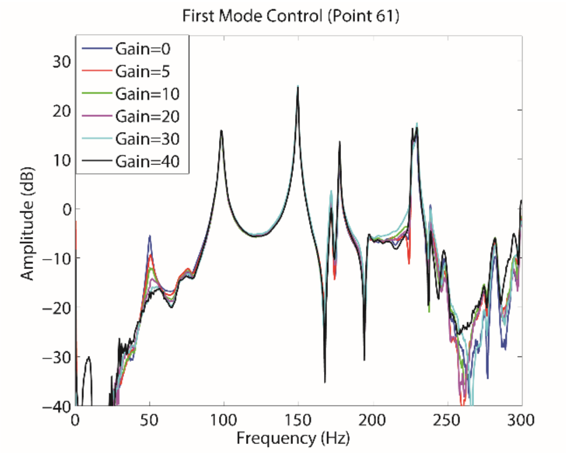

Figure 8.42 First mode control using STF based phase-lead controller for different control gains (Point 61)

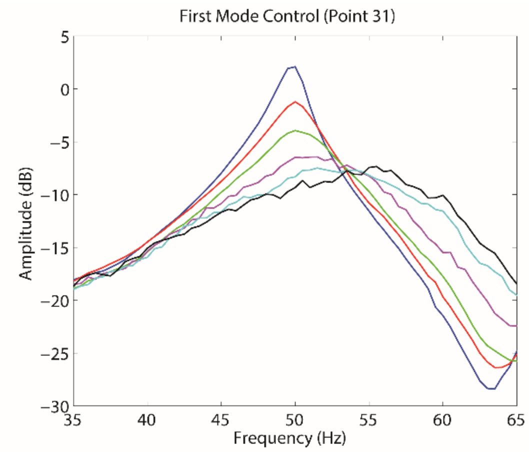

Figure 8.43 First mode control (Point 31)

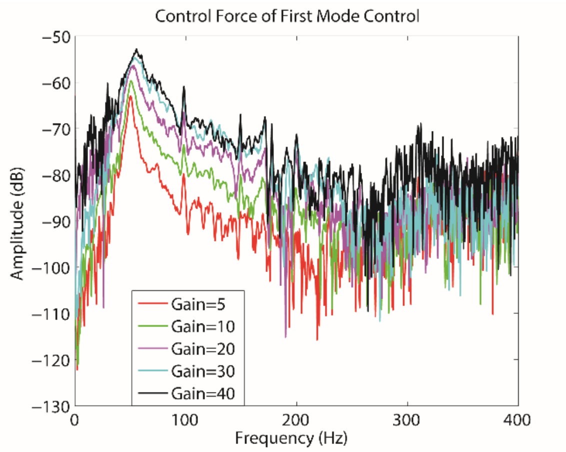

Figure 8.44 Control force outputs for different control gains (first mode)

Figure 8.44 shows the corresponding DSP control outputs. It is found that the spillover effects of higher modes can be neglected for the first mode control. Since a high pass filter is used, the low frequency noise and the responses of actuator dynamics around 20Hz are effectively reduced even for higher values of gain.

Figure 8.45 through Figure 8.50 illustrate the results of the second mode control. Similar to the first mode control, the STF performs excellent to extract the specified mode, and the phase lead compensator is found to function as to assure the control performance. Furthermore, these plots show uniform amplitude reduction of the second mode response at all the four sensor locations (compare the curves corresponding to a specific gain). This characteristics indicates that the global response reduction is achieved by the STF based controller.

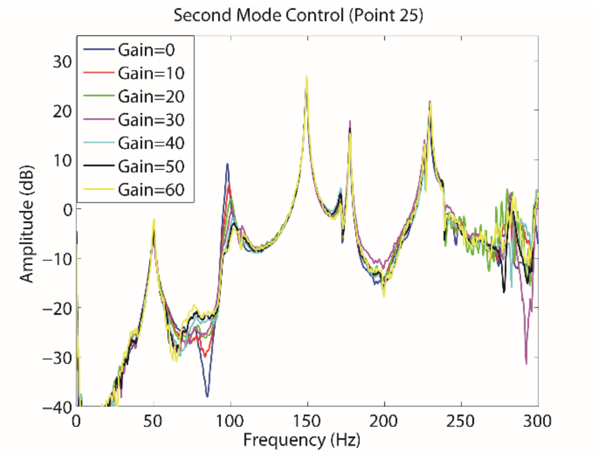

Figure 8.45 Second mode control using STF based phase-lead controller (Point 25)

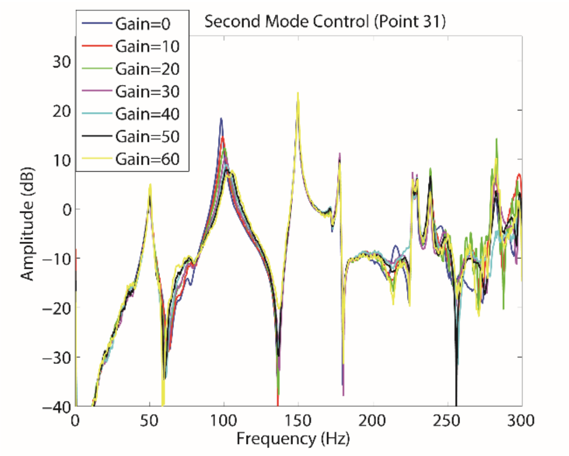

Figure 8.46 Second mode control using STF based phase-lead controller (Point 31)

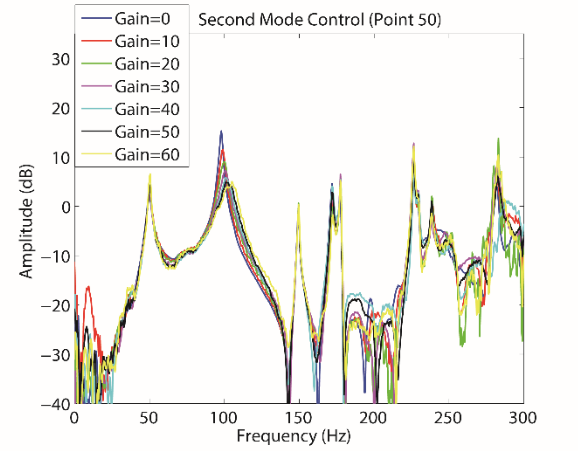

Figure 8.47 Second mode control using STF based phase-lead controller (Point 50)

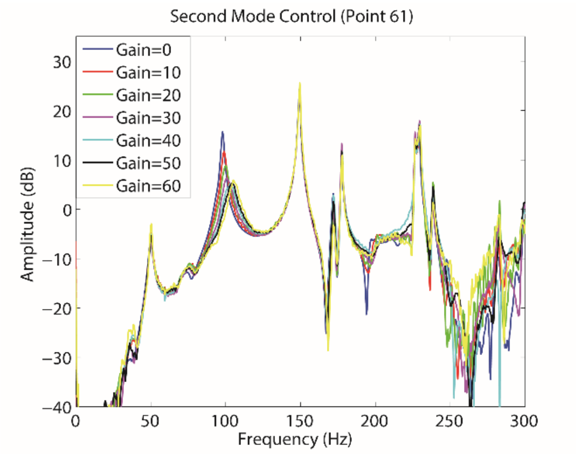

Figure 8.48 Second mode control using STF based phase-lead controller (Point 61)

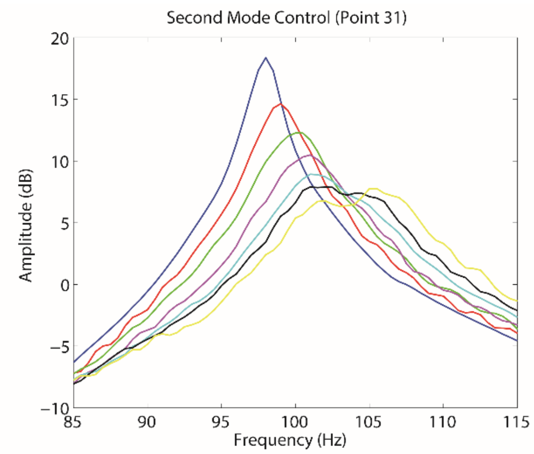

Figure 8.49 Second mode control (Point 31)

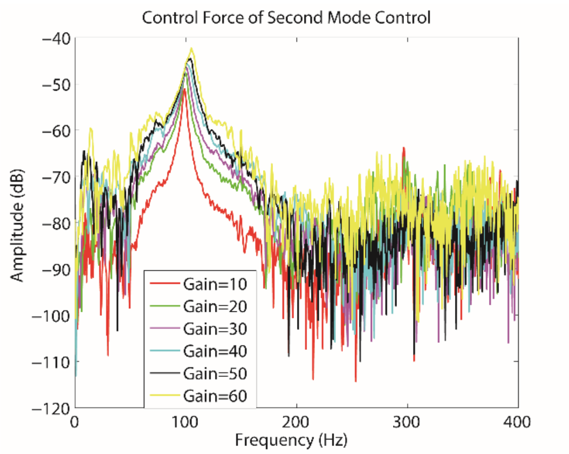

Figure 8.50 Control force outputs for different control gains (second mode)

8.6.3 STF based phase compensated controller

In this section, the STF combined with the phase compensated controller proposed in Sec. 7.2.2 is used to control the lowest three modes of the plate. Similarly to Sec. 8.6.2, the number of sensors is set to $NS = 4$ and the number of past sample is set to $N = 20$.

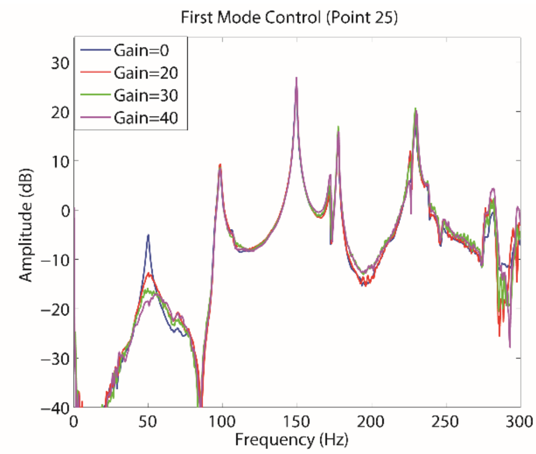

Figure 8.51 First mode control using STF based phase compensated controller for different control gains (Point 25)

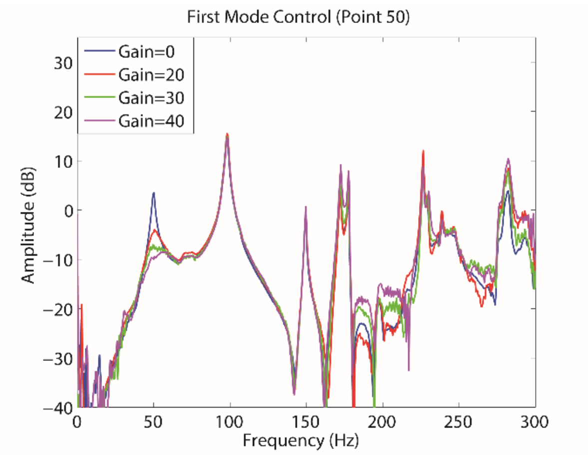

Figure 8.52 First mode control using STF based phase compensated controller for different control gains (Point 50)

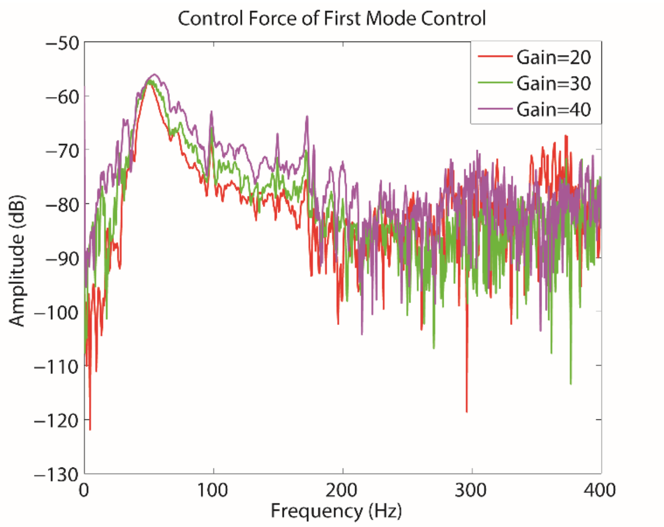

Figure 8.53 Control force outputs for different control gains (first mode)

The results of the first mode control are shown in Figure 8.51 through Figure 8.53. For simplification, only the results of two points are shown. It can be observed that the damping ratio of this mode increases while the frequency does not changes with the increase of the control gain.

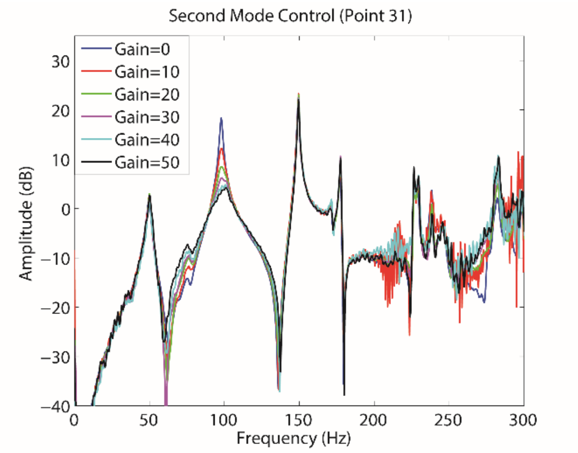

Figure 8.54 Second mode control using STF based phase compensated controller for different control gains (Point 31)

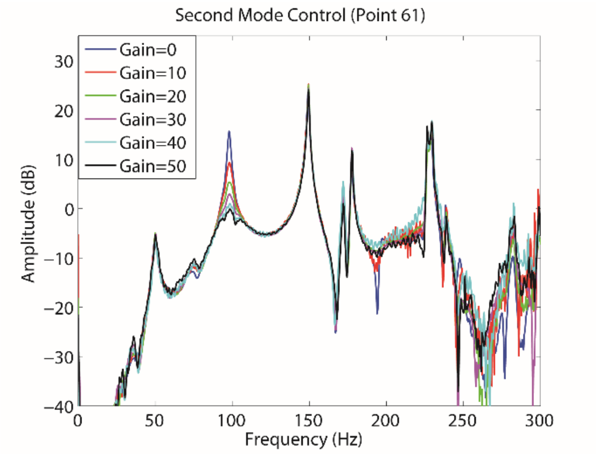

Figure 8.55 Second mode control using STF based phase compensated controller for different control gains (Point 61)

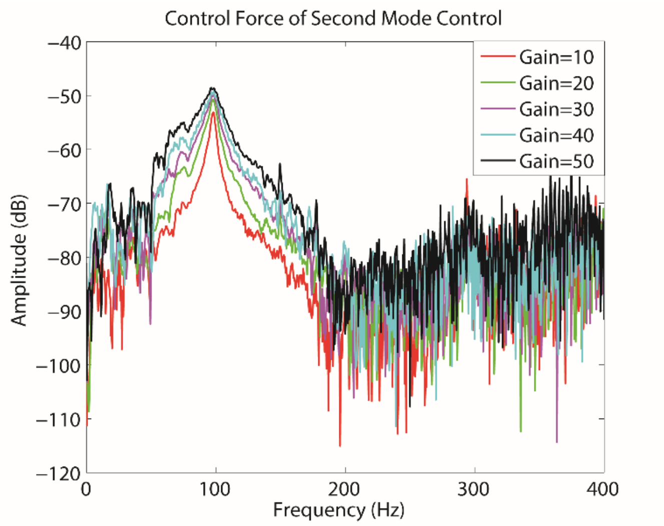

Figure 8.56 Control force outputs for different control gains (second mode)

The results of the second mode control are shown in Figure 8.54 to Figure 8.56. As can be seen from these figures, both of the STF and the phase compensation technique work considerably well for this mode.

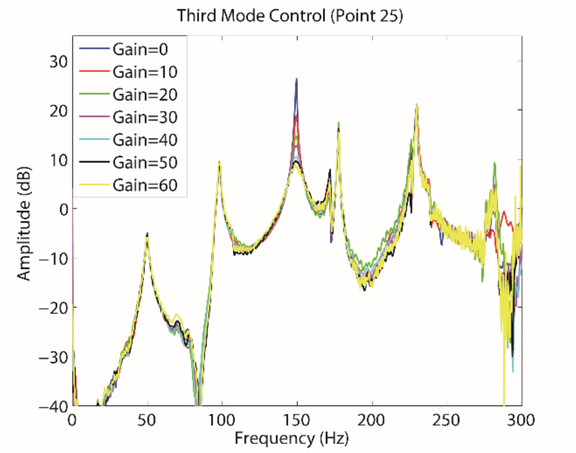

Figure 8.57 Third mode control using STF based phase compensated controller for different control gains (Point 25)

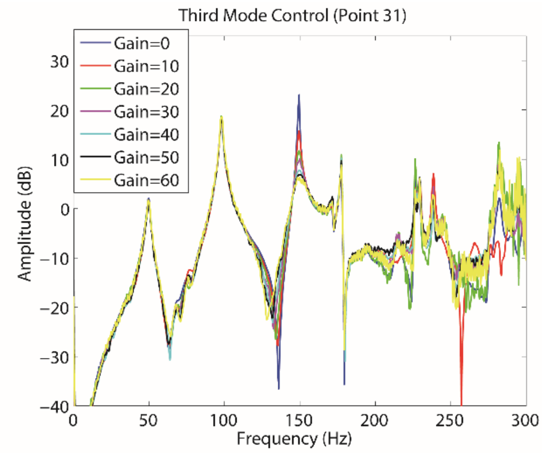

Figure 8.58 Third mode control using STF based phase compensated controller for different control gains (Point 31)

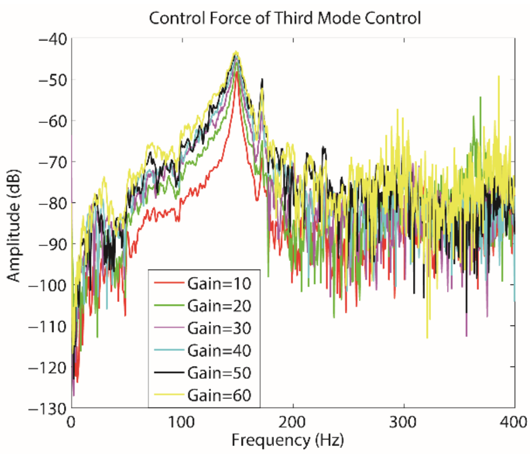

Figure 8.59 Control force outputs for different control gains (third mode)

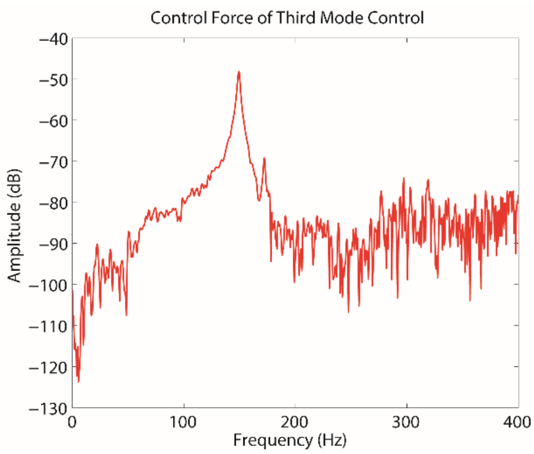

Figure 8.60 Control force outputs for small control gain (third mode)

Finally, testing of the STF based phase compensated controller is conducted for the third mode control, and the results are shown in Figure 8.57 through Figure 8.59. From Figure 8.59, the spillover effect of the fourth mode (172Hz) is observed. In fact, the spillover effect is negligible when the control gain is small, as shown in Figure 8.60. However, as the control gain increases, the peak of the fourth mode in Figure 8.59 considerably grows. This is because when the control gain is large, the poles of the fourth mode moves and reaches near the imaginary axis of the *s*-plane and therefore appear as the sharp peak of the frequency response function. The existence of the fourth mode responses even with STF application may be due to the inaccurate identified values of the modal frequency and damping ratio that have been used for the STF coefficients estimation. Further study is required.

8.6.4 STF based phase compensated controller using one sensor

In Secs. 8.3.2 and 8.3.3, it has been pointed out that extracting a specific mode with only one sensor is possible if the elite value (EV) for that mode at the sensor point is large. In this section, applicability of this idea to control the first mode is experimentally verified.

From Table 8.6, the sensor location with the greatest EV for the first mode is Point 50. Therefore, this point is used as the only sensor location to control the first mode using the STF based phase compensated controller. Two cases, $N = 20$ and $N = 40$, are tested and the test results are compared with the case of four sensors obtained in the previous section.

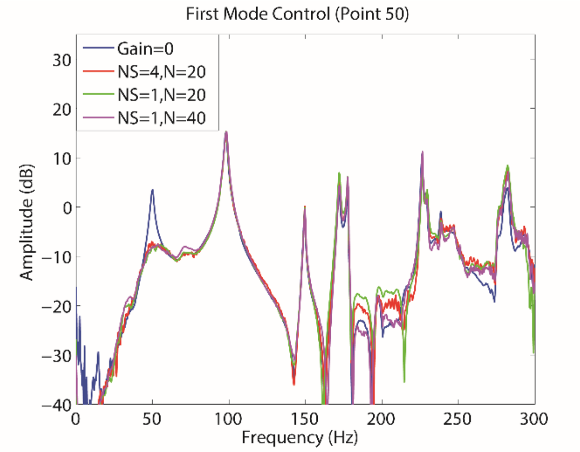

Figure 8.61 First mode control results of Point 50 using one sensor at Point 50 (Gain=30)

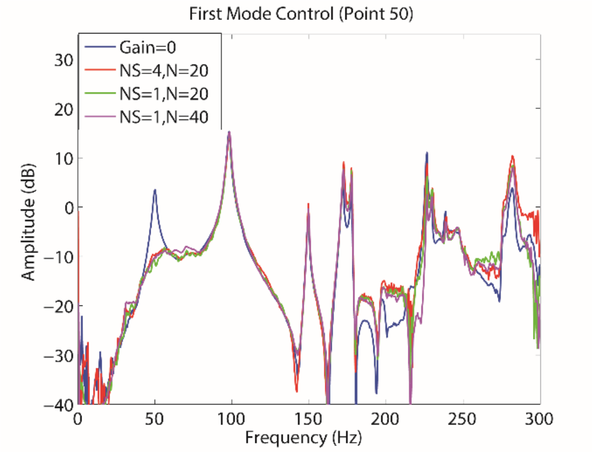

Figure 8.62 First mode control results of Point 50 using one sensor at Point 50 (Gain=40)

The measured plate response at Point 50 is shown in Figure 8.61 and Figure 8.62 for the control gains of 30 and 40, respectively. It is clearly shown by these figures that control of the first mode with one sensor is successful, with almost the same control performance as the four sensor case.

The responses of other three points are shown in Figure 8.63 through Figure 8.68. The results show that control of the other points with one sensor is also achieved.

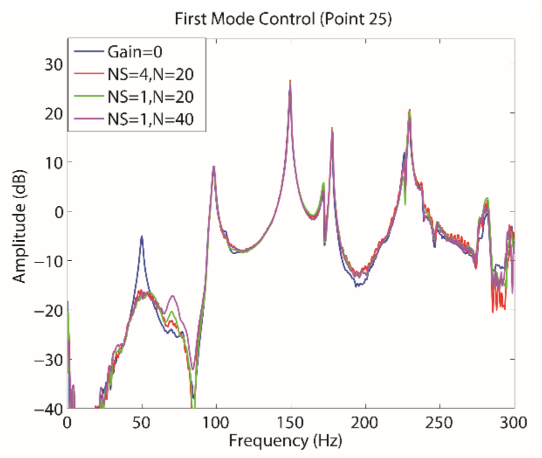

Figure 8.63 First mode control results of Point 25 using one sensor at Point 50 (Gain=30)

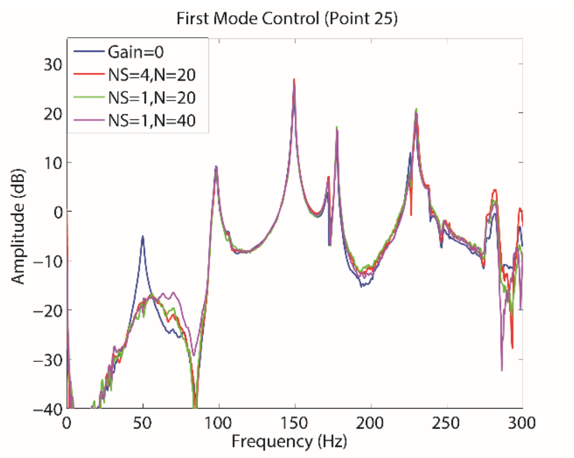

Figure 8.64 First mode control results of Point 25 using one sensor at Point 50 (Gain=40)

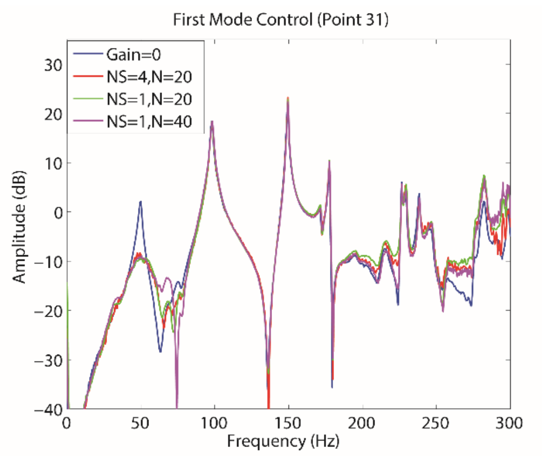

Figure 8.65 First mode control results of Point 31 using one sensor at Point 50 (Gain=30)

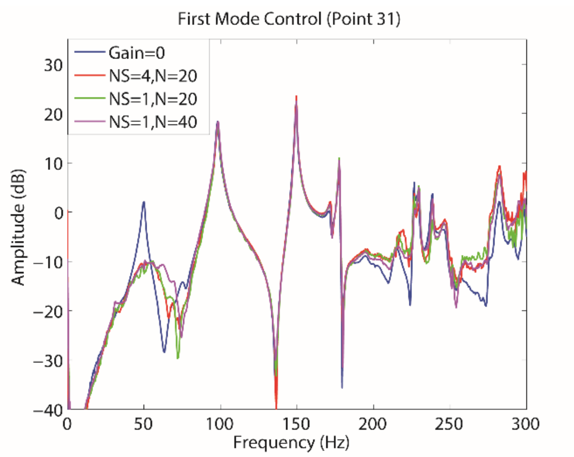

Figure 8.66 First mode control results of Point 31 using one sensor at Point 50 (Gain=40)

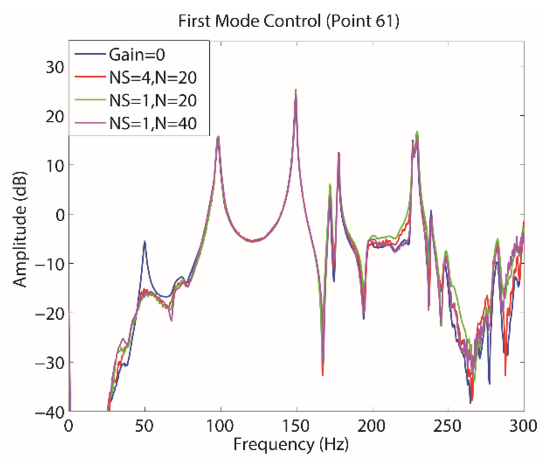

Figure 8.67 First mode control results of Point 61 using one sensor at Point 50 (Gain=30)

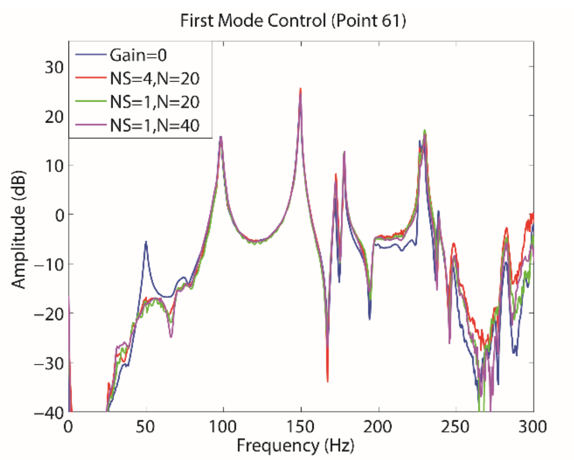

Figure 8.68 First mode control results of Point 61 using one sensor at Point 50 (Gain=40)

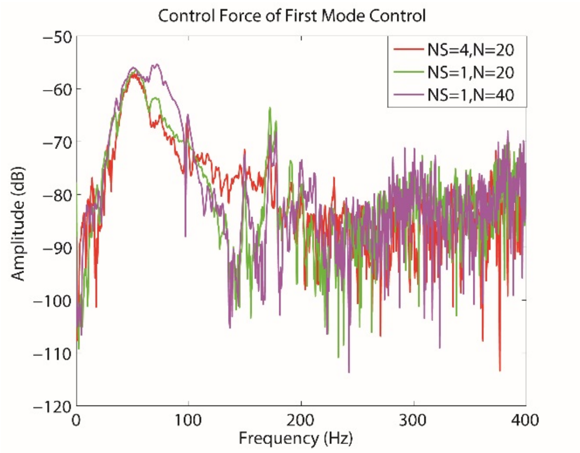

Figure 8.69 Control force outputs (Gain=30)

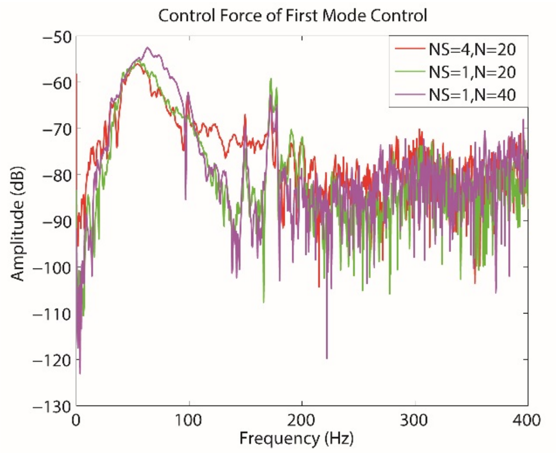

Figure 8.70 Control force outputs (Gain=40)

Figure 8.69 and Figure 8.70 show the corresponding DSP control force outputs. It can be observed that the performance of the $NS = 4$ case is the best while the width of the first mode peak of the control force spectrum for the case of $NS = 1$ and $N = 40$ becomes wider than that of the other two cases. The reason is due to the overfitting of the model when $NS = 1$ and $N = 40$ is used, which means that the fitted model is too closely to the particularities of the training data set (the white noise excitation) and obtain a model that works well on the training data but is not able to fit the new data set (hammer loading).

While the same location Point 50 can also be used for the second mode control, it is not effective to use Point 50 to control the third mode, based on the EV value criterion. Therefore, if control of multiple modes is considered, use of multiple sensors is recommended.

8.6.5 STF based phase compensated control of multiple modes

In this final section, the tests of multiple mode control using the STF based phase compensated controller are conducted. The time domain responses and the corresponding frequency response functions are shown in order to deeply understand the mechanism of model-based active control.

Figure 8.71 and Figure 8.72 show the acceleration response at Point 25 with and without the first-and-second-mode control. Although the spectral responses in the first and second modes are reduced, effects on the peak and decay of the acceleration response cannot be seen in Figure 8.72. This is because the contribution of the lowest two modes to the response at Point 25, which is dominated by the third and higher modes, is minor, as shown in Figure 8.71. On the other hand, at Point 50 where the principal contribution to the response is of the lowest two modes, the measured acceleration is remarkably reduced as shown in Figure 8.73 and Figure 8.74. Figure 8.75 and Figure 8.76 give the corresponding DSP control outputs. It is observed that the spillover effects of higher modes can be neglected for the first-and-second-mode control. The low frequency noise and the responses of actuator dynamics around 20Hz are also effectively reduced due to the use of the high pass filter.

The results of first and third mode control are shown in Figure 8.77 through Figure 8.82, indicating the acceleration responses at Points 25 and 31. Because the responses at these points contain considerable second mode and fourth or higher mode components, the response decay is not outstanding. Nonetheless, the response at Point 25 shown by Figure 8.78 is more efficiently reduced compared with the response under first-and-second-mode control shown by Figure 8.72, due to the higher proportion of the third mode content in the original response at Point 25.

Figure 8.83 to Figure 8.88 show the response of Point 31 and 61 to indicate the result of the second-and-third-mode control. At these two points, the effectiveness of the control is notable.

Finally, the responses at Points 25 and 31 when first-second-third-mode control is applied are shown in Figure 8.89 through Figure 8.94. Considerable fourth and higher mode components are still visible in the response at Point 25, these higher modes must be controlled to further improve the control performance. On the other hand, since the responses of higher modes are relatively small, the control performance at Point 31 is excellent since the higher mode response at Point 31 is relatively small.

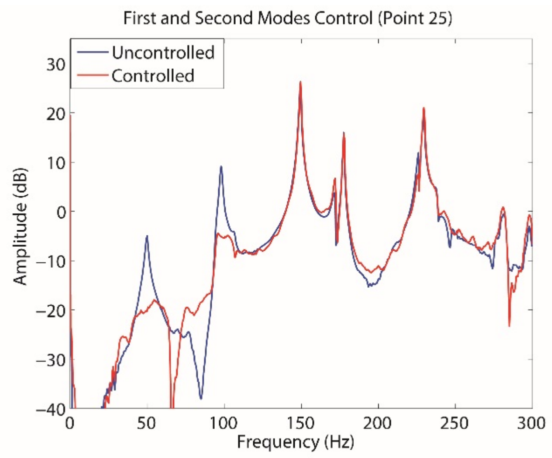

Figure 8.71 Test result: lowest two modes control at Point 25 (frequency domain)

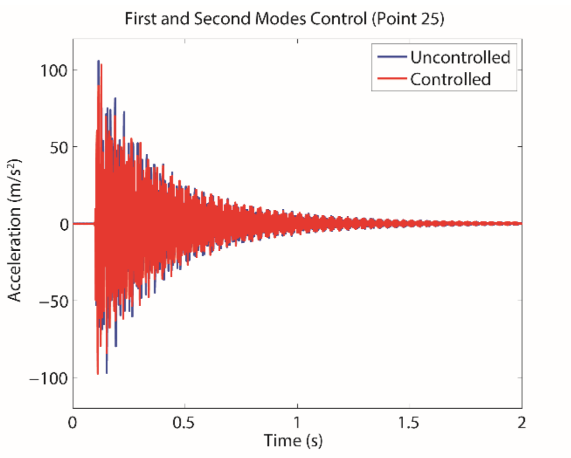

Figure 8.72 Test result: lowest two modes control at Point 25 (time domain)

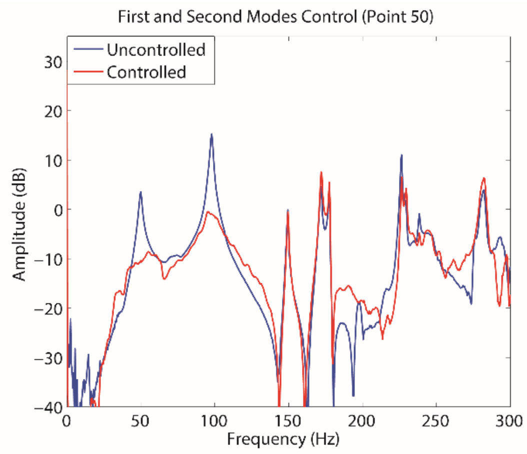

Figure 8.73 Test result: lowest two modes control at Point 50 (frequency domain)

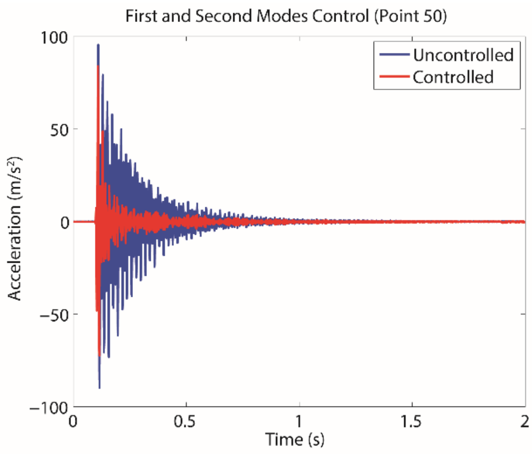

Figure 8.74 Test result: lowest two modes control at Point 50 (time domain)

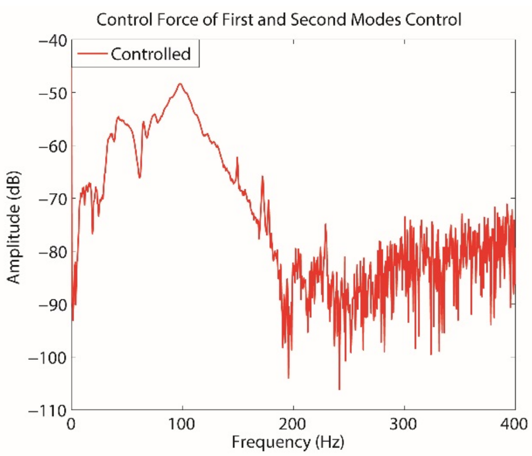

Figure 8.75 Test result: lowest two modes control output (frequency domain)

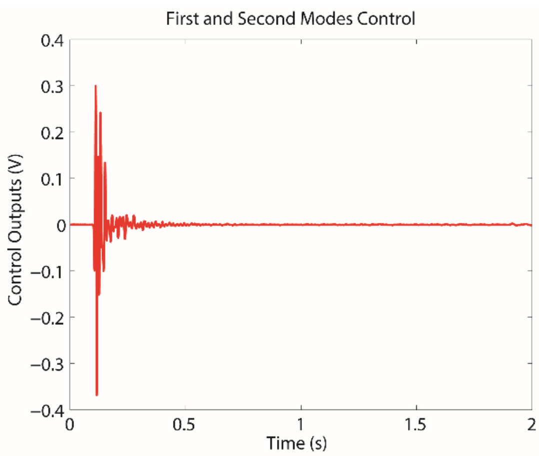

Figure 8.76 Test result: lowest two modes control output (time domain)

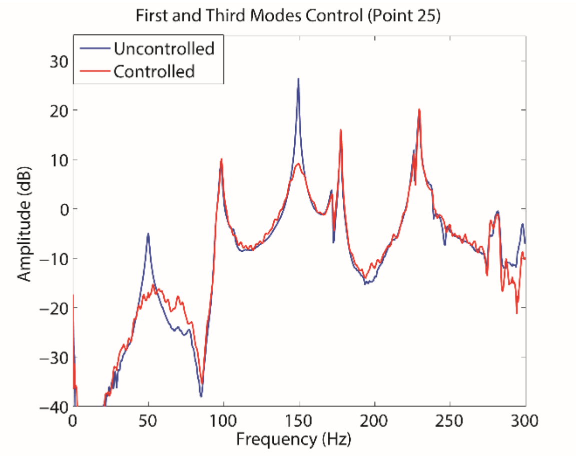

Figure 8.77 Test result: first and third modes control at Point 25 (frequency domain)

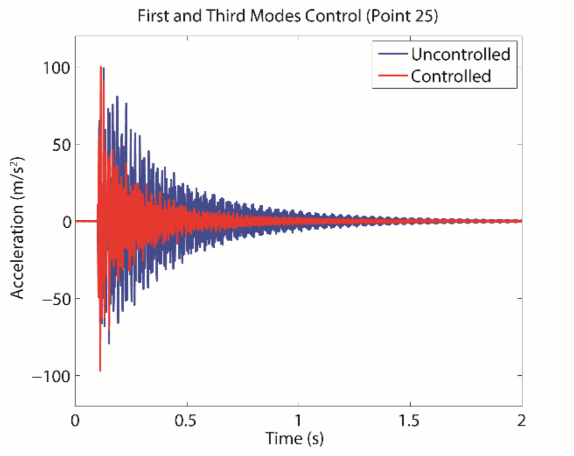

Figure 8.78 Test result: first and third modes control at Point 25 (time domain)

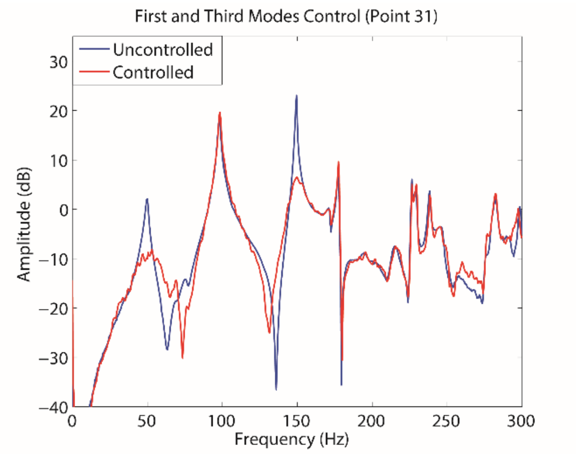

Figure 8.79 Test result: first and third modes control at Point 31 (frequency domain)

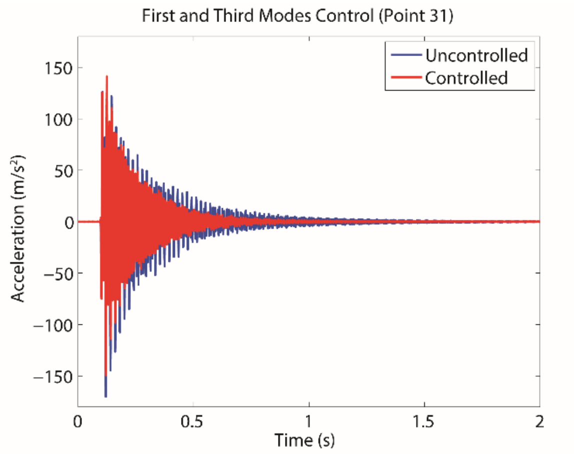

Figure 8.80 Test result: first and third modes control at Point 31 (time domain)

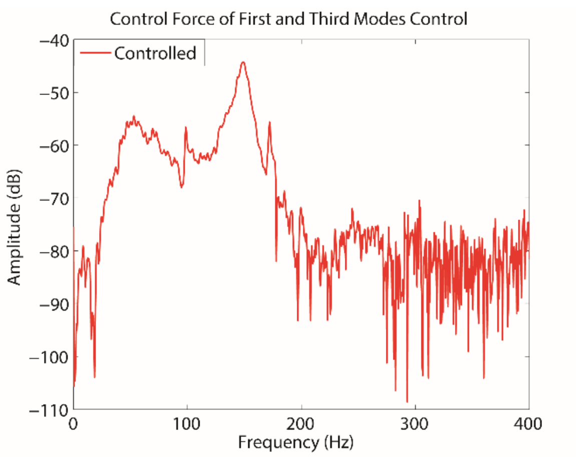

Figure 8.81 Test result: first and third modes control output (frequency domain)

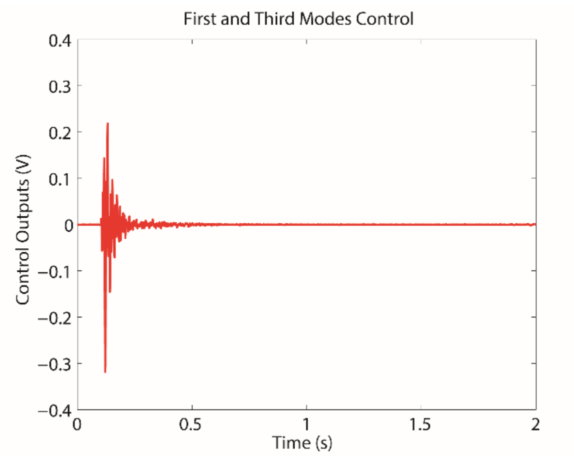

Figure 8.82 Test result: first and third modes control output (time domain)

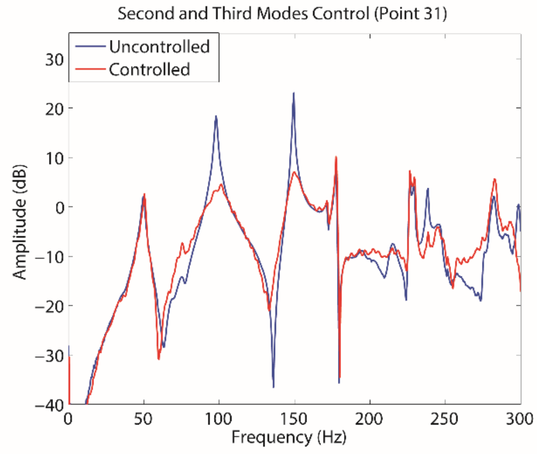

Figure 8.83 Test result: second and third modes control at Point 31 (frequency domain)

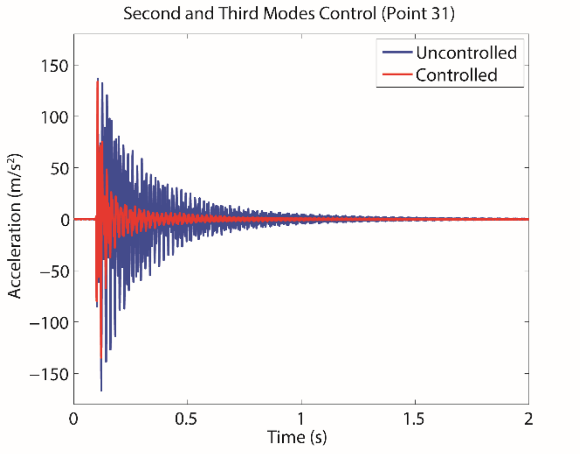

Figure 8.84 Test result: second and third modes control at Point 31 (time domain)

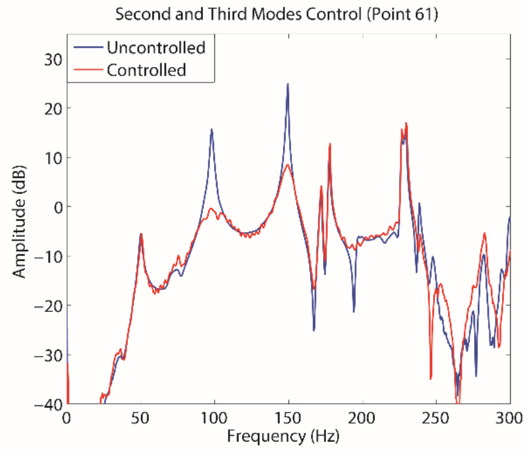

Figure 8.85 Test result: second and third modes control at Point 61 (frequency domain)

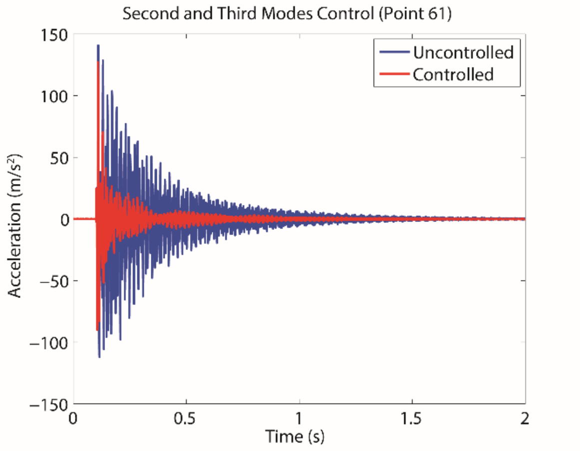

Figure 8.86 Test result: second and third modes control at Point 61 (time domain)

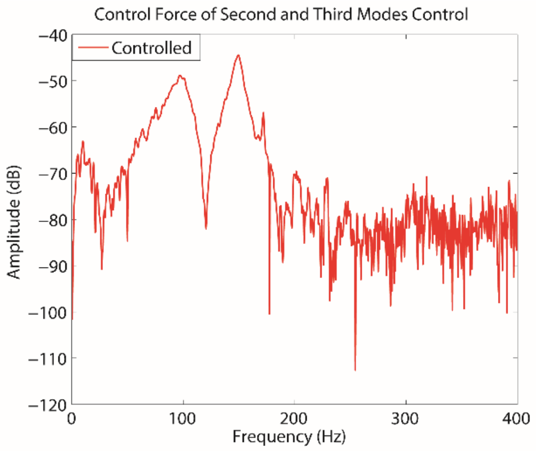

Figure 8.87 Test result: second and third modes control output (frequency domain)

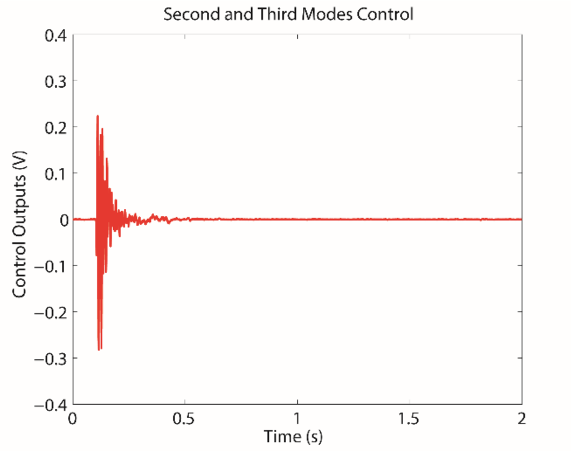

Figure 8.88 Test result: second and third modes control output (time domain)

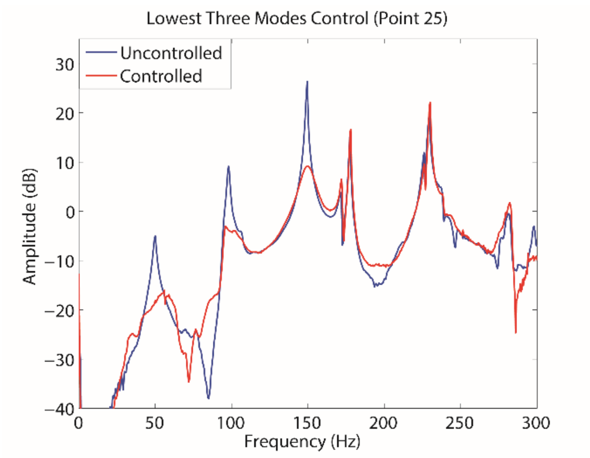

Figure 8.89 Test result: lowest three modes control at Point 25 (frequency domain)

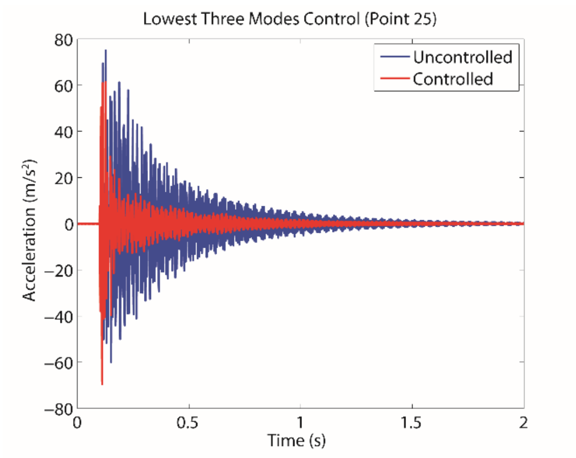

Figure 8.90 Test result: lowest three modes control at Point 25 (time domain)

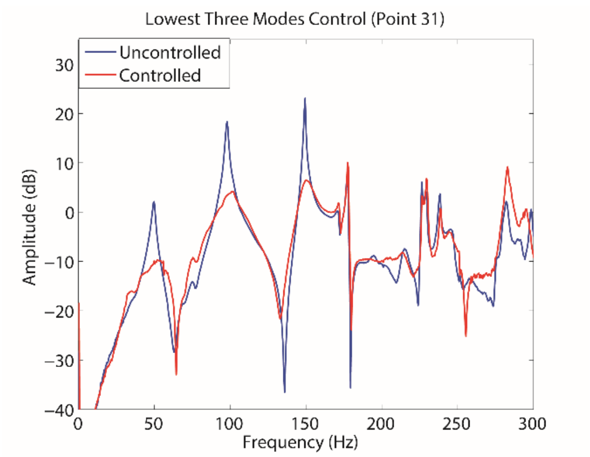

Figure 8.91 Test result: lowest three modes control at Point 31 (frequency domain)

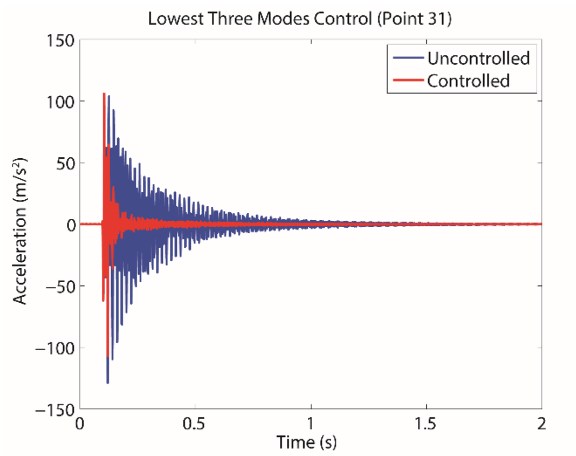

Figure 8.92 Test result: lowest three modes control at Point 31 (time domain)

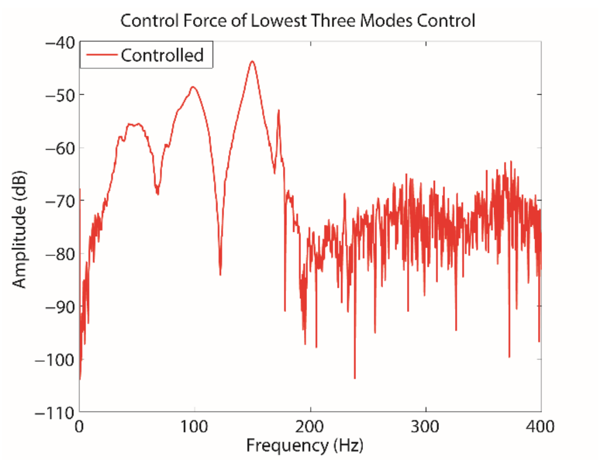

Figure 8.93 Test result: lowest modes control output (frequency domain)

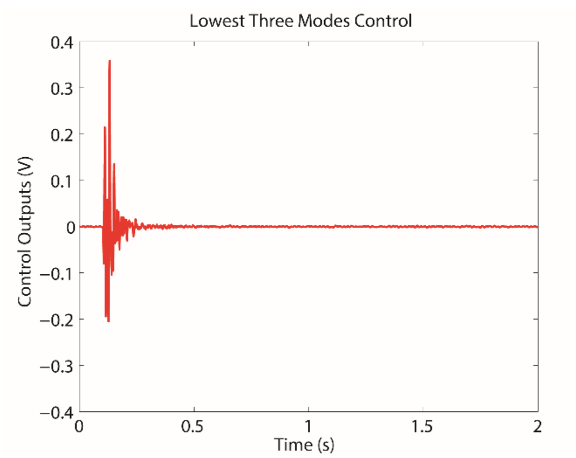

Figure 8.94 Test result: lowest modes control output (time domain)

It should be noted that the impact excitation with the hammer is applied to Point 21 in all the cases. It can be confirmed that the second and third modes are fully excited with the impact, based on the information in Table 4.5. Therefore, the control performance for the second and third modes is significantly superior to the control performance for the other modes. However, if the impact is applied to the center of the plate, control of the first mode becomes effective.

Therefore, the model-based active control is particularly effective when several modes of the floor are intensely excited. Focusing the control power resource on the target modes is practically efficient not only in avoiding force and stroke saturation which may cause system instability, but also in reducing initial and running costs for active control operation.

8.7 Summary

Non-adaptive spatial-temporal filtering (STF) combined with a phase-compensated modal velocity feedback control strategy is proposed in this chapter. The proposed control scheme is expected to achieve a simple and robust active control strategy without requiring extensive and accurate system models. One of the merits of this approach is that complete modelling of the floor, actuator and other dynamic components is not necessary, and it enables the control system to be implemented to difficult real-world applications.

The theory of STF is described first and the off-line search method of STF coefficients is proposed. Two indices of separation performance of STF, Root-Mean-Square (RMS) error and the coefficient of determination R^2, are introduced.

Then, the performance of the proposed non-adaptive STF is examined using the test results of three cases with five sensor points. The effects of the past sample numbers, sensor numbers, sensor and actuator locations are studied. The numbers of the sensors and past samples are important parameters for accurate estimate of modal coordinates. It is found that there is a trade-off between the sensor numbers and the past sample numbers. The concepts of effective points (EP), elite point (ELP) and elite value (EV) are introduced for sensor and actuator placement and it is shown that estimation of modal coordinates is possible with only a single sensor if the location of the sensor has a high EV. Observability and controllability should be considered during the sensor and actuator placement.

It is found that the STF is effective and robust against the change of the modal frequency and damping ratio if the number of sensors is sufficient. Even if the number of sensor is few, the effectiveness and robustness are still acceptable.

Chapter 9 Conclusions and Recommendations

9.1 Conclusions

In the studies presented in this dissertation, model-based strategies for real-time active control of floor structures were developed and the control performance of the proposed strategies was investigated by verification tests using a steel plate model under impact loading and control system hardware. In the developed control system, the individual natural modes of vibration of the floor structures are extracted with the modal filtering (MF) and spatio-temporal filtering (STF) techniques. For the separated modal responses to be controlled, the time delays caused by dynamic components involved in the system can be efficiently compensated using a simple PI framework in the actual implementation of the control strategies to control hardware. Real-time active control experiments were successfully conducted using the test systems with a DSP system, piezoelectric accelerometers and a magneto-electric actuator. The proposed model-based active control strategy is a promising approach to reduce the vibration of real-world floor structures, since extensive and accurate system models are not required for the implementation.

The background for this study was provided in Chapter 1, 2 and 3. Current methods for real-time active control of floor structures and the history of modal filtering methods were reviewed. Emphasis was placed on the modal filtering method, the modal direct velocity feedback controller, the spillover effects and actuator-structure interaction and the effects of time delays of the dynamic components were identified.

The experimental setup for the testing of real-time active control was presented in Chapter 4. The test system consists of a square steel plate and real-time signal processing hardware including a high-performance actuator system. The capability of the system in high speed computations and communication is demonstrated by preliminary test results. Five natural vibration modes with associated natural frequencies less than 200Hz were identified. The time delays caused by the dynamic components in the test system were also identified, and it was found that time delays associated with the A/D-D/A Conversions as well as with the dynamics of the actuator and Butterworth filters were the major factors, while the computing time and delays related to communication were, in general, relatively small.

In Chapter 5, a procedure for the optimal sensor and actuator placement applicable to modal filtering based active control of floor vibration was proposed. The method provides a solution to the problems of minimization of the spillover effects, consideration for orthogonality of the natural vibration modes and system observability. The proposed method is effective in the reduction of the spillover effect of the residual modes and enhancing the separation performance of the modelled modes. The procedure for the determination of the optimal sensor placement and optimal actuator placement was presented. The effectiveness of the proposed method was demonstrated by an example of the four-sensor placement problem in the test system. However, limitation of the method was also revealed from the test result showing that the spillover effects of the residual modes cannot be completely eliminated.

In Chapter 6, design of the phase-lead compensator based on the dynamic characteristics of the actuator and controller hardware is described. The first-order phase-lead compensator was investigated in order to achieve sufficient system stability margin and damping for the control modes. The root locus method was used to calculate the phase-lead compensator parameters for individual control modes. The experimental verification of the application of the MDOF controller to individual mode control was conducted. Although the MDOF controller did not perform well for the second and third modes of the plate, when the phase-lead compensators are combined, a good performance with significant reduction of the response of the specified modes to be controlled was obtained.

In Chapter 7, the PI-based mode-by-mode phase compensation technique was developed. As long as the modal frequency of one control mode is known, the PI parameters can be automatically obtained through several on-site experiments. Two techniques of PI parameter search were developed – Standard phase compensation and modified phase compensation. The modified procedure incorporating the bandpass filtering of the response measurement signal is more stable than the standard procedure even in the presence of severe transient response caused by higher order dynamic components. Combination of the PI-based mode-by-mode phase compensation technique and modal direct velocity feedback control was proposed as the Phase Compensated Velocity Feedback control (PCVFB control). The test results showed the improved while limited performance of the PCVFB controller. The PCVFB control combined with a bandpass filter was found to be most effective in the tests.

In Chapter 8, use of non-adaptive spatial-temporal filtering (STF) was proposed to solve the problems of the need of complete information on the modes in the modal filtering technique. The performance of the proposed non-adaptive STF were examined based on numerical simulation with the effects of past sample numbers, sensor numbers, sensor and actuator locations. The effectiveness and robustness of STF were also investigated to show that the number of the sensors can be reduced by using STF. The control performance of the STF based phase-lead, phase-compensated mode-by-mode control were found to be excellent, circumventing the spillover effects of higher modes.

9.2 Future Studies

This section provides recommendations for future research related to this study.

- In the experiments conducted in this study, a steel plate was used as the floor structure. Effectiveness of the proposed active control strategies should be verified using real-world floor structures.
- Impact loading was applied to the same location with a hammer for all the tests. Excitation at different locations and other type of impact loadings, including human induced footsteps, should be used to demonstrate the performance of the proposed control strategies.
- Only one actuator was used in the experiments in this study. Extension of the methodologies and techniques for multiple actuators should be investigated.
- The proposed sensor and actuator placement method were only studied using a small number of sensors and one actuator. Verification tests for a large number of sensors and multiple actuators should be conducted.
- During real-time active control, the control gains were tuned by trial and error experiments, which becomes time consuming and troublesome when multiple actuators and a greater number of modes are considered. Techniques for searching the optimal control gain in such situations using a wider range of methodologies, including the genetic algorithm (GA) for example, should be investigated.
- Fixed bandpass filters (cut-off frequencies for high pass and low pass are 20Hz and 200Hz, respectively) were used for the tests. Use of diffident bandpass filters depending on the mode to be controlled should be investigated so that the effects of spillover can be sufficiently reduced for the normal modal filtering based controller.
- As opposed to the non-adaptive STF used in this study, an adaptive STF based controller should be developed, so that the modal frequencies and modal damping ratios are identified first and the corresponding STF coefficients and control gains are computed in real-time. (e.g. combining the adaptive STF and ERA)
- The aim of the proposed feedback controllers is enhancement of the modal damping to reduce the response of the modes of the floor structures to be controlled. However, feedback control is not suitable for reduction of the amplitude of first peak in the time domain responses under impact loading. Therefore, feedforward control to suppress the first peak combined with the proposed feedback controllers should be investigated to improve the control performance. (e.g. disturbance observer based controller)

References

[1] M. J. Hudson and P. Reynolds, "Implementation considerations for active vibration control in the design of floor structures," *Eng. Struct.*, vol. 44, pp. 334–358, 2012.

[2] A. L. Smith, S. J. Hicks, and P. J. Devine, *Design of floors for vibration - A new approach*. The Steel Construction Institute, 2007.

[3] H. Bachmann, "Case studies of structures with man-induced vibrations," *J. Struct. Eng.*, vol. 118, no. 3, pp. 631–647, 1992.

[4] A. Ebrahimpour and R. L. Sack, "A review of vibration serviceability criteria for floor structures," *Comput. Struct.*, vol. 83, no. 28, pp. 2488–2494, 2005.

[5] L. M. Hanagan and T. M. Murray, "Active control approach for reducing floor vibration," *J. Struct. Eng.*, vol. 123, no. 11, pp. 1497–1505, 1997.

[6] S. Živanovic and A. Pavic, "Probabilistic modeling of walking excitation for building floors," *J. Perform. Constr. Facil.*, vol. 23, no. 3, pp. 132–143, 2009.

[7] J. M. W. Brownjohn and C. J. Middleton, "Procedures for vibration serviceability assessment of high-frequency floors," *Eng. Struct.*, vol. 30, no. 6, pp. 1548–1559, 2008.

[8] C. J. Middleton and J. M. W. Brownjohn, "Response of high frequency floors: A literature review," *Eng. Struct.*, vol. 32, no. 2, pp. 337–352, 2010.

[9] Z. M. Miskovic, A. Pavic, and P. Reynolds, "Effects of full-height nonstructural partitions on modal properties of two nominally identical building floors," *Can. J. Civ. Eng.*, vol. 36, no. 7, pp. 1121–1132, 2009.

[10] M. Setareh and R. D. Hanson, "Tuned mass dampers to control floor vibration from humans," *J. Struct. Eng.*, vol. 118, no. 3, pp. 741–762, 1992.

[11] L. M. Hanagan, T. M. Murray, and K. Premaratne, "Controlling floor vibration with active and passive Devices," *Shock Vib. Dig.*, vol. 35, no. 5, pp. 347–365, 2003.

[12] W. O. Wong and Y. L. Cheung, "Optimal design of a damped dynamic vibration absorber for vibration control of structure excited by ground motion," *Eng. Struct.*, vol. 30, no. 1, pp. 282–286, 2008.

[13] K. F. Liu and G. Coppola, “Optimal design of damped dynamic vibration absorber for damped primary systems,” *Trans. Can. Soc. Mech. Eng.*, vol. 34, no. 1, pp. 119–135, 2010.

[14] G. B. Warburton, “Optimum absorber parameters for various combinations of response and excitation parameters,” *Earthq. Eng. Struct. Dyn.*, vol. 10, no. 3, pp. 381–402, 1982.

[15] C. Li, “Optimum multiple tuned mass dampers for structures under the ground acceleration based on DDMF and ADMF,” *Earthq. Eng. Struct. Dyn.*, vol. 31, no. 4, pp. 897–919, Apr. 2002.

[16] H. Yamaguchi and N. Harnpornchai, “Fundamental characteristics of multiple tuned mass dampers for suppressing harmonically forced oscillations,” *Earthq. Eng. Struct. Dyn.*, vol. 22, no. 1, pp. 51–62, Jan. 1993.

[17] B. F. Spencer and T. T. Soong, “New applications and development of active, semi-active and hybrid control techniques for seismic and non-seismic vibration in the USA,” *Proc. Int. PostSMiRT Conf. Semin. Seism. Isol. Passiv. Energy Dissipation Act. Control Vib. Struct.*, vol. 25, 1999.

[18] D. A. Wang and Y. M. Huang, “Modal space vibration control of a beam by using the feedforward and feedback control loops,” *Int. J. Mech. Sci.*, vol. 44, no. 1, pp. 1–19, 2002.

[19] T. T. Soong and B. F. Spencer, “Supplemental energy dissipation: state-of-the-art and state-of-the-practice,” *Eng. Struct.*, vol. 24, no. 3, pp. 243–259, 2002.

[20] Y. Xia and A. Ghasempoor, “Active Vibration Suppression Using Neural Networks,” in *Proceedings of the World Congress on Engineering*, 2009, vol. 2, pp. 1–6.

[21] S. Korkmaz, “A review of active structural control: challenges for engineering informatics,” *Comput. Struct.*, vol. 89, no. 23, pp. 2113–2132, 2011.

[22] G. W. Housner, L. A. Bergman, T. K. Caughey, A. G. Chassiakos, R. O. Claus, S. F. Masri, R. E. Skelton, T. T. Soong, B. F. Spencer, and J. T. P. Yao, “Structural control: past, present, and future,” *J. Eng. Mech.*, vol. 123, no. 9, pp. 897–971, 1997.

[23] M. J. Balas, “Direct velocity feedback control of large space structures,” *J. Guid. Control. Dyn.*, vol. 2, no. 3, pp. 252–253, 1979.

[24] I. M. Díaz and P. Reynolds, “Acceleration feedback control of human-induced floor vibrations,” *Eng. Struct.*, vol. 32, no. 1, pp. 163–173, 2010.

[25] I. M. Díaz, E. Pereira, M. J. Hudson, and P. Reynolds, “Enhancing active vibration control of pedestrian structures using inertial actuators with local feedback control,” *Eng. Struct.*, vol. 41, pp. 157–166, 2012.

[26] J. C. Wu, H. H. Chih, and C. H. Chen, “A robust control method for seismic protection of civil frame building,” *J. Sound Vib.*, vol. 294, no. 1, pp. 314–328, 2006.

[27] J. C. Wu, J. N. Yang, and W. E. Schmitendorf, “Reduced-order H∞ and LQR control for wind-excited tall buildings,” *Eng. Struct.*, vol. 20, no. 3, pp. 222–236, 1998.

[28] M. D. Symans and M. C. Constantinou, “Semi-active control systems for seismic protection of structures: a state-of-the-art review,” *Eng. Struct.*, vol. 21, no. 6, pp. 469–487, 1999.

[29] N. Jalili, “A comparative study and analysis of semi-active vibration-control systems,” *Am. Soc. Mech. Eng.*, vol. 124, no. 4, pp. 593–605, 2002.

[30] M. Setareh, “Floor vibration control using semi-active tuned mass dampers,” *Can. J. Civ. Eng.*, vol. 29, no. 1, pp. 76–84, 2002.

[31] M. I. Friswell and J. E. Mottershead, *Finite element model updating in structural dynamics*. Springer Science & Business Media, 2013.

[32] L. M. Hanagan, “Walking-Induced Floor Vibration Case Studies,” *J. Archit. Eng.*, vol. 11, no. 1, pp. 14–18, 2005.

[33] I. M. Díaz and P. Reynolds, “On-off nonlinear active control of floor vibrations,” *Mech. Syst. Signal Process.*, vol. 24, no. 6, pp. 1711–1726, 2010.

[34] I. M. Diaz and P. Reynolds, “Robust saturated control of human-induced floor vibrations via a proof-mass actuator,” *Smart Mater. Struct.*, vol. 18, no. 12, 2009.

[35] E. Shahabpoor, P. Reynolds, and D. Nyawako, “A comparison of direct velocity, direct and compensated acceleration feed-back control systems in mitigation of low-frequency floor vibrations,” *Dyn. Civ. Struct.*, vol. 4, pp. 177–187, 2011.

[36] D. Nyawako and P. Reynolds, “Response-dependent velocity feedback control for mitigation of human-induced floor vibrations,” *Smart Mater. Struct.*, vol. 18, no. 7, 2009.

[37] D. Nyawako, P. Reynolds, and E. Hudson, “Incorporating a disturbance observer with direct velocity feedback for control of human-induced vibrations,” in *Proceedings of the Society of Photo-optical Instrumentation Engineers (SPIE)*, 2016.

[38] M. J. Hudson, P. Reynolds, and D. Nyawako, “Efficient design of floor structures using active vibration control,” in *Structures Congress*, 2011, pp. 404–415.

[39] M. Zilletti, S. J. Elliott, and P. Gardonio, “Self-tuning control systems of decentralised velocity feedback,” *J. Sound Vib.*, vol. 329, no. 14, pp. 2738–2750, 2010.

[40] E. Pereira, I. M. Díaz, E. J. Hudson, and P. Reynolds, “Optimal control-based methodology for active vibration control of pedestrian structures,” *Eng. Struct.*, vol. 80, pp. 153–162, 2014.

[41] A. Bosse, T. W. Lim, and S. Shelley, “Modal filters and neural networks for adaptive vibration control,” *J. Vib. Control*, vol. 6, no. 4, pp. 631–648, 2000.

[42] P. R. Houlston, S. D. Garvey, and A. A. Popov, “Modal control of vibration in rotating machines and other generally damped systems,” *J. Sound Vib.*, vol. 302, no. 1, pp. 104–116, 2007.

[43] F. Resta, F. Ripamonti, G. Cazzulani, and M. Ferrari, “Independent modal control for nonlinear flexible structures: An experimental test rig,” *J. Sound Vib.*, vol. 329, no. 8, pp. 961–972, 2010.

[44] J. Suhardjo, B. F. Spencer, and A. Kareem, “Active control of wind excited buildings: A frequency domain based design approach,” *J. Wind Eng. Ind. Aerodyn.*, vol. 43, no. 1, pp. 1985–1996, 1992.

[45] B. F. Spencer, J. Suhardjo, and M. K. Sain, “Frequency domain optimal control strategies for aseismic protection,” *J. Eng. Mech.*, vol. 120, no. 1, pp. 135–158, 1994.

[46] D. S. Nyawako, P. Reynolds, and M. J. Hudson, “Approximate pole-placement controller using inverse plant dynamics for floor vibration control,” in *Proceedings of the Society of Photo-optical Instrumentation Engineers (SPIE)*, 2013.

[47] S. Daley and J. Wang, “A geometric approach to the design of remotely located vibration control systems,” *J. Sound Vib.*, vol. 318, no. 4, pp. 702–714, 2008.

[48] D. S. Nyawako and P. Reynolds, “Comparative studies of global and targeted control of walkway bridge resonant frequencies,” *J. Vib. Control*, 2016.

[49] L. Meirovitch and H. Baruh, “The implementation of modal filters for control of structures,” *J. Guid. Control. Dyn.*, vol. 8, no. 6, pp. 707–716, 1985.

[50] Q. Zhang, R. J. Allemang, and D. L. Brown., “Modal filter: Concept and applications,” in *Proceedings of the 8th International Modal Analysis Conference*, 1990, pp. 487–496.

[51] S. J. Shelly, R. J. Allemang, L. Freudinger, and Q. Zhang, “Implementation of a modal filter on a five meter truss structure,” in *Proceedings of the 9th International Modal Analysis Conference*, 1991, vol. 2, pp. 1036–1044.

[52] S. J. Shelley, H. Vold, and T. Sharp, “Structural control and monitoring using adaptive spatio-temporal filtering,” in *SPIE - The International Society for Optical Engineering*, 1997, pp. 732–738.

[53] S. J. Shelley, K. L. Lee, T. Aksel, and A. E. Aktan, “Active-control and forced-vibration studies on highway bridge,” *J. Struct. Eng.*, vol. 121, no. 9, pp. 1306–1312, 1995.

[54] S. J. Shelley, R. J. Allemang, G. L. Slater, and J. F. Schultze, “Active vibration control utilizing an adaptive modal filter based modal control method,” in *SPIE - The International Society for Optical Engineering*, 1993, pp. 751–751.

[55] C. K. Lee and F. C. Moon, “Modal Sensors/Actuators,” *J. Appl. Mech.*, vol. 57, no. 2, pp. 434–441, 1990.

[56] A. B. Bosse, T. D. Sharp, S. J. Shelley, K. K. Denoyer, and R. S. Erwin, “Control of the UltraLITE precision deployable test article using adaptive spatio-temporal filtering based control,” in *SPIE - 6th Annual International Symposium on Smart Structures and Materials*, 1999, vol. 3668, pp. 1–11.

[57] S. J. Shelley, T. D. Sharp, and K. K. Denoyer, “Robust line-of-sight stability and jitter compensation using spatio-temporal-filtering based control approaches,” in *Novel Optical Systems and Large-aperture Imaging:*, 1998, vol. 3430, pp. 236–247.

[58] S. J. Shelly, T. D. Sharp, and K. T. Moore, “Active vibration control of optical space systems,” in *Proceedings of the 17th International Modal Analysis Conference*, 1999.

[59] H. Sumali, K. Meissner, and H. H. Cudney, “A piezoelectric array for sensing vibration modal coordinates,” *Sensors Actuators, A Phys.*, vol. 93, no. 2, pp. 123–131, 2001.

[60] A. Elka and I. Bucher, “Optimal electrode shaping for precise modal electromechanical filtering,” *Struct. Multidiscip. Optim.*, vol. 38, no. 6, pp. 627–641, 2009.

[61] A. Preumont, A. François, P. De Man, and V. Piefort, “Spatial filters in structural control,” *J. Sound Vib.*, vol. 265, no. 1, pp. 61–79, 2003.

[62] F. Charette, A. Berry, and C. Guigou, “Active control of sound radiation from a plate using a polyvinylidene fluoride volume displacement sensor,” *J. Acoust. Soc. Am.*, vol. 103, no. 3, pp. 1493–1503, 1998.

[63] J. Kim, J.-S. Hwang, and S. J. Kim, “Design of modal transducers by optimizing spatial distribution of discrete gain weights,” *AIAA J.*, vol. 39, no. 10, pp. 1969–1976, 2001.

[64] S. E. Burke and J. E. Hubbard, “Active vibration control of a simply supported beam using a spatially distributed actuator,” *IEEE Control Systems Magazine*, vol. 7, no. 4, pp. 25–30, 1987.

[65] C. K. Lee, “Theory of laminated piezoelectric plates for the design of distributed sensors/actuators. Part I: Governing equations and reciprocal relationships,” *J. Acoust. Soc. Am.*, vol. 87, no. 3, pp. 1144–1158, 1990.

[66] M. J. Balas, “Feedback control of flexible systems,” *IEEE Trans. Automat. Contr.*, vol. 23, no. 4, pp. 673–679, 1978.

[67] M. J. Balas, “Active control of flexible systems,” *J. Optim. Theory Appl.*, vol. 25, no. 3, pp. 415–436, 1978.

[68] E. J. Hudson, P. Reynolds, and D. S. Nyawako, “Fundamental studies of AVC with actuator dynamics,” in *Dynamics of Coupled Structures*, 2016, vol. 4, pp. 147–154.

[69] S. Beskhyroun, L. D. Wegner, and B. F. Sparling, “New methodology for the application of vibration-based damage detection techniques,” *Struct. Control Heal. Monit.*, vol. 19, no. 8, pp. 632–649, 2012.

[70] S. W. Smith, *Digital signal processing*. California Technical Publishing, 1999.

[71] M. H. Richardson and D. L. Formenti, “Parameter estimation from frequency response measurements using rational fraction polynomials,” in *Proceedings of the 1st International Modal Analysis Conference*, 1982, pp. 167–182.

[72] M. H. Richardson and D. L. Formenti, “Global curve fitting of frequency response measurements using the rational fraction polynomial method,” in *Proceedings of the 3rd International Modal Analysis Conference*, 1985, pp. 390–397.

[73] M. H. Richardson, “Global Frequency & Damping Estimates From Frequency Response Measurements,” in *Proceedings of the 4rd International Modal Analysis Conference*, 1986, pp. 465–470.

[74] T. Wandowski, P. H. Malinowski, and W. M. Ostachowicz, “Circular sensing networks for guided waves based structural health monitoring,” *Mech. Syst. Signal Process.*, vol. 66–67, pp. 248–267, 2016.

[75] K. Worden and A. P. Burrows, “Optimal sensor placement for fault detection,” *Eng. Struct.*, vol. 23, no. 8, pp. 885–901, 2001.

[76] M. Meo and G. Zumpano, “On the optimal sensor placement techniques for a bridge structure,” *Eng. Struct.*, vol. 27, no. 10, pp. 1488–1497, 2005.

[77] C. Papadimitriou, “Optimal sensor placement methodology for parametric identification of structural systems,” *J. Sound Vib.*, vol. 278, no. 4, pp. 923–947, 2004.

[78] W. Liu, W. Gao, Y. Sun, and M. Xu, “Optimal sensor placement for spatial lattice structure based on genetic algorithms,” *J. Sound Vib.*, vol. 317, no. 1, pp. 175–189, 2008.

[79] M. Kozek, C. Benatzky, A. Schirrer, and A. Stribersky, “Vibration damping of a flexible car body structure using piezo-stack actuators,” *Control Eng. Pract.*, vol. 19, no. 3, pp. 298–310, 2011.

[80] D. S. Li, H. N. Li, and C. P. Fritzen, “The connection between effective independence and modal kinetic energy methods for sensor placement,” *J. Sound Vib.*, vol. 305, no. 4, pp. 945–955, 2007.

[81] T. Hanis and M. Hromcik, “Optimal sensors placement and spillover suppression,” *Mech. Syst. Signal Process.*, vol. 28, pp. 367–378, 2012.

[82] S. Cinquemani, D. Ferrari, and I. Bayati, “Reduction of spillover effects on independent modal space control through optimal placement of sensors and actuators,” *Smart Mater. Struct.*, vol. 24, no. 8, 2015.

[83] L. Meirovitch and H. Baruh, “On the problem of observation spillover in self-adjoint distributed-parameter systems,” *J. Optim. Theory Appl.*, vol. 39, no. 2, pp. 269–291, 1983.

[84] N. K. and H. Fukunaga, “Vibration Measurement/Control of CFRP Laminated Plates Based on the Optimal Placement of Sensors/Actuators Part I: Numerical Simulation(In Japanese),” *J. Japan Soc. Aeronaut. Sp. Sci.*, vol. 52, no. 610, pp. 499–506, 2004.

[85] N. Kawabata and H. Fukunaga, “Vibration Measurement/Control of CFRP Laminated Plates Based on the Optimal Placement of Sensors/Actuators Part 2: Experiment(In Japanese),” *J. Japan Soc. Aeronaut. Sp. Sci.*, vol. 53, no. 618, pp. 295–301, 2005.

[86] D. R. Morgan, “An adaptive modal-based active control system,” *J. Acoust. Soc. Am.*, vol. 89, no. 1, pp. 248–256, 1991.

[87] A. K. Agrawal, J. N. Yang, W. E. Schmitendorf, and F. Habbari, “Stability of Actively Controlled Structures with Actuator saturation,” *J. Struct. Eng.*, vol. 123, no. 4, pp. 505–512, 1997.

[88] D. Sun, L. Tong, and D. Wang, “Vibration control of plates using discretely distributed piezoelectric quasi-modal actuators/sensors,” in *AIAA Journal*, 2001, vol. 39, no. 9, pp. 1766–1772.

[89] D. C. Kammer, “Optimal sensor placement for modal identification using system-realization methods,” *J. Guid. Control. Dyn.*, vol. 19, no. 3, pp. 729–731, 1996.

[90] D. C. Kammer, “Effect of model error on sensor placement for on-orbit modal identification of large space structures,” *J. Guid. Control. Dyn.*, vol. 15, no. 2, pp. 334–341, 1992.

[91] D. C. Kammer and M. L. Tinker, “Optimal placement of triaxial accelerometers for modal vibration tests,” *Mech. Syst. Signal Process.*, vol. 18, no. 1, pp. 29–41, 2004.

[92] D. C. Kammer, “Sensor set expansion for modal vibration testing,” *Mech. Syst. Signal Process.*, vol. 19, no. 4, pp. 700–713, 2005.

[93] D. C. Kammer, “Sensor placement for on-orbit modal identification and correlation of large space structures,” in *American Control Conference*, 1990, pp. 2984–2990.

[94] R. J. Allemang and D. L. Brown, “A correlation coefficient for modal vector analysis,” in *Proceedings of the 1st International Modal Analysis Conference*, 1982, pp. 110–116.

[95] R. J. Allemang, “The modal assurance criterion–twenty years of use and abuse,” *Sound Vib.*, vol. 37, no. 8, pp. 14–23, 2003.

[96] L. Yao, W. A. Sethares, and D. C. Kammer, “Sensor placement for on-orbit modal identification via a genetic algorithm,” in *AIAA Journal*, 1993, vol. 31, no. 10, pp. 1922–1928.

[97] C. B. Larson, D. C. Zimmerman, and E. L. Marek, “A comparison of modal test planning techniques: excitation and sensor placement using the NASA 8-bay truss,” in *SPIE - The International Society for Optical Engineering*, 1994.

[98] T. H. Yi and H. N. Li, “Methodology developments in sensor placement for health monitoring of civil infrastructures,” *Int. J. Distrib. Sens. Networks*, vol. 8, no. 8, 2012.

[99] B. K. Jung, J. R. Cho, and W. B. Jeong, “Sensor placement optimization for structural modal identification of flexible structures using genetic algorithm,” *J. Mech. Sci. Technol.*, vol. 29, no. 7, pp. 2775–2783, 2015.

[100] K. Ogata, *Modern Control Engineering*. Prentice Hall, 2009.

[101] D. E. Seborg, T. F. Edgar, and D. A. Mellichamp, *Process dynamics and control*. John Wiley & Sons, 2010.

[102] G. A. F. Seber and C. J. Wild, *Nonlinear regression*. John Wiley & Sons, 2003.

[103] J. F. Schultze, R. W. Rost, and S. J. Shelley, “Adaptive modal space control of flexible structures: Applications,” in *SPIE - The International Society for Optical Engineering*, 1997, pp. 745–751.

[104] J. min He and Z. F. Fu, *Modal Analysis*. Butterworth-Heinemann, 2001.

[105] J. N. Juang and R. S. Pappa, “An eigensystem realization algorithm for modal parameter identification and model reduction,” *J. Guid.*, vol. 8, no. 5, pp. 620–627, 1985.

[106] J. M. Caicedo, S. J. Dyke, and E. A. Johnson, “Natural excitation technique and eigensystem realization algorithm for phase I of the IASC-ASCE benchmark problem: Simulated data,” *J. Eng. Mech.*, vol. 130, no. 1, pp. 49–60, 2004.

[107] N. C. Nigam and P. C. Jennings, “Calculation of Respose Spectra from Strong-Motion Erathquake Records.,” *Bull. Seismol. Soc. Am.*, vol. 59, no. 2, pp. 909–922, 1969.

[108] S. Haykin, “Adaptive filter theory.” Prentice Hall, 2002.

[109] T. O. Kvålseth, “Cautionary Note about R2,” *Am. Stat.*, vol. 39, no. 4, pp. 279–285, 1985.

[110] V. Zabel, M. Brehm, and S. Nikulla, “The influence of temperature varying material parameters on the dynamic behavior of short span railway bridges,” in *International Conference on Noise and Vibration Engineering*, 2010, pp. 1519–1530.

Appendix A Genetic Algorithm

A.1 Introduction

Genetic algorithms (GA) are numerical optimisation algorithms enlightened by the natural selection and natural genetics and have been applied to an extremely wide range of problems. Unlike the traditional optimisation methods which are typically starting from a single point or guessing within the search space, GAs are initialised with a population of guesses. These guesses are usually random chosen and will be spread throughout the search space. In general, these initial guesses of the variables are expressed as binary encodings of the true variables and then this initial population is processed by the three operators, named selection, crossover and mutation, to direct the population (over a series of time steps or generations) towards convergence at the global optimum.

GA is invented with the following fundamentals:

1. In a population, individuals compete for resources and mates.
2. Those most successful individuals will produce more offspring than those who performed poorly.
3. Genes from 'superior' individuals propagate throughout the population (two good parents will sometimes produce offspring that are better than either parent).
4. Hence, each successive generation will become more suited to their environment.

A.2 Elements of GA

The genetic algorithm mainly involves the following elements:

1. Population

The initial population is generated considering range of possible values each parameter can take. The M unknown parameters are each represented as binary sub-strings of length l and then these sub-strings are joined together to form an individual population number of length L, where:

$$L = \sum_{j=1}^{M} l_j \tag{A-1}$$

All the N numbers of the initial population are random chosen and is expected to be spread throughout the possible range.

2. Evaluation

For the purpose of selecting the most appropriate individuals from the population, aptitude of each individual should be evaluated. In terms of GA, this aptitude is called fitness, which is used to measure the suitability of each individual. Those with high fitness survive, whereas those with low fitness fade and disappear. In general, a target function (objective function) $f(\boldsymbol{x})$ of parameter $\boldsymbol{x}$ optimization is set to evaluate the fitness.

3. Selection

Once each individual has been assigned certain fitness, parents to create next population should be chosen. Probability for each individual of being chosen is estimated by Eq. (A-2), giving to the individuals as probability to be chosen proportional to their fitness values.

$$p_i = \frac{f(\boldsymbol{x}_i)}{\sum_{j=1}^{N} f(\boldsymbol{x}_j)} \tag{A-2}$$

4. Elitism

Fitness-proportional selection may not guarantee the selection of fittest individual unless that one is much fitter than any other individual. Even in this case, it will occasionally not be selected. Therefore with the fitness-proportional selection the best solution discovered can be regularly thrown away. In fact, the searching speed can be greatly improved by not losing the best, or elite, member between generations.

5. Crossover

Two point crossover as shown in Figure A.1 is used in this study. For a chromosome of a length L, a random number c between 1 and L is generated. Offspring 1 is formed by appending the last $L - c$ elements of the first parent to the first c element of the second parent. Offspring 2 is formed by appending the last $L - c$ elements of the second parent to the first c elements of the first parent.

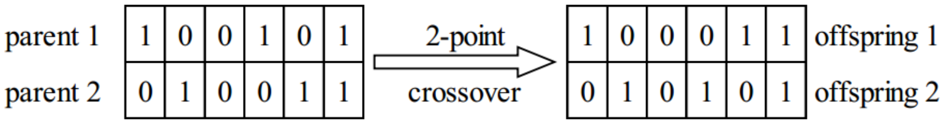

Fig. A.1 Two points crossover method

6. Mutation

Mutation is essentially an arbitrary modification which helps to prevent premature convergence, and operates independently on each individual by stochastically perturbing each bit string. Mutation is performed by generating first a random number *m* between 1 and *L*, and then flipping the *m*th bit from 0 to 1 or from 1 to 0, as shown in Figure A.2.

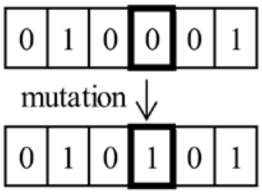

Fig. A.2 Genetic mutation scheme

7. Termination condition

The termination condition is chosen as it gives reasonable target function and the time employed is not very long. Termination condition is selected in terms of iteration, considering the time each iteration takes. A terminator G for the total generation can be set to stop the searching.

A.3 Procedure of the Little Genetic Algorithm

Having defined the mutation, selection, crossover and elitism operators, then this knowledge can be brought together to generate the famous Little Genetic Algorithm as the following steps:

1. Generate an initial *N* members (*g*=1) population of random binary strings of length $\sum_{j=1}^{M} l_j$, where *M* is the number of unknowns and l_j is the length of binary string required by any unknowns.
2. Decode each individual, i, within the population to integers and then to real numbers to obtain the unknown parameters.
3. Test each individual in turn on the problem and convert the objective function of each individual to a fitness f_i, where a better solution implies a higher fitness.

4. Using fitness proportional selection to select pairs of individuals and apply with probability P_c two points crossover. Repeat until a new temporary population of *N* individuals is formed.
5. Apply the mutation operator to each individual in the temporary population with the mutating probability of P_m. Typically, P_m is very small.
6. If the temporary population does not contain the elite member of the previous generation, randomly replace one member of the temporary population with the elite member.
7. Replace the old population by the new temporary generation.
8. Increment, by 1, the generational counter (g=g+1) and repeat from step 2 until G generations have finished.

The flowchart of the Little Genetic Algorithm is shown in Figure 5.2.

References

[1] L. Davis, "*Handbook of genetic algorithms*.", 1991.

[2] M. Mitchell, "*An introduction to genetic algorithms*.", MIT press, 1998.

[3] D. A. Coley, "*An introduction to genetic algorithms for scientists and engineerings*.", World Scientific Publishing Co Inc, 1999.

Appendix B Routh's Stability Criterion and Root Locus Method

B.1 Introduction

It is known that in the theory of system control, a system is stable if and only if all of the closed-loop poles lie in the left-half *s* plane. The Routh's stability criterion is a mathematical test that is used to check the stability of a linear time invariant system. This criterion provides a way to determine whether the transfer function of a linear system have only stable poles without solving the system directly.

The characteristic of the transient response of a closed-loop system is related to the location of system poles, which depend on the value of the loop gain chosen if the system has a variable loop gain. Therefore, it is significantly important to know how the closed-loop poles move as the loop gain is varied in the *s* plane. The method, called root-locus method, has been developed by W. R. Evans for finding the roots of the characteristic equation of the closed-loop system and used extensively in control engineering. In this method, the roots of the characteristic equation are plotted for a system parameter, which is usually the control gain, to be varied from zero to infinity. Then the design problem may become the selection of an appropriate control gain. When the gain adjustment alone does not give a desire result, addition of compensators to the system will become necessary and the new closed-loop system can be checked by the root locus again until a desire result is achieved. In our application, the root locus method is used for designing the compensator such that the open-loop poles of the floor system can be modified to achieve a good system performance.

B.2 Routh's stability criterion

In general, most linear closed-loop systems have the transfer function of the form:

$$H(s) = \frac{b_0 s^m + b_1 s^{m-1} + \cdots + b_{m-1}s + b_m}{a_0 s^n + a_1 s^{n-1} + \cdots + a_{n-1}s + a_n} = \frac{B(s)}{A(s)} \tag{B-1}$$

where the a_i's and b_i's are real constants and $m \leq n$. Instead of factoring the denominator polynomial, the Routh's stability criterion can be used to determine the number of closed-loop poles in the right-half s plane without solving the roots. This criterion applies to polynomial $A(s)$ with only a finite number of terms and the information about absolute stability can be obtained directly from the coefficients of $A(s)$.

The procedure of the Routh's stability criterion is as follows:

1. Factor out the roots at the origin and multiply by -1 if necessary to obtain:

$$a_0 s^n + a_1 s^{n-1} + \cdots + a_{n-1}s + a_n = 0 \tag{B-2}$$

where $a_n \neq 0$ and $a_0 > 0$. If any of the coefficients a_i (i=1, …, n-1) is zero or negative when at least one positive coefficient exists, there is at least one root that have positive real part, which means the system is not stable. However, all the coefficients be positive is not sufficient to assure stability.

2. To obtain the precise number of roots with nonnegative real parts, arrange the coefficients a_i (i=0, 1, …, n) and values subsequently calculated from them as shown in the following pattern:

$$\begin{array}{cccccc} s^n & a_0 & a_2 & a_4 & a_6 & \cdots \\ s^{n-1} & a_1 & a_3 & a_5 & a_7 & \cdots \\ s^{n-2} & b_1 & b_2 & b_3 & b_4 & \cdots \\ s^{n-3} & c_1 & c_2 & c_3 & c_4 & \cdots \\ s^{n-4} & d_1 & d_2 & d_3 & d_4 & \cdots \\ \vdots & \vdots & \vdots & & & \\ s^2 & e_1 & e_2 & & & \\ s^1 & f_1 & & & & \\ s^0 & g_1 & & & & \end{array} \tag{B-3}$$

where the coefficients b_i are generated until all subsequent coefficients are zero:

$$b_1 = \frac{a_1 a_2 - a_0 a_3}{a_1} \tag{B-4}$$

$$b_2 = \frac{a_1 a_4 - a_0 a_5}{a_1} \tag{B-5}$$

$$b_3 = \frac{a_1 a_6 - a_0 a_7}{a_1} \tag{B-6}$$

$$\vdots$$

In the same way, cross multiply the coefficients of the two previous rows to obtain the other coefficients c_i, d_i, etc:

$$c_1 = \frac{b_1 a_3 - a_1 b_2}{b_1} \tag{B-7}$$

$$c_2 = \frac{b_1 a_5 - a_1 b_3}{b_1} \tag{B-8}$$

$$c_3 = \frac{b_1 a_7 - a_1 b_4}{b_1} \tag{B-9}$$

$$\vdots$$

$$d_1 = \frac{c_1 b_2 - b_1 c_2}{c_1} \tag{B-10}$$

$$d_2 = \frac{c_1 b_3 - b_1 c_3}{c_1} \tag{B-11}$$

$$\vdots$$

The process lasts until the *n*th row of the array has been completed and the missing coefficients are replaced by zeros. The resulting triangular array is named the Routh array.

3. Count the number of sign changes in the first column of the array, and the Routh's stability criterion states that this number is equal to the roots of Eq. (B-2) with positive real parts. The necessary and sufficient condition for all the roots of Eq. (B-2) to be located in the left half plane of *s* plane is that all the coefficients a_i are positive and all of the coefficients in the first column have positive signs.

B.3 Root locus method

For the closed-loop system shown in Figure B.1, the closed-loop transfer function is expressed as:

$$\frac{C(s)}{R(s)} = \frac{G(s)}{1 + G(s)H(s)} \tag{B-12}$$

The characteristic equation for the closed-loop system is:

$$1 + G(s)H(s) = 0 \tag{B-13}$$

Or

$$G(s)H(s) = -1 \tag{B-14}$$

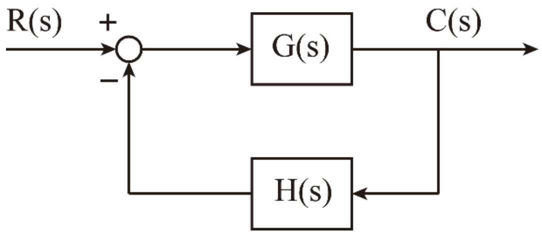

Fig. B.1 Closed-loop control system

In many cases, $G(s)H(s)$ contains a gain K and the characteristic equation of Eq. (B-14) can be written as:

$$1 + \frac{K(s+z_1)(s+z_2)\cdots(s+z_m)}{(s+p_1)(s+p_2)\cdots(s+p_n)} = 0 \tag{B-15}$$

Because $G(s)H(s)$ is a complex quantity, Eq. (B-14) can be divided into the angle and magnitude equations as following:

Angle condition:

$$\angle\, G(s)H(s) = \pm\pi(2k+1) \qquad k \in \mathbb{N} \tag{B-16}$$

Magnitude condition:

$$|G(s)H(s)| = 1 \tag{B-17}$$

Therefore, the values of s for different gain K that satisfy the above both conditions are the roots of the characteristic equation, or the poles of the closed-loop system. In the root locus method, the locus of the points in the complex s plane can be drawn from the angle condition alone and the roots corresponding to the specified gain K can be determined from the magnitude condition. The root locus for the closed-loop system is the loci of the closed-loop poles as the gain K is changing from zero to infinity.

It should be noted that the drawing of the root locus is started from knowing the location of poles and zeros of $G(s)H(s)$, which is corresponding to K=0. It should also be noted that the angles of the complex quantities originating from the open-loop poles and zeros to the test point s are measured in the counter clockwise direction as shown in Figure B.2.

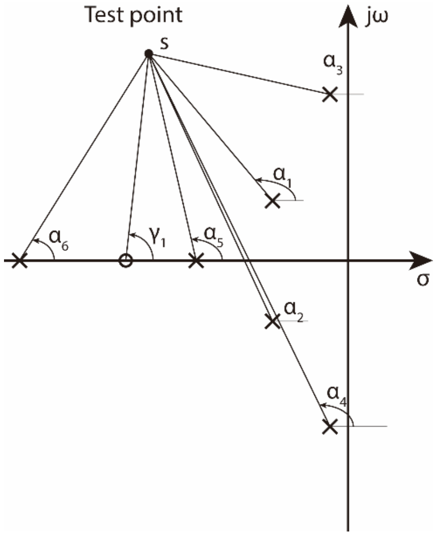

Fig. B.2 Angle measurements from open-loop poles and zero to test point *s*

The details of the rules for graphically constructing root locus will not be given here, while the root locus plot can be easily drawn using the software MATLAB. For more details about the rules of plotting root locus, see reference [1].

References

[1] O. Katsuhiko, “*Modern Control Engineering*.”, Prentice Hall, 2010.

Appendix C Lebenberg-Marquardt algorithm (LMA)

C.1 Introduction

In regression problems, one of the variables which is called dependent or response variable is of particular interest and is denoted by y. The other variables x_1, x_2, …, x_k, usually called independent variables, are mainly used to predict the behavior of y. If plots of data suggest a certain relationship between y and x_i's, then it is expected to express this relationship via the function f, namely:

$$y \approx f(x_1, x_2, \dots, x_k) \tag{C-1}$$

It can then using f to predict y for a given set of x_i's, As in Eq. (C-1), relationships can never hold exactly since data will unavoidable contain noise and some degree of measurement error.

The Lebenberg-Marquardt algorithm (LMA) is a standard technique for non-linear least-squares problems and widely used in a broad spectrum of disciplines. LMA is considered as the combination of steepest descent and the Gauss-Newton method. When the current solution is far from the correct one, the LMA behaves like a steepest descent method, while if the current solution is close to the correct solution, it behaves as the Gauss-Newton method. In the following, a brief introduction of the LMA is given and this algorithm will be used for the non-linear regression problem in Chapter 7.

C.2 Non-linear least-squares problems

In the non-linear least-squares problems, the object function S has the following form:

$$S(\boldsymbol{x}) = \frac{1}{2}\sum_{j=1}^{m} r_j^2(\boldsymbol{x}) = \frac{1}{2}\sum_{j=1}^{m}[y_j - f_j(\boldsymbol{x})]^2 \tag{C-2}$$

where the total number of measured data is m, y_j is the measured data at number j. $f_j(\boldsymbol{x})$ is the non-linear function calculated at number j with the estimate independent variables $\boldsymbol{x}$ which is a vector of dimension k. r_j is a smooth function from $\boldsymbol{R}^k$ to $\boldsymbol{R}$, in which k is the number of variables. r_j is referred as a residual at number j. In general, $m \geq k$ should be satisfied.

In order to solve the problem of minimizing $S(\boldsymbol{x})$ in Eq. (C-2) that based on the real variables $\boldsymbol{x}$, algorithm have been developed which exploit the special structure of Eq. (C-2) as a sum of squares. The algorithm is based on a modification to the Newton method introduced by Gauss and known as the Gauss-Newton algorithm.

At the regression step a, by taking a linear Taylor series approximation to $f_j(\boldsymbol{x})$ about $\boldsymbol{x}^{(a)}$ to obtain:

$$f_j(\boldsymbol{x}) \approx f_j\left(\boldsymbol{x}^{(a)}\right) + \frac{\partial f_j\left(\boldsymbol{x}^{(a)}\right)}{\partial \boldsymbol{x}^T}(\boldsymbol{x} - \boldsymbol{x}^{(a)}) \tag{C-3}$$

Using the approximation of Eq. (C-3) in Eq. (C-2), the minimization problem was converted to a linear least-squares problem, namely:

$$Minimize\ \frac{1}{2}\left\|\boldsymbol{r}^{(a)} - \boldsymbol{F}.^{(a)}\,(\boldsymbol{x} - \boldsymbol{x}^{(a)})\right\|^2 \tag{C-4}$$

where the vector $\boldsymbol{r}^{(a)}$ is $\boldsymbol{y} - \boldsymbol{f}(\boldsymbol{x}^{(a)})$ and $\boldsymbol{F}.^{(a)}$ is $\partial\boldsymbol{f}/\,\partial\boldsymbol{x}^T$ evaluated at $\boldsymbol{x}^{(a)}$. Note that Eq. (C-2) is written in vector form. Based on the algorithm of linear least-squares, Eq. (C-4) has the following solution:

$$\boldsymbol{x} - \boldsymbol{x}^{(a)} = (\boldsymbol{F}.^{(a)^T}\,\boldsymbol{F}.^{(a)})^{-1}\boldsymbol{F}.^{(a)^T}\,\boldsymbol{r}^{(a)} \tag{C-5}$$

Leading to the Gauss-Newton algorithm:

$$\boldsymbol{x}^{(a+1)} = \boldsymbol{x}^{(a)} + \boldsymbol{\delta}^{(a)} \tag{C-6}$$

Where:

$$\boldsymbol{\delta}^{(a)} = (\boldsymbol{F}.^{(a)^T}\,\boldsymbol{F}.^{(a)})^{-1}\boldsymbol{F}.^{(a)^T}\,\boldsymbol{r}^{(a)} \tag{C-7}$$

For the purpose of explanation of the above Gauss-Newton algorithm, now let us see the objective function expressed in terms of Eq. (C-2), the gradient and Hessian of $S(\boldsymbol{x})$ are, respectively:

$$\boldsymbol{g}(\boldsymbol{x}) = \frac{\partial S(\boldsymbol{x})}{\partial \boldsymbol{x}} = \sum_{j=1}^{m} r_j(\boldsymbol{x}) \frac{\partial r_j(\boldsymbol{x})}{\partial \boldsymbol{x}} = \boldsymbol{J}^T \boldsymbol{r} \tag{C-8}$$

And:

$$\boldsymbol{H}(\boldsymbol{x}) = \frac{\partial^2 S(\boldsymbol{x})}{\partial \boldsymbol{x} \partial \boldsymbol{x}^T} = \sum_{j=1}^{m} \frac{\partial r_j(\boldsymbol{x})}{\partial \boldsymbol{x}} \frac{\partial r_j(\boldsymbol{x})}{\partial \boldsymbol{x}^T} + \sum_{j=1}^{m} r_j(\boldsymbol{x}) \frac{\partial^2 r_j(\boldsymbol{x})}{\partial \boldsymbol{x} \partial \boldsymbol{x}^T} = \boldsymbol{J}^T \boldsymbol{J} + \boldsymbol{A} \tag{C-9}$$

Here:

$$\boldsymbol{J} = \boldsymbol{J}(\boldsymbol{x}) = \left[\left(\frac{\partial r_j}{\partial \boldsymbol{x}_j} \right) \right] = -\boldsymbol{F}.(x) \tag{C-10}$$

And:

$$\boldsymbol{A} = \boldsymbol{A}(\boldsymbol{x}) = \sum_{j=1}^{m} r_j(\boldsymbol{x}) \frac{\partial^2 r_j(\boldsymbol{x})}{\partial \boldsymbol{x} \partial \boldsymbol{x}^T} \tag{C-11}$$

Thus the Newton step is:

$$Newton: \qquad \boldsymbol{\delta}^{(a)} = -{\boldsymbol{H}^{(a)}}^{-1} \boldsymbol{g}^{(a)} = -({\boldsymbol{J}^{(a)}}^T \boldsymbol{J}^{(a)} + \boldsymbol{A}^{(a)})^{-1} {\boldsymbol{J}^{(a)}}^T \boldsymbol{r}^{(a)} \tag{C-12}$$

Based on Eq. (C-10), $\boldsymbol{F}.^{(a)} = -\boldsymbol{J}^{(a)}$ and therefore the Gauss-Newton algorithm of Eq. (C-7) is simply obtained from the Newton algorithm by ignoring part of the Hessian, that is $\boldsymbol{A}^{(a)}$ of Eq. (C-12) and setting the step length α to 1. This dropping of $\boldsymbol{A}(\boldsymbol{x})$ from the Hessian matrix is leading to both the strengths and the weaknesses of Gauss-Newton-based algorithms.

Based on Eq. (C-7), only the first derivatives of the $r_j(\boldsymbol{x})$ stored in $\boldsymbol{J}(\boldsymbol{x})$ are required. No separate approximation to the Hessian need to be stored. Thus each step is less expensive than its Newton counterpart in terms of both time and storage. In problems where $\boldsymbol{A}(\boldsymbol{x})$ is small compared with $\boldsymbol{J}^T\boldsymbol{J}$ in Eq. (C-9), Gauss-Newton-based algorithms often take a similar number of iterative to a full modified Newton algorithm and are thus much more efficient.

For the purpose of solving non-linear regression problem, there are many Gauss-Newton-based algorithms for small residual problems and the famous Levenberg-Marquardt method will be introduced as following.

C.3 Levenberg-Marquardt method

Levenberg-Marquardt algorithms allow for singular or ill-conditioned matrices ${\boldsymbol{J}^{(a)}}^T \boldsymbol{J}^{(a)}$ of Eq. (C-7) by modifying the Gauss-Newton step to:

$$\boldsymbol{\delta}^{(a)} = -(\boldsymbol{J}^{(a)^T}\boldsymbol{J}^{(a)} + \eta^{(a)}\boldsymbol{D}^{(a)})^{-1}\boldsymbol{J}^{(a)^T}\boldsymbol{r}^{(a)} \tag{C-13}$$

where $\boldsymbol{D}^{(a)}$ is a diagonal matrix with positive diagonal elements. A popular choice is to set the diagonal elements of $\boldsymbol{D}^{(a)}$ to be the same as those of $\boldsymbol{J}^{(a)^T}\boldsymbol{J}^{(a)}$ so that the algorithm is approximately invariant under rescaling of the $\boldsymbol{x}$. Also, for simplicity, we could chose $\boldsymbol{D}^{(a)} = \boldsymbol{I}$.

When $\boldsymbol{D}^{(a)} = \boldsymbol{I}$, the Levenberg-Marquardt direction (i.e. the direction of $\boldsymbol{\delta}^{(a)}$ in Eq. (C-13)) interpolates between the Gauss-Newton direction ($\eta^{(a)} \to 0$) and the steepest-descent direction ($\eta^{(a)} \to \infty$).

For $\eta^{(a)} > 0$, $\boldsymbol{J}^{(a)^T}\boldsymbol{J}^{(a)} + \eta^{(a)}\boldsymbol{D}^{(a)}$ is positive definite since $\boldsymbol{D}^{(a)}$ is positive definite. Thus, $\boldsymbol{\delta}^{(a)}$ of Eq. (C-13) is a descent direction. As noted from Eq. (C-13), as $\eta^{(a)} \to \infty$, the length $\boldsymbol{\delta}^{(a)}$ tends to zero, therefore by choosing $\boldsymbol{\delta}^{(a)}$ significantly large we can reduce $S(\boldsymbol{x}) = \frac{1}{2}\sum_{j=1}^{m} r_j^2(\boldsymbol{x})$. However, if $\boldsymbol{\delta}^{(a)}$ is too large for too many iterations, the algorithm will take too many small steps and make little progress.

Then the problem is how to choose the value of $\eta^{(a)}$ for each iterate. Marquardt adopted a strategy which are easy to implement as following. Initially a small positive value was taken, e.g. $\eta^{(1)} = 0.01$, if, at the a th iteration, the step $\boldsymbol{\delta}^{(a)}$ reduces $S(\boldsymbol{x})$, he sets $\boldsymbol{x}^{(a+1)} = \boldsymbol{x}^{(a)} + \boldsymbol{\delta}^{(a)}$ and divides η by a factor e.g. $\eta^{(a+1)} = \eta^{(a)}/10$, to push the algorithm closer to Gauss-Newton (and to bigger steps for the next iteration, by Eq. (C-13)). If within the ath iteration the step $\boldsymbol{\delta}^{(a)}$ does not reduce $S(\boldsymbol{x})$, he progressively increases η by a factor e.g. $\eta^{(a+1)} = 10\eta^{(a)}$, each time re-computing $\eta^{(a)}$ until a reduction in $S(\boldsymbol{x})$ is achieved.

References

[1] G. A. F. Seber and C. J. Wild, “*Nonlinear Regression*.”, John Wiley & Sons, 2003.

Appendix D Eigensystem Realization Algorithm (ERA)

D.1 Introduction

Numerous methods are available for identification of the modal parameters from the experimental data. Here the ERA is adopted since it is effective for identifying the lightly damped structures and is applicable to multi-input/multi-output systems.

The ERA was initially developed for modal parameter identification and model reduction for dynamical systems from test data by J. N. Juang and R. S. Pappa. Two major parts are involved in this algorithm, namely, basic formulation of the minimum order realization and modal parameter identification. In the part of basic formulation, the Hankel matrix which contains the pulse-response histories (system Markov parameters) is generated. Through the use of the Hankel matrix, a linear model is realized which matching the input and output relationship of the dynamical system combined with the singular value decomposition technique. The realized system model is then used for the modal parameter identification.

D.2 Basic formulation

In the discrete time domain, the state-space representation for the linear time invariant system is written in the following form:

$$\boldsymbol{x}(k+1) = \boldsymbol{A}\boldsymbol{x}(k) + \boldsymbol{B}\boldsymbol{u}(k) \tag{D-1}$$

$$\boldsymbol{y}(k) = \boldsymbol{C}\boldsymbol{x}(k) \tag{D-2}$$

where $\boldsymbol{x}$ is an n dimensional state vector, $\boldsymbol{u}$ is an m dimensional control input and $\boldsymbol{y}$ is an p dimensional measurement vector. k is the time indicator. $\boldsymbol{A}$ is the $n \times n$ dimensional state (or system) matrix. $\boldsymbol{B}$ is the $n \times m$ input matrix and $\boldsymbol{C}$ is the $p \times n$ output matrix. The problem of system realization is defined that given the measurement functions $\boldsymbol{y}(k)$, construct the matrices [$\boldsymbol{A}$, $\boldsymbol{B}$, $\boldsymbol{C}$] such that the $\boldsymbol{y}$ can be reproduced by the state-space representation. For the multi-input multi-output case, the time-domain description is expressed by the pulse-response (or initial-state-response) function:

$$\boldsymbol{Y}(k) = \boldsymbol{C}\boldsymbol{A}^{k-1}\boldsymbol{B} = \boldsymbol{C}\boldsymbol{A}^{k}[x_1(0), x_2(0), x_3(0), \dots, x_m(0)] \tag{D-3}$$

$\boldsymbol{Y}(k)$ is a $p \times m$ pulse response matrix at the kth time step which is known as the Markov parameter, and $x_i(0)$ represents the ith set of initial condition. First, the Hankel matrix is formed by:

$$\boldsymbol{H}(k-1) = \begin{bmatrix} \boldsymbol{Y}(k) & \boldsymbol{Y}(k+1) & \cdots & \boldsymbol{Y}(k+s-1) \\ \boldsymbol{Y}(k+1) & \boldsymbol{Y}(k+2) & \cdots & \boldsymbol{Y}(k+s) \\ \vdots & \vdots & \vdots & \vdots \\ \boldsymbol{Y}(k+r-1) & \boldsymbol{Y}(k+r) & \cdots & \boldsymbol{Y}(k+r+s-2) \end{bmatrix} \tag{D-4}$$

The parameters *s* and *r* correspond to the number of columns and rows in the Hankel matrix. In order to achieve good results, *s* should be selected to be approximately ten times the number of modes to be identified and *r* should be selected to be 2~3 times *s*.

If $s \geq N$ and $r \geq N$, the matrix $\boldsymbol{H}(k-1)$ is of rank *N*. Substituting the Markov parameter of Eq. (D-3) into Eq. (D-4), the Hankel matrix $\boldsymbol{H}(k-1)$ can be factorized as:

$$\boldsymbol{H}(k-1) = \boldsymbol{\mathcal{P}}_r \boldsymbol{A}^{k-1} \boldsymbol{Q}_s \tag{D-5}$$

For the case of $k = 1$, Eq. (D-4) is written as:

$$\boldsymbol{H}(0) = \begin{bmatrix} \boldsymbol{Y}(1) & \boldsymbol{Y}(2) & \cdots & \boldsymbol{Y}(s) \\ \boldsymbol{Y}(2) & \boldsymbol{Y}(3) & \cdots & \boldsymbol{Y}(s+1) \\ \vdots & \vdots & \vdots & \vdots \\ \boldsymbol{Y}(r) & \boldsymbol{Y}(r+1) & \cdots & \boldsymbol{Y}(r+s-1) \end{bmatrix} \tag{D-6}$$

And based on the SVD technique, $\boldsymbol{H}(0)$ can be factorized as:

$$\boldsymbol{H}(0) = \boldsymbol{R}\Xi\boldsymbol{S}^T \tag{D-7}$$

where the columns of $\boldsymbol{R}$ and $\boldsymbol{S}$ are orthonormal and Ξ is:

$$\Xi = \begin{bmatrix} \Xi_N & \boldsymbol{0} \\ \boldsymbol{0} & \boldsymbol{0} \end{bmatrix} \tag{D-8}$$

in which $\boldsymbol{0}$ s are zero matrices of appropriate dimensions and $\Xi_N = diag[\sigma_1, \sigma_2, \dots, \sigma_i, \sigma_{i+1}, \dots, \sigma_N]$ and $\sigma_1 \geq \sigma_2 \geq \cdots \geq \sigma_i \geq \sigma_N \geq 0$.

From Eq. (D-8), it is assumed that the matrix $\boldsymbol{H}(0)$ has a rank of *N* since the singular values $\sigma_i(i = N+1, N+2, \dots)$ are set to be 0. When singular values $\sigma_i(i = N+1, N+2, \dots)$ are not exactly zero but very small, then it can easily recognize that $\boldsymbol{H}(0)$ is not far away from an *N*-rank matrix. However, in the actual operation, one has to make efforts to determine a gap between the computed last nonzero singular value and what should be effectively considered zero caused by the measurement noise, computer round-off and instrument imperfections.

After determining the order of the system, let $\boldsymbol{R}_N$ and $\boldsymbol{S}_N$ be the matrices formed by the first N columns of $\boldsymbol{R}$ and $\boldsymbol{S}$, respectively. Then:

$$\boldsymbol{H}(0) = \boldsymbol{R}_N \Xi_N \boldsymbol{S}_N^T = \left[\boldsymbol{R}_N \Xi_N^{1/2}\right]\left[\Xi_N^{1/2} \boldsymbol{S}_N^T\right] \tag{D-9}$$

And also, $\boldsymbol{R}_N^T \boldsymbol{R}_N = \boldsymbol{S}_N^T \boldsymbol{S}_N = \boldsymbol{I}_N$. From Eq. (D-5), for $k = 1$, the following relationship holds:

$$\boldsymbol{H}(0) = \boldsymbol{\mathcal{P}}_r \boldsymbol{Q}_s \tag{D-10}$$

From Eqs. (D-9) and (D-10):

$$\boldsymbol{\mathcal{P}}_r = \boldsymbol{R}_N \Xi_N^{1/2} \tag{D-11}$$

$$\boldsymbol{Q}_s = \Xi_N^{1/2} \boldsymbol{S}_N^T \tag{D-12}$$

From Eq. (D-3), it is known that:

$$\boldsymbol{Y}(1) = \boldsymbol{CB} \tag{D-13}$$

Based on Eqs. (D-6) and (D-10)~(D-13), $\boldsymbol{B}$ is the first m columns of $\boldsymbol{Q}_s$ and $\boldsymbol{C}$ is the first p rows of $\boldsymbol{\mathcal{P}}_r$, which means:

$$\boldsymbol{B} = \Xi_N^{1/2} \boldsymbol{S}_N^T \boldsymbol{E}_m \tag{D-14}$$

$$\boldsymbol{C} = \boldsymbol{E}_p^T \boldsymbol{R}_N \Xi_N^{1/2} \tag{D-15}$$

where $\boldsymbol{E}_p^T = [\boldsymbol{I}_p, \boldsymbol{0}]$ and $\boldsymbol{E}_m^T = [\boldsymbol{I}_m, \boldsymbol{0}]$. In order to determine the state matrix $\boldsymbol{A}$, from Eq. (D-4), $\boldsymbol{H}(1)$ can be written as:

$$\boldsymbol{H}(1) = \begin{bmatrix} \boldsymbol{Y}(2) & \boldsymbol{Y}(3) & \cdots & \boldsymbol{Y}(s+1) \\ \boldsymbol{Y}(3) & \boldsymbol{Y}(4) & \cdots & \boldsymbol{Y}(s+2) \\ \vdots & \vdots & \vdots & \vdots \\ \boldsymbol{Y}(r+1) & \boldsymbol{Y}(r+2) & \cdots & \boldsymbol{Y}(r+s) \end{bmatrix} \tag{D-16}$$

From Eq. (D-5), it is found that $\boldsymbol{H}(1)$ can be factorized using SVD as:

$$\boldsymbol{H}(1) = \boldsymbol{\mathcal{P}}_r \boldsymbol{A} \boldsymbol{Q}_s = \boldsymbol{R}_N \Xi_N^{1/2} \boldsymbol{A} \Xi_N^{1/2} \boldsymbol{S}_N^T \tag{D-17}$$

And then:

$$\boldsymbol{A} = \Xi_N^{-1/2} \boldsymbol{R}_N^T \boldsymbol{H}(1) \boldsymbol{S}_N \Xi_N^{-1/2} \tag{D-18}$$

D.3 Modal parameter identification

After the test of mode cut-off values, assume that the matrix $\boldsymbol{H}(0)$ has rank *N*. The eigenvalues matrix $\boldsymbol{Z}$ and eigenvectors $\boldsymbol{\Psi}$ can be determined such that:

$$\boldsymbol{\Psi}^{-1}\boldsymbol{A}\boldsymbol{\Psi} = \boldsymbol{Z} \tag{D-19}$$

The modal damping rates and damped natural frequencies are simply achieved through the real and imaginary parts of system poles, after the transformation of poles from z-plane to *s*-plane using the relationship:

$$s = [\ln(z)]/\Delta t \tag{D-20}$$

where Δt is the data sampling interval.

The mode shapes of the system corresponding to the measured points can be determined using the following relationship:

$$\boldsymbol{\Gamma} = \boldsymbol{C}\boldsymbol{\Psi} \tag{D-21}$$

Two accuracy indicators, namely, the modal parameter amplitude coherence and the modal phase collinearity can then be used to quantify the system modes and noise modes. These two indicators will not be mentioned here.

D.4 Procedure of ERA

The computational steps of ERA are summarized as follows:

1. Based on the test input and output data, calculating the pulse-response functions $\boldsymbol{Y}$(k).
2. Constructing the matrix $\boldsymbol{H}(0)$ by arranging the pulse-response functions $\boldsymbol{Y}$(k) with given *s* and *r*. (Eq. (D-6))
3. Decomposing the matrix $\boldsymbol{H}(0)$ using the singular value decomposition method. (Eq. (D-7))
4. Determining the order of the system by examining the singular values of the matrix $\boldsymbol{H}(0)$. (Eq. (D-8))
5. Calculating the minimum-order realization [$\boldsymbol{A}$, $\boldsymbol{B}$, $\boldsymbol{C}$] using the results of 4 and the hankel matrix $\boldsymbol{H}(1)$. (Eqs. (D-14), (D-15) and (D-18))
6. Finding the eigensolutions of the identified state matrix $\boldsymbol{A}$ and compute the modal damping ratios and modal frequencies of individual modes. (Eq. (D-19))
7. Checking the reduced system model based on the two accuracy indicators.

References

[1] J. N. Juang and R. S. Pappa, “An eigensystem realization algorithm for modal parameter identification and model reduction,” *J. Guid.*, vol. 8, no. 5, pp. 620–627, 1985.

[2] J. M. Caicedo, S. J. Dyke, and E. A. Johnson, “Natural excitation technique and eigensystem realization algorithm for phase I of the IASC-ASCE benchmark problem: Simulated data,” *J. Eng. Mech.*, vol. 130, no. 1, pp. 49–60, 2004.

Appendix E Nigam Jennings Method

E.1 Introduction

The Nigam Jennings method is developed for computing response spectra from strong-motion earthquake records based on the exact solution to the governing differential equation. If the excitation record is digitized at equal time intervals, this method gives a three to four-fold saving in computing time compared to a third Runge-Kutta method of comparable accuracy. In our application, the task is to estimate the reference modal coordinates q^r for the interest SDOF modes with the recorded actuator acceleration. The natural frequencies and damping ratios of individual SDOF modes are known. It is known that the spectra which are calculated from recorded acceleration are plots of the maximum response of a simple one degree of freedom system over a range of values of its natural period and damping. Therefore, it is perfectly suitable to use the Nigam Jennings method to solve our problem.

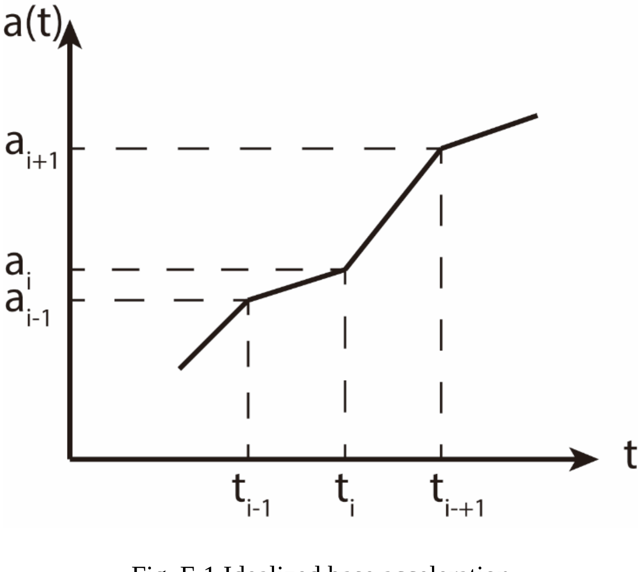

Fig. E.1 Idealized base acceleration

E.2 Formulation of the Nigam Jennings method

The equation of motion of the SDOF system subjected to base acceleration $a(\mathrm{t})$ is expressed as:

$$\ddot{x}(t) + 2\beta\omega\dot{x}(t) + \omega^2 x(t) = -a(t) \tag{E-1}$$

where β is the damping ratio and ω is the natural frequency of the SDOF system.

If the $a(\mathrm{t})$ is assumed as a segmentally linear function shown in Fig. E.1, Eq. (E-1) can be written as:

$$\ddot{x} + 2\beta\omega\dot{x} + \omega^2 x = -a_i - \frac{\Delta a_i}{\Delta t_i}(t - t_i) \qquad t_i \le t \le t_{i+1} \tag{E-2}$$

$$\Delta t_i = t_{i+1} - t_i$$

$$\Delta a_i = a_{i+1} - a_i$$

The solution of Eq. (E-2) for $t_i \le t \le t_{i+1}$ is given by:

$$x = e^{-\beta\omega(t-t_i)}\left[C_1 sin\omega\sqrt{1-\beta^2}(t-t_i) + C_2 cos\omega\sqrt{1-\beta^2}(t-t_i)\right] - \frac{a_i}{\omega^2} + \frac{2\beta}{\omega^3}\frac{\Delta a_i}{\Delta t_i} - \frac{1}{\omega^2}\frac{\Delta a_i}{\Delta t_i}(t-t_i) \tag{E-3}$$

By setting $x = x_i$ and $\dot{x} = \dot{x}_i$ at $t = t_i$ the unknowns C_1 and C_2 are found to be:

$$C_1 = \frac{1}{\omega\sqrt{1-\beta^2}}\left(\beta\omega x_i + \dot{x}_i - \frac{2\beta^2 - 1}{\omega^2}\frac{\Delta a_i}{\Delta t_i} + \frac{\beta}{\omega}a_i\right) \tag{E-4}$$

$$C_2 = x_i - \frac{2\beta}{\omega^3}\frac{\Delta a_i}{\Delta t_i} + \frac{a_i}{\omega^2} \tag{E-5}$$

Substituting of Eqs. (E-4) and (E-5) into Eq. (E-3) give x and $\dot{x}$ at $t = t_{i+1}$:

$$\bar{x}_{i+1} = \mathrm{A}(\beta, \omega, \Delta t_i)\bar{x}_i + \mathrm{B}(\beta, \omega, \Delta t_i)\bar{a}_i \tag{E-6}$$

in which:

$$\bar{x}_i = \begin{Bmatrix} x_i \\ \dot{x}_i \end{Bmatrix} \quad \text{and} \quad \bar{a}_i = \begin{Bmatrix} a_i \\ a_{i+1} \end{Bmatrix} \tag{E-7}$$

$$A = \begin{bmatrix} a_{11} & a_{12} \\ a_{21} & a_{22} \end{bmatrix} \quad \text{and} \quad B = \begin{bmatrix} b_{11} & b_{12} \\ b_{21} & b_{22} \end{bmatrix} \tag{E-8}$$

The elements of matrices *A* and *B* are:

$$
\begin{aligned}
a_{11} &= e^{-\beta\omega\Delta t_i}\left(\frac{\beta}{\sqrt{1-\beta^2}} sin\omega\sqrt{1-\beta^2}\Delta t_i + cos\omega\sqrt{1-\beta^2}\Delta t_i\right) \\
a_{12} &= \frac{e^{-\beta\omega\Delta t_i}}{\omega\sqrt{1-\beta^2}} sin\omega\sqrt{1-\beta^2}\Delta t_i \\
a_{21} &= -\frac{\omega}{\sqrt{1-\beta^2}} e^{-\beta\omega\Delta t_i} sin\omega\sqrt{1-\beta^2}\Delta t_i \\
a_{22} &= e^{-\beta\omega\Delta t_i}\left(cos\omega\sqrt{1-\beta^2}\Delta t_i - \frac{\beta}{\sqrt{1-\beta^2}} sin\omega\sqrt{1-\beta^2}\Delta t_i\right)
\end{aligned}
\tag{E-9}
$$

And:

$$
\begin{aligned}
b_{11} &= e^{-\beta\omega\Delta t_i}\left[\left(\frac{2\beta^2-1}{\omega^2\Delta t_i} + \frac{\beta}{\omega}\right)\frac{sin\omega\sqrt{1-\beta^2}\Delta t_i}{\omega\sqrt{1-\beta^2}} + \left(\frac{2\beta}{\omega^3\Delta t_i} + \frac{1}{\omega^2}\right) cos\omega\sqrt{1-\beta^2}\Delta t_i\right] - \frac{2\beta}{\omega^3\Delta t_i} \\
b_{12} &= -e^{-\beta\omega\Delta t_i}\left[\left(\frac{2\beta^2-1}{\omega^2\Delta t_i}\right)\frac{sin\omega\sqrt{1-\beta^2}\Delta t_i}{\omega\sqrt{1-\beta^2}} + \frac{2\beta}{\omega^3\Delta t_i} cos\omega\sqrt{1-\beta^2}\Delta t_i\right] - \frac{1}{\omega^2} + \frac{2\beta}{\omega^3\Delta t_i} \\
b_{21} &= e^{-\beta\omega\Delta t_i}\left[\left(\frac{2\beta^2-1}{\omega^2\Delta t_i} + \frac{\beta}{\omega}\right)\left(cos\omega\sqrt{1-\beta^2}\Delta t_i - \frac{\beta}{\sqrt{1-\beta^2}} sin\omega\sqrt{1-\beta^2}\Delta t_i\right) \right. \\
&\quad - \left(\frac{2\beta}{\omega^3\Delta t_i} + \frac{1}{\omega^2}\right)\left(\omega\sqrt{1-\beta^2} sin\omega\sqrt{1-\beta^2}\Delta t_i \right. \\
&\quad \left.\left. + \beta\omega cos\omega\sqrt{1-\beta^2}\Delta t_i\right)\right] + \frac{1}{\omega^3\Delta t_i} \\
b_{22} &= -e^{-\beta\omega\Delta t_i}\left[\frac{2\beta^2-1}{\omega^2\Delta t_i}\left(cos\omega\sqrt{1-\beta^2}\Delta t_i - \frac{\beta}{\sqrt{1-\beta^2}} sin\omega\sqrt{1-\beta^2}\Delta t_i\right) \right. \\
&\quad \left. - \frac{2\beta}{\omega^3\Delta t_i}\left(\omega\sqrt{1-\beta^2} sin\omega\sqrt{1-\beta^2}\Delta t_i + \beta\omega cos\omega\sqrt{1-\beta^2}\Delta t_i\right)\right] \\
&\quad - \frac{1}{\omega^3\Delta t_i}
\end{aligned}
\tag{E-10}
$$

Based on Eq. (E-2), the absolute acceleration $\ddot{z}_i$ of the mass at time t_i can be calculated as:

$$\ddot{z}_i = \ddot{x}_i + a_i = -(2\beta\omega\dot{x}_i + \omega^2 x_i) \tag{E-11}$$

Therefore is the initial displacement and velocity of the SDOF system are known, the state of the system at all times t_i can be calculated exactly in an iterative way using Eqs. (E-9), (E-10) and (E-11). It is realized that the calculation of *A* and *B* of Eq. (E-8) depend only on β, ω and Δt_i. If these parameters are constants, *A* and *B* can be evaluated before the evaluation of the system state x_i, $\dot{x}_i$ and $\ddot{z}_i$, which makes it very easy for each step of integration.

E.3 Force excitation

In Eq. (E-1), the SDOF system is subjected to base acceleration, while in the situation of our case, the excitation is the actuator force $F_{act}(t)$, which means that the equation of motion of the SDOF system is:

$$M\ddot{x}(t) + C\dot{x}(t) + Kx(t) = F_{act}(t) \tag{E-12}$$

where M, C and K are the mass damping coefficient and stiffness of the SDOF system. Because the measurements of the excitation is the acceleration of the mass of the actuator, Eq. (E-12) can be rewritten as:

$$M\ddot{x}(t) + C\dot{x}(t) + Kx(t) = ma_{act}(t) \tag{E-13}$$

where m is the mass of the actuator. It then divides both sides of Eq.(E-13) by the system mass *M* gives:

$$\ddot{x}(t) + 2\beta\omega\dot{x}(t) + \omega^2 x(t) = \frac{m}{M} a_{act}(t) \tag{E-14}$$

Since the coefficient $\frac{m}{M}$ can be compensated by the control gain later, without of loss generality, Eq. (E-14) can be written as:

$$\ddot{x}(t) + 2\beta\omega\dot{x}(t) + \omega^2 x(t) = a_{act}(t) \tag{E-15}$$

Then the equations of the Nigam Jennings method derived in Sec. E.2 can be used to estimate the reference modal coordinates q^r.

References

[1] N. C. Nigam and P. C. Jennings, "Calculation of Respose Spectra from Strong-Motion Erathquake Records.," *Bull. Seismol. Soc. Am.*, vol. 59, no. 2, pp. 909–922, 1969.

Appendix F Least Squares Filter

F.1 Introduction

The method of Least Squares is a model-dependent procedure to solve the linear filtering problem. To illustrate the basic idea of least squares, suppose it has a set of real-valued sensor measurements $u(1), u(2), \ldots, u(N)$, measured at times $t_1, t_2, \ldots, t_N$, respectively, and the requirement is to build a curve that is used to fit these measurements in some optimum way. For the method of Least Squares, the best fit is obtained by minimizing the sum of squares of difference between $u(i)$ for $i = 1,2, \ldots, N$ and the corresponding points on the fitted curve.

The method of Least Squares is deterministic in approach. It uses the time averages with the result that the filter depends on the total number of samples used in the computation.

F.2 The Least Squares estimation problem

For a physical phenomenon that has two sets of variables $d(i)$ and $u(i)$. It is assumed that the variable $d(i)$ is observed at time step i in response to the subset of variables $u(i)$, $u(i-1)$,…, $u(i-M+1)$ applied as inputs, which means that $d(i)$ is a function of the inputs $u(i)$, $u(i-1)$,…, $u(i-M+1)$. Therefore, the response $d(i)$ is modelled as:

$$d(i) = \sum_{k=0}^{M-1} w_{ok}^{*} u(i-k) + e_o(i) \tag{F-1}$$

where the w_{ok} are the unknown parameters of the model, and $e_o(i)$ is the measurement error. This model is called the multiple linear regression model.

The measurement error $e_o(i)$, which is an unobservable random variable, is customary to assume as the white with zero mean and variance σ^2. Therefore, Eq. (F-1) can be rewrite in the ensemble-averaged form:

$$E[d(i)] = \sum_{k=0}^{M-1} w_{ok}^{*} u(i-k) \tag{F-2}$$

The problem is to estimate the unknown parameters w_{ok} given the two observable sets of variables $d(i)$ and $u(i)$, $i = 1,2,\dots,N$. Defining the estimation error $e(i)$ as the difference between the desired response $d(i)$ and the filter output $y(i)$ as:

$$e(i) = d(i) - y(i) \tag{F-3}$$

where:

$$y(i) = \sum_{k=0}^{M-1} w_{k}^{*} u(i-k) \tag{F-4}$$

Therefore, Eq. (F-3) can be written as:

$$e(i) = d(\mathrm{i}) - \sum_{k=0}^{M-1} w_{k}^{*} u(i-k) \tag{F-5}$$

In the method of Least Squares, the optimal parameters w_k are chosen such that the following sum of error squares objective function can be minimized:

$$\mathrm{F}_{obj}(w_0, w_1, \dots, w_{M-1}) = \sum_{i=M}^{N} |e(i)|^2 \tag{F-6}$$

F.3 Principle of orthogonality

Eq. (F-6) can be written as:

$$\mathrm{F}_{obj}(w_0, w_1, \dots, w_{M-1}) = \sum_{i=M}^{N} e(i)e^{*}(i) \tag{F-7}$$

Let the kth tap-weight w_k be expressed in term of its real and imaginary parts as:

$$w_k = a_k + jb_k, \quad k = 0,1,\dots,M-1 \tag{F-8}$$

Then from Eq. (F-5):

$$e(i) = d(\mathrm{i}) - \sum_{k=0}^{M-1} (a_k - jb_k) u(i-k) \tag{F-9}$$

By defining the *k*th component of the gradient vector $\boldsymbol{\nabla}\mathrm{F}_{obj}$ as the derivative of the objective function $\mathrm{F}_{obj}(w_0, w_1, \dots, w_{M-1})$ with respect to the real and imaginary parts of tap-weight w_k as:

$$\nabla_k \mathrm{F}_{obj} = \frac{\delta \mathrm{F}_{obj}}{\delta a_k} + \mathrm{j}\frac{\delta \mathrm{F}_{obj}}{\delta b_k} \tag{F-10}$$

Substituting Eq. (F-7) into Eq. (F-10) gives:

$$\nabla_k \mathrm{F}_{obj} = -\sum_{i=M}^{N}\left[e(i)\frac{\delta e^*(i)}{\delta a_k} + e^*(i)\frac{\delta e(i)}{\delta a_k} + je(i)\frac{\delta e^*(i)}{\delta b_k} + je(i)\frac{\delta e(i)}{\delta b_k}\right] \tag{F-11}$$

where from Eq. (F-9):

$$\begin{aligned}\frac{\delta e(i)}{\delta a_k} &= -u(i-k)\\ \frac{\delta e^*(i)}{\delta a_k} &= -u^*(i-k)\\ \frac{\delta e(i)}{\delta b_k} &= ju(i-k)\\ \frac{\delta e^*(i)}{\delta b_k} &= -ju^*(i-k)\end{aligned} \tag{F-12}$$

Substituting Eq. (F-12) into Eq. (F-11) gives:

$$\nabla_k \mathrm{F}_{obj} = -2\sum_{i=M}^{N} u(i-k)\, e^*(i) \tag{F-13}$$

For the minimum problem of the objective function, the following conditions must be satisfied simultaneously:

$$\nabla_k \mathrm{F}_{obj} = 0, \quad k = 0,1,\dots,M-1 \tag{F-14}$$

Therefore the orthogonal equations can be derived as:

$$\sum_{i=M}^{N} u(i-k)\, e^*_{min}(i) = 0, \quad k = 0,1,\dots,\mathrm{M}-1 \tag{F-15}$$

The time average on the left hand side of Eq. (F-15) means that the cross-correlation between the tap input $u(i-k)$ and the minimum estimation error $e_{min}(i)$ over the values of time i in the range of [*M*, *N*] for a fixed value of *k*.

F.4 Least Squares Filter

If the optimal tap weights are assumed to be $\widehat{w}_t,\ t = 0,1,\dots,\mathrm{M}-1$ then From Eq. (F-5):

$$e_{min}(i) = d(i) - \sum_{t=0}^{M-1} \widehat{w}_t^* u(i-k) \tag{F-16}$$

Substituting Eq. (F-16) into Eq. (F-15) gives:

$$\sum_{t=0}^{M-1} \widehat{w}_t \sum_{i=M}^{N} u(i-k)u^*(i-t) = \sum_{i=M}^{N} u(i-k)d^*(i)\,,\quad k = 0,1,\dots,\mathrm{M}-1 \tag{F-17}$$

Here, it is assumed that:

$$\Phi(t,k) = \sum_{i=M}^{N} u(i-k)u^*(i-t)\,,\quad 0 \le (t,k) \le M-1 \tag{F-18}$$

And:

$$z(-k) = \sum_{i=M}^{N} u(i-k)d^*(i) \tag{F-19}$$

Then, Eq. (F-17) can be written as:

$$\sum_{t=0}^{M-1} \widehat{w}_t \Phi(t,k) = z(-k),\quad k = 0,1,\dots,\mathrm{M}-1 \tag{F-20}$$

It can recast the equations of (F-20) in matrix form by introducing the following definitions.

The *M*-by-*M* time-averaged correlation matrix $\boldsymbol{\Phi}$:

$$\boldsymbol{\Phi} = \begin{bmatrix} \Phi(0,0) & \Phi(1,0) & \cdots & \Phi(\mathrm{M}-1,0) \\ \Phi(0,1) & \Phi(1,1) & \cdots & \Phi(\mathrm{M}-1,1) \\ \vdots & \vdots & \ddots & \vdots \\ \Phi(0,\mathrm{M}-1) & \Phi(1,\mathrm{M}-1) & \cdots & \Phi(\mathrm{M}-1,\mathrm{M}-1) \end{bmatrix} \tag{F-21}$$

The *M*-by-1 time-averaged cross-correlation vector:

$$\boldsymbol{z} = [z(0), z(-1), \dots, z(-M+1)]^T \tag{F-22}$$

The *M*-by-1 tap weight vector of the least squares filter:

$$\hat{\boldsymbol{w}} = [\hat{w}_0, \hat{w}_1, \dots, \hat{w}_{M-1}]^T \tag{F-23}$$

Therefore, Eq. (F-20) can be rewritten as:

$$\boldsymbol{\Phi}\hat{\boldsymbol{w}} = \boldsymbol{z} \tag{F-24}$$

The above equation is the matrix form of the normal equations for linear least-squares filter. If the matrix $\boldsymbol{\Phi}$ is non-singular, the tap weight vector of the linear least squares filter can be solved as:

$$\hat{\boldsymbol{w}} = \boldsymbol{\Phi}^{-1}\boldsymbol{z} \tag{F-25}$$

References

[1] H. Simon, "*Adaptive filter theory*.", Prentice Hall, 2002.